OPTICAL TRANSITIONS
IN
AMORPHOUS SEMICONDUCTORS

A Thesis

Submitted to the Faculty of Graduate Studies and Research

In Partial Fulfillment of the Requirements

for the Degree of

Doctor of Philosophy

in Electronic Systems Engineering

UNIVERSITY OF REGINA

By

Farida Orapunt

Regina, Saskatchewan

April 2012

© Copyright 2012: F. Orapunt

UNIVERSITY OF REGINA

FACULTY OF GRADUATE STUDIES AND RESEARCH

SUPERVISORY AND EXAMINING COMMITTEE

Farida Orapunt, candidate for the degree of Doctor of Philosophy in Engineering, has presented a thesis titled, ***Optical Transitions in Amorphous Semiconductors,*** in an oral examination held on February 8, 2012. The following committee members have found the thesis acceptable in form and content, and that the candidate demonstrated satisfactory knowledge of the subject material.

External Examiner: Dr. Javshri Sabarinathan, University of Western Ontario

Supervisor: Dr. Stephen OLeary, Adjunct

Committee Member: *Dr. Luigi Benedicenti, Software Systems Engineering

Committee Member: Dr. Paul Laforge, Electronic Systems Engineering

Committee Member: *Dr. Ron Palmer, Electronic Systems Engineering

Committee Member: Dr. Garth Huber, Department of Physics

Chair of Defense: Dr. Dongyan Blachford, Faculty of Graduate Studies and Research

*Not present at defense

ABSTRACT

In this thesis, a quantitative analysis of the optical response of an amorphous semiconductor is presented. The entire analysis is cast within the framework of an empirical model for the valence band and conduction band density of states functions, that captures the basic features expected of these functions. A novel aspect of this analysis is the introduction of the density of localized valence band and conduction band electronic states and the establishment of a means of evaluating these densities from knowledge of the density of states functions coupled with the locations of the valence band and conduction band mobility edges. The determination of the contributions to the joint density of states function attributable to the various types of optical transitions, as a function of the location of these mobility edges, is another novel feature of this analysis. This formalism is then applied in order to determine the spectral dependence of the normalized dipole matrix element squared average corresponding to such a semiconductor. A means of determining the spectral dependence of the optical absorption coefficient is also provided. Finally, this formalism is applied to the specific case of plasma enhanced chemical vapor deposition deposited hydrogenated amorphous silicon, this being the most widely used amorphous semiconductor at present. It is found that the mobility gap value suggested by Jackson *et al.* [*Physical Review B*, vol. 31, pp. 5187-5198, 1985] is discordant with the experimentally measured optical response. It is also found that the effective masses associated with the electrons and holes within plasma enhanced chemical vapor deposition are greater than those that oc-

cur in crystalline silicon. The prospects for future work in this field, that builds upon the results presented herein, are commented upon.

ACKNOWLEDGMENT

First and foremost, I want to thank my advisor, Dr. Stephen Karrer O'Leary. It has an honor to be his Ph. D. Student. I gratefully appreciate his contributions, in terms of time, ideas, and funding. These made my my Ph. D. experience productive and stimulating. His advice and comments greatly helped me with my progress. I also appreciated his open mind and confidence, allowing me to propose and develop my own ideas. The joy and enthusiasm he has for his research was contagious and motivational for me, even during the tough times. I am also thankful for the excellent role model he has provided for me.

I would like to thank my committee members, Dr. Luigi Benedicenti, Dr. Garth Huber, and Dr. Paul Laforge, and Dr. Jayshri Sabarinathan, for their contributions which have helped shape the final form of this thesis. I would especially thank Dr. Luigi Benedicenti for his assistance and cooperation with regards to my funding. I gratefully acknowledge the funding sources that made my Ph. D. work possible. I was funded by the Natural Sciences and Engineering Research Council of Canada (NSERC) through the Faculty of Graduate Studies and Research in the University of Regina for my first three years.

Lastly, I offer my regards and blessing to all those who supported me in any respect during the completion of this thesis.

Farida Orapunt

DEDICATION

This page is to honor and thank those who have helped me along the way. My time at the University of Regina was made enjoyable in large part due to the many friends and groups that became a part of my life. I am grateful for the time I spent with roommates and friends, and for the many great memories.

Especially, I would like to thank my family for all their love and encouragement. For my parents who raised me with a love of science and supported me in all of my pursuits. Most of all, I would like to thank my loving, supportive, encouraging, and patient husband, Gary, whose faithful support during the final stages of this Ph. D. is so appreciated. Thank you.

TABLE OF CONTENTS

ABSTRACT ii

ACKNOWLEDGMENT iv

DEDICATION v

LIST OF TABLES x

LIST OF FIGURES xxxvi

LIST OF SYMBOLS xxxvii

GLOSSARY OF ACRONYMS xli

CHAPTERS

1 INTRODUCTION 1

1.1 The role that disorder plays in shaping the distribution of electronic states 5

1.2 Optical response 9

1.3 Thesis objectives 14

2 A DENSITY OF STATES ANALYSIS 16

2.1 Introduction 16

2.2 Types of solids 19

2.3 The electronic configuration of isolated atoms 21

2.4 Energy levels in solids 24

2.5 Energy band diagrams 28

2.6 Localization and the role of disorder 30

2.7 The free electron model and the density of states 36

2.8 Empirical models for the distribution of electronic states: a review . 41

2.9 General empirical DOS model 48

2.10 The mobility edges 54

3 A JOINT DENSITY OF STATES ANALYSIS 63

3.1 Introduction 63

3.2 The relationship between the imaginary part of the dielectric function and the valence band and conduction band DOS functions . . . 66

3.3 The spectral dependence of the JDOS integrand and the JDOS function 72

3.4 The various types of optical transitions 88

3.5 Means of evaluating the contributions to the JDOS function attributable to the various types of optical transitions 90

3.6 Numerical JDOS results 97

3.7 Spectral dependence of the optical transition matrix element 108

3.8 The spectral dependence of the optical absorption coefficient 115

4 APPLICATION OF THE DOS AND JDOS FORMALISM TO THE SPECIFIC CASE OF PECVD A-SI:H 120

4.1 Introduction 120

4.2 The DOS functions associated with PECVD a-Si:H 122
4.3 DOS modeling parameter selections for subsequent analysis 136
4.4 JDOS evaluation for PECVD a-Si:H 139
4.5 Evaluation of n_{vloc} and n_{cloc} for PECVD a-Si:H 142
4.6 Evaluation of the JDOS contributions corresponding to PECVD a-Si:H 145
4.7 Evaluation of the spectral dependence of the matrix element associated with PECVD a-Si:H 154
4.8 Spectral variations in the optical transition matrix element and their impact on the optical properties associated with PECVD a-Si:H . . 159
4.9 Evaluation of the optical absorption coefficient associated with PECVD a-Si:H 167
4.10 A quantitative characterization of the optical absorption spectrum associated with PECVD a-Si:H 179
4.11 Effective mass determinations 191

5 CONCLUSIONS 195

REFERENCES 202

LIST OF TABLES

2.1 The nominal DOS modeling parameter selections used for the purposes of this analysis. 54

3.1 The nominal DOS modeling parameter selections used for the purposes of this analysis. 73

4.1 The DOS modeling parameter determinations corresponding to PECVD a-Si:H. These parameters were determined through fits of Eqs. (4.7) and (4.8) to the square of the experimental PECVD a-Si:H DOS data of Jackson *et al* [49]. The values corresponding to γ_{V} and γ_{C} could not be determined. 130

4.2 The DOS modeling parameter determinations corresponding to PECVD a-Si:H. These parameters were determined through fits of Eqs. (4.3) and (4.4) to the PECVD a-Si:H DOS data of Jackson *et al.* [49] over the exponential regions. The first set of DOS modeling parameter selections is determined by setting N_{VO} and N_{CO} to the values set in Table 4.1. The second set of DOS modeling parameter selections is determined by setting E_{V} and E_{C} to the values set in Table 4.1 . 134

4.3 The DOS modeling parameters for fixed band tail breadths. All of the DOS modeling parameters are from O'Leary [46]. 140

4.4 The DOS modeling parameters for varying tail breadths. All of the other DOS modeling parameters are from O'Leary [46]. 142

4.5 The PECVD a-Si:H DOS modeling parameter selections used for the purposes of this analysis. The relationship between the valence band and conduction band tail breadths, γ_V and γ_C, is as described in Eq. (4.11). These modeling parameters were found through a fit with the PECVD a-Si:H JDOS experimental results of Jackson *et al.* [49]. Most of these DOS modeling parameter selections are from Table 4.4. 143
4.6 The PECVD a-Si:H DOS modeling parameter selections used for the purposes of this analysis. 163
4.7 The DOS modeling parameters corresponding to each data set. Data sets from Cody *et al.* [12], Remeš [58], and Viturro and Weiser [59] are considered. 174
4.8 The DOS modeling parameters corresponding to the other data sets from Viturro and Weiser [59] are tabulated. 177

LIST OF FIGURES

1.1 Semiconductor and flat panel display shipments plotted as a function of year. In the two decades since their introduction, flat panel displays have developed into a multi-billion dollar market. This data was obtained from the Information Society Technology website [1]. . 4

1.2 The distribution of electronic states associated with: (a) a hypothetical crystalline semiconductor, and (b) its disordered counterpart [9]. 7

1.3 The wave functions associated with a representative disordered system: (a) the wave function associated with an extended electronic state; (b) the wave function associated with a localized electronic state. 8

1.4 The distribution of electronic states associated with a hypothetical disordered semiconductor. The ranges of energy corresponding to the VBE, VBL, CBE, and CBL electronic states are clearly depicted. The valence band and conduction band mobility edges, $E_{\mathrm{V}\mu}$ and $E_{\mathrm{C}\mu}$, respectively, are also depicted. 10

1.5 The variation in the relative intensity, $I(z)/I_0$, with the penetration depth, z, for various selections of the optical absorption coefficient, α. 11

2.1 The arrangement of atoms within hypothetical crystalline, polycrystalline, and amorphous semiconductors. This figure is from Nguyen [28]. 20

2.2 A schematic illustration of the shell model associated with an isolated Si atom, with the associated energy levels being explicitly depicted. (a) The shell model of an isolated Si atom, showing the 10 core electrons, associated with the completely filled $n = 1$ and $n = 2$ shells, and the 4 valence electrons associated with the 3s and 3p subshells; (b) The energy levels in the potential well of the nucleus are also depicted schematically. The size of the nucleus has been greatly exaggerated for the purposes of illustration. 23

2.3 The energy bands for diamond as a function of the lattice constant, a. Isolated carbon atoms contain six electrons, which occupy the $1s$, $2s$, and $2p$ orbitals in pairs. The energy of an electron occupying the $2s$ and $2p$ orbitals is indicated on the figure. As the lattice constant is reduced, there is an overlap between the electron wave functions associated with the adjacent atoms. This leads to a splitting of the energy levels, consistent with the Pauli exclusion principle. This splitting results in an energy band containing $2N$ states in the $2s$ band and $6N$ states in the $2p$ band, where N denotes the number of atoms in the crystal. A further reduction in the lattice constant causes the $2s$ and $2p$ energy bands to merge and split yet again into two bands, containing $4N$ states each. In this illustration, E_g denotes the energy gap. This figure is after Streetman [31]. This particular image was borrowed from Malik [32]. 27

2.4 The relationship between the electron energy and the electron wavevector, k, for a free electron for the one-dimensional case. 29

2.5 A two-dimensional schematic representation of the distribution of atoms within a hypothetical sample of a-Si. The coordination number associated with each Si atom within the network, i.e., the number of nearest neighbor atoms, is depicted. The amount of disorder present within a-Si has been exaggerated for the purposes of illustration. 31
2.6 Localized and extended wave functions. These plots are drawn from the author's conception. 33
2.7 A schematic representation of Anderson's model. 34
2.8 The potential energy configuration for the one-dimensional case. . . 38
2.9 The potential energy configuration for the three-dimensional case. This figure is after Thevaril [36]. 40
2.10 The distribution of electronic states associated with hypothetical crystalline and disordered semiconductors. The distribution of electronic states associated with a crystalline semiconductor is depicted with the dashed lines, while that associated with the disordered semiconductor is shown with the solid lines. While there is no true energy gap for the case of a disordered semiconductor, often the diminished region in the distribution of electronic states is referred as the 'pseudo-gap' region. The states between the conduction band and valence band mobility edges are localized while the other states are extended. The conduction band and valence band mobility edges are depicted with the dotted lines. This particular image was borrowed from Nguyen [37]. 42

2.11 The valence band DOS function, $N_{\mathrm{V}}(E)$, corresponding to various selections of γ_{V}, N_{VO} being set to $2 \times 10^{22}\mathrm{cm}^{-3}\mathrm{eV}^{-3/2}$ and E_{V} being set to 0 eV for all cases. This plot is cast on a linear scale. 50

2.12 The valence band DOS function, $N_{\mathrm{V}}(E)$, corresponding to various selections of γ_{V}, N_{VO} being set to $2 \times 10^{22}\mathrm{cm}^{-3}\mathrm{eV}^{-3/2}$ and E_{V} being set to 0 eV for all cases. This plot is cast on a logarithmic scale. . . 51

2.13 The conduction band DOS function, $N_{\mathrm{C}}(E)$, corresponding to various selections of γ_{C}, N_{CO} being set to $2 \times 10^{22}\mathrm{cm}^{-3}\mathrm{eV}^{-3/2}$ and E_{C} being set to 0 eV for all cases. This plot is cast on a linear scale. . . 52

2.14 The conduction band DOS function, $N_{\mathrm{C}}(E)$, corresponding to various selections of γ_{C}, N_{CO} being set to $2 \times 10^{22}\mathrm{cm}^{-3}\mathrm{eV}^{-3/2}$ and E_{C} being set to 0 eV for all cases. This plot is cast on a logarithmic scale. 53

2.15 The valence band and conduction band DOS functions, $N_{\mathrm{V}}(E)$ and $N_{\mathrm{C}}(E)$, corresponding to a-Si:H, specified in Eq. (2.28) and Eq. (2.29), determined assuming the nominal a-Si:H DOS modeling parameter selections of O'Leary [47]. These nominal DOS modeling parameter selections are tabulated in Table 2.1. 55

2.16 The valence band and conduction band DOS functions, $N_{\mathrm{V}}(E)$ and $N_{\mathrm{C}}(E)$, with the mobility edge locations indicated. The nominal DOS modeling parameter selections, i.e., the values set in Table 2.1, are employed for the purposes of this analysis. The valence band and conduction band mobility edge locations, $E_{\mathrm{V}\mu}$ and $E_{\mathrm{C}\mu}$, respectively, are indicated with the dotted lines and the arrows. For the purposes of this analysis, it is assumed that $E_{\mathrm{V}\mu}$ is equal to E_{vt} and that $E_{\mathrm{C}\mu}$ is equal to E_{ct}. The locations of the VBE, VBL, CBE, and CBL electronic sates are indicated. Representative VBE-CBE, VBE-CBL, VBL-CBE, and VBL-CBL optical transitions are shown with the arrows. 58

2.17 The total density of VBL electronic states, n_{VBL}, as a function of the valence band mobility edge location, $E_{\mathrm{V}\mu}$, for a number of selections of the valence band tail breadth, γ_{V}. All other DOS modeling parameters are set to their nominal values, i.e., the values set in Table 2.1. 60

2.18 The total density of CBL electronic states, n_{CBL}, as a function of the conduction band mobility edge location, $E_{\mathrm{C}\mu}$, for a number of selections of the conduction band tail breadth, γ_{C}. All other DOS modeling parameters are set to their nominal values, i.e., the values set in Table 2.1 61

3.1 The optical transitions permitted from a given single-spin electronic state associated with the valence band for both c-Si and PECVD a-Si:H. This figure is from Thevaril [38]. 70

3.2 The JDOS integrand, $N_{\mathrm{V}}(E)N_{\mathrm{C}}(E+\hbar\omega)$, as a function of energy, E, for the photon energy, $\hbar\omega$, set to 1.7 eV. The nominal DOS modeling parameter selections, specified in Table 3.1, are used for the purposes of this analysis. This plot is cast on a linear scale. . . 74

3.3 The JDOS integrand, $N_{\mathrm{V}}(E)N_{\mathrm{C}}(E+\hbar\omega)$, as a function of energy, E, for the photon energy, $\hbar\omega$, set to 2.3 eV. The nominal DOS modeling parameter selections, specified in Table 3.1, are used for the purposes of this analysis. This plot is cast on a linear scale. . . 75

3.4 The JDOS integrand, $N_{\mathrm{V}}(E)N_{\mathrm{C}}(E+\hbar\omega)$, as a function of energy, E, for a number of photon energies, i.e., $\hbar\omega$ set to 1.7, 1.9, 2.1, and 2.3 eV. The nominal DOS modeling parameter selections, specified in Table 3.1, are used for the purposes of this analysis. This plot is cast on a logarithmic scale. 77

3.5 The JDOS function, J, as a function of the photon energy, $\hbar\omega$. The nominal DOS modeling parameter selections, specified in Table 3.1, are used for the purposes of this analysis. This plot is cast on a linear scale. 78

3.6 The JDOS function, J, as a function of the photon energy, $\hbar\omega$. The nominal DOS modeling parameter selections, specified in Table 3.1, are used for the purposes of this analysis. This plot is cast on a logarithmic scale. 79

3.7 The JDOS function, J, as a function of the photon energy, $\hbar\omega$, for a number of selections of γ, where $\gamma = \gamma_{\mathrm{V}} = \gamma_{\mathrm{C}}$. The nominal DOS modeling parameter selections, specified in Table 3.1, with the exception of γ_{V} and γ_{C}, are used for the purposes of this analysis. This plot is cast on a linear scale. 80

3.8 The JDOS function, J, as a function of the photon energy, $\hbar\omega$, for a number of selections of γ, where $\gamma = \gamma_{\mathrm{V}} = \gamma_{\mathrm{C}}$. The nominal DOS modeling parameter selections, specified in Table 3.1, with the exception of γ_{V} and γ_{C}, are used for the purposes of this analysis. This plot is cast on a logarithmic scale. 81

3.9 The JDOS function, J, as a function of the photon energy, $\hbar\omega$. The exact result with band tails taken into account, i.e., $\gamma_{\mathrm{V}} = \gamma_{\mathrm{C}} =$50 meV, determined through numerical integration, i.e., Eq. (3.12), depicted with the solid line, is contrasted with the analytical result, Eq. (3.15), which is depicted with the dashed line. The nominal DOS modeling parameter selections, specified in Table 3.1, are used for the purposes of this analysis. This plot is cast on a linear scale. 83

3.10 The JDOS function, J, as a function of the photon energy, $\hbar\omega$. The exact result with band tails taken into account, i.e., $\gamma_V = \gamma_C$ =50 meV, determined through numerical integration, i.e., Eq. (3.12), depicted with the solid line, is contrasted with the analytical result, Eq. (3.15), which is depicted with the dashed line. The nominal DOS modeling parameter selections, specified in Table 3.1, are used for the purposes of this analysis. This plot is cast on a logarithmic scale. 84

3.11 The square-root of the JDOS function as a function of the photon energy, $\hbar\omega$, for the nominal DOS modeling parameter selections specified in Table 3.1. A linear extrapolation to the abscissa axis, and the resultant "effective energy gap," are also depicted. This plot is cast on a linear scale. 86

3.12 The square-root of the JDOS function as a function of the photon energy, $\hbar\omega$, for a number of selections of γ, where $\gamma = \gamma_V = \gamma_C$. The nominal DOS modeling parameter selections, specified in Table 3.1, with the exception of γ_V and γ_C, are used for the purposes of this analysis. The linear extrapolations to the abscissa axis, and the resultant "effective energy gaps," are also depicted. This plot is cast on a linear scale. 87

3.13 The factors in the JDOS integrand, $N_{\mathrm{V}}(E)$ and $N_{\mathrm{C}}(E + \hbar\omega)$, as functions of energy, E, for the photon energy, $\hbar\omega$, set to 1.7 eV, all DOS modeling parameter selections being set to their nominal values, i.e., the values set in Table 3.1, with $E_{\mathrm{V}\mu}$ set to E_{vt} and $E_{\mathrm{C}\mu}$ set to E_{ct}. It is noted that this case corresponds to the condition that $E_{\mathrm{C}\mu} - \hbar\omega > E_{\mathrm{V}\mu}$, i.e., $\hbar\omega < E_{\mathrm{C}\mu} - E_{\mathrm{V}\mu}$. The location of energies $E_{\mathrm{C}\mu} - \hbar\omega$ and $E_{\mathrm{V}\mu}$ are indicated with the light dotted lines and the arrows. The location of the VBE, VBL, CBE, and CBL electronic states are indicated. 91

3.14 The factors in the JDOS integrand, $N_{\mathrm{V}}(E)$ and $N_{\mathrm{C}}(E + \hbar\omega)$, as functions of energy, E, for the photon energy, $\hbar\omega$, set to 2.3 eV, all DOS modeling parameter selections being set to their nominal values, i.e., the values set in Table 3.1, with $E_{\mathrm{V}\mu}$ set to E_{vt} and $E_{\mathrm{C}\mu}$ set to E_{ct}. It is noted that this case corresponds to the condition that $E_{\mathrm{C}\mu} - \hbar\omega \leq E_{\mathrm{V}\mu}$, i.e., $\hbar\omega \geq E_{\mathrm{C}\mu} - E_{\mathrm{V}\mu}$. The location of energies $E_{\mathrm{C}\mu} - \hbar\omega$ and $E_{\mathrm{V}\mu}$ are indicated with the light dotted lines and the arrows. The location of the VBE, VBL, CBE, and CBL electronic states are indicated. 92

3.15 The JDOS integrand, $N_{\rm V}(E)N_{\rm C}(E+\hbar\omega)$, as a function of energy, E, for the photon energy, $\hbar\omega$, set to 1.7 eV, all DOS modeling parameter selections being set to their nominal values, i.e., the values set in Table 3.1, with $E_{\rm V\mu}$ set to $E_{\rm vt}$ and $E_{\rm C\mu}$ set to $E_{\rm ct}$. It is noted that this case corresponds to the condition that $E_{\rm C\mu}-\hbar\omega > E_{\rm V\mu}$, i.e., $\hbar\omega < E_{\rm C\mu}-E_{\rm V\mu}$. The location of energies $E_{\rm V\mu}$ and $E_{\rm C\mu}-\hbar\omega$ are indicated with the light dotted lines and the arrows. The region of the JDOS integrand corresponding to the overlap of the VBE electronic states and the CBL electronic states, this region corresponding to the contribution to the JDOS function corresponding to the VBE-CBL optical transitions, is indicated. The region of the JDOS integrand corresponding to the overlap of the VBL electronic states and the CBL electronic states, this region corresponding to the contribution to the JDOS function corresponding to the VBL-CBL optical transitions, is indicated. The region of the JDOS integrand corresponding to the overlap of the VBL electronic states and the CBE electronic states, this region corresponding to the contribution to the JDOS function corresponding to the VBL-CBE optical transitions, is indicated. For this particular selection of $\hbar\omega$, i.e., $\hbar\omega < E_{\rm C\mu}-E_{\rm V\mu}$, there is no overlap in the JDOS integrand between the VBE electronic states and the CBE electronic states, i.e., the contribution to the JDOS function corresponding to VBE-CBE optical transitions, is nil. 93

3.16 The JDOS integrand, $N_{\mathrm{V}}(E)N_{\mathrm{C}}(E+\hbar\omega)$, as a function of energy, E, for the photon energy, $\hbar\omega$, set to 2.3 eV, all DOS modeling parameter selections being set to their nominal values, i.e., the values set in Table 3.1, with $E_{\mathrm{V}\mu}$ set to E_{vt} and $E_{\mathrm{C}\mu}$ set to E_{ct}. It is noted that this case corresponds to the condition that $E_{\mathrm{C}\mu} - \hbar\omega \leq E_{\mathrm{V}\mu}$, i.e., $\hbar\omega \geq E_{\mathrm{C}\mu} - E_{\mathrm{V}\mu}$. The location of energies $E_{\mathrm{V}\mu}$ and $E_{\mathrm{C}\mu} - \hbar\omega$ are indicated with the light dotted lines and the arrows. The region of the JDOS integrand corresponding to the overlap of the VBE electronic states and the CBE electronic states, this region corresponding to the contribution to the JDOS function corresponding to the VBE-CBE optical transitions, is indicated. The region of the JDOS integrand corresponding to the overlap of the VBE electronic states and the CBL electronic states, this region corresponding to the contribution to the JDOS function corresponding to the VBE-CBL optical transitions, is indicated. The region of the JDOS integrand corresponding to the overlap of the VBL electronic states and the CBE electronic states, this region corresponding to the contribution to the JDOS function corresponding to the VBL-CBE optical transitions, is indicated. For this particular selection of $\hbar\omega$, i.e., $\hbar\omega \geq E_{\mathrm{C}\mu} - E_{\mathrm{V}\mu}$, there is no overlap in the JDOS integrand between the VBL electronic states and the CBL electronic states, i.e., the contribution to the JDOS function corresponding to VBL-CBL optical transitions, is nil. 94

3.17 The contributions to the JDOS function corresponding to the VBE-CBE, VBE-CBL, VBL-CBE, and VBL-CBL optical transitions, i.e., J, $J_{\text{VBE-CBE}}$, $J_{\text{VBE-CBL}}$, $J_{\text{VBL-CBE}}$, and $J_{\text{VBL-CBL}}$, as functions of the photon energy, $\hbar\omega$, all DOS modeling parameter selections being set to their nominal values, i.e., the values set in Table 3.1, with $E_{\text{v}\mu}$ set to E_{vt} and $E_{\text{c}\mu}$ set to E_{ct}. The overall JDOS function, J, is also plotted as a function of the photon energy, $\hbar\omega$. 99

3.18 The fractional contributions to the JDOS function corresponding to the VBE-CBE, VBE-CBL, VBL-CBE, and VBL-CBL optical transitions, i.e., $\frac{J_{\text{VBE-CBE}}}{J}$, $\frac{J_{\text{VBE-CBL}}}{J}$, $\frac{J_{\text{VBL-CBE}}}{J}$, and $\frac{J_{\text{VBL-CBL}}}{J}$, as functions of the photon energy, $\hbar\omega$, all DOS modeling parameter selections being set to their nominal values, i.e., the values set in Table 3.1, with $E_{\text{v}\mu}$ set to E_{vt} and $E_{\text{c}\mu}$ set to E_{ct}. 101

3.19 The contribution to the JDOS function corresponding to the VBE-CBL and VBL-CBE optical transitions, i.e., $J_{\text{VBL-CBE}}$ and $\text{J}_{\text{VBE-CBL}}$, as functions of the photon energy, $\hbar\omega$, with $\gamma_{\text{v}} = \gamma_{\text{c}} = 25$ meV, $\gamma_{\text{v}} = \gamma_{\text{c}} = 50$ meV, $\gamma_{\text{v}} = \gamma_{\text{c}} = 100$ meV, and $\gamma_{\text{v}} = \gamma_{\text{c}} = 200$ meV, all other DOS modeling parameters being set to their nominal values, i.e., the values set in Table 3.1, with $E_{\text{v}\mu}$ set to E_{vt} and $E_{\text{c}\mu}$ set to E_{ct}. Note that $J_{\text{VBE-CBL}}$ and $J_{\text{VBL-CBE}}$ are completely coincident over the entire spectrum for all cases. The mobility gap, $E_{\text{c}\mu} - E_{\text{v}\mu}$, marked with the arrows for the different cases, varies from case to case, $E_{\text{c}\mu} - E_{\text{v}\mu}$ being equal to $E_{\text{c}} - E_{\text{v}} + \frac{\gamma_{\text{v}}}{2} + \frac{\gamma_{\text{c}}}{2}$, for the case of $E_{\text{v}\mu}$ set to E_{vt} and $E_{\text{c}\mu}$ set to E_{ct}. 104

3.20 The fractional contributions to the JDOS function corresponding to the VBE-CBL and VBL-CBE optical transitions, i.e., $\frac{J_{\text{VBE-CBL}}}{J}$ and $\frac{J_{\text{VBL-CBE}}}{\text{J}}$, as functions of the photon energy, $\hbar\omega$, with $\gamma_{\text{V}} = \gamma_{\text{C}} =$ 25 meV, $\gamma_{\text{V}} = \gamma_{\text{C}} = 50$ meV, $\gamma_{\text{V}} = \gamma_{\text{C}} = 100$ meV, and $\gamma_{\text{V}} = \gamma_{\text{C}} =$ 200 meV, all other DOS modeling parameter selections being set to their nominal values, i.e., the values set in Table 3.1, with $E_{\text{V}\mu}$ set to E_{vt} and $E_{\text{C}\mu}$ set to E_{ct}. Note that $J_{\text{VBE-CBL}}$ and $J_{\text{VBL-CBE}}$ are completely coincident over the entire spectrum. The mobility gap, $E_{\text{C}\mu} - E_{\text{V}\mu}$, marked with the arrows for the different cases, varies from case to case, $E_{\text{C}\mu} - E_{\text{V}\mu}$ being equal to $E_{\text{C}} - E_{\text{V}} + \frac{\gamma_{\text{V}}}{2} + \frac{\gamma_{\text{C}}}{2}$ for the particular case of $E_{\text{V}\mu}$ set to E_{vt} and $E_{\text{C}\mu}$ set to E_{ct}. 105
3.21 The contributions to the JDOS function corresponding to the VBE-CBL and VBL-CBE optical transitions, i.e., $J_{\text{VBE-CBL}}$ and $J_{\text{VBL-CBE}}$, as functions of the photon energy, $\hbar\omega$, with $E_{\text{V}\mu} = E_{\text{vt}} - 200$ meV and $E_{\text{C}\mu} = E_{\text{ct}} + 200$ meV, $E_{\text{V}\mu} = E_{\text{vt}} - 100$ meV and $E_{\text{C}\mu} = E_{\text{ct}} + 100$ meV, $E_{\text{V}\mu} = E_{\text{vt}}$ and $E_{\text{C}\mu} = E_{\text{ct}}$, $E_{\text{V}\mu} = E_{\text{vt}} + 100$ meV and $E_{\text{C}\mu} = E_{\text{ct}} - 100$ meV, and $E_{\text{V}\mu} = E_{\text{vt}} + 200$ meV and $E_{\text{C}\mu} = E_{\text{ct}} - 200$ meV, all other DOS modeling parameter selections being set to their nominal values, i.e., the values set in Table 3.1. Note that $J_{\text{VBE-CBL}}$ and $J_{\text{VBL-CBE}}$ are completely coincident over the entire spectrum. The mobility gap, $E_{\text{C}\mu} - E_{\text{V}\mu}$, varies from case to case. . 107

3.22 The fractional contributions to the JDOS function corresponding to the VBE-CBL and VBL-CBE optical transitions, i.e., $\frac{J_{\text{VBE-CBL}}}{J}$ and $\frac{J_{\text{VBL-CBE}}}{J}$, as functions of the photon energy, $\hbar\omega$, with $E_{\text{v}\mu} = E_{\text{vt}} - 200$ meV and $E_{\text{c}\mu} = E_{\text{ct}} + 200$ meV, $E_{\text{v}\mu} = E_{\text{vt}} - 100$ meV and $E_{\text{c}\mu} = E_{\text{ct}} + 100$ meV, $E_{\text{v}\mu} = E_{\text{vt}}$ and $E_{\text{c}\mu} = E_{\text{ct}}, E_{\text{v}\mu} = E_{\text{vt}}+100$ meV and $E_{\text{c}\mu} = E_{\text{ct}}-100$ meV, and $E_{\text{v}\mu} = E_{\text{vt}}+200$ meV and $E_{\text{c}\mu} = E_{\text{ct}} - 200$ meV, all other DOS modeling parameter selections being set to their nominal values, i.e., the values set in Table 3.1. Note that $\frac{J_{\text{VBE-CBL}}}{J}$ and $\frac{J_{\text{VBL-CBE}}}{J}$ are completely coincident over the entire spectrum. The mobility gap, $E_{\text{c}\mu} - E_{\text{v}\mu}$, varies from case to case, this gap occurring when $\frac{J_{\text{VBE-CBL}}}{J}$ and $\frac{J_{\text{VBL-CBE}}}{J}$ achieve their maxima, i.e., $\frac{1}{2}$. 109

3.23 The fractional contribution to the JDOS function, J_{frac}, as defined in Eq. (3.23), as a function of the photon energy, $\hbar\omega$. All DOS modeling parameters are set to their nominal values, i.e., the values set in Table 3.1, with $E_{\text{v}\mu}$ set to E_{vt} and $E_{\text{c}\mu}$ set to E_{ct}. 111

3.24 The fractional contributions to the JDOS function, J_{frac}, as defined in Eq. (3.23), as a function of the photon energy, $\hbar\omega$, for a number of selections of γ_{v} and γ_{c}, i.e., for the cases of $\gamma_{\text{v}} = \gamma_{\text{c}} = 25$ meV, $\gamma_{\text{v}} = \gamma_{\text{c}} = 50$ meV, $\gamma_{\text{v}} = \gamma_{\text{c}} = 100$ meV, and $\gamma_{\text{v}} = \gamma_{\text{c}} = 200$ meV. All DOS modeling parameters are set to their nominal values, i.e., the value set in Table 3.1, with $E_{\text{v}\mu}$ set to E_{vt} and $E_{\text{c}\mu}$ set to E_{ct}. 112

3.25 The fractional contributions to the JDOS function, J_{frac}, as defined in Eq. (3.23), as a function of the photon energy, $\hbar\omega$, for a number of selection of $E_{\text{v}\mu}$ and $E_{\text{c}\mu}$, i.e., for the cases of $E_{\text{v}\mu} = E_{\text{vt}} -$ 200 meV and $E_{\text{c}\mu} = E_{\text{ct}} + 200$ meV, $E_{\text{v}\mu} = E_{\text{vt}} - 100$ meV, and $E_{\text{c}\mu} = E_{\text{ct}} + 100$ meV, $E_{\text{v}\mu} = E_{\text{vt}}$ and $E_{\text{c}\mu} = E\text{ct}$, $E_{\text{v}\mu} = E_{\text{vt}} +$ 100 meV and $E_{\text{c}\mu} = E_{\text{ct}} - 100$ meV, and $E_{\text{v}\mu} = E_{\text{vt}} + 200$ meV and $E_{\text{c}\mu} = E_{\text{ct}} - 200$ meV, respectively. The other DOS modeling parameter selections are set to their nominal values, i.e., the values set in Table 3.1. 114

3.26 The spectral dependence of the normalized optical transition matrix element squared average, $\Re^2(\hbar\omega)$. The other DOS modeling parameter selections are set to their nominal values, i.e., the values set in Table 3.1. 116

3.27 The spectral dependence of the imaginary part of the dielectric function, $\epsilon_2(\hbar\omega)$. Eq. (3.9) is used for the purposes of this analysis. $\Re^2(\hbar\omega)$ is as specified in Figure 3.26. The other DOS modeling parameter selections are set to their nominal values, i.e., the values set in Table 3.1. 117

3.28 The spectral dependence of the optical absorption coefficient, $\alpha(\hbar\omega)$. Eq. (3.24) is employed for the purposes of this determination. This spectrum is determined assuming the nominal DOS modeling parameters selections specified in Table 3.1. For the purposes of this analysis, $n(\hbar\omega)$ is set to $\sqrt{11.7}$. 119

4.1 The experimental PECVD a-Si:H DOS data of Jackson *et al.* [49]. A linear scale is employed. 125

4.2 The experimental PECVD a-Si:H DOS data of Jackson *et al.* [49]. A logarithmic scale is employed. 126

4.3 The square of the DOS functions corresponding to PECVD a-Si:H. The square of the experimental PECVD a-Si:H DOS data of Jackson *et al.* [49] is depicted with the solid points. The resultant fits, i.e., Eqs. (4.7) and (4.8), for the DOS modeling parameter selections $N_{\mathrm{VO}} = 2.39 \times 10^{22}$ cm^{-3}eV$^{-3/2}$, $N_{\mathrm{CO}} = 3.03 \times 10^{22}$ cm^{-3}eV$^{-3/2}$, $E_{\mathrm{V}} = -1.79$ eV, and $E_{\mathrm{C}} = 0.04$ eV, are clearly shown with the bold solid lines, between energies -3.0 and -1.75 eV for the valence band and between energies 0.0 and 0.75 eV for the conduction band. Extrapolations of these fits are depicted with the dashed lines. These fits were obtained in linear least-squares manners. 129

4.4 The experimental PECVD a-Si:H DOS data of Jackson *et al.* [49] and the fits of this data to Eqs. (4.5) and (4.6) for the DOS modeling parameter selections tabulated in Table 4.1. The experimental data points are depicted with the solid points. The fits are depicted with the bold solid lines. The light solid lines correspond to the upper and lower DOS prefactor selections specified in Table 4.1. This plot is cast on a linear scale. 131

4.5 The DOS functions corresponding to PECVD a-Si:H. The experimental PECVD a-Si:H DOS data of Jackson *et al.* [49] is depicted with the solid points. The resultant exponential fits are shown with the solid lines over the regions over which these fits were determined. Extrapolations of these fits are depicted with the dashed lines. These fits were obtained in linear least-squares manners. . . . 133

4.6 The DOS functions associated with PECVD a-Si:H. The experimental PECVD a-Si:H DOS results of Jackson *et al.* [49] are depicted with the solid points. The fits of Eqs. (4.3) and (4.4) to this experimental data are shown with the lines. For the first set of DOS modeling parameter selections provided in Table 4.2, the corresponding fits are shown with the heavy solid lines. For the second set of DOS modeling parameter selections provided in Table 4.2, the corresponding fits are shown with dotted lines. This plot is cast on a logarithmic scale. 135

4.7 The correlation between the conduction band tail breadth and the valence band tail breadth. The line shows the resultant linear least-squares fit. The experimental data associated with the line is from Sherman *et al.* [22]. The other experimental data point is from Tiedje *et al.* [41]. This figure is after Sherman *et al.* [22]. 138

4.8 The JDOS function corresponding to a-Si:H. The experimental JDOS result of Jackson *et al.* [49] is depicted with solid points. The fit obtained is indicated with the solid line. It is seen that there is almost complete agreement, except for $\hbar\omega < 1.4$ eV, at which point defect absorption dramatically alters the character of the JDOS function, and for $\hbar\omega > 5$ eV, at which point the non-parabolically of the VBB and CBB distributions distorts the resultant JDOS function. Both of these effects are beyond the framework of the present analysis. The parameters used for this fitting are tabulated in Table 4.3. . . . 141

4.9 The dependence of the total densities of VBL and CBL electronic states, n_{VBL} and n_{CBL}, respectively, on the conduction band tail breadth, γ_{C}, for the case of PECVD a-Si:H. γ_{V} is determined assuming the validity of the linear least-squares fit relationship between γ_{V} and γ_{C}, i.e., Eq. (4.11). All DOS modeling parameters are set to their PECVD a-Si:H values, i.e., the values set in Table 4.5. Results corresponding to the range of γ_{C} specified in Figure 4.7 are indicated with the solid lines. Results beyond this range are indicated with dotted lines. 144

4.10 The contributions to the JDOS function corresponding to the VBE-CBE, VBE-CBL, VBL-CBE, and VBL-CBL optical transitions, i.e., $J_{\text{VBE-CBE}}$, $J_{\text{VBE-CBL}}$, $J_{\text{VBL-CBE}}$ and $J_{\text{VBL-CBL}}$, as functions of the photon energy, $\hbar\omega$, for PECVD a-Si:H. The overall JDOS function, J, is also plotted as a function of the photon energy, $\hbar\omega$. The PECVD a-Si:H DOS modeling parameter selections, used for the purposes of this analysis, are tabulated in Table 4.5. 146

4.11 The fractional contributions to the JDOS function corresponding to the VBE-CBE, VBE-CBL, VBL-CBE, and VBL-CBL optical transitions, i.e., $\frac{J_{\text{VBE-CBE}}}{J}$, $\frac{J_{\text{VBE-CBL}}}{J}$, $\frac{J_{\text{VBL-CBE}}}{J}$ and $\frac{J_{\text{VBL-CBL}}}{J}$, as functions of the photon energy, $\hbar\omega$, for γ_{C} set to 10 meV. γ_{V} is determined using the linear least-squares fit relationship between γ_{V} and γ_{C}, i.e., Eq. (4.11). All DOS modeling parameters are set to their PECVD a-Si:H values, i.e., the values set in Table 4.5. 148

4.12 The contributions to the JDOS function corresponding to the VBE-CBE, VBE-CBL, VBL-CBE, and VBL-CBL optical transitions, i.e., $J_{\text{VBE-CBE}}$, $J_{\text{VBE-CBL}}$, $J_{\text{VBL-CBE}}$ and $J_{\text{VBL-CBL}}$, as functions of the photon energy, $\hbar\omega$, for $\gamma_{\text{C}} = 40$ meV. γ_{V} is determined using the linear least-squares fit relationship between γ_{C} and γ_{V}, i.e., Eq. (4.11). All DOS modeling parameters are set to their PECVD a-Si:H values, i.e., the value set in Table 4.5. The overall JDOS function, J, is also plotted as a function of the photon energy, $\hbar\omega$. 150

4.13 The fractional contributions to the JDOS function corresponding to the VBE-CBE, VBE-CBL, VBL-CBE, and VBL-CBL optical transitions, i.e., $\frac{J_{\text{VBE-CBE}}}{J}$, $\frac{J_{\text{VBE-CBL}}}{J}$, $\frac{J_{\text{VBL-CBE}}}{J}$ and $\frac{J_{\text{VBL-CBL}}}{J}$, as functions of the photon energy, $\hbar\omega$, for γ_{C} set to 40 meV. γ_{V} is determined using the linear least-squares fit relationship between γ_{V} and γ_{C}, i.e., Eq. (4.11). All DOS modeling parameters are set to their PECVD a-Si:H values, i.e., the values set in Table 4.5. 152

4.14 The fractional contributions to the JDOS function corresponding to the VBL-CBE and VBL-CBL optical transitions, i.e., $\frac{J_{\text{VBL-CBE}}}{J}$, and $\frac{J_{\text{VBL-CBL}}}{J}$, as functions of the conduction band tail breadth, γ_{C}, evaluated for $\hbar\omega$ set to 1 eV. γ_{V} is determined using the linear least-squares fit relationship between γ_{V} and γ_{C}, i.e., Eq. (4.11). All DOS modeling parameters are set to their PECVD a-Si:H values, i.e., the values set in Table 4.5. 153

4.15 The fractional contributions to the JDOS function corresponding to the VBE-CBL and VBL-CBE optical transitions, i.e., $\frac{J_{\text{VBE-CBL}}}{J}$, and $\frac{J_{\text{VBL-CBE}}}{J}$, as functions of the conduction band tail breadth, γ_{C}, evaluated for $\hbar\omega$ set to $E_{\text{C}\mu} - E_{\text{V}\mu}$. γ_{V} is determined using the linear least-squares fit relationship between γ_{V} and γ_{C}, i.e., Eq. (4.11). All DOS modeling parameters are set to their PECVD a-Si:H values, i.e., the values of the set in Table 4.5. 155

4.16 The fractional contributions to the JDOS function, J_{frac}, as defined in Eq. (4.12), as a function of the photon energy, $\hbar\omega$, for γ_{C} set to 10 meV, γ_{V} being determined using the linear least-squares fit relationship between γ_{V} and γ_{C}, i.e., Eq. (4.11). All DOS modeling parameters are set to their PECVD a-Si:H values, i.e., the values set in Table 4.5. 157

4.17 The fractional contributions to the JDOS function, J_{frac}, as defined in Eq. (4.12), as a function of the photon energy, $\hbar\omega$, for γ_{C} set to 40 meV, γ_{V} being determined using the linear least-squares fit relationship between γ_{V} and γ_{C}, i.e., Eq. (4.11). All DOS modeling parameters are set to their PECVD a-Si:H values, i.e., the values set in Table 4.5. 158

4.18 The fraction of the JDOS function that is attributable solely to the VBE-CBE, VBE-CBL, and VBL-CBE optical transitions, $J_{\text{frac}}(\hbar\omega)$, for the case of PECVD a-Si:H when the mobility gap, $E_{\text{C}\mu} - E_{\text{V}\mu}$, is set to $E_{\text{ct}} - E_{\text{vt}} + 0.2$ eV. Three cases are considered; (1) $E_{\text{V}\mu} = E_{\text{vt}}$ and $E_{\text{C}\mu} = E_{\text{ct}} + 0.2$ eV, (2) $E_{\text{V}\mu} = E_{\text{vt}} - 0.1$ eV and $E_{\text{C}\mu} = E_{\text{ct}} + 0.1$ eV, and (3) $E_{\text{V}\mu} = E_{\text{vt}} - 0.2$ eV and $E_{\text{C}\mu} = E_{\text{ct}}$. For all cases, the DOS modeling parameters are set to the PECVD a-Si:H values assigned in Table 4.6. 160

4.19 The fraction of the JDOS function that is attributable solely to the VBE-CBE, VBE-CBL, and VBL-CBE optical transitions, $J_{\mathrm{frac}}(\hbar\omega)$, for the case of PECVD a-Si:H when the mobility gap, $E_{\mathrm{c}\mu} - E_{\mathrm{v}\mu}$, is set to $E_{\mathrm{ct}} - E_{\mathrm{vt}}$. Three cases are considered; (1) $E_{\mathrm{v}\mu} = E_{\mathrm{vt}} + 0.1$ eV and $E_{\mathrm{c}\mu} = E_{\mathrm{ct}} + 0.1$ eV, (2) $E_{\mathrm{v}\mu} = E_{\mathrm{vt}}$ and $E_{\mathrm{c}\mu} = E_{\mathrm{ct}}$, and (3) $E_{\mathrm{v}\mu} = E_{\mathrm{vt}} - 0.1$ eV and $E_{\mathrm{c}\mu} = E_{\mathrm{ct}} - 0.1$ eV. For all cases, the DOS modeling parameters are set to the PECVD a-Si:H values assigned in Table 4.6. 161

4.20 The fraction of the JDOS function that is attributable solely to the VBE-CBE, VBE-CBL, and VBL-CBE optical transitions, $J_{\mathrm{frac}}(\hbar\omega)$, for the case of PECVD a-Si:H when the mobility gap, $E_{\mathrm{c}\mu} - E_{\mathrm{v}\mu}$, is set to $E_{\mathrm{ct}} - E_{\mathrm{vt}} - 0.2$ eV. Three cases are considered; (1) $E_{\mathrm{v}\mu} = E_{\mathrm{vt}} + 0.2$ eV and $E_{\mathrm{c}\mu} = E_{\mathrm{ct}}$, (2) $E_{\mathrm{v}\mu} = E_{\mathrm{vt}} + 0.1$ eV and $E_{\mathrm{c}\mu} = E_{\mathrm{ct}} - 0.1$ eV, and (3) $E_{\mathrm{v}\mu} = E_{\mathrm{vt}}$ and $E_{\mathrm{c}\mu} = E_{\mathrm{ct}} - 0.2$ eV. For all cases, the DOS modeling parameters are set to the PECVD a-Si:H values assigned in Table 4.6. 162

4.21 The imaginary part of the dielectric function corresponding to PECVD a-Si:H. The experimental data of Jackson *et al.* [49] is depicted with the solid points. The calculated result with $J_{\mathrm{frac}}(\hbar\omega)$ taken into account, for the specific case of $E_{\mathrm{V}\mu} = E_{\mathrm{vt}} - 0.1$ eV and $E_{\mathrm{C}\mu} = E_{\mathrm{ct}} + 0.1$ eV, is shown with the solid line and indicated with an arrow. The calculated result corresponding to the case of $J_{\mathrm{frac}}(\hbar\omega)$ set to unity, i.e., a low mobility gap, is also depicted with the solid line and the arrow. The PECVD a-Si:H DOS modeling parameters are set to the values assigned in Table 4.6. 165

4.22 The index of refraction, n, of a PECVD a-Si:H sample. The experimental data, depicted with the solid points, is from Klazes *et al.* [56]. A first-order polynomial fit to this experimental data is depicted with the solid line. 169

4.23 The index of refraction, n, of a PECVD a-Si:H sample. The experimental data, depicted with the solid points, is from Klazes *et al.* [56]. A third-order polynomial fit to this experimental data is depicted with the solid line. 170

4.24 The index of refraction, n, of a PECVD a-Si:H sample. The experimental data, depicted with the solid points, is from Klazes *et al.* [56]. A tenth-order polynomial fit to this experimental data is depicted with the solid line. A similar fit is shown by Mok and O'Leary [57]. 171

4.25 Three experimental PECVD a-Si:H optical absorption data sets, from Cody *et al.* [12], Remeš [58], and Viturro and Weiser [59], are depicted with the solid points, the upward triangles, and the downward triangles, respectively. The fit to these data sets are depicted with the corresponding solid lines. 173

4.26 The energy gap as a function of the valence band tail breadth. The fit values, corresponding to the fits depicted in Figure 4.25, and tabulated in Table 4.7, are indicated with the solid points. Results corresponding to Cody *et al.* [12] are shown with the open points. The fit values, corresponding to the other experimental data from Viturro and Weiser [59], depicted in Figure 4.27, and tabulated in Table 4.8, are indicated with the asterisks. 175

4.27 The 9 other experimental PECVD a-Si:H optical absorption data sets from Viturro and Weiser [59] are depicted with the open points. The fits to these data sets are depicted with the corresponding solid lines. 176

4.28 The optical absorption spectrum associated with PECVD a-Si:H. The three distinct regions of behavior, suggested by Wood and Tauc [60], are clearly indicated. The experimental data, determined from direct measurements of optical transmission, from the collection efficiency, and from the photoconductivity of the diode and coplanar structures, are from Abeles [64]. 181

4.29 The determination of the breadth of the optical absorption tail for a number of different ranges of optical absorption. The PECVD a-Si:H experimental data, depicted with the open points, is from Remeš [58]. The linear least-squares fit of Eq. (4.15) to this experimental data are taken over the ranges 1×10^{-1} cm^{-1} $\leq \alpha(\hbar\omega) \leq$ 3×10^{-1} cm^{-1}, 2×10^{0} cm^{-1} $\leq \alpha(\hbar\omega) \leq 8 \times 10^{0}$ cm^{-1}, 1×10^{1} cm^{-1} $\leq \alpha(\hbar\omega) \leq 8 \times 10^{1}$ cm^{-1}, 4×10^{2} cm^{-1} $\leq \alpha(\hbar\omega) \leq 2 \times 10^{3}$ cm^{-1}, and 8×10^{3} cm^{-1} $\leq \alpha(\hbar\omega) \leq 2 \times 10^{4}$ cm^{-1}, the resultant fits, labeled 1, 2, 3, 4, and 5, respectively, being depicted with the light solid lines. The E_o values found, for fits 1, 2, 3, 4, and 5, are 187 ± 9 meV, 52 ± 3 meV, 43 ± 2 meV, 67 ± 2 meV, and 119 ± 3 meV, respectively. The upper bound result, depicted with a light dotted line, corresponds to the DOS modeling parameter selections $N_{\mathrm{VO}} = N_{\mathrm{CO}} = 2.0 \times 10^{22}$ cm^{-3}eV$^{-3/2}$, $E_{\mathrm{V}} = 0.0$ eV, $E_{\mathrm{C}} = 1.5$ eV, $\gamma_{\mathrm{V}} = 60$ meV, and $\gamma_{\mathrm{C}} = 27$ meV. The lower bound result, also depicted with a light dotted line, corresponds to the DOS modeling parameter selections $N_{\mathrm{VO}} = N_{\mathrm{CO}} = 4.0 \times 10^{22}$ cm^{-3}eV$^{-3/2}$, $E_{\mathrm{V}} = 0.0$ eV, $E_{\mathrm{C}} = 1.9$ eV, $\gamma_{\mathrm{V}} = 40$ meV, and $\gamma_{\mathrm{C}} = 27$ meV. It is found that one is able to satisfactorily capture the experimental results of Remeš [58] with the DOS modeling parameter selections $N_{\mathrm{VO}} = 2.38 \times 10^{22}$ cm^{-3}eV$^{-3/2}$, $E_{\mathrm{V}} = 0.00$ eV, $E_{\mathrm{C}} = 1.66$ eV, $\gamma_{\mathrm{V}} = 43$ meV, and $\gamma_{\mathrm{C}} = 27$ meV. This fit is also depicted with a light dotted line. 182

4.30 The dependence of E_o on α. The data points, depicted with the open points, correspond to the fit of Eq. (4.15) to the experimental data for various ranges of optical absorption. Results corresponding to the representative fits depicted in Figure 4.29 are shown with the asterisk points, the corresponding error bars being explicitly shown for these particular points. The evaluation of Eq. (4.18), for the case of the upper bound result, i.e., for the DOS modeling parameter selections $N_{\mathrm{VO}} = N_{\mathrm{CO}} = 2.0 \times 10^{22}$ cm^{-3}eV$^{-3/2}$, $E_{\mathrm{V}} = 0.0$ eV, $E_{\mathrm{C}} = 1.5$ eV, $\gamma_{\mathrm{V}} = 60$ meV, and $\gamma_{\mathrm{C}} = 27$ meV, is shown with a heavy solid line. The evaluation of Eq. (4.18), for the case of the lower bound result, i.e., for the DOS modeling parameter selections $N_{\mathrm{VO}} = N_{\mathrm{CO}} = 4.0 \times 10^{22}$ cm^{-3}eV$^{-3/2}$, $E_{\mathrm{V}} = 0.0$ eV, $E_{\mathrm{C}} = 1.9$ eV, $\gamma_{\mathrm{V}} = 40$ meV, and $\gamma_{\mathrm{C}} = 27$ meV, is also shown with a heavy solid line. The evaluation of Eq. (4.18), for the case of this fit with the experimental results of Remeš [58], i.e., for the DOS modeling parameter selections $N_{\mathrm{VO}} = N_{\mathrm{CO}} = 2.38 \times 10^{22}$ cm^{-3}eV$^{-3/2}$, $E_{\mathrm{V}} =$ 0.0 eV, $E_{\mathrm{C}} = 1.66$ eV, $\gamma_{\mathrm{V}} = 43$ meV, and $\gamma_{\mathrm{C}} = 27$ meV, is shown with the dotted line. 187

4.31 A comparison of the DOS effective masses associated with PECVD a-Si:H and c-Si. 194

LIST OF SYMBOLS

α, $\alpha(\hbar\omega)$ .... optical absorption coefficient, optical absorption spectrum

a_o .... interatomic spacing

B .... band width

c .... speed of light in vacuum

$D^2(\hbar\omega)$ ..... optical transition matrix element

$\epsilon_1(\hbar\omega)$ ...... real part of the dielectric function

$\epsilon_2(\hbar\omega)$ ...... imaginary part of the dielectric function

E .... energy level

E_{c} .... conduction band edge

E_{ct} .... critical energies at which the square-root and exponential distributions interface in conduction band

$E_{\mathrm{c}\mu}$ .... conduction band mobility edge

E_{g} .... energy gap

E_{v} .... valence band edge

E_{vt} .... critical energies at which the square-root and exponential distributions interface in valence band

$E_{\mathrm{v}\mu}$ .... valence band mobility edge

E_n .... energy of the electron orbital

γ_{c} .... conduction band tail breadth

γ_{v} .... valence band tail breadth

Δx .... scattering length

$\hbar\omega$ .... photon energy

I .... intensity of light

I_0 .... intensity of light at $z = 0$

$I(z)$ .... optical power per unit area at position z

$J(\hbar\omega)$ .... joint density of states function

$J_{\text{frac}}(\hbar\omega)$ .... fraction of the overall JDOS function attributable to VBE-CBE, VBE-CBL, and VBL-CBE optical transitions

$J_{\text{VBE-CBE}}(\hbar\omega)$ JDOS function attributable to the VBE-CBE optical transitions

$J_{\text{VBE-CBL}}(\hbar\omega)$ JDOS function attributable to the VBE-CBL optical transitions

$J_{\text{VBL-CBE}}(\hbar\omega)$ JDOS function attributable to the VBL-CBE optical transitions

$J_{\text{VBL-CBL}}(\hbar\omega)$ JDOS function attributable to the VBL-CBL optical transitions

k .... electron wave-vector

$\vec{k}$ .... crystal momentum

m_e .... electron mass

m_{C}^* .... DOS effective mass associated with the conduction band

m_{V}^* .... DOS effective mass associated with the valence band

n_x .... effect of confinement in the x direction

n_y .... effect of confinement in the y direction

n_z .... effect of confinement in the z direction

$n(\hbar\omega)$ .... spectral dependence of the refractive index

$n_{\text{CBL}}(E_{\text{C}\mu})$ .. total density of conduction band localized electronic states

$n_{\text{VBL}}(E_{\text{V}\mu})$ .. total density of valence band localized electronic states

∇^2 .... mathematical operator $\nabla \cdot \nabla$

$N_\mathrm{C}(E)$ ...... conduction band density of states function

$N_\mathrm{C}(E)\Delta E$ .. number of conduction band electronic states between energies per unit volume

N_CO .... conduction band DOS prefactor

$N_\mathrm{V}(E)$ ...... valence band density of states function

$N_\mathrm{V}(E)\Delta E$ .. number of valence band electronic states between energies $[E, E + \Delta E]$, per unit volume

N_VO .... valence band DOS prefactor

ω .... angular frequency of the light

p .... momentum of the particle

q .... electron charge

Ψ .... wave function associated with the electron

ρ_A .... atomic density of PEVCD a-Si:H

$\vec{\eta}$ .... polarization vector of the incident light

$\vec{R}$ .... dipole operator

$R_\mathrm{c,v}$ .... amplitude of the dipole matrix element

$\Re^2(\hbar\omega)$ ...... normalized dipole matrix element squared average optical transition matrix element

$U(\vec{r})$ .... potential energy for an arbitrary electron

V .... illuminated volume

V_0 .... average amplitude of the random fluctuation in the potential well

V_0/B .... critical value at zero probability for electron at any site to diffuse away

z .... depth

$[\acute{R}(\hbar\omega)]^2$ .... squared average matrix element over all possible single-spin optical transitions between the valence band and conduction band electronic states separated by the photon energy, $\hbar\omega$

$|\mathrm{c}\rangle$ .... single-spin electronic state associated with the conduction band

$|\mathrm{v}\rangle$ .... single-spin electronic state associated with the valence band

Glossary of ACRONYMS

a-Si	amorphous silicon
a-Si:H	hydrogenated amorphous silicon
CBB	conduction band band
CBE	conduction band extended
CBL	conduction band localized
CBT	conduction band tail
DOS	density of states
c-Si	crystalline silicon
H	Hamiltonian
InSb	indium antimonide
JDOS	joint density of states
PECVD	plasma enhanced chemical vapor deposition
rms	root-mean square
Se	selenium
Si	silicon
VBB	valence band band
VBE	valence band extended
VBL	valence band localized
VBT	valence band tail
VBE-CBE	optical transitions from a valence band extended electronic state to a conduction band extended electronic state
VBE-CBL	optical transitions from a valence band extended electronic state to a conduction band localized electronic state

VBL-CBE	optical transitions from a valence band localized electronic state to a conduction band extended electronic state
VBL-CBL	optical transitions from a valence band localized electronic state to a conduction band localized electronic state

1. INTRODUCTION

The development of the first transistor in 1947 spawned a revolution in electronic technologies that continues today. In contemporary society, the transistor is ubiquitous. Electron devices, employed in all aspects of modern life, are comprised of billions of transistors. These devices are found in our communication systems, our information processing systems, our automobiles, and our homes. In order for the transistor to become the backbone of the electronics age, as it is today, a detailed and quantitative understanding of the material properties of the materials found within transistors was necessary. This continues to be the case today, as new generations of electron devices are designed and put into production. As transistors are fabricated from conductors, insulators, and semiconductors, interest in the material properties of these materials remains intense. This seems likely to remain to be the case for the foreseeable future.

Progress in conventional electronics is usually achieved by making the constituent transistors within electron devices faster, smaller, cheaper, and more reliable. There are, however, electron devices that require larger size in order to be useful. Solar cells, displays, scanners, and digital x-ray imagers are all examples of large area electron devices. While the focus in conventional electronics is on sub-micron device features, in large area electronics, the focus instead is on the deposition of electronic materials over substrates of the order of a square-meter. Unfortunately, crystalline silicon (c-Si), the workhorse of conventional electronics, can not be deposited over such large areas; at present, the largest commercially available c-Si wafers are 30 cm in diameter, and are very expensive. As a result,

alternate electronic materials must be employed instead in order to fabricate large area electron devices.

Typically, large area electron devices are deposited as thin-films over a substrate. While the exact means of preparation and the particular substrate employed can vary, all deposition techniques used in large area electronics focus on producing thin-films uniformly and inexpensively over large areas. As the deposition processes used in the fabrication of large area electron devices are distinct from those employed in conventional electronics, it is found that the properties of the resultant materials are different as well. While conventional electronics is primarily built upon c-Si, in large area electronics, polycrystalline and amorphous materials are found. While the atoms within c-Si are periodically distributed throughout its volume, in polycrystalline and amorphous materials, disorder is present within the distribution of atoms. In a polycrystalline material, small crystalline regions, referred to as grains, are randomly arranged throughout the volume, the crystalline order within each grain being abruptly interrupted by the grain boundary. In an amorphous material, however, no residual crystalline order remains, variations in the bonding lengths and bonding angles being present at all length scales; this is not to say that the distribution of atoms within an amorphous semiconductor is completely without order, as many amorphous semiconductors, such as amorphous silicon (a-Si), retain a short-range order similar to that found within their crystalline counterparts, i.e., the nearest neighbor bond lengths and bond angles found within a-Si are similar to those found within c-Si. The nature of the disorder present within these disordered materials is further discussed in Chapter 2.

Large area electronics, as this field is now referred to as, is a growing component of the overall electronics industry. Initially, large area electronics started as a niche field, with limited applications in consumer electronic products. An early application for a-Si, for example, was as a solar cell for solar powered calculators. In 1990, however, the a-Si based thin-film transistor was commercialized, allowing for the development of the flat panel display. This has dramatically increased the market share for large area electron devices. In Figure 1.1, for example, the market share only for flat panel displays is plotted as a function of year [1]. For the purposes of comparison, this plot is contrasted with that corresponding to the entire market for all semiconductor-based products; this forms an upper bound to the other plot, of course. It is clear that the sales of flat panel displays has made large area electronics a significant player within the overall electronics field.

The applications of large area electron devices are quite numerous today. In addition to flat panel displays, large area electronic products are found in scanners [2], solar cells [3, 4], and digital x-ray image detectors [5, 6]. The solar cell application, while relatively minor today, is expected to become significant in the near future, as a number of forms of thin-film silicon compete for their share of the overall photovoltaics market; at present, c-Si is still the dominant material being used in solar cells, the efficiency of such cells being greater than those of their thin-film silicon counterparts. New applications for large area electronic products are being developed with each passing year. Accordingly, interest in the material properties of the materials used in large area electronics remains intense.

One of the triumphs of physics during the 20th Century was the development of theoretical tools for the quantitative description of the material properties of

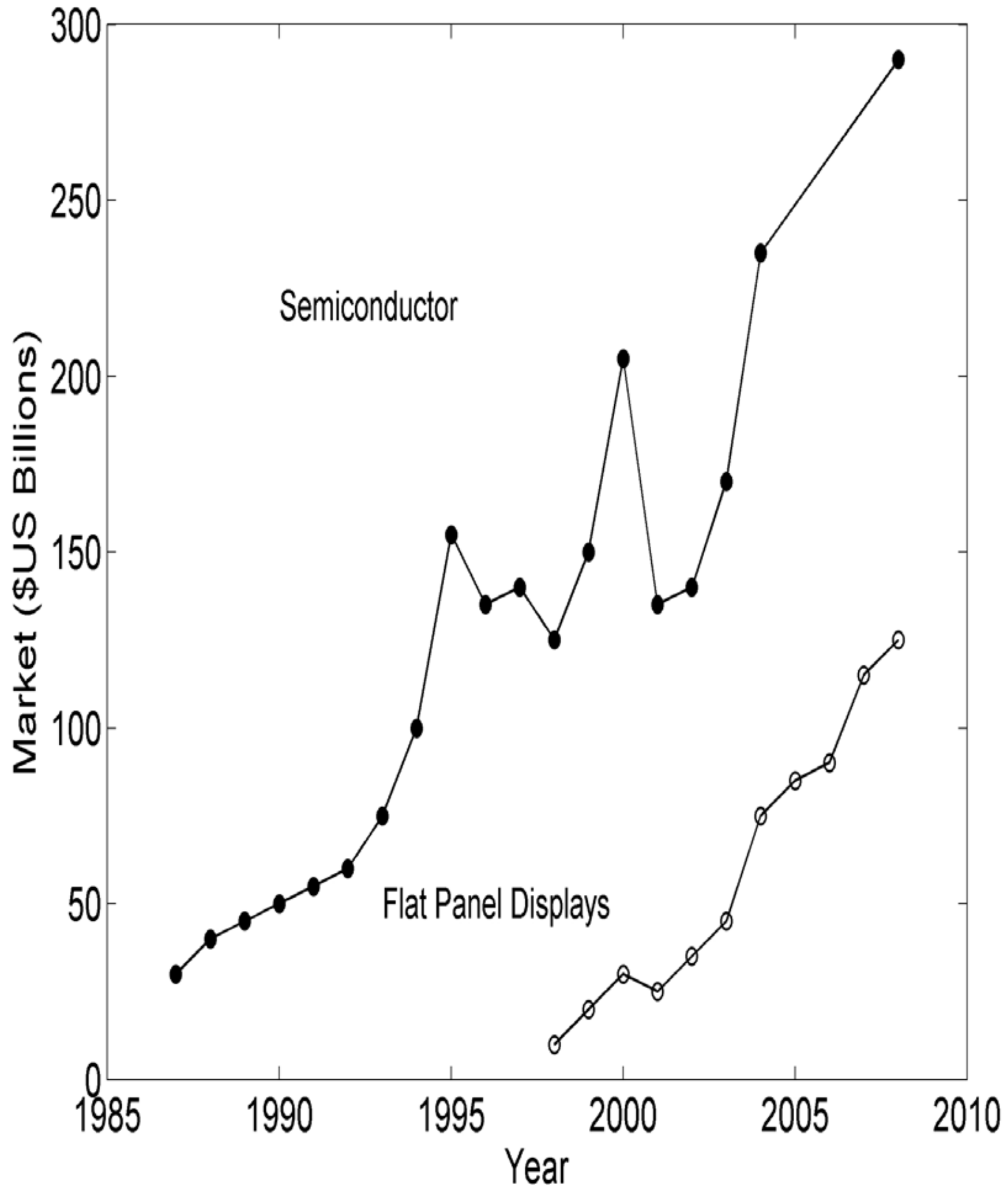

Figure 1.1: Semiconductor and flat panel display shipments plotted as a function of year. In the two decades since their introduction, flat panel displays have developed into a multi-billion dollar market. This data was obtained from the Information Society Technology website [1].

crystalline materials. Building upon the periodic order characteristic of a crystal, techniques, of great precision, were developed in order to determine the properties of these crystals. The physical interpretations engendered were ultimately found to be correct through a detailed comparison with the results of experiment. Unfortunately, disordered materials, such as those found within large area electron devices, are not amenable to these theoretical techniques. Accordingly, alternate means of understanding the corresponding material properties must be sought. While some work has been performed on understanding the role that disorder plays in influencing the properties of disordered materials, this understanding is rudimentary when contrasted with that of crystalline semiconductors. It is the aim of this thesis to develop means whereby the material properties of disordered materials may be better understood. For the purposes of this thesis, the focus is on the optical properties of the materials employed for large area electronics.

1.1 The role that disorder plays in shaping the distribution of electronic states

The disorder that is present within polycrystalline and amorphous semiconductors plays an important role in altering the corresponding distribution of electronic states. In a defect-free crystalline semiconductor, the distribution of electronic states terminates abruptly at the valence band and conduction band band edges, E_{V} and E_{C}, respectively. In contrast, in a disordered semiconductor, tails of electronic states encroach into the otherwise empty gap region [7, 8]. The exact form of the tail states is critically influenced by the exact nature of the disorder that is present. It should be noted that tail states are present, even in ‘ideal’ disordered

semiconductors, i.e., disordered semiconductors for which all bonds are satisfied, the disorder arising as a consequence of variations in the bond lengths and bond angles; this type of disorder may be referred to as intrinsic disorder. For real disordered semiconductors, in addition to these variations in the bond lengths and bond angles, there are dangling bonds, vacancies, and other forms of disorder present; this type of disorder is sometimes referred as extrinsic disorder. These non-ideal defects that are present will typically lead to electronic states deep within the gap region. Thus, a distribution of deep electronic states occurs. The contrast between the distribution of electronic states associated with a hypothetical crystalline semiconductor and its disordered counterpart is depicted in Figure 1.2 [9].

The disorder that is present within a disordered semiconductor also has the potential to change the character of the electronic states. In a defect-free crystalline semiconductor, the electron wave function associated with each of the electronic states extends throughout the entire semiconductor. In a disordered semiconductor, however, analysis indicates that the disorder that is present may also lead to the localization of many of the electronic states within the tails in the distribution of electronic states. That is, the electron wave function associated with each localized electronic state is only present within a localized region of the volume. Electrons within localized electronic states do not contribute to conduction, i.e., these electrons are not free to move under the action of an applied electric field. The wave functions, corresponding to representative extended and localized electronic states, are depicted in Figure 1.3.

In a disordered semiconductor, both localized and extended electronic states can co-exist. Analysis has indicated that there exist two critical energies, termed

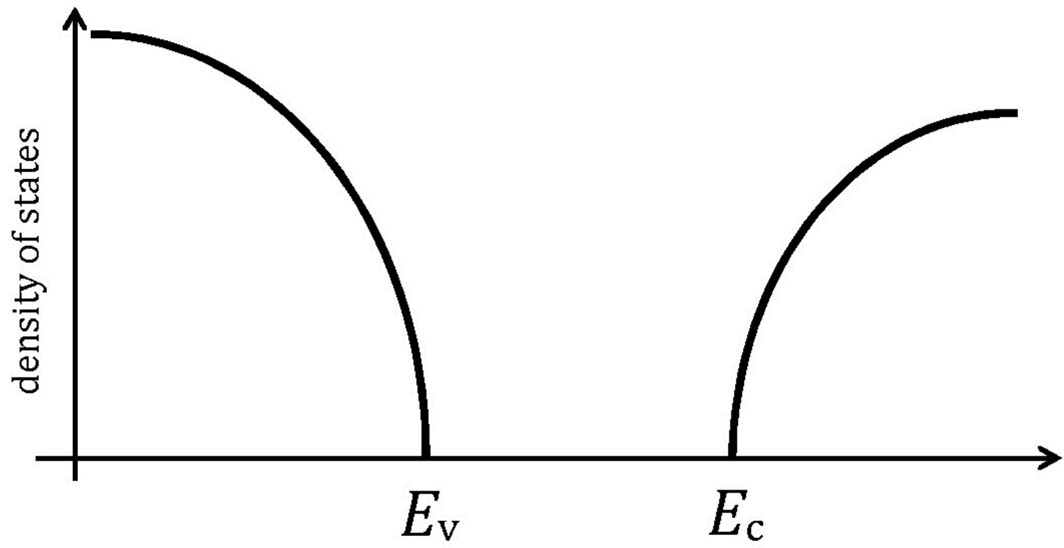

(a)

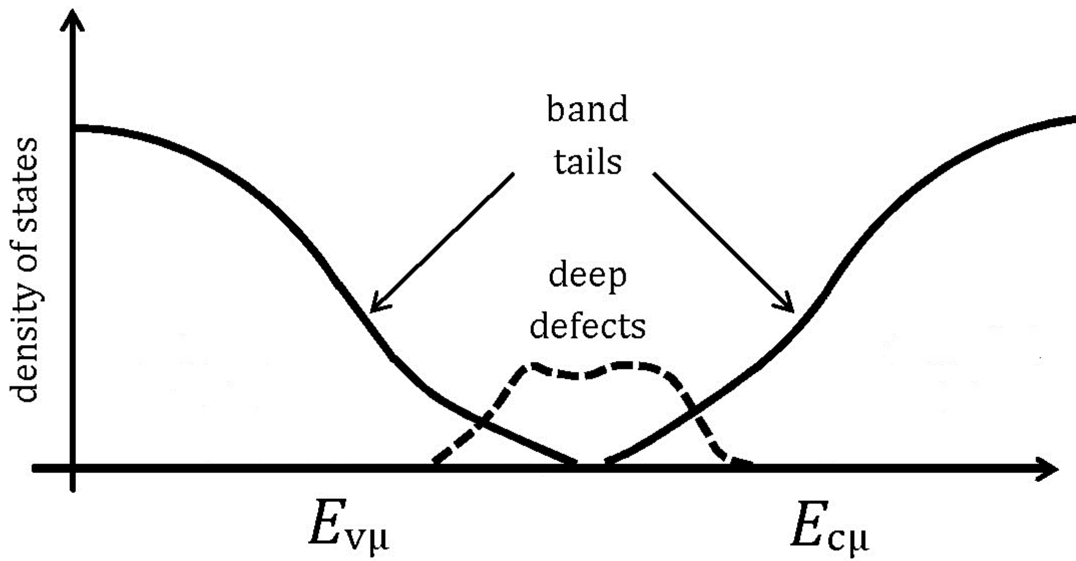

(b)

Figure 1.2: The distribution of electronic states associated with: (a) a hypothetical crystalline semiconductor, and (b) its disordered counterpart [9].

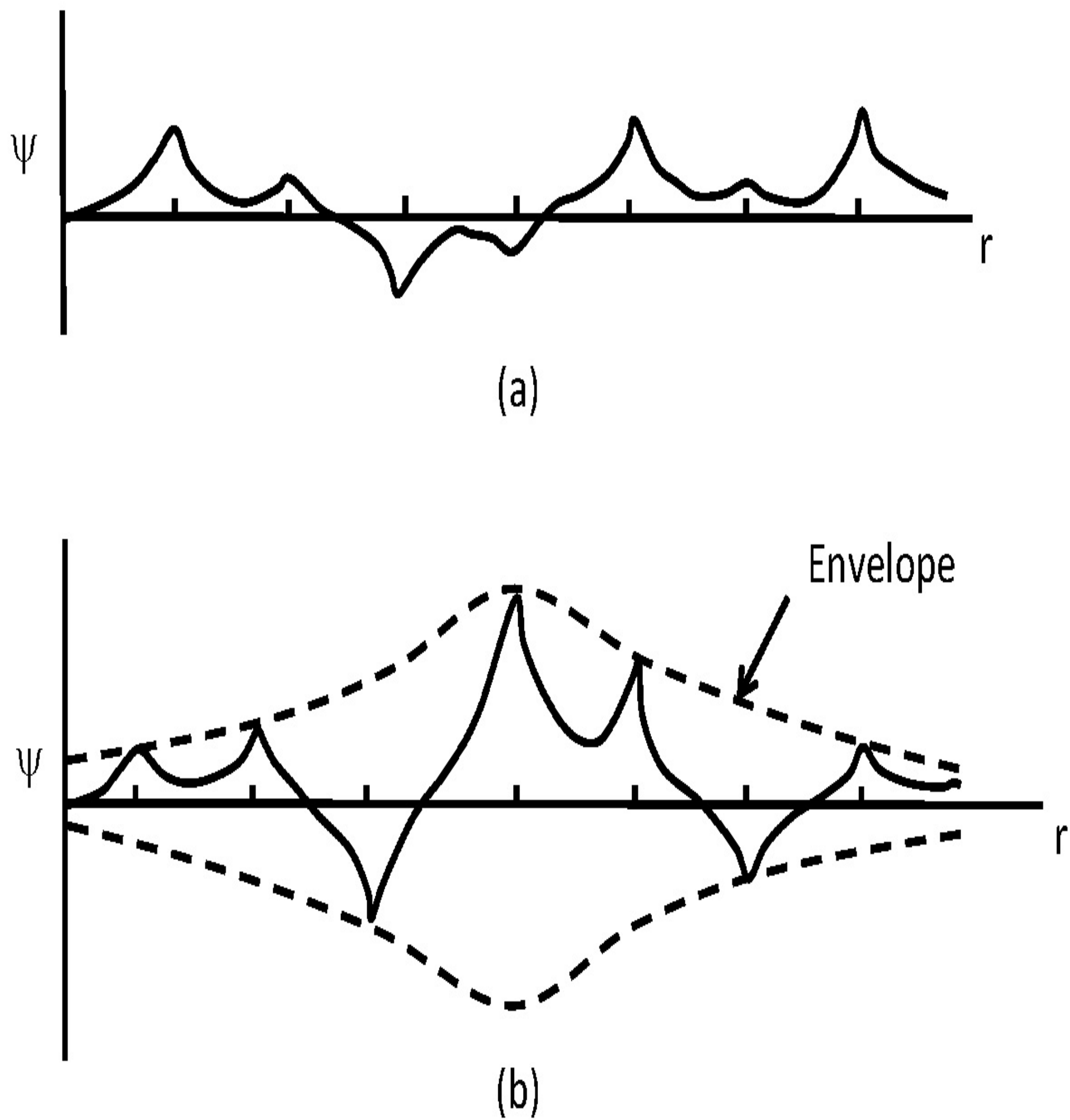

Figure 1.3: The wave functions associated with a representative disordered system: (a) the wave function associated with an extended electronic state; (b) the wave function associated with a localized electronic state.

mobility edges, which separate the localized electronic states from their extended counterparts [10]. That is, in the valence band associated with a disordered semiconductor, there are both valence band extended (VBE) and valence band localized (VBL) electronic states, these states being separated by the valence band mobility edge, $E_{\mathrm{V}\mu}$. Similarly, in the conduction band associated with a disordered semiconductor, there are both conduction band extended (CBE) and conduction band localized (CBL) electronic states, these states being separated by the conduction band mobility edge, $E_{\mathrm{C}\mu}$. The locations of the mobility edges depends critically on the degree of disorder that is present. The localized tail states are responsible for many of the unique features characteristic of a disordered semiconductor. A distribution of electronic states, corresponding to a hypothetical disordered semiconductor, with valence band and conduction band mobility edges, $E_{\mathrm{V}\mu}$ and $E_{\mathrm{C}\mu}$, respectively, is depicted in Figure 1.4.

1.2 Optical response

In this thesis, the primary focus of investigation centers on how light interacts with a given material. As light passes through a material, its intensity diminishes. Consider the case of light incident upon a material from the left. If it is assumed that the interface between the vacuum and the material occurs at $z = 0$, in the absence of reflection, the intensity of the light within the material exponentially attenuates with the depth into the material, as shown in Figure 1.5 for various selections of α, i.e.,

$$I(z) = I_0 \exp(-\alpha z), \tag{1.1}$$

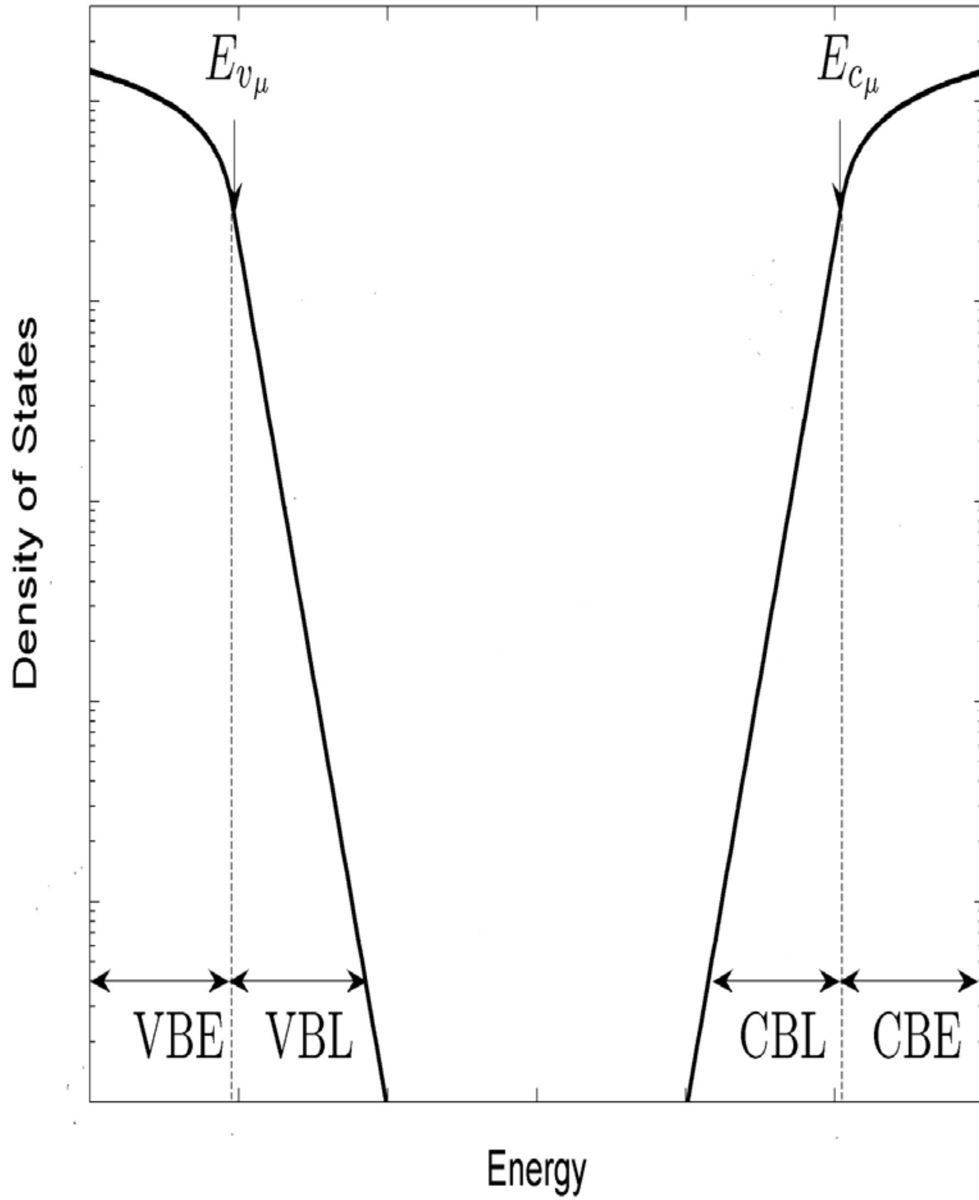

Figure 1.4: The distribution of electronic states associated with a hypothetical disordered semiconductor. The ranges of energy corresponding to the VBE, VBL, CBE, and CBL electronic states are clearly depicted. The valence band and conduction band mobility edges, $E_{\mathrm{V}\mu}$ and $E_{\mathrm{C}\mu}$, respectively, are also depicted.

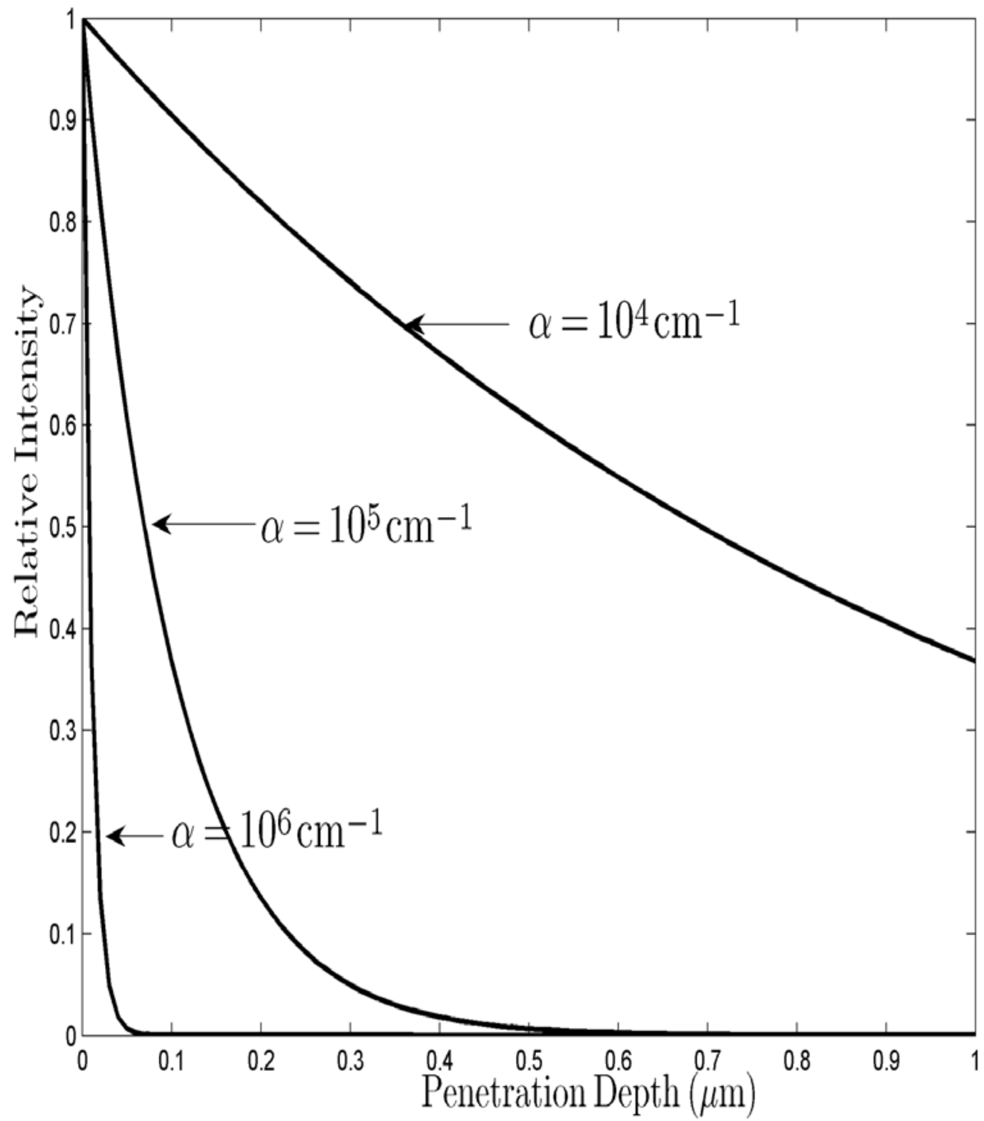

Figure 1.5: The variation in the relative intensity, $I(z)/I_0$, with the penetration depth, z, for various selections of the optical absorption coefficient, α.

where I_0 denotes the intensity of the light at $z = 0$, z representing the depth into the material, and α being the corresponding optical absorption coefficient [11].

The optical response of a material is often characterized in terms of the optical absorption spectrum, i.e., the dependence of the optical absorption coefficient, α, on the photon energy of the incident light, $\hbar\omega$. While the optical absorption spectrum associated with a defect-free 'ideal' crystalline semiconductor terminates abruptly at the fundamental energy gap, in a disordered semiconductor, a tail encroaches into the otherwise empty gap region [12]. This tail in the optical absorption spectrum, arising as a result of optical transitions involving the aforementioned tail states [13, 14, 15, 16, 17, 18], is responsible for many of the unique features characteristic of the optical response of disordered semiconductors. Accordingly, the optical absorption tail associated with disordered semiconductors has been the subject of a number of studies [12, 18, 19, 20, 21, 22, 23].

At zero-temperature, it may be shown that the spectral dependence of the optical absorption coefficient,

$$\alpha(\hbar\omega) = D^2(\hbar\omega)J(\hbar\omega), \tag{1.2}$$

where $D^2(\hbar\omega)$ denotes the optical transition matrix element and $J(\hbar\omega)$ represents the joint density of states (JDOS) function; this JDOS function

$$J(\hbar\omega) \equiv \int_{-\infty}^{\infty} N_{\mathrm{V}}(E)N_{\mathrm{C}}(E+\hbar\omega)dE, \tag{1.3}$$

$N_{\mathrm{V}}(E)$ being the valence band density of states (DOS) function and $N_{\mathrm{C}}(E)$ being the conduction band DOS function, i.e., $N_{\mathrm{V}}(E)\Delta E$ and $N_{\mathrm{C}}(E)\Delta E$ representing the number of valence band and conduction band electronic states, per unit volume, between energies $[E, E+\Delta E]$. As optical response is a key requirement

for many of the device applications implemented or envisaged for polycrystalline and amorphous semiconductors, this response has been the focus of a considerable amount of study over the years [12, 14, 20, 24, 25, 26, 27].

The key optical functions related to a semiconductor, i.e., the imaginary part of the dielectric function, $\epsilon_2(\hbar\omega)$, and the optical absorption coefficient, $\alpha(\hbar\omega)$, are directly related to one another. In particular, it may be shown that

$$\alpha(\hbar\omega) = \frac{\omega}{c\, n(\hbar\omega)}\, \epsilon_2(\hbar\omega), \tag{1.4}$$

where c is the speed of light in a vacuum, $n(\hbar\omega)$ represents the spectral dependence of the refractive index, and ω represents the angular frequency of the light. The determination of the spectral dependence of the real and imaginary parts of the dielectric function, $\epsilon_1(\hbar\omega)$ and $\epsilon_2(\hbar\omega)$, and other key optical properties, has been a central goal of disordered semiconductor research for many years. In a defect-free crystalline semiconductor, the thermally-induced disorder present leads to a narrow tail in $\epsilon_2(\hbar\omega)$. In a disordered semiconductor, however, the tail exhibited by $\epsilon_2(\hbar\omega)$ is much broader [12]. This tail in $\epsilon_2(\hbar\omega)$ is responsible for many of the unique features characteristic of the optical response of disordered semiconductors.

Unfortunately, the tails that occur in $\epsilon_2(\hbar\omega)$ and $\alpha(\hbar\omega)$ make the optical absorption edge associated with a disordered semiconductor difficult to define experimentally. As a consequence, a number of empirical measures for the optical gap and the optical absorption tail breadth have been devised over the years. While these empirical measures facilitate the quantitative analysis of the optical absorption edge, their physical meaning has remained unclear. In particular, exactly how these empirical measures associated with the optical absorption edge are related to the underlying distribution of electronic states remains unknown.

As measurements of the optical absorption spectrum are often used to determine the underlying distribution of electronic states, the resolution of this ambiguity represents a critical challenge to the development of this field.

1.3 Thesis objectives

The overall goal of this thesis is the quantitative characterization of the optical response of amorphous semiconductors; the optical response of a polycrystalline semiconductor is a greater challenge, as the partial retention of order complicates matters. This goal will be pursued within the framework of an empirical model for the DOS functions that includes VBE, VBL, CBE, and CBL electronic states. The analysis begins with a detailed examination of the contributions to the JDOS function attributable to the various types of optical transitions that can occur; the empirical model for the DOS functions that is employed allows for the consideration of four different types of optical transitions, (1) optical transitions from the VBE electronic states to the CBE electronic states (VBE-CBE optical transitions), (2) optical transitions from the VBE electronic states to the CBL electronic states (VBE-CBL optical transitions), (3) optical transitions from the VBL electronic states to the CBE electronic states (VBL-CBE optical transitions), and (4) optical transitions from the VBL electronic states to the CBL electronic states (VBL-CBL optical transitions). Then, from the insights gleaned from this JDOS analysis, the spectral dependence of the imaginary part of the dielectric function, $\epsilon_2(\hbar\omega)$, and the optical absorption coefficient, $\alpha\,(\hbar\omega)$, will be evaluated. The application of this formalism to the specific case of hydrogenated amorphous silicon (a-Si:H) pro-

duced through plasma enhanced chemical vapor deposition (PECVD), the most common form of amorphous semiconductor in use today, will then be pursued.

This thesis is organized in the following manner. In Chapter 2, background material, relevant to this thesis, is presented. In particular, an empirical model for the DOS functions, which is the key to the subsequent analysis, is presented. Then, in Chapter 3, within the framework of this empirical model for the DOS functions, the various contributions to the JDOS function are determined. The application of this formalism to the specific case of PECVD a-Si:H is then presented in Chapter 4. Finally, the conclusions of this thesis are enumerated in Chapter 5.

2. A DENSITY OF STATES ANALYSIS

2.1 Introduction

Pioneering studies into the material properties of amorphous semiconductors were initiated in the 1950s [28, 29]. Intensive research into these disordered semiconductors began in earnest shortly thereafter. Much of the fundamental research that has occurred in this field has focused upon developing a detailed and quantitative understanding of the electronic and optical responses associated with these materials. Usually, these analyzes are cast within the framework of a model for the distribution of electronic states. Accordingly, understanding how the electronic states are distributed within a disordered semiconductor remains a matter of great fundamental concern in the study of these materials.

Fundamental studies of disordered semiconductors, such as a-Si:H, represents a true 'frontier' area of condensed matter physics. While solids with crystalline order may be quantitatively characterized with great accuracy using very sophisticated theoretical formalisms, theories that aim to predict the behavior of disordered semiconductors remain in a comparatively primitive stage. The exact role that the various forms of disorder play in shaping the distribution of electronic states remains unknown. In addition, the location of the mobility edges associated with each band, i.e., the threshold energy level that separates the extended states from their localized counterparts, is unknown, even for the most well studied disordered semiconductors. Accordingly, there are rich opportunities for research and development within this field.

The aim of this thesis is to enrich the understanding of the operation of amorphous semiconductor based devices. This will be achieved through the quantitative modeling of the optical response of this class of materials, the optical response determining the performance of many amorphous semiconductor-based devices. The analysis starts with an empirical model for the distribution of electronic states, this model capturing the fundamental character of amorphous semiconductors. From this empirical model, the JDOS function is then evaluated, this function determining, in large measure, the optical response of an amorphous semiconductor. By identifying the contributions to this JDOS function attributable to the various types of optical transitions, insights into the optical response of this class of materials may be drawn. Through a comparison with the results of experiment, the underlying modeling parameters may be determined. Conclusions, into the optical response of these materials, will thus be gleaned from the results of this analysis.

In this chapter, background material for this work is provided. Initially, the various types of solids are described. Then, the electronic configuration associated with the isolated atom, and the corresponding energy levels, are presented. An examination into what happens to these energy levels as isolated atoms are brought together in order to form a solid is then featured. Building upon this, energy band diagrams, and their use in the characterization of crystalline semiconductors, is then elucidated. The role that disorder plays in shaping the character of the electronic states associated with amorphous semiconductors, and how disorder introduces localized electronic states, are then discussed. The free electron model, and its corresponding distribution of electronic states, are then presented. A number of empirical models for this distribution of electronic states are then

reviewed. A generalized empirical model for this distribution of electronic states, that will be employed for the purposes of this analysis of amorphous semiconductors, is then featured. Finally, this model is employed in order to determine the density of localized valence band and conduction band electronic states.

This chapter is organized in the following manner. In Section 2.2, the various types of solids are described. Then, in Section 2.3, the electronic configuration associated with isolated atoms is described, the energy levels associated with these electronic states being discussed. The examination into what happens to these energy levels as isolated atoms are brought together in order to form a solid is then featured in Section 2.4. In Section 2.5, energy band diagrams, and their use in the characterization of crystalline semiconductors, is detailed. The role that disorder plays in shaping the nature of the electronic states associated with an amorphous semiconductor, and its role in producing localized electronic states, are then presented in Section 2.6. The free electron model, and its corresponding distribution of electronic states, are then presented in Section 2.7. A number of empirical models for this distribution of electronic states are then reviewed in Section 2.8. A generalized empirical model for this distribution of electronic states, that will be employed for the purposes of this analysis of amorphous semiconductors, is then featured in Section 2.9. Finally, this model is employed in order to determine the density of localized valence band and conduction band electronic states in Section 2.10.

2.2 Types of solids

There are three general types of solids; (1) crystalline, (2) polycrystalline, and (3) amorphous. The differences between these solids relate to how their constituent atoms are arranged. In a crystalline solid, the atoms are arranged in a periodic and ordered fashion. Accordingly, the atomic distribution associated with a crystalline semiconductor is said to possess long-range order. In a polycrystalline semiconductor, however, small crystalline regions, referred to as grains, are distributed throughout the material. Each grain, which can be thought of as a small crystal, possesses the long-range order of its crystalline counterpart within its limited volume. This order, however, is abruptly terminated at the boundaries separating the grains. In an amorphous solid, no residual crystalline order remains. That is, the atoms within an amorphous solid instead are arranged in a random and disordered fashion. The distinction between the arrangement of atoms within crystalline, polycrystalline, and amorphous solids is conceptually illustrated in Figure 2.1 [21, 30].

It should be noted that while there is an absence of long-range order in the amorphous solid atomic distribution, many amorphous solids possess a form of short-range order. That is, the nearest neighbor environment around a typical atom within most amorphous solids is similar to that of most of the other atoms in the material, the nearest neighbor separation distances being comparable to that of its crystalline counterpart; this short-range order is evident in Figure 2.1. As the electronic properties of a solid are primarily determined by the nearest neighbor environment, amorphous solids share many properties with their crystalline counterparts. In particular, it is found that many of the mechanical, optical, mag-

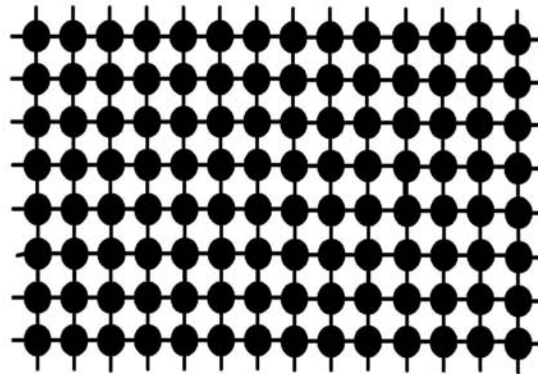

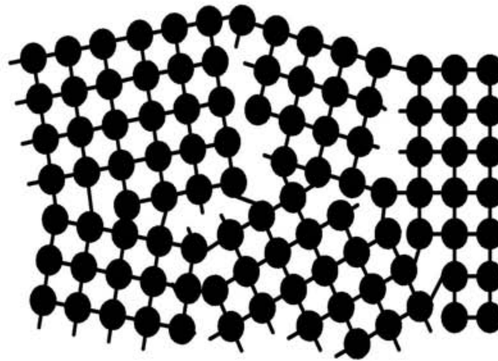

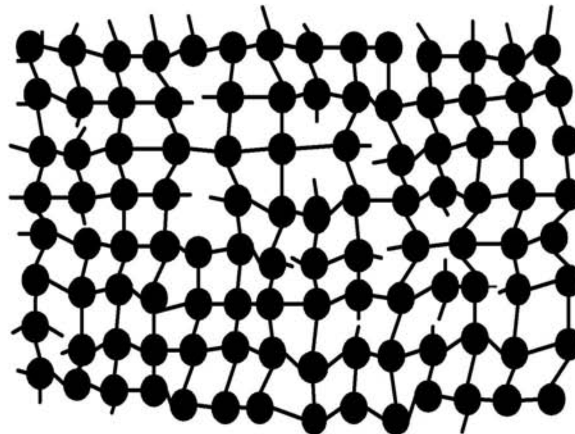

Figure 2.1: The arrangement of atoms within hypothetical crystalline, polycrystalline, and amorphous semiconductors. This figure is from Nguyen [28].

netic, and electronic properties of amorphous solids are similar to those exhibited by their crystalline counterparts.

2.3 The electronic configuration of isolated atoms

Quantum mechanics forms the key cornerstone of modern chemistry. To zeroth-order, the electronic states associated with an atom may be described using the shell model. Within the framework of this model, the electrons associated with an atom may be viewed as 'orbiting' the positivity charged nucleus; of course, electrons do not actually 'orbit' a nucleus as planets orbit the Sun, but the notion of 'orbiting' electrons provides an intuitive picture of the nature of the electrons within an atom. As the electrons within these 'orbits' are moving about the nucleus at a rapid rate, over a sufficient time scale, they appear as a continuum of charge at their orbital radii. Accordingly, each electron can be viewed as forming a shell of negative charge at the given orbital radius about the nucleus.

Quantum mechanics dictates that only certain 'orbits' are stable. As a result, the electrons associated with an atom maybe thought of as only being allowed to be present at these discrete radii, i.e., the corresponding shells are centered at these radii. The shells associated with an electron are classified according to the value of the principal quantum number, n, n being a positive integer. Within each shell, there may be a number of subshells, each subshell associated with the nth-shell being distinguished according to the value of the orbital angular momentum quantum number, l, where l is an integer that is greater than or equal to zero and less than or equal to $n-1$. The nth-shell can accommodate up to $2n^2$ electrons, the lth-subshell of this shell accommodating up to $2(2l+1)$ electrons. The $n = 1$ shell,

for example, can accommodate up to 2 electrons, both being in the $l = 0$ subshell. The $n = 2$ shell, however, can accommodate up to 8 electrons, 2 such electrons being in the $l = 0$ subshell, the other 6 being in the $l = 1$ subshell. Shells that are completely filled constitute the core electrons associated with an atom. Electrons in partially filled shells are referred to as valence electrons, and the nature of the bonding that can occur within a material is determined by such electrons.

The electronic configuration associated with an atom may be characterized by listing the number of shells and subshells and by indicating how the electrons occupy these shells and subshells. Typically, shells and subshells are characterized using a standard nomenclature. Associating the $l = 0, 1, 2$, and 3 values of the orbital angular momentum quantum number with the indices s, p, d, and f, respectively, the number nl is used to identify the shell and the subshell, a superscript being used to identify the occupancy of the subshell by electrons. For the ground state, the electrons fill up all the available subshells, from the lowest energy subshell up, until all the electrons associated with the atom are placed in a subshell. The electronic configuration associated with the ground state of the carbon (C) atom, for example, which has an atomic number of 6, may be succinctly expressed as $1s^2 2s^2 2p^2$; this means there are 2 electrons in the first shell associated with $n = 1$, there being only one subshell corresponding to the $l = 0$ subshell, 2 electrons in the $l = 0$ subshell associated with $n = 2$ shell, and 2 electrons in the $l = 1$ subshell associated with $n = 2$ shell; this latter subshell could have accommodated up to six electrons, however. The electronic configuration associated with the ground state of silicon (Si), with an atomic number of 14, may be expressed as $1s^2 2s^2 2p^6 3s^2 3p^2$. Figure 2.2 schematically illustrates the shell model of

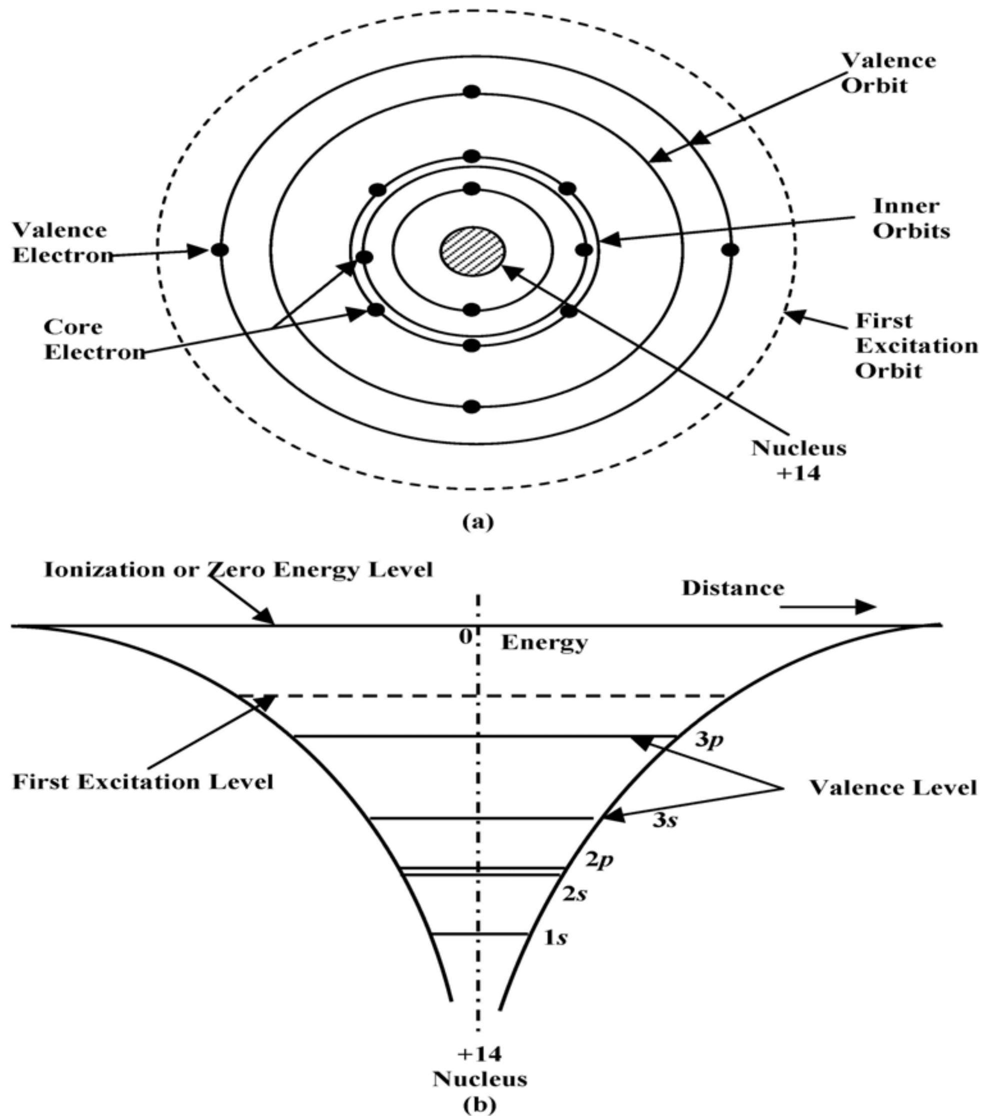

Figure 2.2: A schematic illustration of the shell model associated with an isolated Si atom, with the associated energy levels being explicitly depicted. (a) The shell model of an isolated Si atom, showing the 10 core electrons, associated with the completely filled $n = 1$ and $n = 2$ shells, and the 4 valence electrons associated with the 3s and 3p subshells; (b) The energy levels in the potential well of the nucleus are also depicted schematically. The size of the nucleus has been greatly exaggerated for the purposes of illustration.

the isolated Si atom, the occupancy of each subshell being explicitly indicated; the ground state is assumed. It is noted that the nucleus is comprised of 14 protons (with a charge of +14) and 14 neutrons (no charge). There are 10 core electrons in the completely filled $n = 1$ and $n = 2$ shells, and 4 valence electrons associated with the $3s$ and $3p$ subshells.

An isolated atom is characterized with a discrete spectrum of electronic energy levels. Each subshell has its own distinct electronic energy level. It is usual to define the zero of the energy scale (known as the vacuum level) as the potential energy of a free electron far from the atom. In Figure 2.2(b), representative discrete energy levels corresponding to the subshells of an isolated Si atom are depicted. It is seen that the potential energy is negative for all the electronic states associated with an isolated Si atom, i.e., the electrons are attracted to the nucleus. It is also noted that the potential energy gradually goes to zero as the orbital's radius approaches infinity, as is shown in Figure 2.2(b).

2.4 Energy levels in solids

As already mentioned, crystalline solids consist of an array of periodically distributed atoms. Si, gallium arsenide (GaAs), and most other crystalline semiconductor materials, possess a diamond or zinc blende structure. In these structures, each atom in the crystal is surrounded by four of its nearest neighbor atoms. Hence, the discrete energy levels corresponding to the isolated atom no longer apply. As isolated atoms are brought closer together in order to form a solid, interactions occur between neighboring atoms. The forces of attraction and repulsion between these atoms finds a balance at an equilibrium interatomic spacing for

the particular crystal being considered. In this process, important changes occur in the electronic energy level configurations, which are responsible for the different electronic properties of materials.

When two atoms are completely isolated from each other, so that there is no interaction between their electron wave functions, they can have identical electronic structures. As the atoms are brought closer to each other, however, Pauli's exclusion principle becomes important. As the distances between the atoms decreases, the wave functions associated with the isolated atoms begin to overlap. The exclusion principle mandates that no two electrons can occupy the same quantum state. Thus, the discrete energy levels of the isolated atoms must split into new levels belonging to the pair rather than to the individual atoms. In a semiconductor, where many atoms are brought together, closely spaced energy levels emerge. In the limit that there are an infinite number of atoms associated with the semiconductor, a continuum of such energy levels will arise over certain bands of energy. These bands are referred to as energy bands and it is the occupancy of such bands that determines the properties of these materials. That is, insulators correspond to fully occupied bands that are separated by reasonably large energy gaps, while conductors correspond to partially occupied bands that can overlap. Semiconductors lie somewhere between these extremes.

Consider the electronic energy levels associated with diamond, i.e., C in the diamond lattice structure, as a function of the interatomic spacing, a. The number of C atoms is set to N, where presumably N is a large number. When the atoms are infinitely separated, all N C atoms will have a spectrum of energy levels corresponding to the isolated energy levels of an isolated C atom. As the atoms are

brought together, however, the wave functions begin to overlap and these energy levels will broaden into bands. The $1s$ and $2s$ levels will broaden into fully occupied bands with $2N$ electronic states each as the atoms are brought together in order to form a solid, i.e., each atom contributes 2 electronic states and 2 electrons. The $2p$ levels will also broaden into a partially occupied band with $6N$ electronic states, $2N$ of which are occupied, i.e., each atom contributes 6 electronic states and 2 electrons. For large interatomic spacings, the band associated with the $2p$ electronic states will correspond to greater energies than that associated with the $2s$ electronic states. As the interatomic spacing is reduced, however, the $2s$ and $2p$ bands will merge into a partially occupied $2s$-$2p$ hybrid band, comprised of $8N$ electronic states, $4N$ of which are occupied. With a further reduction in the interatomic spacing, the $2s$-$2p$ hybrid states will split yet again, the energy difference between these split bands being referred to as the energy gap, E_g. The formation of the energy gap, for the case of C, is schematically illustrated in Figure 2.3 [31, 32].

The lower energy branch of the split $2s$-$2p$ hybrid band, which has $4N$ electronic states, will be fully occupied at zero temperature, i.e., it will host $4N$ electrons. The upper energy branch of the split $2s$-$2p$ hybrid band, which also has $4N$ electronic states, will be completely unoccupied at zero temperature, i.e., it will host no electrons. The energy gap, i.e., the difference in energy between the band edges of the fully occupied and unoccupied bands, plays an important role in determining the electronic properties of a semiconductor. Semiconductors with large energy gaps act like insulators, while those with small energy gaps act as conductors. Semiconducting materials exhibit a wide range of energy gaps. In particular, the

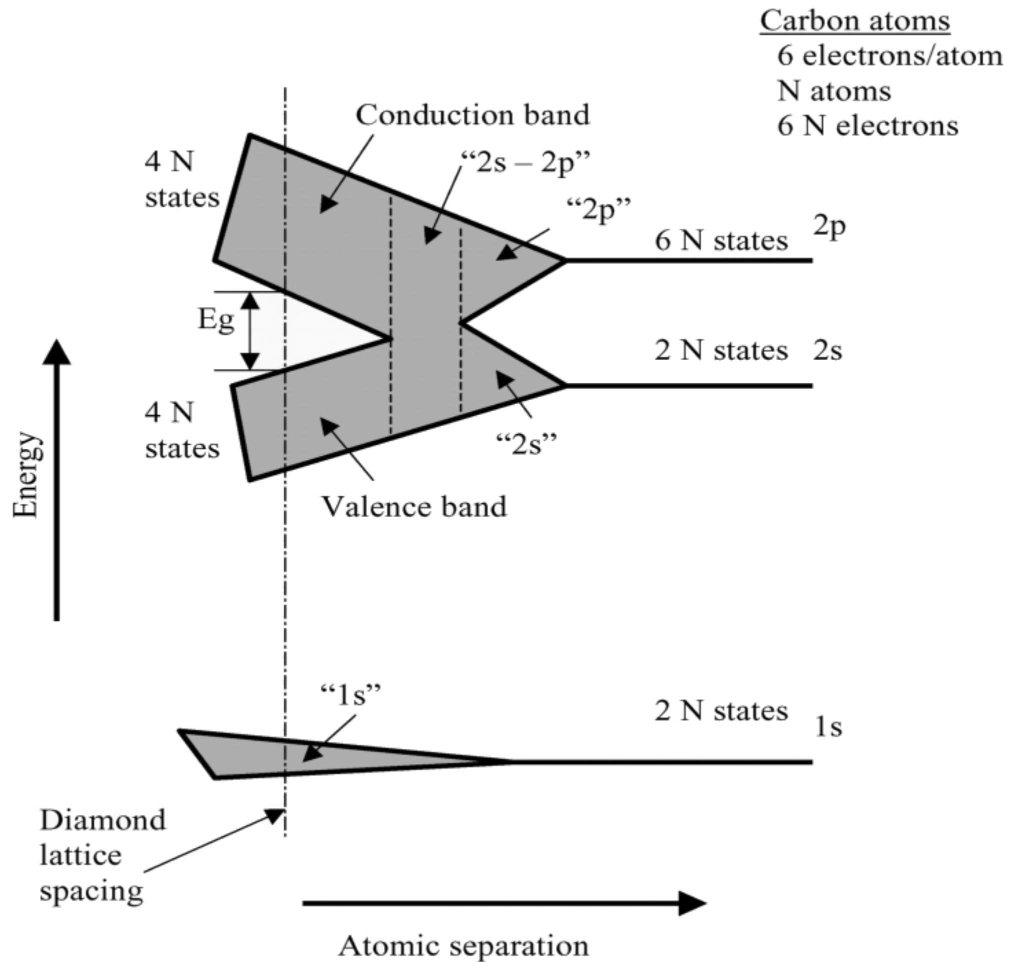

Figure 2.3: The energy bands for diamond as a function of the lattice constant, a. Isolated carbon atoms contain six electrons, which occupy the $1s$, $2s$, and $2p$ orbitals in pairs. The energy of an electron occupying the $2s$ and $2p$ orbitals is indicated on the figure. As the lattice constant is reduced, there is an overlap between the electron wave functions associated with the adjacent atoms. This leads to a splitting of the energy levels, consistent with the Pauli exclusion principle. This splitting results in an energy band containing $2N$ states in the $2s$ band and $6N$ states in the $2p$ band, where N denotes the number of atoms in the crystal. A further reduction in the lattice constant causes the $2s$ and $2p$ energy bands to merge and split yet again into two bands, containing $4N$ states each. In this illustration, E_g denotes the energy gap. This figure is after Streetman [31]. This particular image was borrowed from Malik [32].

energy gap of semiconductors ranges from 0.17 eV for the case of indium antimonide (InSb) to 6.2 eV for the case of aluminium nitride (AlN).

2.5 Energy band diagrams

It is often instructive to relate these energy bands, i.e., the range of energies over which the electronic states are distributed, to the underlying momentum. For a free particle, the energy and momentum may be related through classical mechanics. That is,

$$E = \frac{p^2}{2m}, \tag{2.1}$$

where p denotes the momentum of the particle and m represents the mass. For the case of electrons, in the quantum domain, $p = \hbar k$, where $\hbar$ denotes the reduced Planck's constant and k represents the electron wave-vector. Thus,

$$E = \frac{\hbar^2 k^2}{2m}. \tag{2.2}$$

The corresponding one-dimensional relationship between the electron energy, E, and the electron wave-vector, k, for this free particle case, is depicted in Figure 2.4.

For crystalline semiconductors, the relationship between energy and momentum is more complex. The electrons within a crystalline semiconductor do not act as free particles. Instead, they are attracted to the nuclei corresponding to the atoms that are distributed throughout the material. Thus, the simple parabolic relationship found previously, i.e., Eq. (2.2), does not apply. In addition, the potential that is encountered depends critically on the exact direction that the electrons are propagating, i.e., semiconducting materials may exhibit a considerable amount of anisotropy. As a result, in general, the three-dimensional dependence of the

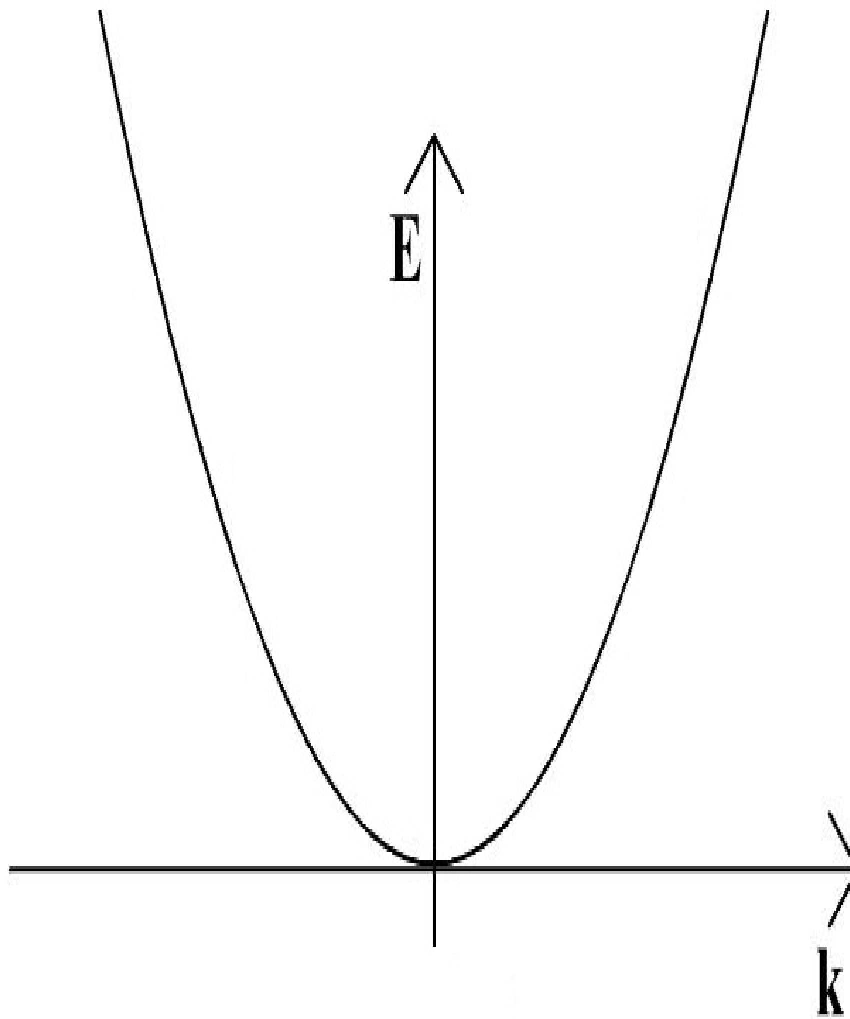

Figure 2.4: The relationship between the electron energy and the electron wave-vector, k, for a free electron for the one-dimensional case.

electron energy levels on the electron wave-vector, $\vec{k}$, must be specified. Usually, this dependence is only presented along critical lines of symmetry.

In an amorphous semiconductor, the disorder that is present renders the electron wave-vector, $\vec{k}$, a poor quantum number. As a result, the band diagrams employed for the crystalline case can not be employed. Nevertheless, as the nearest neighbor environment of most amorphous semiconductors is similar to that of their crystalline counterparts, it is expected that there will still be bands, of roughly the same dimensions [33, 34]. In the silicon case, for example, the covalent bonds between the silicon atoms within a-Si:H are similar to those found within c-Si, with the same number of neighbors and the same average bond lengths and bond angles. This short-range order, however, quickly gives way to the long-range disorder of the amorphous atomic distribution, the spatial correlation between atomic positions decreasing rapidly beyond a few interatomic spacings. A representative two-dimensional schematic depiction of the distribution of atoms associated with a-Si is depicted in Figure 2.5.

2.6 Localization and the role of disorder

The disorder inherent to amorphous semiconductors has a profound influence on the electronic and optical properties associated with these materials. Accordingly, the properties exhibited by amorphous semiconductors, while being qualitatively similar to those of their crystalline counterparts, are distinct. Fundamentally, increased disorder leads to increased electron scattering. If the disorder is sufficiently strong, this scattering will lead to electron localization, in which the wave function associated with an electron is confined to a small volume rather than being

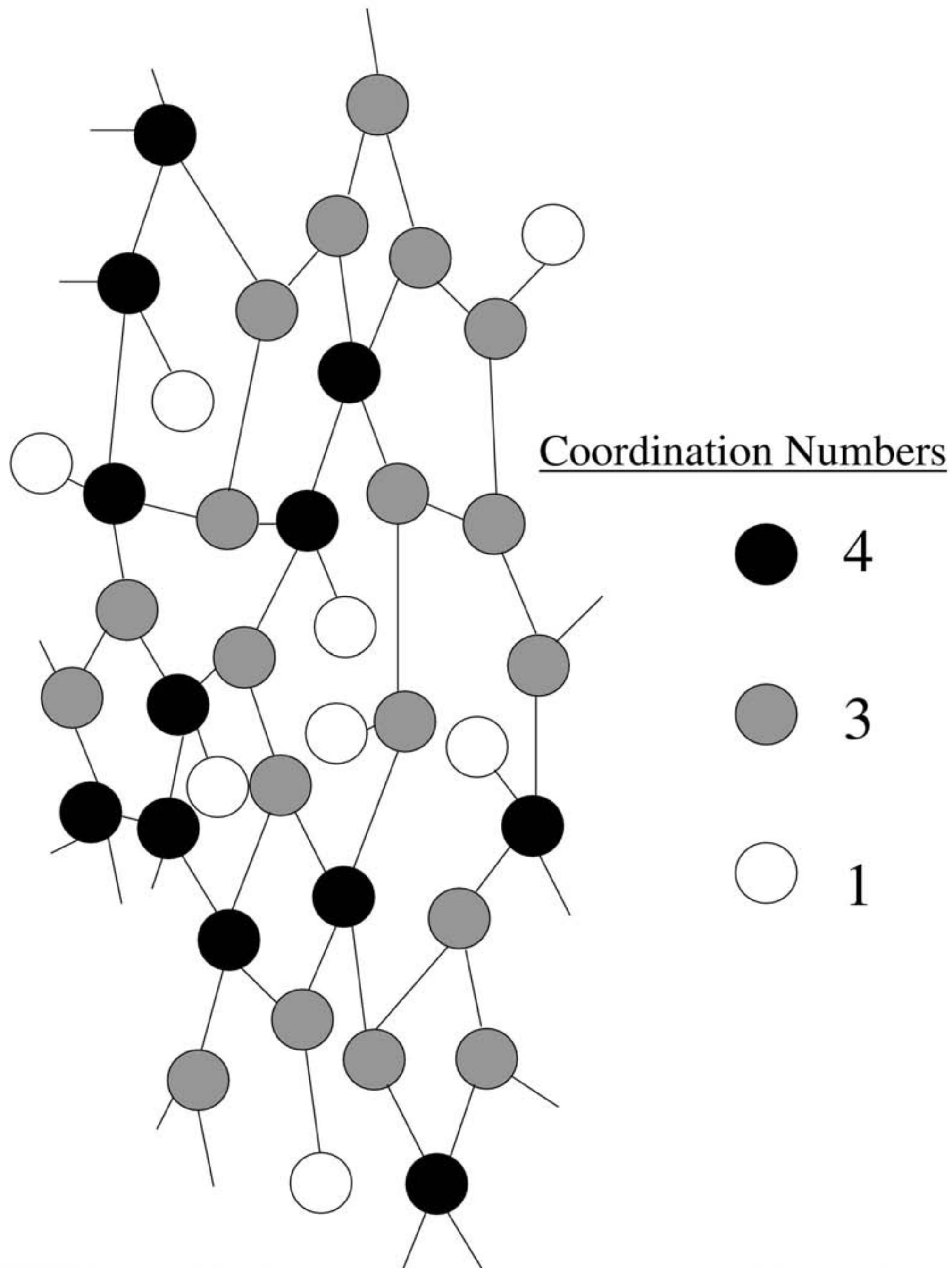

Figure 2.5: A two-dimensional schematic representation of the distribution of atoms within a hypothetical sample of a-Si. The coordination number associated with each Si atom within the network, i.e., the number of nearest neighbor atoms, is depicted. The amount of disorder present within a-Si has been exaggerated for the purposes of illustration.

extended throughout the entire material; the wave functions associated with the electronic states of a crystalline semiconductor are instead distributed throughout the entire material. A representative localized wave function is contrasted with its extended counterpart in Figure 2.6

The role that disorder plays in modifying the nature of the electronic states within a material was first brought to light through the work of Anderson [35]. Anderson's theory of localization, as it is now referred to as, may be intuitively understood by considering the one-dimensional potential models depicted in Figure 2.7, one potential representing that associated with an ordered material, the other representing a disordered material; it should be noted that while Anderson himself never actually employed this simplistic model in order to understand the role of disorder within disordered materials, it is nevertheless often referred to as the Anderson model. These potentials may be thought of as describing the interaction of an electron with the nuclei associated with the constituent atoms of the material, each well representing the attraction between the electrons and these nuclei. The breadth of the band associated with this potential structure, B, arises as a consequence of the interactions between the atoms. For disordered materials, however, a random potential is added onto this periodic array of potential wells, the random fluctuations in the potential well having an average amplitude of V_0. Anderson's theory may be used to show that, when V_0/B exceeds a certain critical value, there is zero probability for an electron at any site to diffuse away. Accordingly, all of the electronic states associated this material are localized, and there is no electrical conduction.

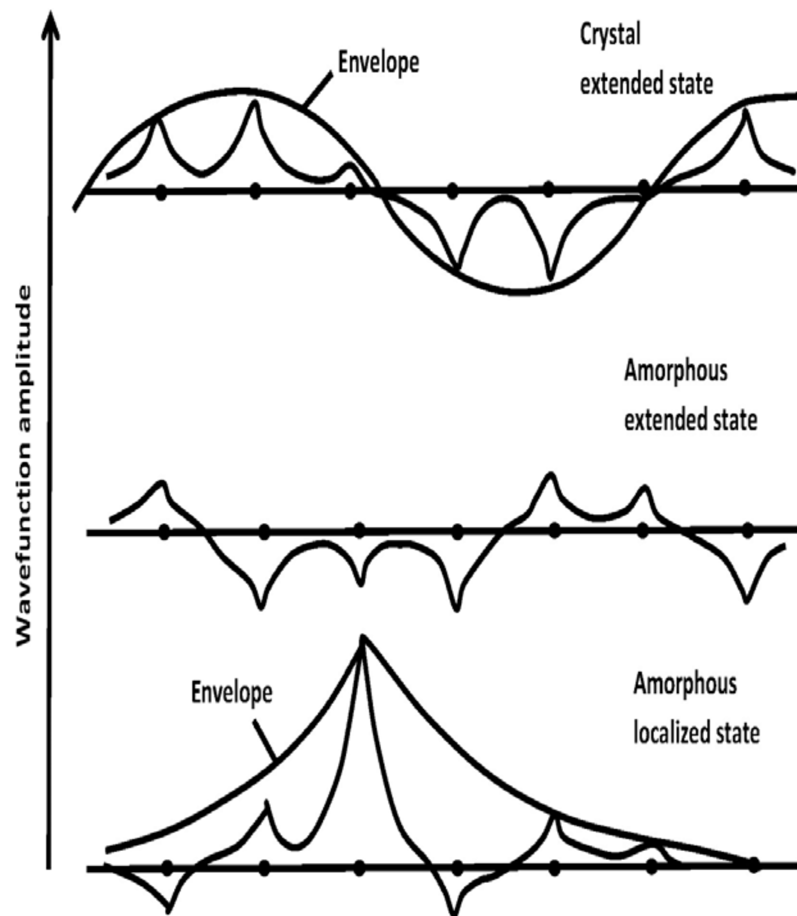

Figure 2.6: Localized and extended wave functions. These plots are drawn from the author's conception.

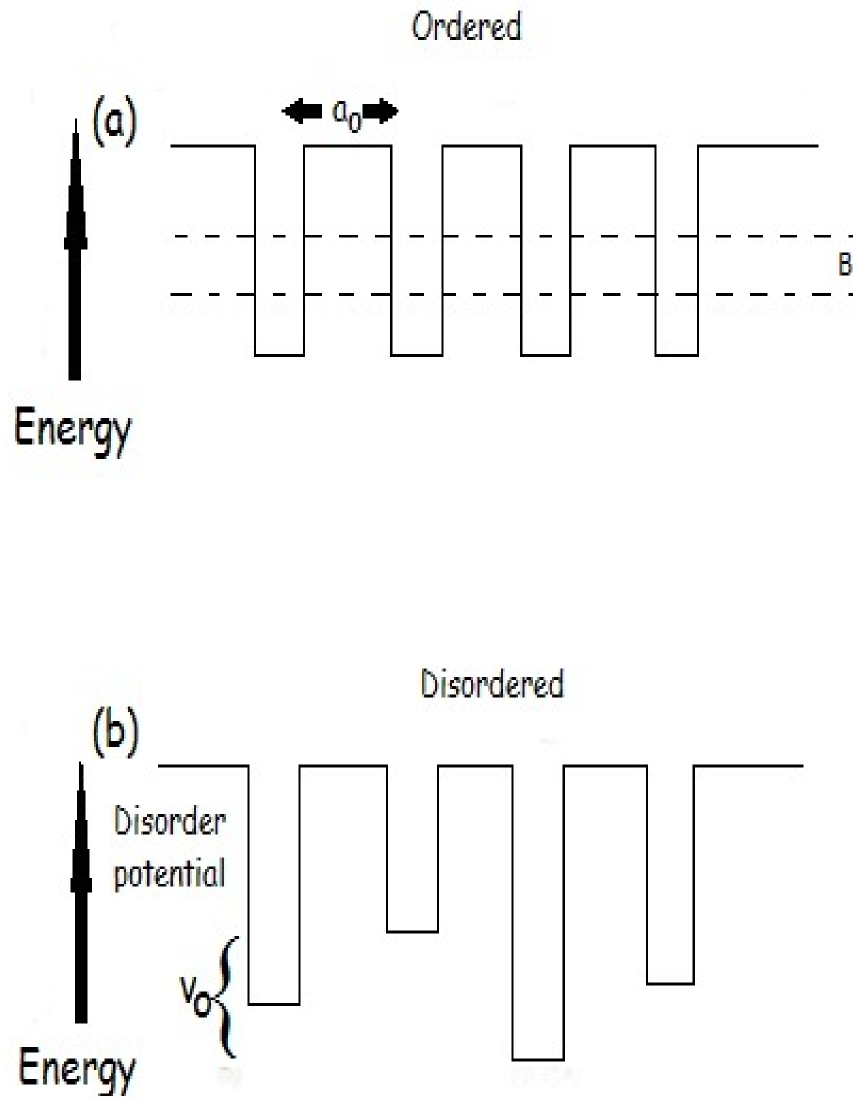

Figure 2.7: A schematic representation of Anderson's model.

The critical value of V_0/B for complete localization, i.e., for all of the electronic states to be localized, is about three [35]. Since the band widths, B, associated with most crystalline semiconductors are of order 5 eV, a very large disorder potential, V_0, is needed in order to achieve complete localization. Studies into amorphous semiconductors reveal that the criterion for complete localization is usually not met for these materials. Amorphous semiconductors, over the short-range at least, exhibit mild variations in the bond lengths and bond angles. Nevertheless, the strong scattering that the electrons experience as they propagate through an amorphous semiconductor leads to a large uncertainty in the electron momentum. Assuming incoherent scattering off each atom, through the uncertainty principle, it may be shown that the uncertainty in the electron wave-vector,

$$\Delta k = \frac{1}{\Delta x} \approx \frac{1}{a_o} \approx k, \tag{2.3}$$

where Δx denotes the scattering length, i.e., $\Delta x = a_o$, where a_o represents the interatomic spacing. Since the uncertainty in k is of the order of k itself, k is a poor quantum number. That is, the electrons are being incoherently scattered off each atomic potential. Accordingly, crystal momentum, $\hbar\vec{k}$, is not conserved for transitions within amorphous semiconductors. The loss of $\vec{k}$-conservation for these materials, coupled with the presence of localized electronic states, puts greater emphasis on the spatial location of the carriers rather than on their momentum.

As has already been mentioned, a very large amount of disorder is needed in order to localize all of the electronic states. Even when the disorder corresponding to an amorphous semiconductor is insufficient to meet Anderson's criterion, some of the electronic states associated with an amorphous semiconductor are localized and that these electronic states lie near the band edges. The center of the band is

comprised of extended states for which there is strong scattering. The extended and localized states are separated by mobility edges, the extended states contributing to conduction, the localized states not. This is the essence of the standard model for amorphous semiconductors proposed by Mott and Davis [36]. The location of the mobility edge depends on the degree of disorder that is present, and is typically between 100 and 500 meV from the band edges for all amorphous semiconductors.

2.7 The free electron model and the density of states

The free electron model is the simplest way to represent the electronic structure of a solid and evaluate its corresponding distribution of electronic states. Although this approach is not appropriate for describing all aspects of the solid state, it leads to many correct results in a relatively straightforward manner [37]. Within the framework of this model, the interaction of the electrons with the atomic nuclei and with the other electrons are neglected. Thus, the electrons are treated as 'free' particles.

In quantum mechanics, the wave functions associated with an electron may be described using Schrödinger's equation. In steady-state, i.e., neglecting variations with respect to time, this equation may be expressed as

$$H\Psi = E\Psi, \tag{2.4}$$

where H denotes the Hamiltonian, Ψ represents the wave function associated with the electron, and E is the corresponding energy level. Neglecting the spin-orbit interaction, the one-electron Hamiltonian, in the absence of an external electro-

magnetic field, may be expressed as

$$H = \frac{-\hbar^2}{2m}\nabla^2 + U(\vec{r}), \tag{2.5}$$

where $U(\vec{r})$ denotes the potential energy for an arbitrary electron, ∇^2 is the mathematical operator $\nabla \cdot \nabla$, and m represents the electron mass. For the case of a free electron, i.e., an electron that is not bounded, the potential energy, $U(\vec{r})$, may be set to zero for all $\vec{r}$.

For the one-dimensional case, an electron may be considered confined between $x = 0$ and $x = L$ by infinite potential barriers, as shown in Figure 2.8. The nth wave function, $\Psi_n(x)$, associated with such an electron, represents a solution to Schrödinger's equation, i.e., $H\Psi_n(x) = E_n\Psi_n(x)$, where E_n is the energy of the electron orbital. Since the potential energy, $U(x)$, is taken to be at zero, Schrödinger's equation for x between 0 and L may be expressed as

$$H\Psi_n(x) = \frac{p^2}{2m}\Psi_n(x) = -\frac{\hbar^2}{2m}\frac{d^2}{dx^2}\Psi_n(x) = E_n\Psi_n(x), \tag{2.6}$$

where $p = \frac{\hbar}{i}\frac{d}{dx}$ denotes electron momentum, electron-electron interactions being neglected for this one-electron equation. Since $\Psi_n(x)$ is a continuous function, and since the potential is infinite both below $x = 0$ and above $x = L$, the boundary conditions for the wave function are $\Psi_n(0) = \Psi_n(L) = 0$. The solutions of Eq. (2.6) are therefore

$$\Psi_n(x) = \sqrt{\frac{2}{L}}\ \sin\left(\frac{\pi n}{L}\ x\right). \tag{2.7}$$

Substituting Eq. (2.7) into Eq. (2.6), the energy associated with wave function $\Psi_n(x)$ is seen to be

$$E_n = \frac{\hbar^2}{2m}\left(\frac{\pi n}{L}\right)^2. \tag{2.8}$$

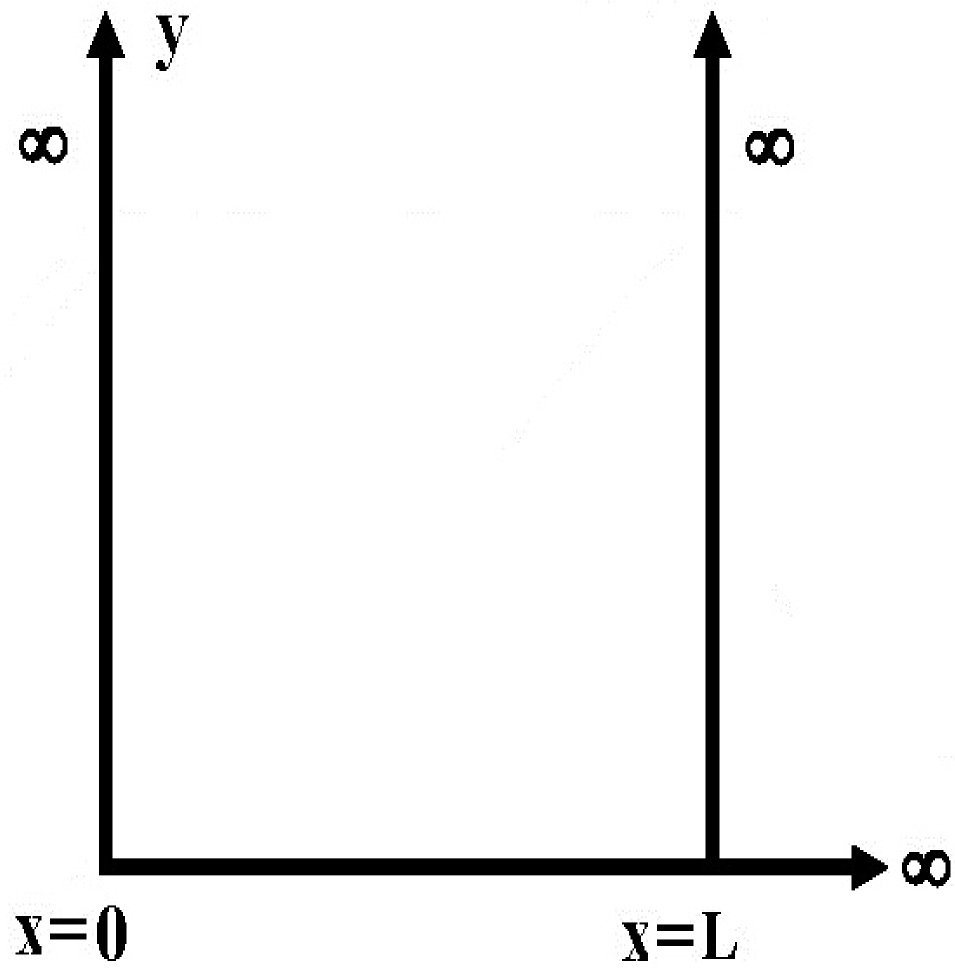

Figure 2.8: The potential energy configuration for the one-dimensional case.

These equations correspond to standing waves with a different number of nodes within this potential well.

In three-dimensions, Schrödinger's equation takes the form

$$\begin{aligned} H\Psi(\mathbf{r}) &= \frac{p^2}{2m}\Psi(\mathbf{r}), && (2.9)\\ &= -\frac{\hbar^2}{2m}\nabla^2\Psi(\mathbf{r}), && (2.10)\\ &= -\frac{\hbar^2}{2m}\left(\frac{\partial^2}{\partial x^2}+\frac{\partial^2}{\partial y^2}+\frac{\partial^2}{\partial z^2}\right)\Psi(\mathbf{r}), && (2.11)\\ &= E\Psi(\mathbf{r}), && (2.12)\end{aligned}$$

where $\Psi(\mathbf{r})$ denotes the corresponding wave function. For the case of electrons confined within a three-dimensional infinite cubic potential well, with $V = 0$ inside and V set to ∞ outside, as depicted in Figure 2.9 [38], it may be shown that the solution of Schrödinger's equation takes the form of a standing wave, i.e.,

$$\Psi(\mathbf{r}) = \left(\frac{2}{L}\right)^{3/2} \sin\left(\frac{\pi n_x}{L}x\right) \sin\left(\frac{\pi n_y}{L}y\right) \sin\left(\frac{\pi n_z}{L}z\right), \qquad (2.13)$$

where n_x, n_y, and n_z represent positive integers, each such integer representing the effect of confinement in the different directions.

Substituting Eq. (2.13) into Eq. (2.12), the energy associated with wave function $\Psi(\mathbf{r})$ is seen to be

$$E_n = \frac{\hbar^2}{2m}\left[\left(\frac{\pi n_x}{L}\right)^2 + \left(\frac{\pi n_y}{L}\right)^2 + \left(\frac{\pi n_z}{L}\right)^2\right]. \qquad (2.14)$$

It may be shown that the corresponding DOS function

$$N(E) = \begin{cases} \sqrt{2}\frac{m^{3/2}}{\pi^2\hbar^3}\sqrt{E}, & E \geq 0 \\ 0, & E < 0 \end{cases}, \qquad (2.15)$$

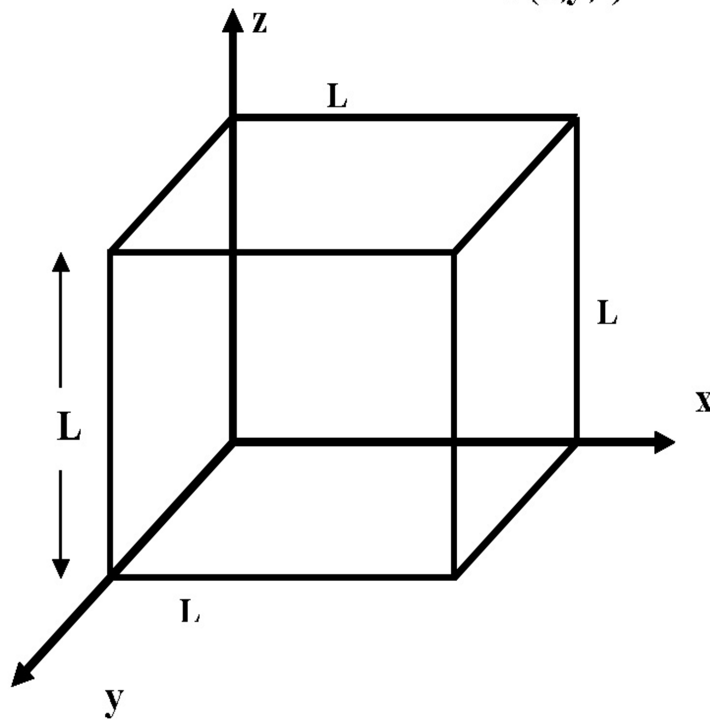

Figure 2.9: The potential energy configuration for the three-dimensional case. This figure is after Thevaril [36].

where $N(E)\Delta E$ represents the number of electronic states, per unit volume, between energies $[E, E + \Delta]$. Eq. (2.15) is often referred to as the free electron DOS model. It will be used in the subsequent analysis.

2.8 Empirical models for the distribution of electronic states: a review

The physics of a semiconductor may be understood, in large measure, through knowledge of the distribution of electronic states. In a disorderless crystalline semiconductor, the distribution of electronic states terminates abruptly at the conduction band and valence band band edges, there being no electronic states within the gap region between these edges. In a disordered semiconductor, however, the disorder inherent to the atomic distribution leads to distributions of electronic states that encroach into the otherwise empty gap region. Research has demonstrated that these encroaching electronic states are primarily what is responsible for the unique properties associated with disordered semiconductors [12]. A schematic illustration of the differences between the distributions of electronic states associated with crystalline and disordered semiconductors is depicted in Figure 2.10 [39].

The disorder inherent to the disordered atomic distribution leads to the formation of localized electronic states. While the electron wave functions associated with all of the electronic states associated with a crystalline semiconductor extend throughout the entire crystal, the localized electronic states within a disordered semiconductor are characterized with electron wave functions that are limited in their extent. Research has demonstrated that the localized electronic states within a disordered semiconductor, which are located within the mobility gap region, are separated from the extended electronic states through abrupt mobility edges,

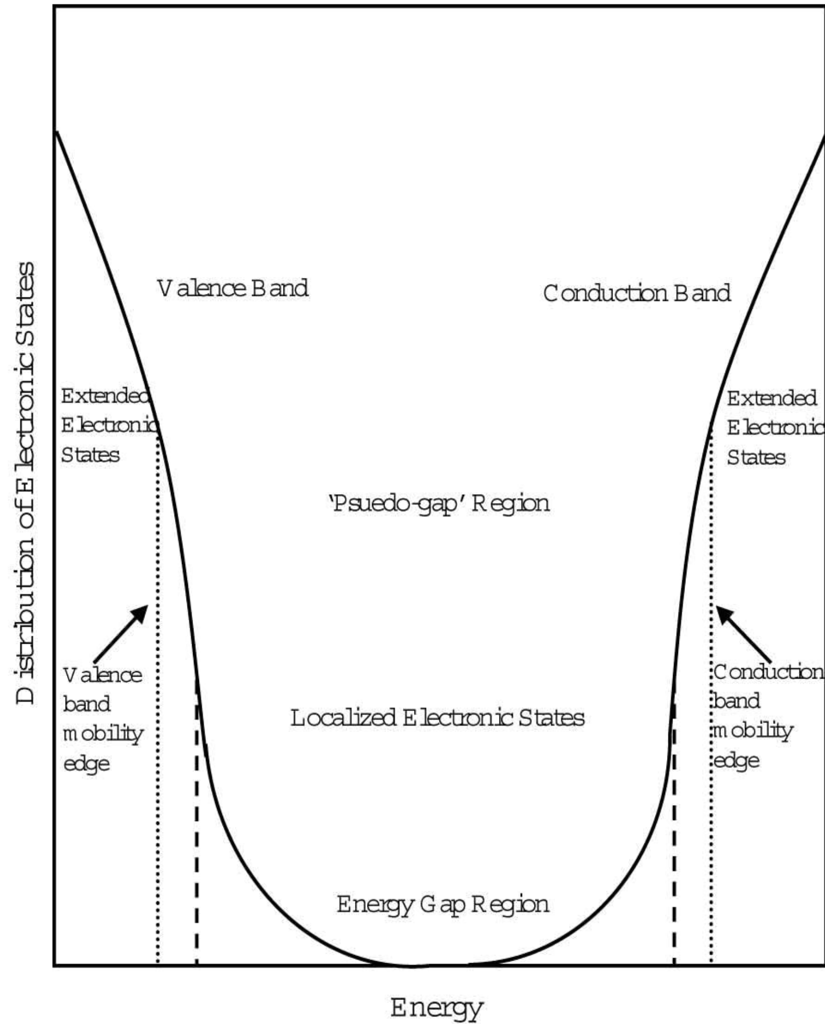

Figure 2.10: The distribution of electronic states associated with hypothetical crystalline and disordered semiconductors. The distribution of electronic states associated with a crystalline semiconductor is depicted with the dashed lines, while that associated with the disordered semiconductor is shown with the solid lines. While there is no true energy gap for the case of a disordered semiconductor, often the diminished region in the distribution of electronic states is referred as the 'pseudo-gap' region. The states between the conduction band and valence band mobility edges are localized while the other states are extended. The conduction band and valence band mobility edges are depicted with the dotted lines. This particular image was borrowed from Nguyen [37].

one associated with the valence band, the other associated with the conduction band [10]; see, for example, Figure 2.10. The localization of the electronic states within a disordered semiconductor is what is commonly held responsible for many of the unique properties associated with disordered semiconductors [10].

As was mentioned previously, in a crystalline semiconductor, the electronic structure is usually characterized in terms of a band structure. The band structure specifies how the energy of the electronic states varies with the crystal-momentum wave-vector, $\vec{k}$. In an amorphous semiconductor, however, the crystal-momentum wave-vector, $\vec{k}$, is a poor quantum number, and an alternate means of characterizing the electronic structure must be sought. Instead, the electronic structure associated with an amorphous semiconductor is usually characterized through the specification of the valence band and conduction band DOS functions, $N_{\text{V}}(E)$ and $N_{\text{C}}(E)$, respectively. These functions represent the number of electronic states per unit energy, per unit volume, i.e., $N_{\text{V}}(E)\triangle E$ and $N_{\text{C}}(E)\triangle E$ represent the number of valence band and conduction band electronic states, between energies $[E, E + \triangle E]$, per unit volume, respectively.

Empirical models for these DOS functions, $N_{\text{V}}(E)$ and $N_{\text{C}}(E)$, are often used in order to interpret the optical properties associated with these materials. These empirical models embody experimentally observed features. Arguing that the band states associated with an amorphous semiconductor should be distributed in a similar manner to their crystalline counterparts, Tauc *et al.* [40] suggest an empirical DOS model with square-root conduction band and valence band DOS functions.

That is, Tauc *et al.* [40] suggest that

$$N_{\mathrm{V}}(E) = \begin{cases} 0, & E > E_{\mathrm{V}} \\ N_{\mathrm{VO}}\sqrt{E_{\mathrm{V}} - E}, & E \leq E_{\mathrm{V}} \end{cases} \tag{2.16}$$

and

$$N_{\mathrm{C}}(E) = \begin{cases} N_{\mathrm{CO}}\sqrt{E - E_{\mathrm{C}}}, & E \geq E_{\mathrm{C}} \\ 0, & E < E_{\mathrm{C}} \end{cases} \tag{2.17}$$

where N_{VO} and N_{CO} denote the valence band and conduction band DOS prefactors, respectively, E_{V} and E_{C} representing the valence band and conduction band band edges; this essentially corresponds to the free electron model discussed earlier in Section 2.7. Drawing upon the free electron case, if we let m_{V}^* and m_{C}^* represent the DOS effective masses associated with the valence band and conduction band, respectively, from the free electron model, i.e., Eq. (2.15), it may be shown that $N_{\mathrm{VO}} = \sqrt{2}\frac{m_{\mathrm{V}}^{*3/2}}{\pi^2\hbar^3}$ and that $N_{\mathrm{CO}} = \sqrt{2}\frac{m_{\mathrm{C}}^{*3/2}}{\pi^2\hbar^3}$. In this model, the DOS functions, $N_{\mathrm{V}}(E)$ and $N_{\mathrm{C}}(E)$, terminate abruptly at the valence band and conduction band band edges, there being no electronic states within the gap region between E_{V} and E_{C}. It should be noted, however, that while the empirical DOS model of Tauc *et al.* [40] accounts for the presence of both valence band band (VBB) and conduction band band (CBB) electronic states, it completely neglects the presence of tail states.

While the empirical DOS model of Tauc *et al.* [40] forms a basis from which the optical properties of amorphous semiconductors may be interpreted, which is required for a complete accounting of the spectral dependence of the optical absorption coefficient, $\alpha(\hbar\omega)$, tail states are neglected. It is generally agreed upon that tail states arise as a consequence of the disorder present in amorphous semiconductors, though there are some unresolved theoretical issues. The breadth of

the tails reflects the amount of disorder. Tiedje *et al.* [41] provided experimental results that suggests the presence of exponential distributions of valence band tail (VBT) and conduction band tail (CBT) electronic states encroaching into the otherwise empty gap region for the case of PECVD a-Si:H; it should be noted, however, that other functional forms cannot be ruled out without experimental results of greater resolution. A range of modifications to the empirical DOS model of Tauc *et al.* [40], i.e., Eqs. (2.16) and (2.17), incorporating exponential distribution of tail states, have been proposed.

In an effort to understand the spectral dependence of the optical absorption coefficient, both above and below the energy gap, Chen *et al.* [42] assumed square-root distributions of VBB and CBB states and an exponential distribution of VBT states. That is, Chen *et al.* [42] assume

$$N_{\mathrm{V}}(E) = \begin{cases} N_{\mathrm{VO}}^{*} \exp\left(\frac{E_{\mathrm{V}}-E}{\gamma_{\mathrm{V}}}\right), & E > E_{\mathrm{V}} \\ N_{\mathrm{VO}}\sqrt{E_{\mathrm{V}}-E}, & E \leq E_{\mathrm{V}} \end{cases} \tag{2.18}$$

and

$$N_{\mathrm{C}}(E) = \begin{cases} N_{\mathrm{CO}}\sqrt{E-E_{\mathrm{C}}}, & E \geq E_{\mathrm{C}} \\ 0, & E < E_{\mathrm{C}} \end{cases} \tag{2.19}$$

where N_{VO}^{*} denotes the VBT DOS prefactor and γ_{V} represents the breadth of the VBT states, $N_{\mathrm{VO}}, N_{\mathrm{CO}}, E_{\mathrm{V}}$, and E_{C} being as defined earlier.

The empirical DOS model of Chen *et al.* [42] is observed to be the empirical DOS model of Tauc *et al.* [40] with the valence band band distribution plus an exponential tail added on at energies above the valence band band edge, E_{V}, this exponential tail representing the distribution of VBT states. A discontinuity occurs in the valence band DOS function, $N_{\mathrm{V}}(E)$. This discontinuity is not physical,

which Chen *et al.* [42] acknowledged, asserting that only a small error is introduced into the resultant optical absorption spectrum through such a discontinuity; the spectral dependence of the optical absorption coefficient is determined through a process of integration over the valence band and conduction band DOS functions.

Another empirical DOS model was presented by Redfield [43], who assumed flat VBB and CBB distributions and exponential VBT and CBT distributions. That is, Redfield [43] assumes that

$$N_{\mathrm{V}}(E) = \begin{cases} N_{\mathrm{VO}}^{*} \exp\left(\frac{E_{\mathrm{V}}-E}{\gamma_{\mathrm{V}}}\right), & E > E_{\mathrm{V}} \\ N_{\mathrm{VO}}^{*}, & E \leq E_{\mathrm{V}} \end{cases} \tag{2.20}$$

and

$$N_{\mathrm{C}}(E) = \begin{cases} N_{\mathrm{CO}}^{*}, & E \geq E_{\mathrm{C}} \\ N_{\mathrm{CO}}^{*} \exp\left(\frac{E-E_{\mathrm{C}}}{\gamma_{\mathrm{C}}}\right), & E < E_{\mathrm{C}} \end{cases} \tag{2.21}$$

where N_{CO}^{*} denotes the CBT DOS prefactor and γ_{C} represents the breadth of the CBT states, E_{V}, E_{C}, γ_{V}, and N_{VO}^{*} being as defined previously. These simplified VBB and CBB distributions are introduced in order to ease the analysis. For the purposes of determining the spectral dependence of the optical absorption spectrum for photon energies below the energy gap, they will play a minor role.

Cody [28] assumed square-root distributions of VBB and CBB states and an exponential distribution of VBT states, based on the approach presented by Chen *et al.* [42], which neglects the CBT states in the empirical DOS model. Cody [28] advocates that the square-root distribution interfaces with the exponential distribution at an energy level below the VBB edge, E_{V}. That is, the VBB distribution does not actually terminate, thus avoiding the discontinuity found in the empirical DOS model of Chen *et al.* [42], who just grafted an exponential distribution onto

a terminated VBB square-root distribution. Thus, it is asserted by Cody [28] that

$$N_{\mathrm{v}}(E) = \begin{cases} N_{\mathrm{vo}}\sqrt{\frac{3}{2}\gamma_{\mathrm{v}}}\exp\left(\frac{-3}{2}\right)\exp\left(\frac{E_{\mathrm{v}}-E}{\gamma_{\mathrm{v}}}\right), & E > E_{\mathrm{v}} - \frac{3}{2}\gamma_{\mathrm{v}} \\ N_{\mathrm{vo}}\sqrt{E_{\mathrm{v}} - E}, & E \leq E_{\mathrm{v}} - \frac{3}{2}\gamma_{\mathrm{v}} \end{cases} \tag{2.22}$$

and

$$N_{\mathrm{c}}(E) = \begin{cases} N_{\mathrm{co}}\sqrt{E - E_{\mathrm{c}}}, & E \geq E_{\mathrm{c}} \\ 0, & E < E_{\mathrm{c}} \end{cases} \tag{2.23}$$

where $N_{\mathrm{vo}}, N_{\mathrm{co}}, E_{\mathrm{v}}, E_{\mathrm{c}}$, and γ_{v} are as defined earlier.

More recently, various proposed empirical models, that capture both square-root distributions of band states and exponential distributions of tail states, with an abrupt interface between the two regions, have been proposed. Such models are special cases of the empirical DOS model of Jiao *et al.* [44]. In this model, the valence band DOS function

$$N_{\mathrm{v}}(E) = \begin{cases} N_{\mathrm{vo}}\sqrt{E_{\mathrm{v}} - E_{\mathrm{vt}}}\exp\left(\frac{E_{\mathrm{vt}}-E_{\mathrm{v}}}{\gamma_{\mathrm{v}}}\right)\exp\left(\frac{E_{\mathrm{vt}}-E}{\gamma_{\mathrm{v}}}\right), & E > E_{\mathrm{vt}} \\ N_{\mathrm{vo}}\sqrt{E_{\mathrm{v}} - E}, & E \leq E_{\mathrm{vt}} \end{cases}, \tag{2.24}$$

and the conduction band DOS function

$$N_{\mathrm{c}}(E) = \begin{cases} N_{\mathrm{co}}\sqrt{E - E_{\mathrm{c}}}, & E \geq E_{\mathrm{ct}} \\ N_{\mathrm{co}}\sqrt{E_{\mathrm{ct}} - E_{\mathrm{c}}}\exp\left(\frac{E_{\mathrm{c}}-E_{\mathrm{ct}}}{\gamma_{\mathrm{c}}}\right)\exp\left(\frac{E-E_{\mathrm{c}}}{\gamma_{\mathrm{c}}}\right), & E < E_{\mathrm{ct}} \end{cases} \tag{2.25}$$

where E_{vt} and E_{ct} represent the critical points at which the exponential and square-root distributions interface, $N_{\mathrm{vo}}, N_{\mathrm{co}}, E_{\mathrm{v}}, E_{\mathrm{c}}$, γ_{v}, and γ_{c} being as defined previously. It should be noted that Eqs. (2.24) and (2.25) require $E_{\mathrm{vt}} \leq E_{\mathrm{v}}$ and $E_{\mathrm{ct}} \geq E_{\mathrm{c}}$.

It is found that the model of Cody [28], i.e., Eqs. (2.22) and (2.23), is a special case of the general empirical DOS model of Jiao *et al.* [44] for which $E_{\mathrm{vt}} = E_{\mathrm{v}} - \frac{3}{2}\gamma_{\mathrm{v}}$

and $E_{\mathrm{ct}} = E_{\mathrm{C}}$. The empirical DOS model of O'Leary *et al.* [45] is also a special case of the general empirical DOS model of Jiao *et al.* [44], where the transition in each of the DOS functions between the band regions and the tail regions is assumed to be a smooth one, i.e., $N_{\mathrm{V}}(E)$ and $N_{\mathrm{C}}(E)$, and the derivatives of $N_{\mathrm{V}}(E)$ and $N_{\mathrm{C}}(E)$, are continuous at E_{vt} and E_{ct}, respectively. For this particular case, analysis shows that $E_{\mathrm{vt}} = E_{\mathrm{V}} - \frac{1}{2}\gamma_{\mathrm{V}}$ and $E_{\mathrm{ct}} = E_{\mathrm{C}} + \frac{1}{2}\gamma_{\mathrm{C}}$ [45]. As a result, Eqs. (2.24) and (2.25) reduce to

$$N_{\mathrm{V}}(E) = \begin{cases} N_{\mathrm{vo}}\sqrt{\frac{1}{2}\gamma_{\mathrm{V}}}\exp\left(\frac{-1}{2}\right)\exp\left(\frac{E_{\mathrm{V}}-E}{\gamma_{\mathrm{V}}}\right), & E > E_{\mathrm{V}} - \frac{1}{2}\gamma_{\mathrm{V}} \\ N_{\mathrm{vo}}\sqrt{E_{\mathrm{V}} - E}, & E \leq E_{\mathrm{V}} - \frac{1}{2}\gamma_{\mathrm{V}} \end{cases}, \tag{2.26}$$

and

$$N_{\mathrm{C}}(E) = \begin{cases} N_{\mathrm{co}}\sqrt{E - E_{\mathrm{C}}}, & E \geq E_{\mathrm{C}} + \frac{1}{2}\gamma_{\mathrm{C}} \\ N_{\mathrm{co}}\sqrt{\frac{1}{2}\gamma_{\mathrm{C}}}\exp\left(\frac{-1}{2}\right)\exp\left(\frac{E-E_{\mathrm{C}}}{\gamma_{\mathrm{C}}}\right), & E < E_{\mathrm{C}} + \frac{1}{2}\gamma_{\mathrm{C}} \end{cases} \tag{2.27}$$

It is noted that in the disorderless limit, i.e., $\gamma_{\mathrm{V}} \to 0$ and $\gamma_{\mathrm{C}} \to 0$, that the empirical DOS model of O'Leary *et al.* [45] reduces to the empirical DOS model of Tauc *et al.* [40]. In this limit, i.e., when $\gamma_{\mathrm{V}} \to 0$, the valence band DOS function, depicted in Eq. (2.26), terminates abruptly at the valence band band edge, E_{V}, which corresponds exactly with Eq. (2.16). Similar results are also observed for the conduction band DOS function, $N_{\mathrm{C}}(E)$. In particular, in this limit, i.e., when $\gamma_{\mathrm{C}} \to 0$, the conduction band DOS function, Eq.(2.27), reduces to Eq. (2.17).

2.9 General empirical DOS model

The distribution of electronic states associated with a disordered semiconductor exhibits square-root functional dependencies in the band regions and exponential

functional dependencies in the tail regions, the tail breadth parameters, γ_{V} and γ_{C}, being reflective of the amount of disorder present in the amorphous semiconductor [22]. In order to examine the impact of disorder, the sensitivity of $N_{\mathrm{V}}(E)$ and $N_{\mathrm{C}}(E)$ to variations in γ_{V} and γ_{C} is examined for the empirical DOS model of O'Leary *et al.* [45], i.e., Eqs. (2.26) and (2.27). In Figure 2.11, the valence band DOS function, $N_{\mathrm{V}}(E)$, is plotted for a number of selections of $\gamma_{\mathrm{V}}, N_{\mathrm{VO}}$ being set to 2×10^{22} cm^{-3}eV$^{-3/2}$ and E_{V} being set to 0.0 eV for all cases. We note that in the disorderless limit, i.e., when $\gamma_{\mathrm{V}} \to 0$, that the valence band DOS function terminates abruptly at the valence band band edge, E_{V}. As γ_{V} increases from this disorderless limit, however, an exponential tail emerges, the total number of tail states increasing as the valence band tail breadth, γ_{V}, is increased, i.e., the distribution of tail states further encroaches into the gap region. This plot is depicted on a logarithmic scale in Figure 2.12. Similar results are also observed for the conduction band DOS function, $N_{\mathrm{C}}(E)$, as may be seen by observing Figures 2.13 and 2.14.

For the purposes of this analysis, an empirical model for the DOS functions, that captures basic amorphous semiconductor phenomenology, is adopted. In particular, following O'Leary [46, 47], it is assumed that the valence band DOS function

$$N_{\mathrm{V}}(E) = \begin{cases} N_{\mathrm{VO}}\sqrt{E_{\mathrm{V}} - E_{\mathrm{vt}}}\exp\left(\frac{E_{\mathrm{vt}}-E_{\mathrm{V}}}{\gamma_{\mathrm{V}}}\right)\exp\left(\frac{E_{\mathrm{V}}-E}{\gamma_{\mathrm{V}}}\right), & E > E_{\mathrm{vt}} \\ N_{\mathrm{VO}}\sqrt{E_{\mathrm{V}} - E} & E \leq E_{\mathrm{vt}} \end{cases}, \quad (2.28)$$

and that the conduction band DOS function

$$N_{\mathrm{C}}(E) = \begin{cases} N_{\mathrm{CO}}\sqrt{E - E_{\mathrm{C}}}, & E \geq E_{\mathrm{ct}} \\ N_{\mathrm{CO}}\sqrt{E_{\mathrm{ct}} - E_{\mathrm{C}}}\exp\left(\frac{E_{\mathrm{C}}-E_{\mathrm{ct}}}{\gamma_{\mathrm{C}}}\right)\exp\left(\frac{E-E_{\mathrm{C}}}{\gamma_{\mathrm{C}}}\right), & E < E_{\mathrm{ct}} \end{cases}, \quad (2.29)$$

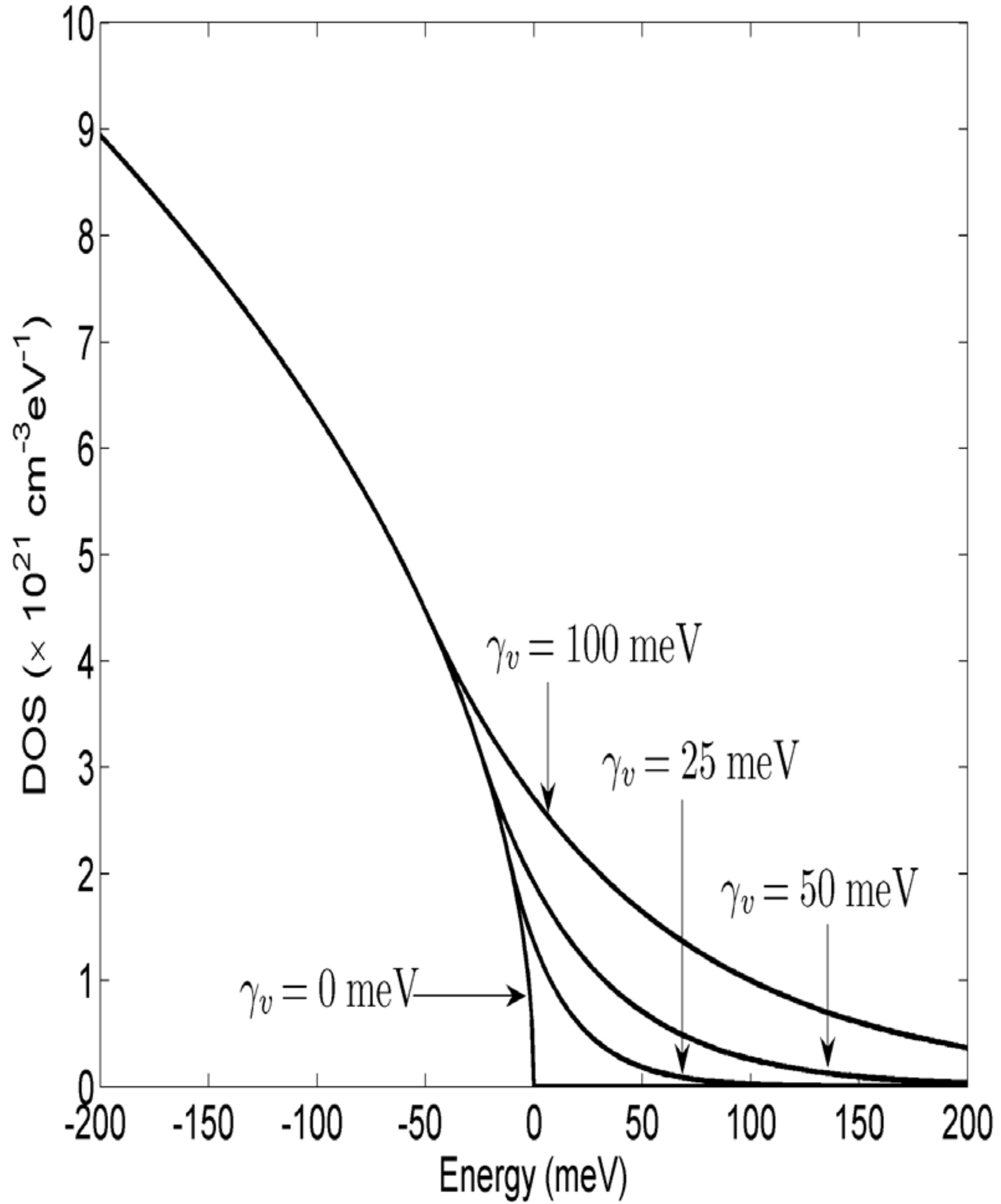

Figure 2.11: The valence band DOS function, $N_{\rm V}(E)$, corresponding to various selections of $\gamma_{\rm V}$, $N_{\rm VO}$ being set to $2 \times 10^{22}{\rm cm}^{-3}{\rm eV}^{-3/2}$ and $E_{\rm V}$ being set to 0 eV for all cases. This plot is cast on a linear scale.

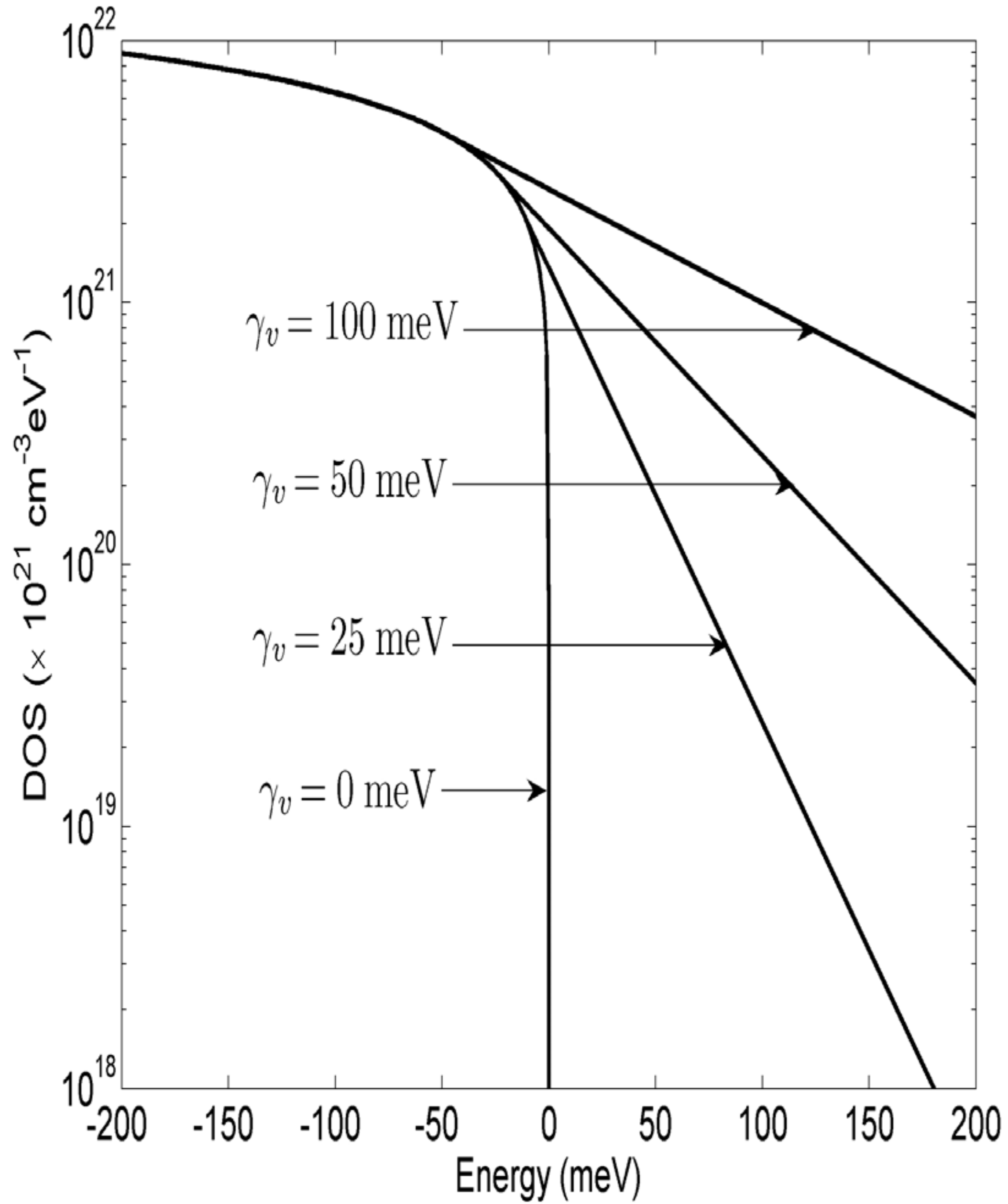

Figure 2.12: The valence band DOS function, $N_{\mathrm{V}}(E)$, corresponding to various selections of γ_{V}, N_{VO} being set to $2 \times 10^{22}\mathrm{cm}^{-3}\mathrm{eV}^{-3/2}$ and E_{V} being set to 0 eV for all cases. This plot is cast on a logarithmic scale.

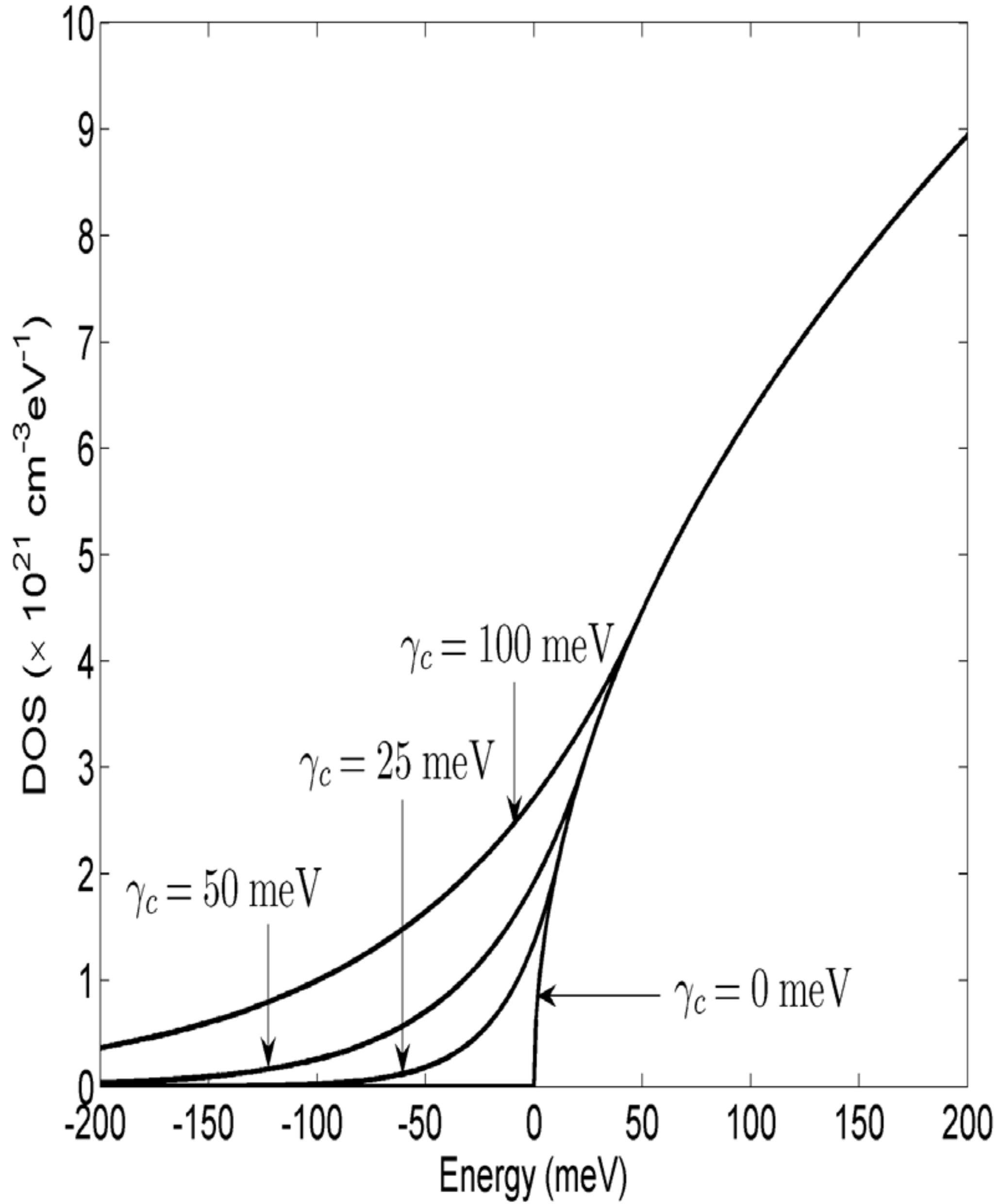

Figure 2.13: The conduction band DOS function, $N_{\mathrm{C}}(E)$, corresponding to various selections of γ_{C}, N_{CO} being set to $2 \times 10^{22}\mathrm{cm}^{-3}\mathrm{eV}^{-3/2}$ and E_{C} being set to 0 eV for all cases. This plot is cast on a linear scale.

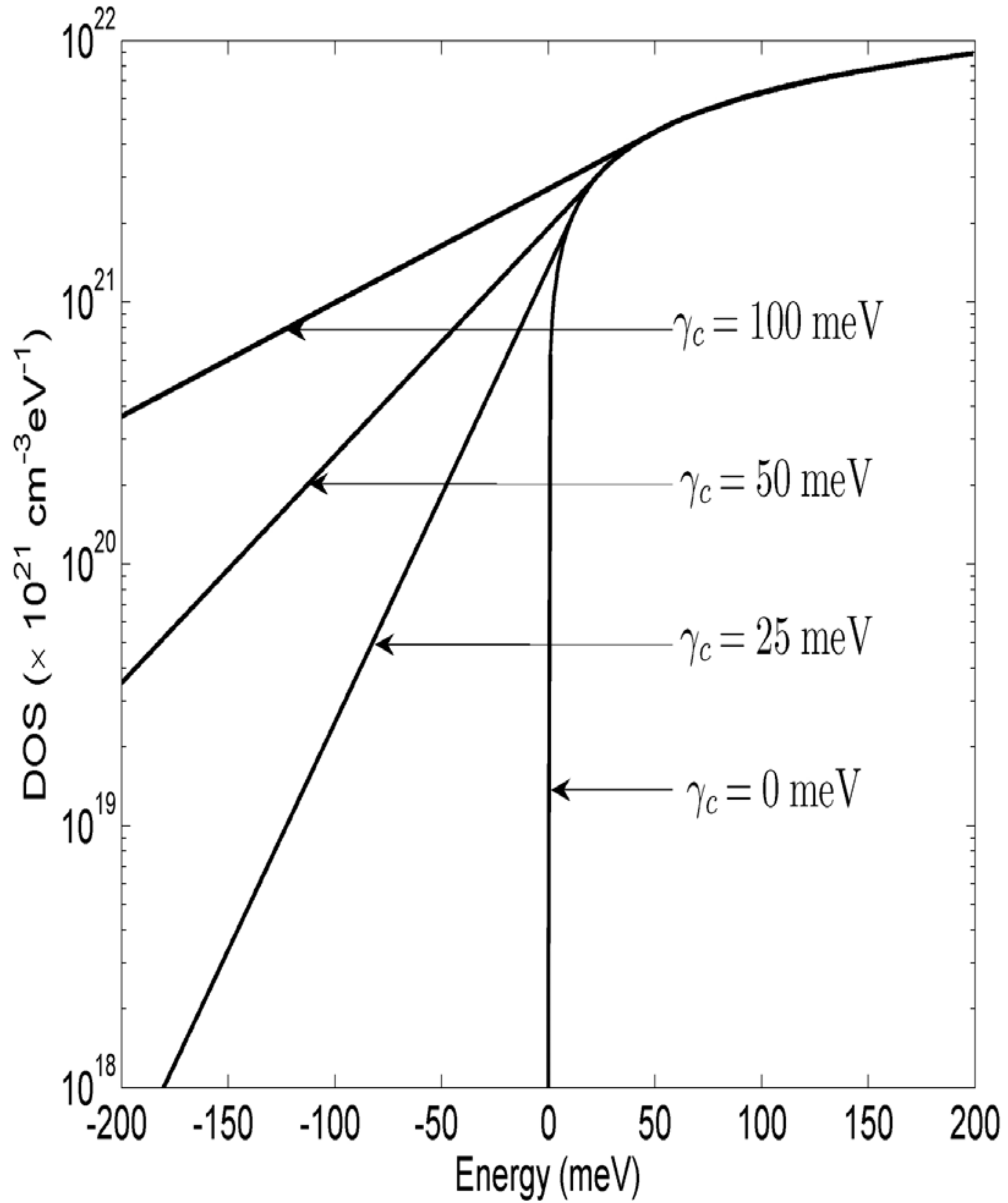

Figure 2.14: The conduction band DOS function, $N_{\mathrm{C}}(E)$, corresponding to various selections of γ_{C}, N_{CO} being set to $2 \times 10^{22}\mathrm{cm}^{-3}\mathrm{eV}^{-3/2}$ and E_{C} being set to 0 eV for all cases. This plot is cast on a logarithmic scale.

Table 2.1: The nominal DOS modeling parameter selections used for the purposes of this analysis.

Valence band		**Conduction band**	
Parameter	**Value**	**Parameter**	**Value**
N_{vo} (cm^{-3}eV$^{-3/2}$)	2×10^{22}	N_{co} (cm^{-3}eV$^{-3/2}$)	2×10^{22}
E_{v} (eV)	0.0	N_{c} (eV)	2.0
E_{vt}	$E_{\text{v}} - \frac{1}{2}\gamma_{\text{v}}$	E_{ct}	$E_{\text{c}} + \frac{1}{2}\gamma_{\text{c}}$
$E_{\text{v}\mu}$	E_{vt}	$E_{\text{c}\mu}$	E_{ct}
γ_{v} (meV)	50	γ_{c} (meV)	50

where N_{vo}, N_{co}, E_{v}, E_{c}, γ_{v}, γ_{c}, E_{vt}, and E_{ct} are as previously defined; it is implicitly assumed that $E_{\text{vt}} \leq E_{\text{v}}$ and $E_{\text{ct}} \geq E_{\text{c}}$. In order to ensure that the DOS functions, $N_{\text{v}}(E)$ and $N_{\text{c}}(E)$, and their derivatives, are continuous at the critical energies, E_{vt} and E_{ct}, at which points the square-root and exponential distributions interface, E_{vt} is set to $E_{\text{v}} - \frac{1}{2}\gamma_{\text{v}}$ and E_{ct} is set to $E_{\text{c}} + \frac{1}{2}\gamma_{\text{c}}$ [45].

In Figure 2.15, the valence band and conduction band DOS functions, $N_{\text{v}}(E)$ and $N_{\text{c}}(E)$, are plotted for a nominal set of DOS modeling parameter selections. That is, the DOS modeling parameters, $N_{\text{vo}} = N_{\text{co}} = 2 \times 10^{22}$ cm^{-3}eV$^{-3/2}$, $E_{\text{v}} = 0.0$ eV, $E_{\text{c}} = 2.0$ eV, $\gamma_{\text{v}} = \gamma\text{c} = 50$ meV, $E_{\text{vt}} = E_{\text{v}} - \frac{1}{2}\gamma_{\text{v}}$, and $E_{\text{ct}} = E_{\text{c}} + \frac{1}{2}\gamma_{\text{c}}$; this selection of parameters is similar to that used by Jiao *et al.* [44] and Malik and O'Leary [48] for the specific case of PECVD a-Si:H. These nominal DOS modeling parameter selections are tabulated in Table 2.1.

2.10 The mobility edges

In order to account for a number of seemingly incongruous amorphous semiconductor experimental observations, Cohen *et al.* [10] posited a fundamentally new

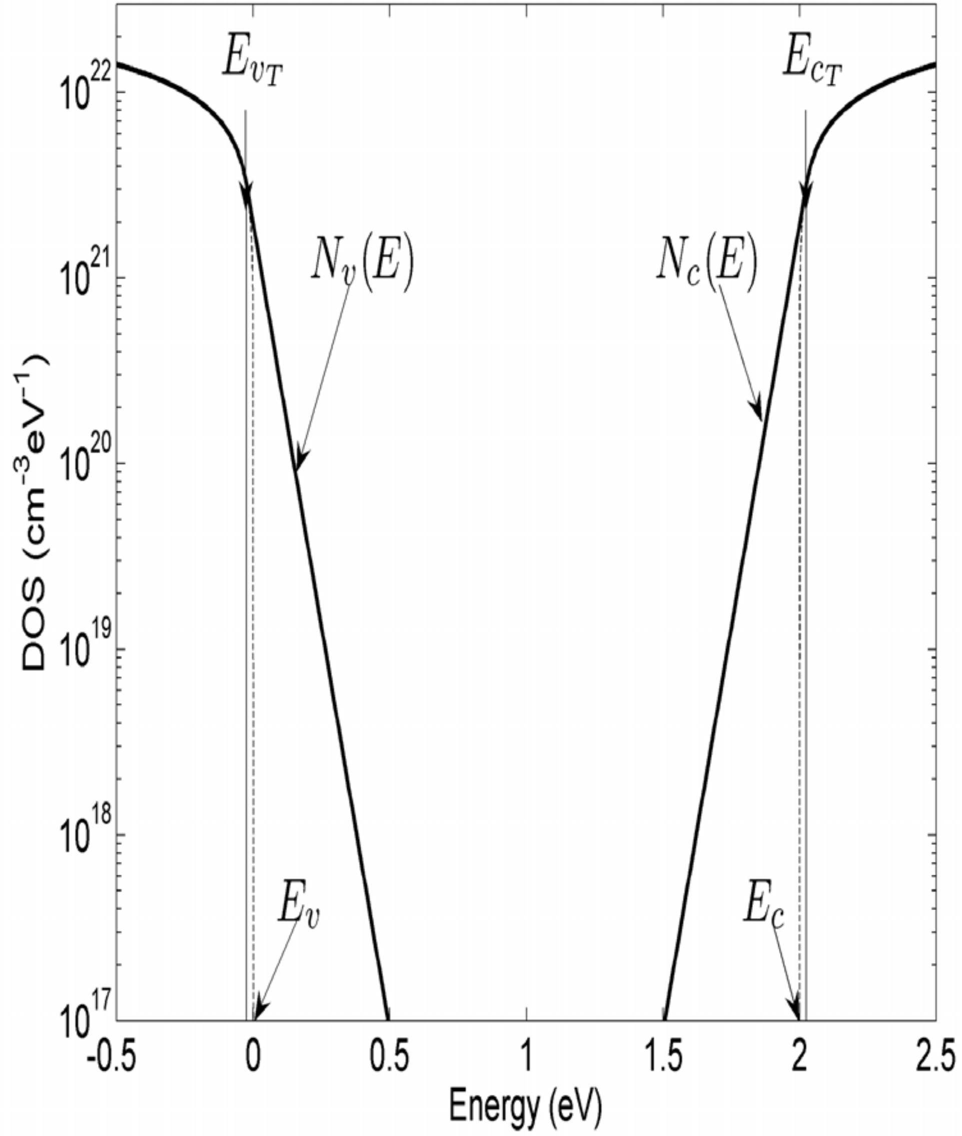

Figure 2.15: The valence band and conduction band DOS functions, $N_{\mathrm{V}}(E)$ and $N_{\mathrm{C}}(E)$, corresponding to a-Si:H, specified in Eq. (2.28) and Eq. (2.29), determined assuming the nominal a-Si:H DOS modeling parameter selections of O'Leary [47]. These nominal DOS modeling parameter selections are tabulated in Table 2.1.

vision for amorphous semiconductors. In particular, following up with Anderson's analysis [35], Cohen *et al.* [10] suggested that the disorder present within such a semiconductor would lead to a distribution of electronic states that encroaches into the otherwise empty gap region coupled with the presence of relatively sharp mobility edges. The distribution of electronic states associated with an amorphous semiconductor is thus characterized by three distinct regions: (1) extended electronic states above the conduction band mobility edge, $E_{\mathrm{C}\mu}$, (2) extended electronic states below the valence band mobility edge, $E_{\mathrm{V}\mu}$, and (3) localized electronic states between these mobility edges. The mobility edges define the mobility gap associated such a material; the mobility gap is the energy difference between $E_{\mathrm{V}\mu}$ and $E_{\mathrm{C}\mu}$, i.e., the mobility gap is equal to $E_{\mathrm{C}\mu} - E_{\mathrm{V}\mu}$. The mobility of the charge carriers within the mobility gap is much less than that within the extended states. For the purposes of this thesis, the viewpoint of Cohen *et al.* [10] is adopted as forming the fundamental basis for our analysis.

Fundamentally, the optical absorption which occurs within an amorphous semiconductor is determined by the number of allowed optical transitions and by the magnitude of the optical transition matrix elements which couple the electronic states between which these optical transitions occur [36, 45, 49, 50]; collectively, the influence of these individual optical transition matrix elements may be treated in terms of an overall aggregate optical transition matrix element. The JDOS function, $J(\hbar\omega)$, provides a measure of the number of allowed optical transitions between the occupied valence band electronic states and the unoccupied conduction band electronic states separated by energy $\hbar\omega$. The magnitude of the optical transition matrix elements may be determined from knowledge of the wave functions

associated with the electronic states. The random phase analysis of Hindley [51] asserts that the optical transition matrix elements associated with optical transitions involving at most one localized electronic state are of equal magnitude, i.e., this includes optical transitions from a VBE electronic state to a CBE electronic state (VBE-CBE optical transitions), optical transitions from a VBE electronic state to a CBL electronic state (VBE-CBL optical transitions), and optical transitions from a VBL electronic state to a CBE electronic state (VBL-CBE optical transitions). Optical transitions from a localized electronic state to another localized electronic state, i.e., optical transitions from a VBL electronic state to a CBL electronic state (VBL-CBL optical transitions), are found to have a negligible optical transition matrix element magnitude by comparison [50].

In order to simplify the analysis, and in the absence of experimental data to suggest the contrary, abrupt mobility edges are assumed. That is, the presence of a critical valence band energy, $E_{\mathrm{v}\mu}$, is assumed, which separates the VBE electronic states from their VBL counterparts. Similarly, the presence of a critical conduction band energy, $E_{\mathrm{c}\mu}$, is assumed, which separates the CBE electronic states from their CBL counterparts. The energy difference between $E_{\mathrm{v}\mu}$ and $E_{\mathrm{c}\mu}$, i.e., $E_{\mathrm{c}\mu}$ - $\mathrm{E}_{\mathrm{v}\mu}$, a parameter often referred to as the mobility gap, occurs frequently in this analysis, most of the dramatic changes in the functional behavior of the JDOS results occurring in the vicinity of $\hbar\omega = E_{\mathrm{c}\mu} - E_{\mathrm{v}\mu}$. In order to be concrete, $E_{\mathrm{v}\mu}$ is nominally placed at E_{vt} and $E_{\mathrm{c}\mu}$ is nominally placed at E_{ct}, i.e., the mobility edges are placed at the critical energies at which the square-root and exponential distributions interface, for all subsequent calculations, unless otherwise stated. The locations of these mobility edges are indicated in Figure 2.16. Representative VBE-

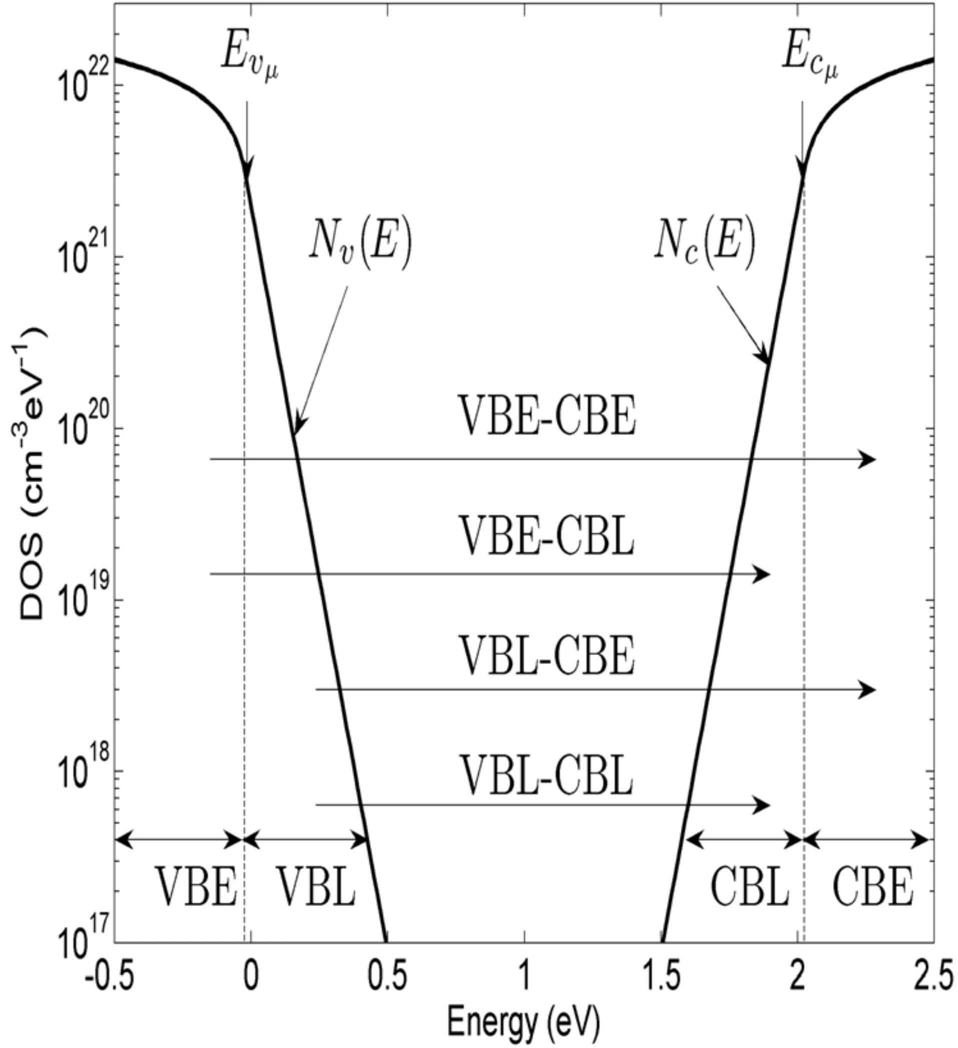

Figure 2.16: The valence band and conduction band DOS functions, $N_{\mathrm{v}}(E)$ and $N_{\mathrm{c}}(E)$, with the mobility edge locations indicated. The nominal DOS modeling parameter selections, i.e., the values set in Table 2.1, are employed for the purposes of this analysis. The valence band and conduction band mobility edge locations, $E_{\mathrm{v}\mu}$ and $E_{\mathrm{c}\mu}$, respectively, are indicated with the dotted lines and the arrows. For the purposes of this analysis, it is assumed that $E_{\mathrm{v}\mu}$ is equal to E_{vt} and that $E_{\mathrm{c}\mu}$ is equal to E_{ct}. The locations of the VBE, VBL, CBE, and CBL electronic sates are indicated. Representative VBE-CBE, VBE-CBL, VBL-CBE, and VBL-CBL optical transitions are shown with the arrows.

CBE, VBE-CBL, VBL-CBE, and VBL-CBL optical transitions are also indicated in this figure.

The total densities of localized electronic states are quantities that may be readily evaluated through knowledge of the DOS functions, $N_{\mathrm{V}}(E)$ and $N_{\mathrm{C}}(E)$, and the locations of the mobility edges, $E_{\mathrm{V}\mu}$ and $E_{\mathrm{C}\mu}$. The total density of VBL electronic states may be shown to be

$$n_{\mathrm{VBL}}(E_{\mathrm{V}\mu}) = \int_{E_{\mathrm{V}\mu}}^{\infty} N_{\mathrm{V}}(E)\mathrm{dE}, \tag{2.30}$$

as all valence band electronic states with energies greater than $E_{\mathrm{V}\mu}$ are localized. The dependence of n_{VBL} on $E_{\mathrm{V}\mu}$ is plotted in Figure 2.17, for a number of selections of γ_{V}, all other DOS modeling parameters being set to their nominal values, i.e., as set in Table 2.1. For a fixed value of γ_{V}, as $E_{\mathrm{V}\mu}$ is increased, it is seen that the total density of VBL electronic states, n_{VBL}, is diminished. It is also found that for a fixed value of $E_{\mathrm{V}\mu}$, as γ_{V} is increased, the total density of VBL electronic states, n_{VBL}, increases.

Similarly, the total density of CBL electronic states may be shown to be

$$n_{\mathrm{CBL}}(E_{\mathrm{C}\mu}) = \int_{-\infty}^{E_{\mathrm{C}\mu}} N_{\mathrm{C}}(E)\mathrm{dE}, \tag{2.31}$$

as all conduction band electronic states with energies less than $E_{\mathrm{C}\mu}$ are localized. The dependence of n_{CBL} on $E_{\mathrm{C}\mu}$ is plotted in Figure 2.18, for a number of selections of γ_{C}. As $E_{\mathrm{C}\mu}$ is increased, it is seen that the total density of CBL electronic states, n_{CBL}, enhances. It is also found that for a fixed value of $E_{\mathrm{C}\mu}$, as γ_{C} is increased, the total density of CBL electronic, n_{CBL}, increases. Optical transitions involving these tail states are believed to be responsible for the tail exhibited by the imaginary part of the dielectric function, $\epsilon_2(\hbar\omega)$ [45]. The relationship between these total

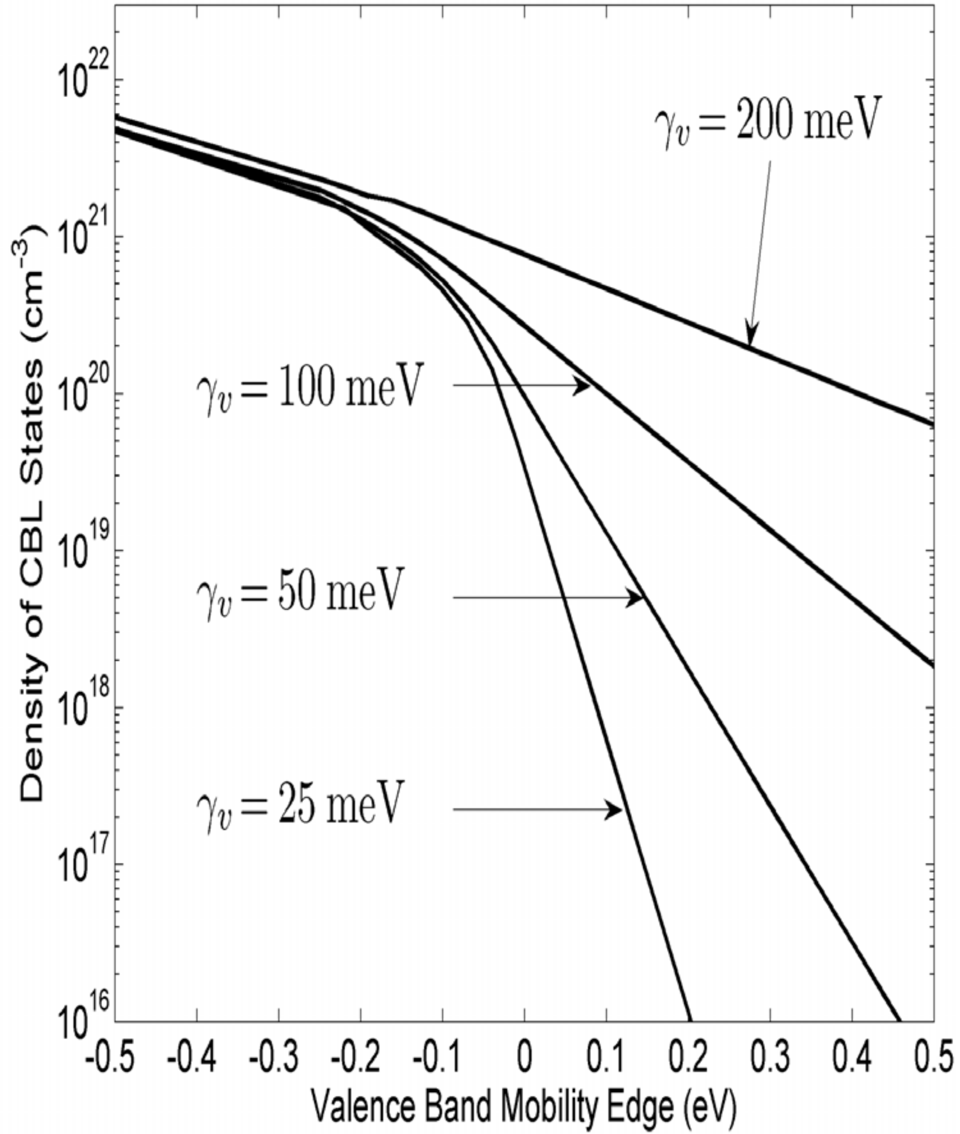

Figure 2.17: The total density of VBL electronic states, n_{VBL}, as a function of the valence band mobility edge location, $E_{\mathrm{V}\mu}$, for a number of selections of the valence band tail breadth, γ_{V}. All other DOS modeling parameters are set to their nominal values, i.e., the values set in Table 2.1.

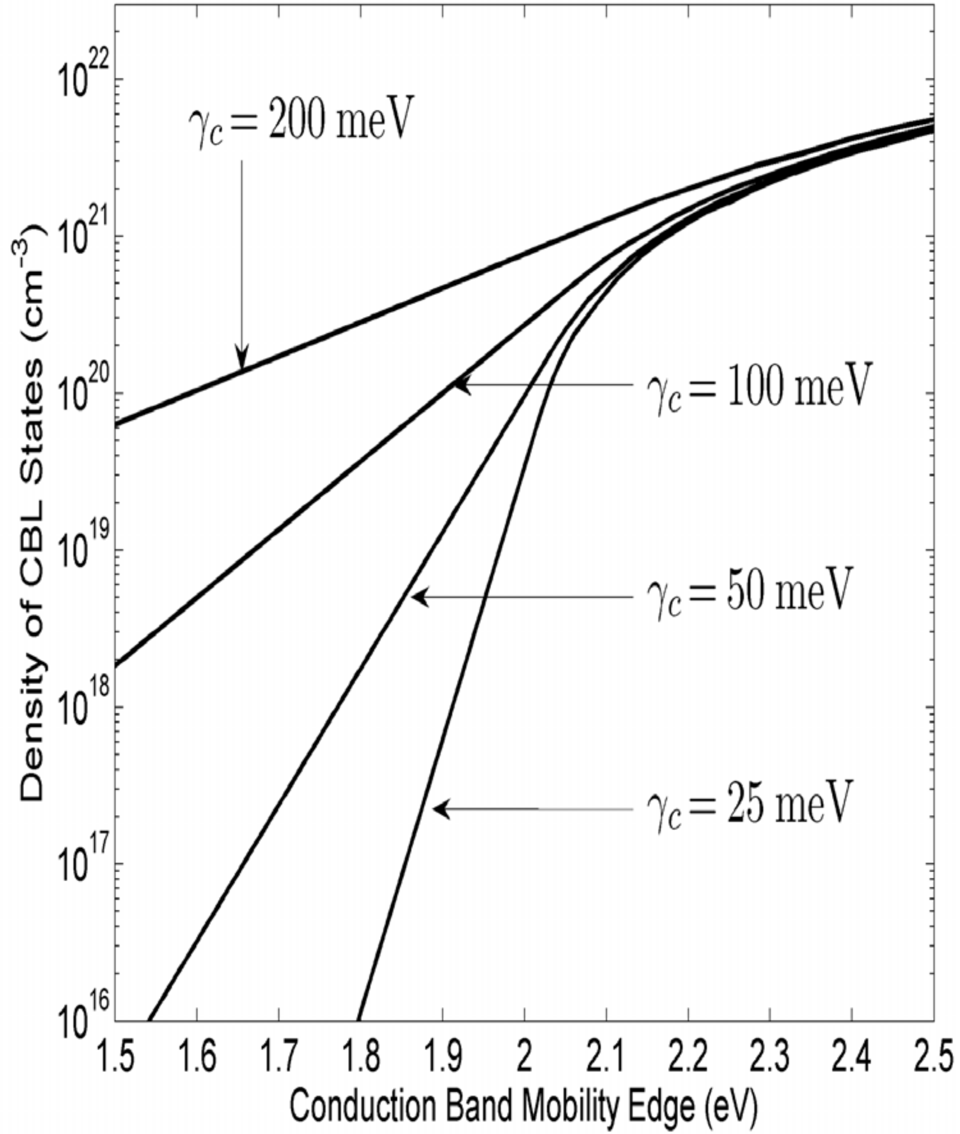

Figure 2.18: The total density of CBL electronic states, n_{CBL}, as a function of the conduction band mobility edge location, $E_{\mathrm{C}\mu}$, for a number of selections of the conduction band tail breadth, γ_{C}. All other DOS modeling parameters are set to their nominal values, i.e., the values set in Table 2.1

densities of VBL and CBL electronic states, and the the forthcoming JDOS results, for the specific case of PECVD a-Si:H, will be explored in Chapter 4.

3. A JOINT DENSITY OF STATES ANALYSIS

3.1 Introduction

Amorphous semiconductors, such as PECVD a-Si:H, possess a number of remarkable electronic properties, making them ideally suited for a wide range of large area electron device applications. It is widely held that the disorder present within an amorphous semiconductor produces distributions of electronic states that encroach into the otherwise empty gap region. These encroaching distributions of electronic states, commonly referred to as tail states, profoundly influence the electronic character of an amorphous semiconductor. Analysis indicates that many of the tail states associated with an amorphous semiconductor are localized by the site disorder, and that there exist critical energies associated with each band, termed mobility edges, which separate the localized electronic states from their extended counterparts [10]. That is, in the valence band associated with an amorphous semiconductor, there are both VBE and VBL electronic states, these states being separated by the valence band mobility edge, $E_{\mathrm{V}\mu}$. Similarly, in the conduction band associated with an amorphous semiconductor, there are both CBE and CBL electronic states, these states being separated by the conduction band mobility edge, $E_{\mathrm{C}\mu}$.

As optical response is a key requirement for many of the device applications implemented or envisaged for such semiconductors, the optical properties of amorphous semiconductors have been a focus of intense interest for many years [12, 14, 20, 24, 25, 26, 27]. The optical response of an amorphous semiconductor is often characterized in terms of the spectral dependence of the optical absorption coeffi-

cient, $\alpha(\hbar\omega)$, this spectrum also being referred to as the optical absorption spectrum. While the optical absorption spectrum associated with a defect-free 'ideal' semiconductor terminates abruptly at the fundamental energy gap, in an amorphous semiconductor, a tail encroaches into the otherwise empty gap region [12]. This tail in the optical absorption spectrum, arising as a result of optical transitions involving the aforementioned tail states [13, 14, 15, 16, 17, 18, 19], is responsible for many of the unique features characteristic of the optical response of an amorphous semiconductor. Accordingly, the optical absorption tail associated with amorphous semiconductors has been the subject of a number of studies [12, 18, 19, 20, 21, 22, 23].

In this chapter, the spectral dependence of the imaginary part of the dielectric function, $\epsilon_2(\hbar\omega)$, is related to the valence band and conduction band DOS functions, $N_{\text{v}}(E)$ and $N_{\text{c}}(E)$, respectively, the spectral dependence of the imaginary part of the dielectric function being a key optical function in the characterization of the optical response of materials. The JDOS function, $J(\hbar\omega)$, is introduced as a corollary. Then, a detailed examination of the JDOS integrand, and of the resultant JDOS function itself, is presented. This JDOS analysis is performed within the framework of the empirical model for the DOS functions presented in Chapter 2, i.e., the valence band DOS function

$$N_{\text{v}}(E) = \begin{cases} N_{\text{vo}}\sqrt{E_{\text{v}} - E_{\text{vt}}}\exp\left(\frac{E_{\text{vt}}-E_{\text{v}}}{\gamma_{\text{v}}}\right)\exp\left(\frac{E_{\text{v}}-E}{\gamma_{\text{v}}}\right), & E > E_{\text{vt}} \\ N_{\text{vo}}\sqrt{E_{\text{v}} - E} & E \leq E_{\text{vt}} \end{cases}, \tag{3.1}$$

while the conduction band DOS function

$$N_{\text{c}}(E) = \begin{cases} N_{\text{co}}\sqrt{E - E_{\text{c}}}, & E \geq E_{\text{ct}} \\ N_{\text{co}}\sqrt{E_{\text{ct}} - E_{\text{c}}}\exp\left(\frac{E_{\text{c}}-E_{\text{ct}}}{\gamma_{\text{c}}}\right)\exp\left(\frac{E-E_{\text{c}}}{\gamma_{\text{c}}}\right), & E < E_{\text{ct}} \end{cases}, \tag{3.2}$$

where N_{vo}, N_{co}, E_{v}, E_{c}, γ_{v}, γ_{c}, E_{vt}, and E_{ct} are as previously defined; recall Eqs. (2.28) and (2.29) for $N_{\text{v}}(E)$ and $N_{\text{c}}(E)$, respectively. A means of determining the spectral dependence of the contributions to the JDOS function, attributable to the VBE-CBE, VBE-CBL, VBL-CBE, and VBL-CBL optical transitions, as a function of the valence band and conduction band mobility edges, $E_{\text{v}\mu}$ and $E_{\text{c}\mu}$, respectively, is then provided. Numerical JDOS results are then presented, these results being obtained using the nominal selection of DOS modeling parameters suggested in Chapter 2. This JDOS formalism is then applied to the determination of the spectral dependence of the optical transition matrix element. Finally, a means whereby the spectral dependence of the optical absorption coefficient, $\alpha(\hbar\omega)$, may be evaluated is presented.

This chapter is organized in the following manner. In Section 3.2, a relationship between $N_{\text{v}}(E)$, $N_{\text{c}}(E)$, and $\epsilon_2(\hbar\omega)$ is developed. The JDOS function, $J(\hbar\omega)$, is introduced as a corollary to this analysis. Then, in Section 3.3, an examination of the spectral dependence of the JDOS integrand, and the JDOS itself, is presented. This analysis is performed within the framework of the empirical model for the DOS functions presented in Chapter 2, i.e., Eqs. (3.1) and (3.2). In Section 3.4, the various types of optical transitions that occur within the framework of the empirical model for the DOS functions used for the purposes of this analysis, i.e., Eqs. (3.1) and (3.2), are presented. In Section 3.5, means of determining the contributions to the JDOS function attributable to the various types of optical transitions, as a function of the valence band and conduction band mobility edges, $E_{\text{v}\mu}$ and $E_{\text{c}\mu}$, respectively, are discussed. Numerical results are then featured in Section 3.6. This JDOS formalism is then applied in order to evaluate the spectral

dependence of the optical transition matrix element in Section 3.7. Finally, the spectral dependence of the optical absorption coefficient is determined in Section 3.8.

3.2 The relationship between the imaginary part of the dielectric function and the valence band and conduction band DOS functions

Fundamentally, the optical response of an amorphous semiconductor is determined by the number of allowed optical transitions and by the magnitude of the optical transition matrix elements that couple the electronic states between which these optical transitions occur [49, 50]. In order to quantify the nature of this response, a relationship between the spectral dependence of the imaginary part of the dielectric function, $\epsilon_2(\hbar\omega)$, and the functional dependencies of the valence band and conduction band DOS functions, $N_{\mathrm{V}}(E)$ and $N_{\mathrm{C}}(E)$, respectively, must be established. For the purposes of this analysis, the approach of Jackson *et al.* [49] is employed. Within the framework of a one-electron perspective, Jackson *et al.* [49] employ a linear response formalism in order to relate $N_{\mathrm{V}}(E)$ and $N_{\mathrm{C}}(E)$ with $\epsilon_2(\hbar\omega)$ While the analysis of Jackson *et al.* [49] is focused on the specific case of PECVD a-Si:H, there is general agreement that other amorphous semiconductors should exhibit a similar relationship between $N_{\mathrm{V}}(E), N_{\mathrm{C}}(E)$, and $\epsilon_2(\hbar\omega)$. This formalism of Jackson *et al.* [49] continues to shape the direction of thought in this field.

Jackson *et al.* [49] developed a dipole operator based formalism. In this formalism, the rate of optical transitions between the valence band and conduction band electronic states is dictated by the magnitude of the dipole matrix elements, $\vec{R}_{\mathrm{C,V}} \equiv \langle \mathrm{c}|\vec{R}|\mathrm{v}\rangle$, where $\vec{R}$ denotes the dipole operator, $|\mathrm{v}\rangle$ being a representa-

tive single-spin electronic state associated with the valence band, and $|c\rangle$ denoting a representative single-spin electronic state associated with the conduction band. The light is assumed to be unpolarized, so that the directional average of $|\vec{\eta}\cdot\vec{R}_{\mathrm{C,V}}|^2$ reduces to $\frac{1}{3}R^2_{\mathrm{C,V}}$, where $\vec{\eta}$ denotes the polarization vector of the incident light and $R_{\mathrm{C,V}}$ represents the amplitude of the dipole matrix element, i.e., $R_{\mathrm{C,V}} = |\vec{R}_{\mathrm{C,V}}|$. In order to simplify matters, zero-temperature statistics are assumed. That is, it is assumed that the valence band electronic states are fully occupied and that the conduction band electronic states are completely unoccupied. With these assumptions being made, Jackson *et al.* [49] assert that

$$\epsilon_2(\hbar\omega) = (2\pi q)^2 \frac{2}{3V} \sum_{\mathrm{C,V}} R^2_{\mathrm{C,V}} \delta(E_{\mathrm{C}} - E_{\mathrm{V}} - \hbar\omega), \tag{3.3}$$

where q denotes the electron charge, V represents the illuminated volume, and E_{V} and E_{C} are the energies of the valence band and conduction band electronic states, $|\mathrm{v}\rangle$ and $|\mathrm{c}\rangle$, respectively, between which optical transitions can occur. The summation in Eq. (3.3) is taken over all single-spin electronic states associated with the valence and conduction bands.

Introducing the aggregate dipole matrix element squared average,

$$[\acute{R}(\hbar\omega)]^2 \equiv \frac{\sum_{\mathrm{C,V}} |R_{\mathrm{C,\ V}}|^2 \delta(E_{\mathrm{C}} - E_{\mathrm{V}} - \hbar\omega)}{\sum_{\mathrm{C,V}} \delta(E_{\mathrm{C}} - E_{\mathrm{V}} - \hbar\omega)}, \tag{3.4}$$

it is seen that Eq. (3.3) may instead be written as

$$\epsilon_2(\hbar\omega) = (2\pi q)^2 \frac{2}{3V} [\acute{R}(\hbar\omega)]^2 \sum_{\mathrm{C,V}} \delta(E_{\mathrm{C}} - E_{\mathrm{V}} - \hbar\omega), \tag{3.5}$$

where $[\acute{R}(\hbar\omega)]^2$ provides for the squared average matrix element over all possible single-spin optical transitions between the valence band and conduction band electronic states separated by the photon energy, $\hbar\omega$.

The expression that has been obtained for the spectral dependence of $\epsilon_2(\hbar\omega)$, i.e., Eq. (3.5), is general, and applies to both crystalline and amorphous materials. In a crystalline material, crystal momentum, $\vec{k}$, must be conserved during an optical transition. In an amorphous semiconductor, however, the disorder present renders $\vec{k}$ a poor quantum number, and, as a result, the $\vec{k}$-conservation criterion is relaxed. While Eq. (3.5) is defined over all single-spin valence band and conduction band electronic states, most studies on crystalline semiconductors focus only on the $\vec{k}$-conserving optical transitions. If it is assumed that the "overall" optical response exhibited by an amorphous semiconductor is similar to that of its crystalline counterpart, it seems reasonable to expect that the matrix elements associated with the $\vec{k}$-conserving optical transitions (associated with a crystalline semiconductor) will be of a greater magnitude than those associated with the non $\vec{k}$-conserving optical transitions (associated with an amorphous semiconductor). If it is assumed that the difference in the magnitude of these matrix elements scales according to the number of possible optical transitions from a given state in the valence band, a direct comparison between the spectral dependence of the aggregate dipole matrix element squared average, i.e., $[\acute{R}(\hbar\omega)]^2$, between the case of a crystalline semiconductor and its amorphous counterpart, may be achieved through a process of normalization, where this normalization may be achieved by dividing by a factor that is proportional to the ratio between the number of possible $\vec{k}$-conserving and non $\vec{k}$-conserving optical transitions from a given electronic state in the valence band.

In order to make this formalism concrete, a course of analysis, paralleling that presented by Jackson *et al.* [49], is presented. Thus, the cases of c-Si and PECVD

a-Si:H are considered. For other materials, presumably a similar course of analysis can be considered. Focusing on the specific case of c-Si, it is noted that in a sample comprised of N atoms, the number of primitive cells is $\frac{N}{2}$. The number of values of crystal momentum, $\vec{k}$, in a band, which in turn is equal to this number of primitive cells, is therefore equal to $\frac{N}{2}$. The total number of electronic states in each band is $4N$, i.e., 4 states per atom, $2N$ of these states being of one type of electron spin, the other $2N$ states being of the other type of electron spin. Thus, for each value of $\vec{k}$, there are 8 electronic states, 4 associated with each type of electron spin. As spin-flips are not permitted during an optical transition, from a given single-spin electronic state in the valence band, 4 possible optical transitions can occur to the conduction band when $\vec{k}$-conservation occurs. In contrast, for the case of PECVD a-Si:H, from any given single-spin electronic state associated with the valence band, $2N$ optical transitions to the conduction band can occur, i.e., there are a total of $4N$ electronic states associated with the conduction band, of which $2N$ will be of the same type of electron spin as the state in the valence band. Thus, for every 4 $\vec{k}$-conserving c-Si optical transitions, there are $2N$ PECVD a-Si:H optical transitions; see Figure 3.1 [38]. In order to achieve a comparison between the optical transition matrix elements associated with c-Si and a-Si:H, letting ρ_{A} denote the atomic density of PEVCD a-Si:H, the dipole matrix element squared average associated with this material is renormalized by the ratio between N and 4, where N, the number of atoms in the illuminated volume, is equal to $\rho_{\mathrm{A}}V$. Thus, a normalized dipole matrix element squared average may be defined, i.e.,

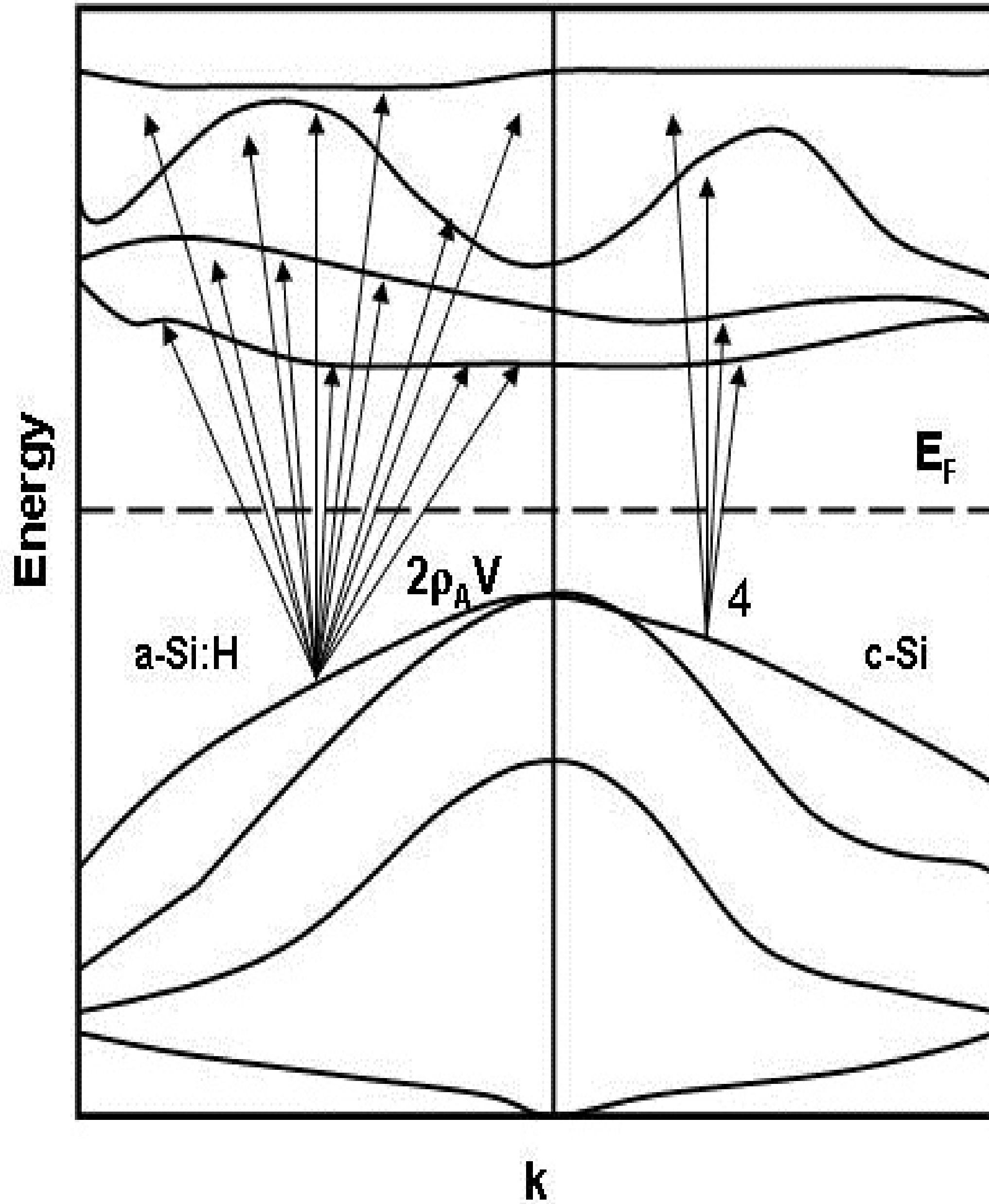

Figure 3.1: The optical transitions permitted from a given single-spin electronic state associated with the valence band for both c-Si and PECVD a-Si:H. This figure is from Thevaril [38].

$$\Re^2(\hbar\omega) \equiv [\acute{R}(\hbar\omega)]^2 \frac{\rho_{\rm A} V}{2}, \tag{3.6}$$

which should have a value that is comparable to the average value obtained by averaging only over the $\vec{k}$-conserving optical transitions for the case of c-Si. Jackson *et al.* [49] showed that this normalized dipole matrix element squared average did indeed allow for a direct comparison between matrix elements associated with c-Si and its amorphous counterpart, PECVD a-Si:H.

With this newly defined matrix element, Eq. (3.5) may thus instead be expressed as

$$\epsilon_2(\hbar\omega) = (2\pi e)^2 \frac{2}{\rho_{\rm A} V} \frac{2}{3V} \Re^2(\hbar\omega) \sum_{\rm c,\ v} \delta(E_{\rm C} - E_{\rm V} - \hbar\omega), \tag{3.7}$$

where the JDOS function can be defined as

$$J(\hbar\omega) \equiv \frac{4}{V^2} \sum_{\rm c,\ v} \delta(E_{\rm C} - E_{\rm V} - \hbar\omega). \tag{3.8}$$

For the specific case of PECVD a-Si:H, where $\rho_{\rm A} = 4.4 \times 10^{22}$ cm^{-3}, Eqs. (3.7) and (3.8) reduce to

$$\epsilon_2(\hbar\omega) = 4.3 \times 10^{-45}\ \Re^2(\hbar\omega) J(\hbar\omega), \tag{3.9}$$

where $\Re^2(\hbar\omega)$ is in units of Å^2 and $J(\hbar\omega)$ is in units of cm^{-6}eV^{-1}. That is, the spectral dependence of $\epsilon_2(\hbar\omega)$ associated with PECVD a-Si:H is chiefly determined by the JDOS function, $J(\hbar\omega)$, and the normalized dipole matrix element squared average optical transition matrix element, $\Re^2(\hbar\omega)$, associated with the various optical transitions that occur within PECVD a-Si:H.

The JDOS function, $J(\hbar\omega)$, provides a measure of the number of possible optical transitions from the valence band electronic states to the conduction band

electronic states separated by the photon energy, $\hbar\omega$. For each single-spin electronic state, there are actually two electronic states, one associated with each type of spin. Accordingly, the one-electron DOS functions, $N_{\mathrm{V}}(E)$ and $N_{\mathrm{C}}(E)$, may be expressed as

$$N_{\mathrm{C}}(E) = \frac{2}{V}\sum_{\mathrm{C}} \delta(E - E_{\mathrm{C}}), \tag{3.10}$$

and

$$N_{\mathrm{V}}(E) = \frac{2}{V}\sum_{\mathrm{V}} \delta(E - E_{\mathrm{V}}), \tag{3.11}$$

respectively. The JDOS function, defined in Eq. (3.8), may thus be expressed as an integral over the valence band and conduction band DOS functions. That is,

$$J(\hbar\omega) = \int_{-\infty}^{\infty} N_{\mathrm{V}}(E) N_{\mathrm{C}}(E + \hbar\omega) dE. \tag{3.12}$$

3.3 The spectral dependence of the JDOS integrand and the JDOS function

In light of the critical role that the JDOS function plays in shaping the optical response of an amorphous semiconductor, it is instructive to consider its functional dependence. Initially, the focus of this analysis will be on the functional dependence of the JDOS integrand itself, i.e., $N_{\mathrm{V}}(E)N_{\mathrm{C}}(E + \hbar\omega)$. Later, the functional dependence of the JDOS function, $J(\hbar\omega)$, evaluated by integrating this integrand over the entire energy range set in Eq. (3.12), is examined. For the purposes of this analysis, the empirical model for the DOS functions, i.e., Eqs. (3.1) and (3.2) for $N_{\mathrm{V}}(E)$ and $N_{\mathrm{C}}(E)$, respectively, will be used. A nominal selection of DOS modeling parameters, these being representative of PECVD a-Si:H, will be used for the purposes of this analysis, this selection of parameters being tabulated in

Table 3.1: The nominal DOS modeling parameter selections used for the purposes of this analysis.

Valence band		**Conduction band**	
Parameter	**Value**	**Parameter**	**Value**
N_{vo} (cm^{-3}eV$^{-3/2}$)	2×10^{22}	N_{co} (cm^{-3}eV$^{-3/2}$)	2×10^{22}
E_{v} (eV)	0.0	E_{c} (eV)	2.0
E_{vt}	$E_{\text{v}} - \frac{1}{2}\gamma_{\text{v}}$	E_{ct}	$E_{\text{c}} + \frac{1}{2}\gamma_{\text{c}}$
$E_{\text{v}\mu}$	E_{vt}	$E_{\text{c}\mu}$	E_{ct}
γ_{v} (meV)	50	γ_{c} (meV)	50

Table 3.1. These are the same DOS modeling parameter selections as those used in Chapter 2; recall Table 2.1.

In Figures 3.2 and 3.3, the JDOS integrand, $N_{\text{v}}(E)N_{\text{c}}(E + \hbar\omega)$, is plotted as a function of energy, E, for two selections of photon energy, $\hbar\omega$, 1.7 and 2.3 eV, respectively, for the nominal DOS modeling parameter selections specified in Table 3.1, these photon energy selections being both below and above the nominal energy gap considered in this analysis, i.e., 2.0 eV. For the case of Figure 3.2, it is clear that the tails in the valence band and conduction band DOS functions are shaping the spectral dependence of the JDOS integrand for low and high energy values. The flat region, corresponding to the intermediate energy values, relates to the attenuating exponential associated with the valence band tail exactly countervailing the rising exponential associated with the conduction band tail; the symmetric selection of DOS modeling parameters, shown in Table 3.1, determines this. In contrast, in Figure 3.3, the overlap between the square-root distributions associated with valence band band and conduction band band DOS functions determines the functional form of the JDOS function, the exponential functions playing a lesser role at the higher and lower energy values. It is noted

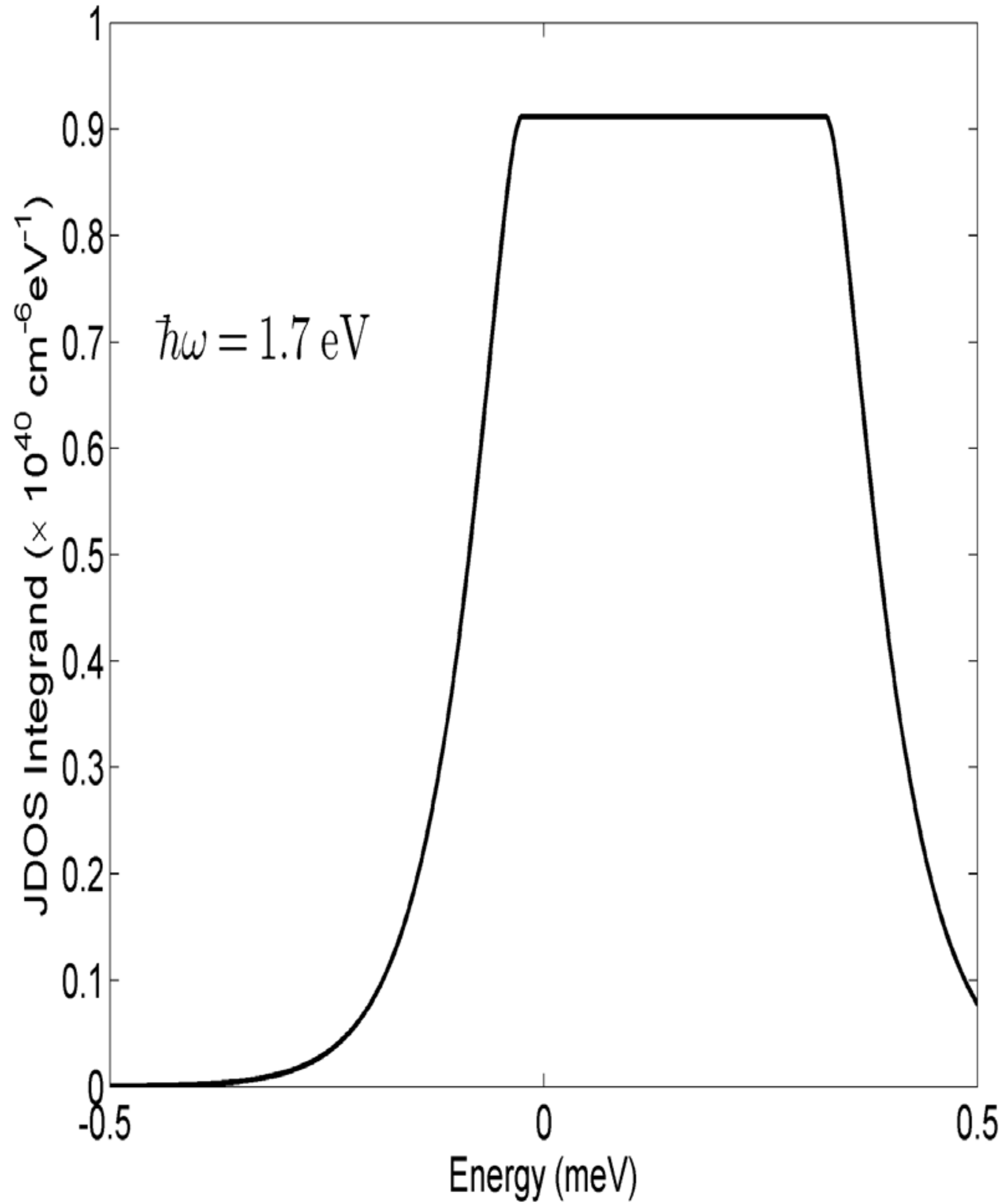

Figure 3.2: The JDOS integrand, $N_{\mathrm{V}}(E)N_{\mathrm{C}}(E+\hbar\omega)$, as a function of energy, E, for the photon energy, $\hbar\omega$, set to 1.7 eV. The nominal DOS modeling parameter selections, specified in Table 3.1, are used for the purposes of this analysis. This plot is cast on a linear scale.

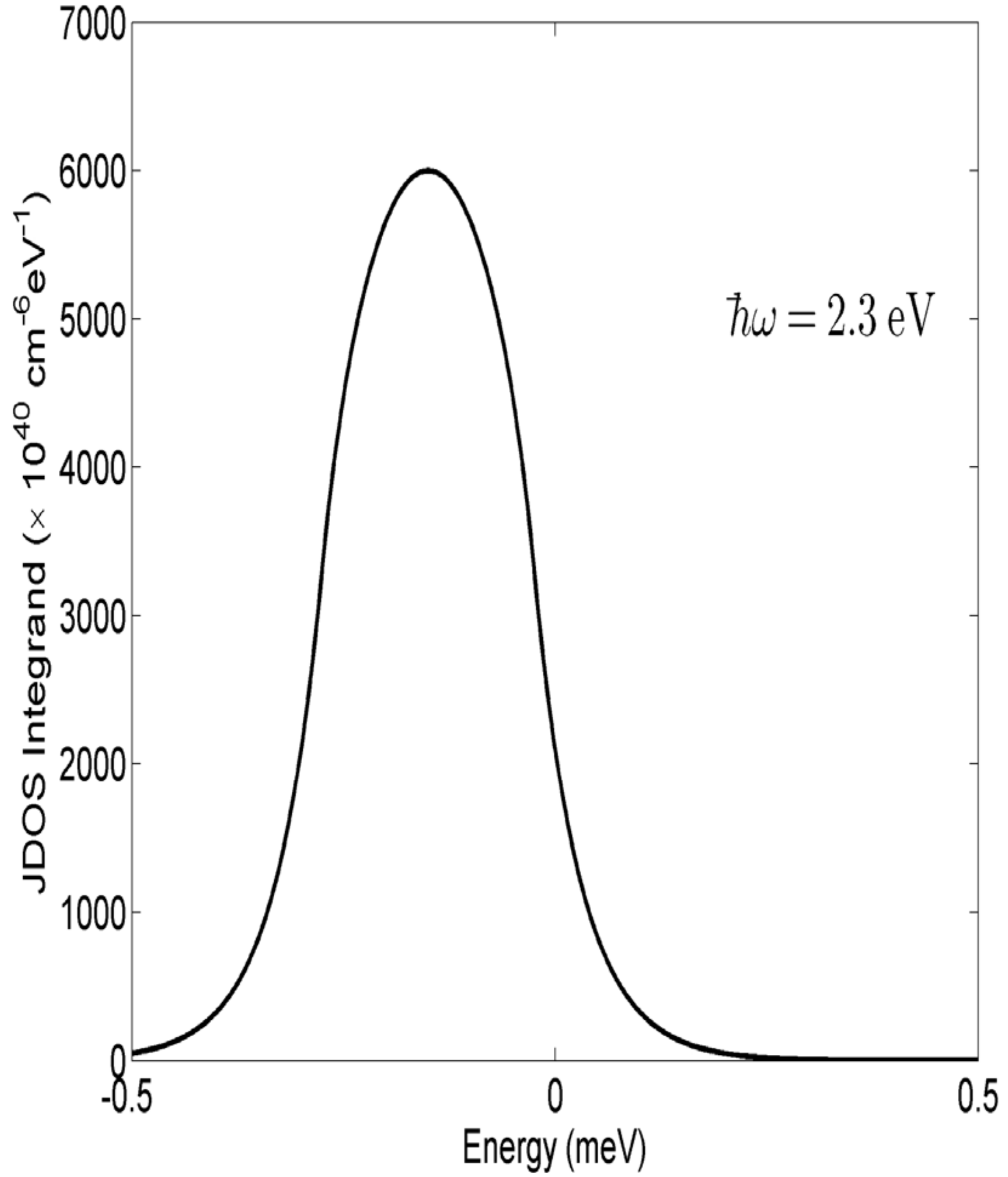

Figure 3.3: The JDOS integrand, $N_{\mathrm{V}}(E)N_{\mathrm{C}}(E+\hbar\omega)$, as a function of energy, E, for the photon energy, $\hbar\omega$, set to 2.3 eV. The nominal DOS modeling parameter selections, specified in Table 3.1, are used for the purposes of this analysis. This plot is cast on a linear scale.

that the JDOS integrand values for this case are much greater, i.e., 3 to 4 orders of magnitude greater, than those associated with the case of $\hbar\omega$ set to 1.7 eV. The dependence of the JDOS integrand, $N_{\mathrm{V}}(E)N_{\mathrm{C}}(E+\hbar\omega)$, on $\hbar\omega$ is further illustrated in Figure 3.4, in which JDOS integrands, corresponding to a variety of $\hbar\omega$ selections, are contrasted, all DOS modeling parameters being set as stipulated in Table 3.1. Clearly, the larger $\hbar\omega$, the more overlap between the states, and thus, the greater the JDOS integrand, $N_{\mathrm{V}}(E)N_{\mathrm{C}}(E+\hbar\omega)$, i.e., the more optical transitions.

In Figure 3.5, the resultant JDOS function is depicted, this being determined through numerical integration, i.e., Eq. (3.12). As before, the nominal DOS modeling parameter selections, specified in Table 3.1, are employed for the purposes of this analysis. It is seen that the JDOS function exhibit a parabolic functional dependence for values of $\hbar\omega$ in excess of the energy gap. However, a tail in the JDOS function is observed for values of $\hbar\omega$ below the energy gap. The nature of this tail in the JDOS function becomes particularly evident when the JDOS function is instead cast on a logarithmic scale, as is shown in Figure 3.6. It is seen that this tail exhibits an exponential functional dependence for these photon energies.

Variations in the breadths of the valence band and conduction band tails, γ_{V} and γ_{C}, play a dramatic role in influencing the spectral dependence of the JDOS function. Consider Figures 3.7 and 3.8, in which the JDOS function, corresponding to a subset of the nominal DOS modeling parameter selections tabulated in Table 3.1, is shown for a number of selections of γ, where $\gamma = \gamma_{\mathrm{V}} = \gamma_{\mathrm{C}}$. It is clear that the greater the breadth of the tails in the valence band and conduction band DOS functions, the greater the breadth of the tail in the JDOS function. Clearly, the tails in the DOS functions are determining the nature of the tail in $J(\hbar\omega)$. This

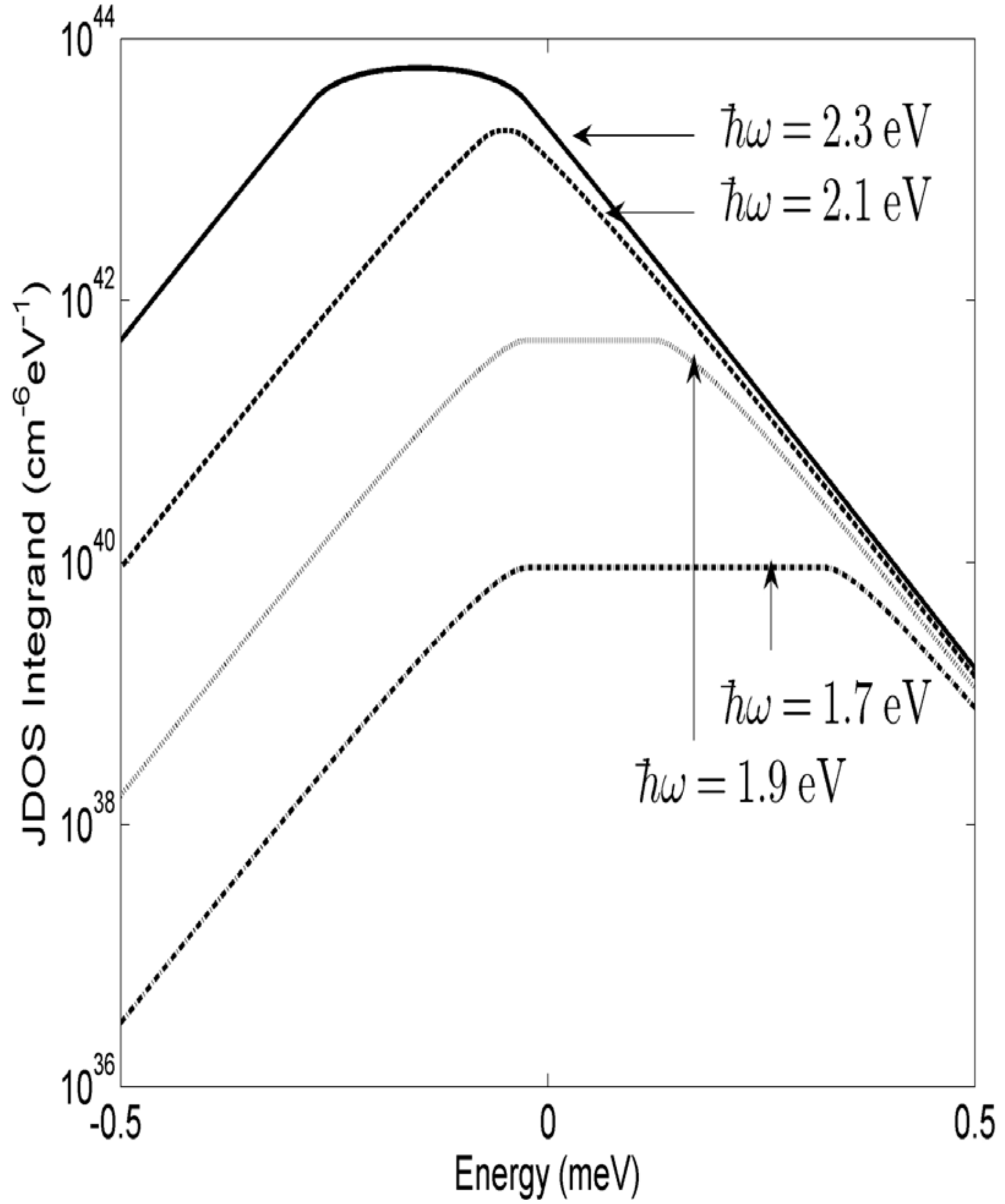

Figure 3.4: The JDOS integrand, $N_{\text{V}}(E)N_{\text{C}}(E + \hbar\omega)$, as a function of energy, E, for a number of photon energies, i.e., $\hbar\omega$ set to 1.7, 1.9, 2.1, and 2.3 eV. The nominal DOS modeling parameter selections, specified in Table 3.1, are used for the purposes of this analysis. This plot is cast on a logarithmic scale.

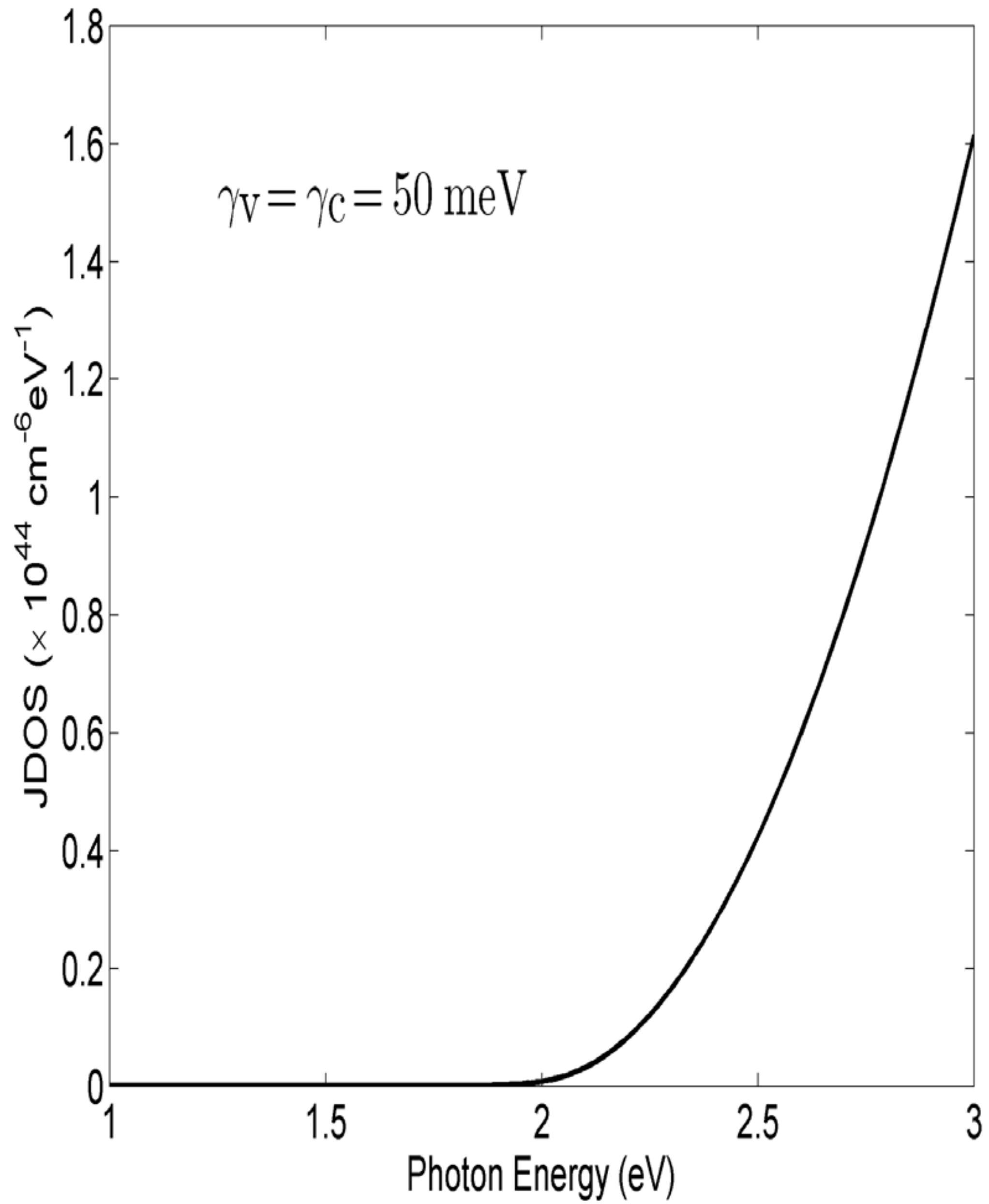

Figure 3.5: The JDOS function, J, as a function of the photon energy, $\hbar\omega$. The nominal DOS modeling parameter selections, specified in Table 3.1, are used for the purposes of this analysis. This plot is cast on a linear scale.

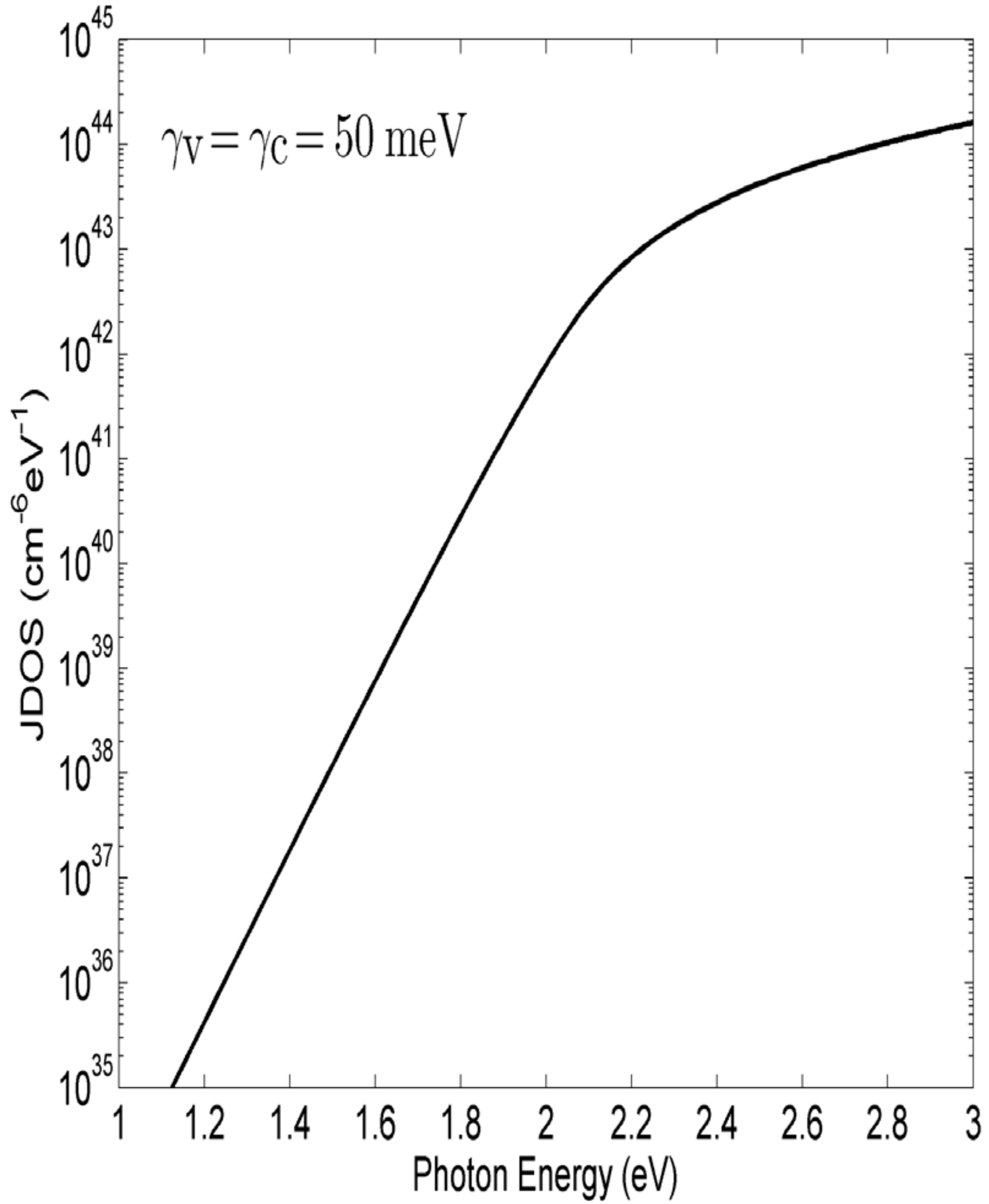

Figure 3.6: The JDOS function, J, as a function of the photon energy, $\hbar\omega$. The nominal DOS modeling parameter selections, specified in Table 3.1, are used for the purposes of this analysis. This plot is cast on a logarithmic scale.

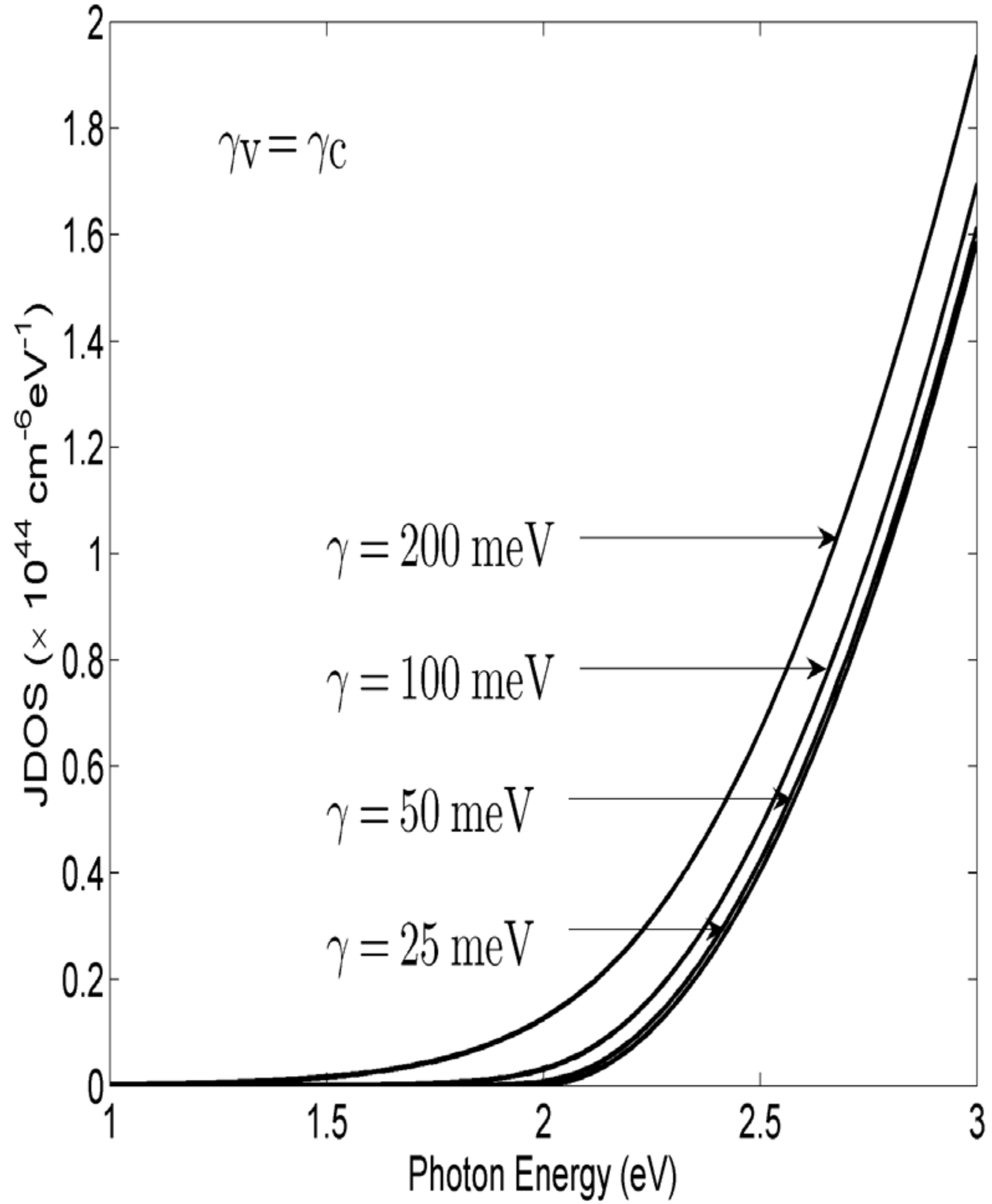

Figure 3.7: The JDOS function, J, as a function of the photon energy, $\hbar\omega$, for a number of selections of γ, where $\gamma = \gamma_V = \gamma_C$. The nominal DOS modeling parameter selections, specified in Table 3.1, with the exception of γ_V and γ_C, are used for the purposes of this analysis. This plot is cast on a linear scale.

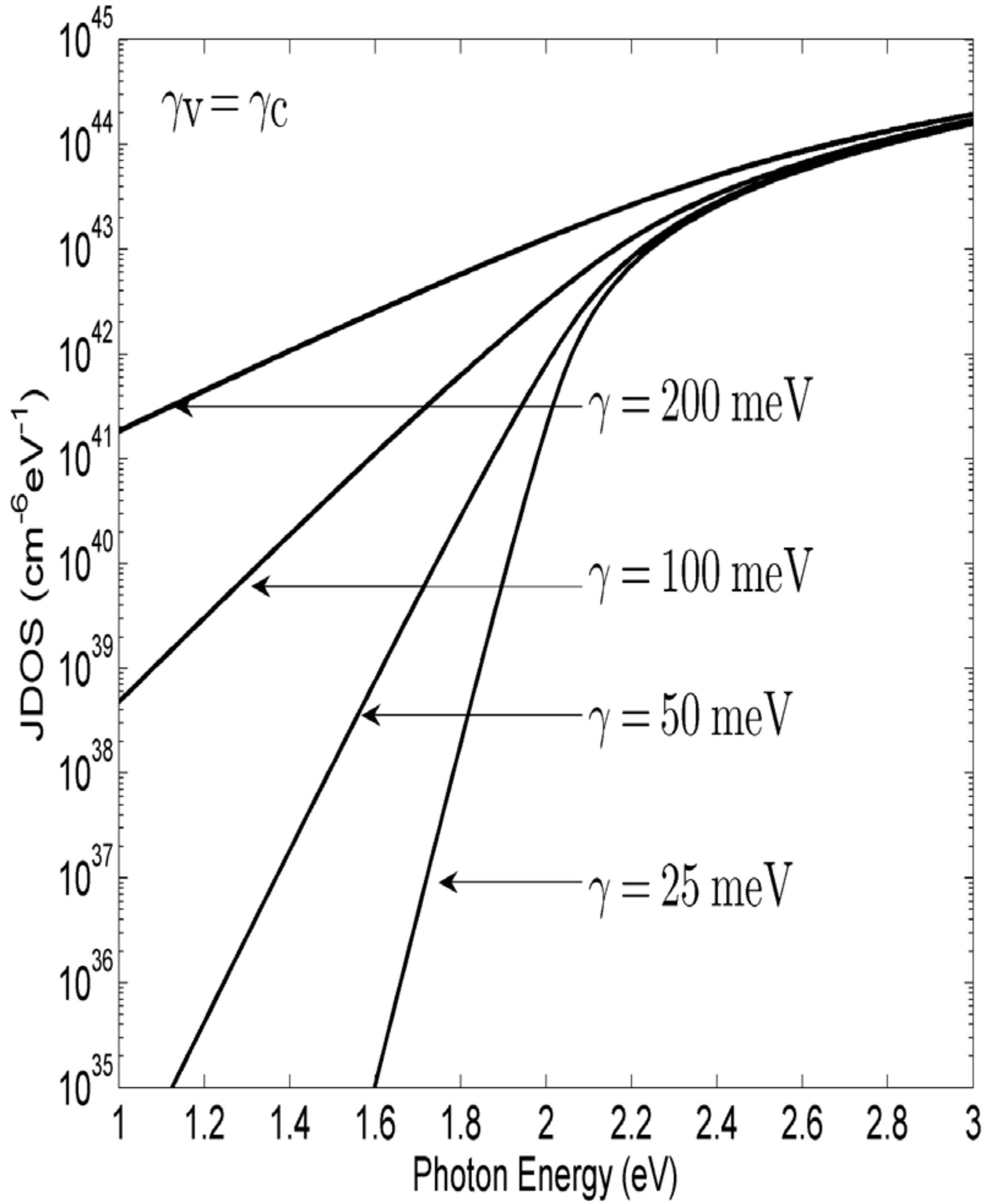

Figure 3.8: The JDOS function, J, as a function of the photon energy, $\hbar\omega$, for a number of selections of γ, where $\gamma = \gamma_V = \gamma_C$. The nominal DOS modeling parameter selections, specified in Table 3.1, with the exception of γ_V and γ_C, are used for the purposes of this analysis. This plot is cast on a logarithmic scale.

dependence arises as a consequence of the fact that with greater $\gamma_{\rm V}$ and $\gamma_{\rm C}$ there are now more states available for optical transitions to occur. As the breadths of the valence band and conduction band tails, $\gamma_{\rm V}$ and $\gamma_{\rm C}$, are directly related to the amount of disorder that is present, it is clear that the tail exhibited by the JDOS function, $J(\hbar\omega)$, is also determined by the amount of disorder that is present.

Finally, an analytical expression for the JDOS function is determined for the special case for which the tail states are neglected in the underlying DOS functions, $N_{\rm V}(E)$ and $N_{\rm C}(E)$; this is mainly done for reasons of analytical simplicity. Letting

$$N_{\rm V}(E) = \begin{cases} 0, & E > E_{\rm V} \\ N_{\rm VO}\sqrt{E_{\rm V} - E}, & E \leq E_{\rm V} \end{cases}, \tag{3.13}$$

and

$$N_{\rm C}(E) = \begin{cases} N_{\rm CO}\sqrt{E - E_{\rm C}}, & E \geq E_{\rm C} \\ 0, & E < E_{\rm C} \end{cases}, \tag{3.14}$$

from Eq. (3.12) it may be shown that

$$J(\hbar\omega) = \begin{cases} N_{\rm VO}N_{\rm CO}\frac{\pi}{8}(\hbar\omega - E_{\rm g})^2, & \hbar\omega \geq E_{\rm g} \\ 0, & \hbar\omega < E_{\rm g} \end{cases}, \tag{3.15}$$

where $E_{\rm g} \equiv E_{\rm C} - E_{\rm V}$ denotes the energy gap. The resultant JDOS function, $J(\hbar\omega)$, is contrasted with that obtained using numerical integration, in Figures 3.9 and 3.10 for the nominal DOS modeling parameters tabulated in Table 3.1. It is seen that the results are virtually indistinguishable for photon energies well above the energy gap, $E_{\rm g}$.

This particular analytical expression, i.e., Eq. (3.15), plays an important in the analysis of the optical properties associated with amorphous semiconductors. In particular, the model of Tauc *et al.* [52], the most common means whereby the

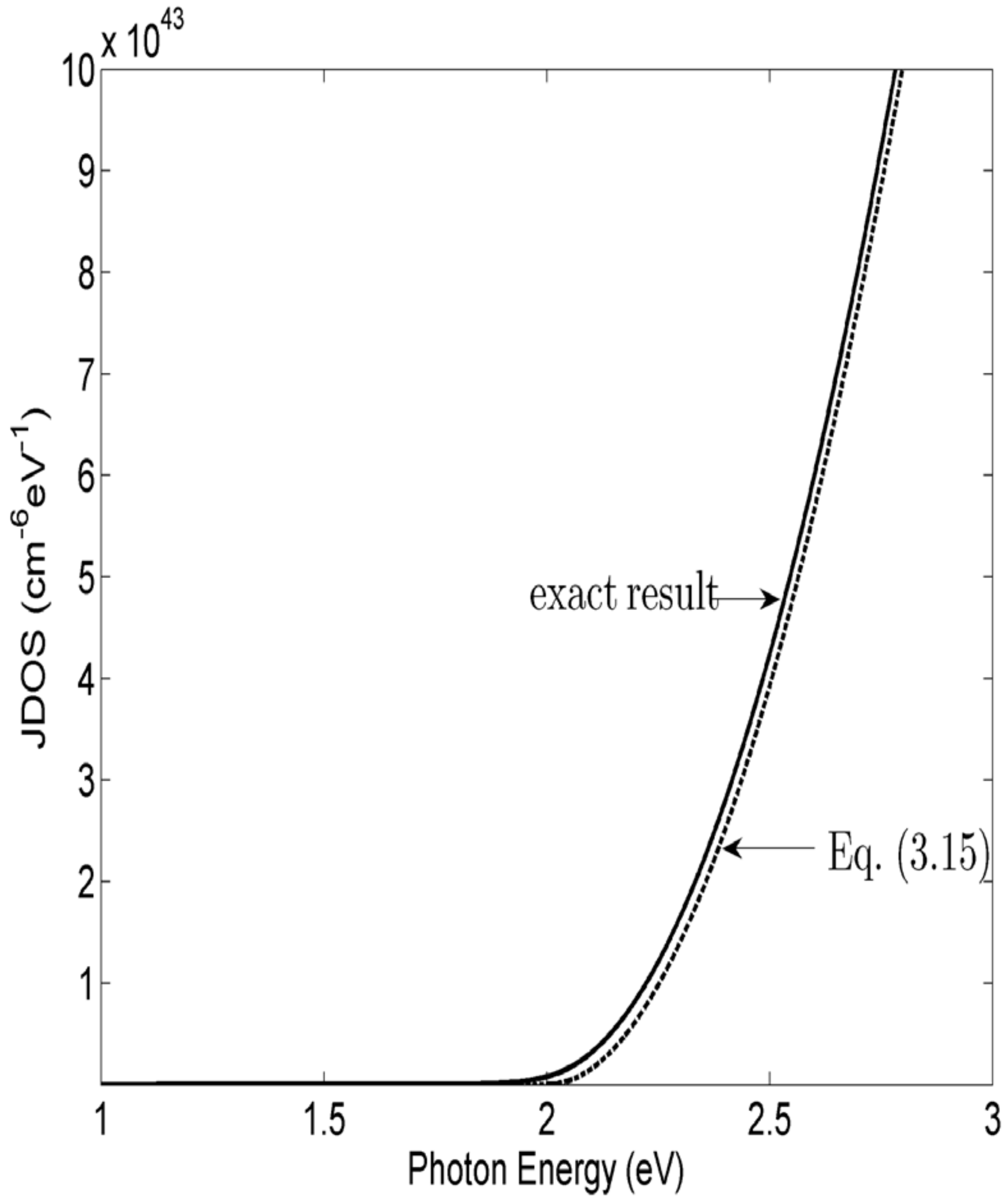

Figure 3.9: The JDOS function, J, as a function of the photon energy, $\hbar\omega$. The exact result with band tails taken into account, i.e., $\gamma_{\mathrm{V}} = \gamma_{\mathrm{C}}$ =50 meV, determined through numerical integration, i.e., Eq. (3.12), depicted with the solid line, is contrasted with the analytical result, Eq. (3.15), which is depicted with the dashed line. The nominal DOS modeling parameter selections, specified in Table 3.1, are used for the purposes of this analysis. This plot is cast on a linear scale.

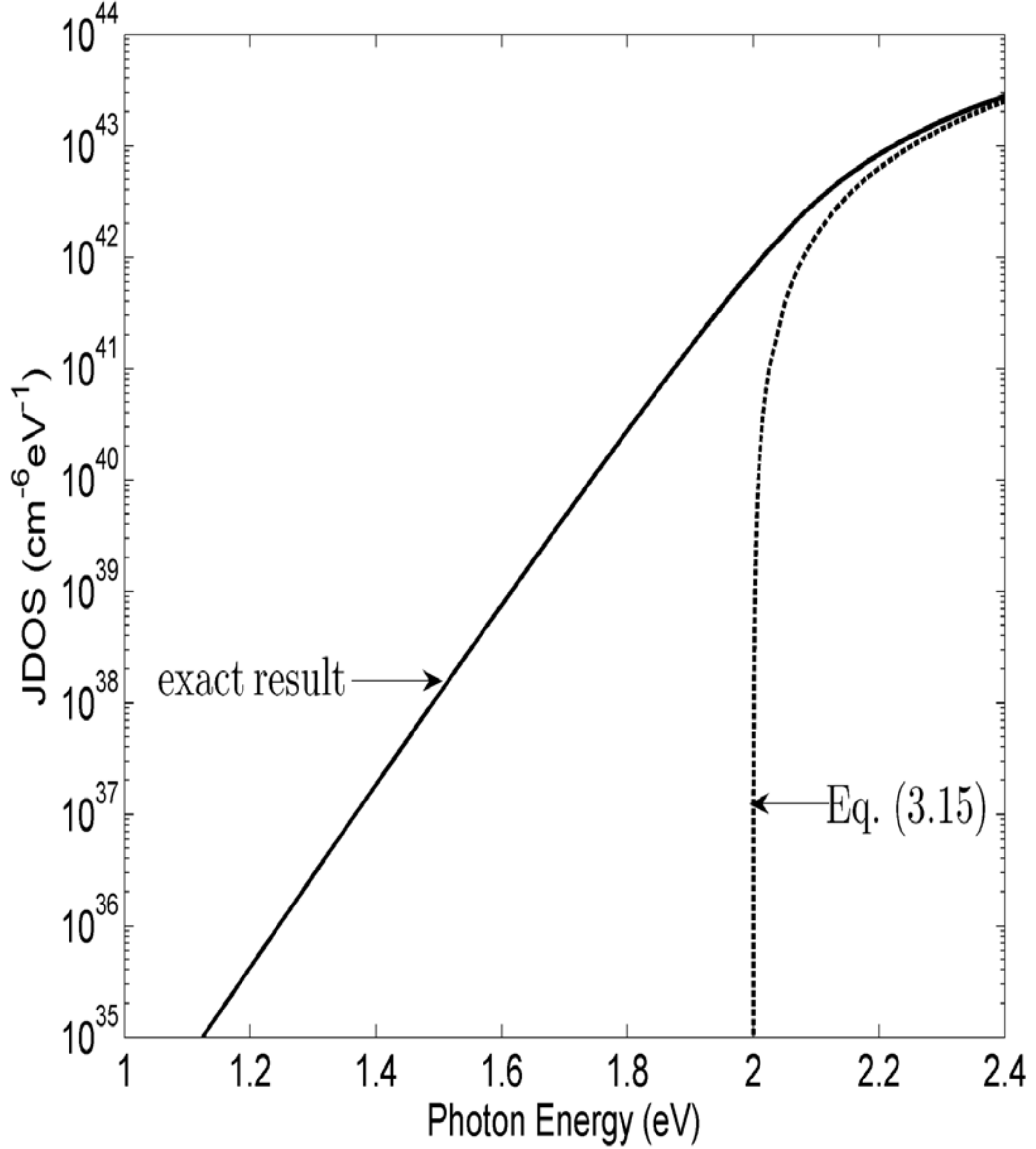

Figure 3.10: The JDOS function, J, as a function of the photon energy, $\hbar\omega$. The exact result with band tails taken into account, i.e., $\gamma_V = \gamma_C$ =50 meV, determined through numerical integration, i.e., Eq. (3.12), depicted with the solid line, is contrasted with the analytical result, Eq. (3.15), which is depicted with the dashed line. The nominal DOS modeling parameter selections, specified in Table 3.1, are used for the purposes of this analysis. This plot is cast on a logarithmic scale.

optical gap associated with an amorphous semiconductor is determined, is based upon it. Specifically, it is noted that the square-root of Eq. (3.15) leads to a linear functional dependence for $\sqrt{J(\hbar\omega)}$ that terminates abruptly at the energy gap, i.e.,

$$\sqrt{J(\hbar\omega)} = \begin{cases} \sqrt{N_{\mathrm{vo}} N_{\mathrm{co}} \frac{\pi}{8}}(\hbar\omega - E_{\mathrm{g}}), & \hbar\omega \geq E_{\mathrm{g}} \\ 0, & \hbar\omega < E_{\mathrm{g}} \end{cases}. \tag{3.16}$$

This suggests that by taking the square-root of the JDOS function, or some function which is proportional to the JDOS function, the linear functional dependence that results may be extrapolated to the abscissa axis in order to obtain an energy gap. For cases for which tail states are present, i.e., either γ_{V} or γ_{C}, or both, are non-zero, the JDOS function will not terminate exactly at this energy gap. Consider Figure 3.11, in which the functional dependence of the square-root of the JDOS function, i.e., $\sqrt{J(\hbar\omega)}$, is plotted as a function of the photon energy, $\hbar\omega$, for the nominal DOS modeling parameters specified in Table 3.1. It is noted that the "effective energy gap," obtained at the point of intersection of the linear extrapolation and the abscissa axis, 1.98 eV, while close the actual energy gap, 2.0 eV, is not exactly equal to it. It is clear that the presence of a tail in the JDOS function is influencing the obtained "effective energy gap."

In order to gauge how the breadth of the valence band and conduction band tail breadth selections, i.e., γ_{V} and γ_{C}, are influencing the determination of the "effective energy gap," in Figure 3.12, the square-root of the JDOS function, i.e., $\sqrt{J(\hbar\omega)}$, is plotted as a function of the photon energy, $\hbar\omega$, for a number of selections of γ, where $\gamma = \gamma_{\mathrm{V}} = \gamma_{\mathrm{C}}$, all other DOS modeling parameter selections being set to their nominal parameter selections specified in Table 3.1; these plots correspond to the same plots that are depicted in Figures 3.7 and 3.8, although

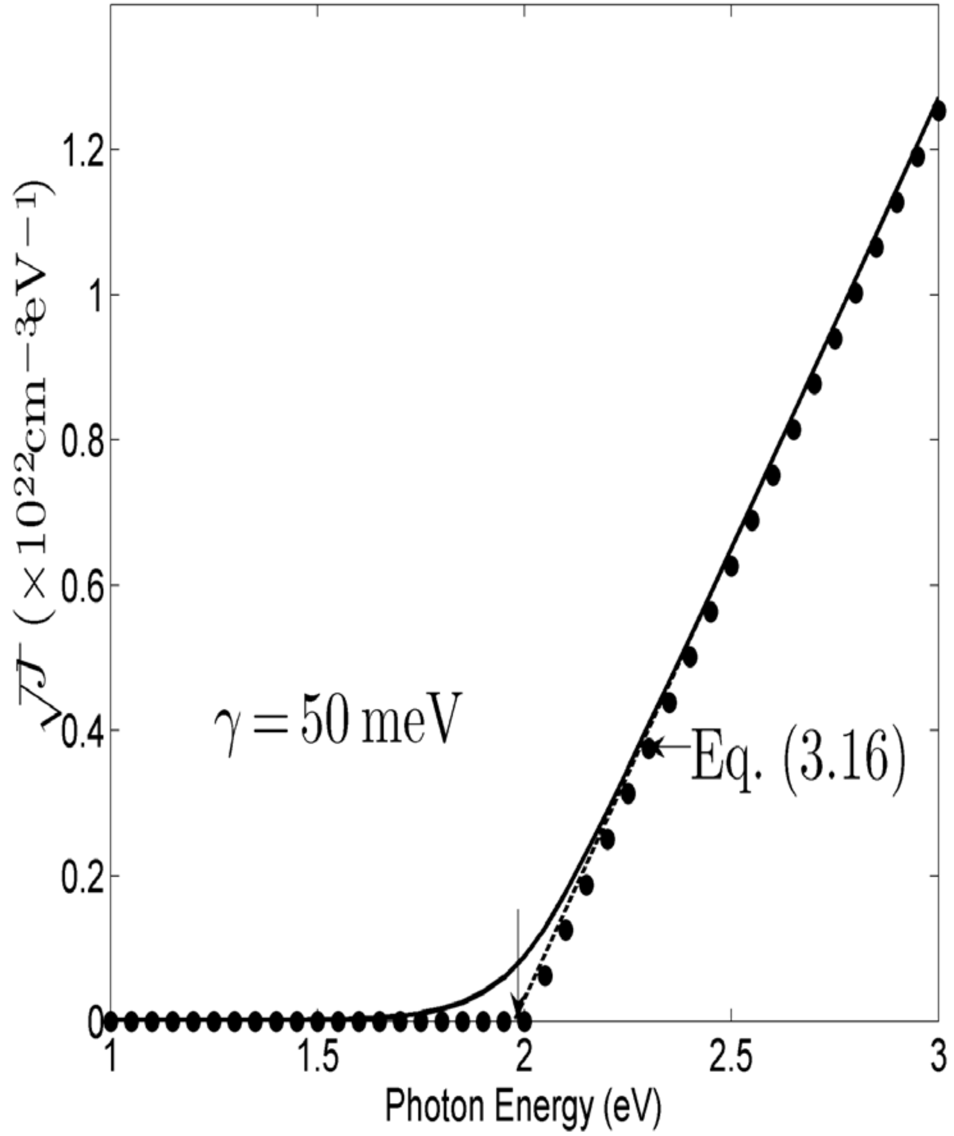

Figure 3.11: The square-root of the JDOS function as a function of the photon energy, $\hbar\omega$, for the nominal DOS modeling parameter selections specified in Table 3.1. A linear extrapolation to the abscissa axis, and the resultant "effective energy gap," are also depicted. This plot is cast on a linear scale.

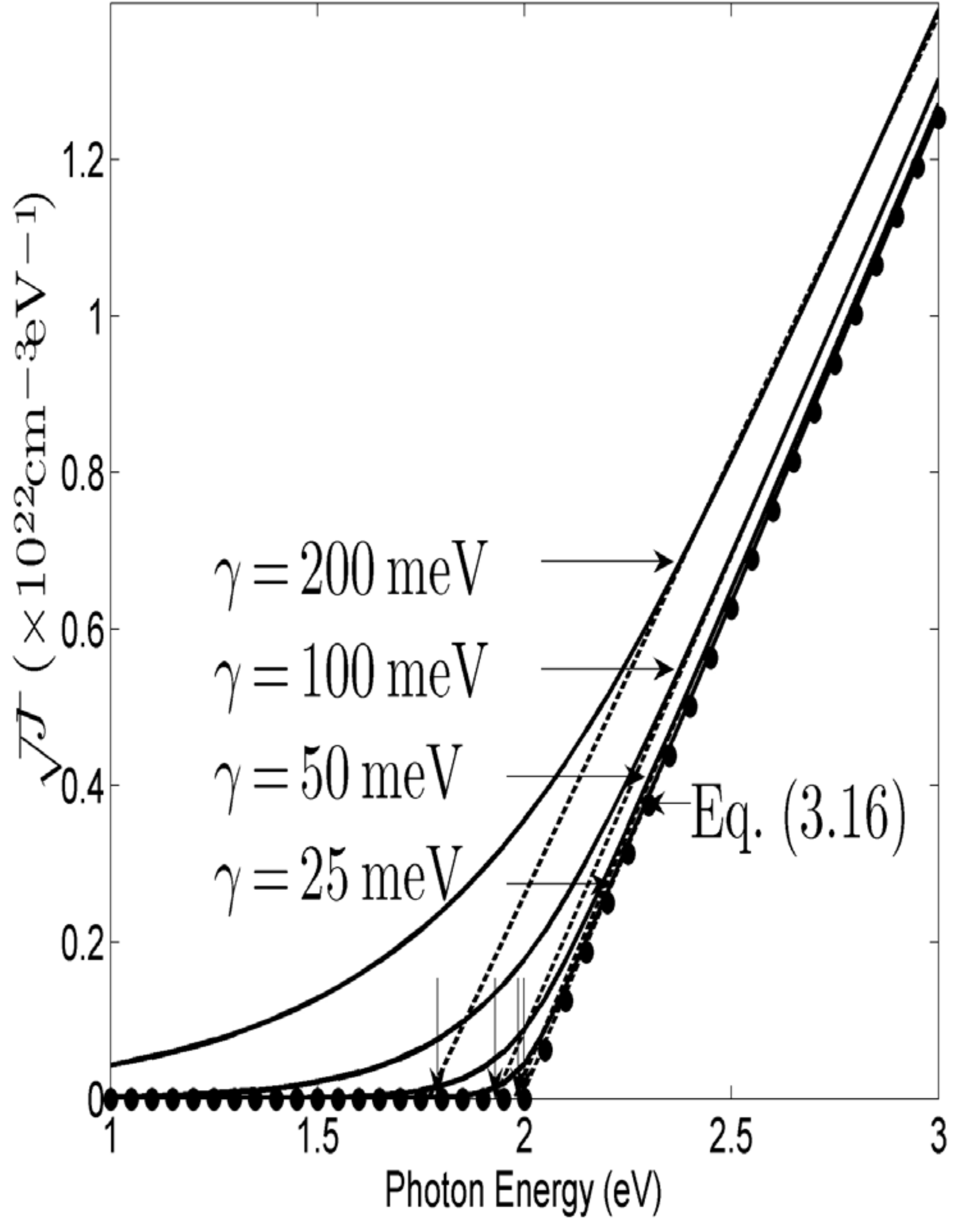

Figure 3.12: The square-root of the JDOS function as a function of the photon energy, $\hbar\omega$, for a number of selections of γ, where $\gamma = \gamma_{\mathrm{V}} = \gamma_{\mathrm{C}}$. The nominal DOS modeling parameter selections, specified in Table 3.1, with the exception of γ_{V} and γ_{C}, are used for the purposes of this analysis. The linear extrapolations to the abscissa axis, and the resultant "effective energy gaps," are also depicted. This plot is cast on a linear scale.

now it is the square-root of the JDOS function that is plotted as a function of the photon energy, $\hbar\omega$, as opposed to the actual JDOS function itself. Each plot exhibits a seemingly linear functional dependence at high photon energies. Extrapolating these linear dependencies to the abscissa axis, and defining the points of intersection with the abscissa axis as the "effective energy gap," it is seen that as the disorder is increased, i.e., as γ is increased, that the "effective energy gap" reduces, even though the actual energy gap remains fixed at 2.0 eV. This approach to determining the energy gap is often used, the resultant energy gap often being referred to as the Tauc optical gap. Its use is further discussed in the literature.

3.4 The various types of optical transitions

It has been shown that $\epsilon_2(\hbar\omega)$ is critically dependent upon the spectral dependence of the JDOS function, $J(\hbar\omega)$. Variations in the spectral dependence of the normalized dipole matrix element squared average, $\Re^2(\hbar\omega)$, also play a role in shaping $\epsilon_2(\hbar\omega)$. The matrix element that couples the electronic states between which optical transitions occur is dependent upon the nature of these electronic states. The random phase analysis of Hindley [51] asserts that the optical transition matrix elements associated with optical transitions involving at most one localized electronic state are of equal magnitude, i.e., this includes optical transitions from a VBE electronic state to a CBE electronic state (VBE-CBE optical transitions), optical transitions from a VBE electronic state to a CBL electronic state (VBE-CBL optical transitions), and optical transitions from a VBL electronic state to a CBE electronic state (VBL-CBE optical transitions). Optical transitions from a localized electronic state to another localized electronic state, i.e., optical

transitions from a VBL electronic state to a CBL electronic state (VBL-CBL optical transitions), are found to have a negligible optical transition matrix element magnitude by comparison [50].

The random phase analysis of Hindley [51] is merely one of a variety of different models that could be employed in order to determine the magnitude of the normalized dipole matrix element squared average associated with an amorphous semiconductor. The fact that the optical transition matrix elements depend upon the nature of the electronic states between which the optical transitions occur, i.e., whether they are localized or extended, suggests that there may be a considerable benefit accrued as a result of identifying the individual contributions to the JDOS function attributable to the various types of optical transitions that occur. Within the framework of the empirical DOS model, i.e, Eqs. (3.1) and (3.2) for $N_{\mathrm{v}}(E)$ and $N_{\mathrm{c}}(E)$, respectively, there are four different types of optical transitions that are possible in an amorphous semiconductor, i.e., VBE-CBE, VBE-CBL, VBL-CBE, and VBL-CBL optical transitions; recall Figure 2.16. The determination of the contributions to the JDOS function attributable to these four types of optical transitions will be the focus of the next section.

The exact locations of the valence band and conduction band mobility edges, $E_{\mathrm{v}\mu}$ and $E_{\mathrm{c}\mu}$, respectively, which separate the extended electronic states from their localized counterparts, remain unknown, even for the most widely studied amorphous semiconductors. In the interests of making this analysis concrete, $E_{\mathrm{v}\mu}$ is nominally set to E_{vt} and $E_{\mathrm{c}\mu}$ is nominally set to E_{ct}, i.e., the mobility edges are nominally set to the critical energies that separate the square-root distributions

from the exponential distributions. The sensitivity of the results to variations in the selection of $E_{\mathrm{V}\mu}$ and $E_{\mathrm{C}\mu}$ will be studied later.

3.5 Means of evaluating the contributions to the JDOS function attributable to the various types of optical transitions

In order to understand how the various types of optical transitions contribute to the JDOS function, it is instructive to study the JDOS integrand, $N_{\mathrm{V}}(E)N_{\mathrm{C}}(E+\hbar\omega)$. In Figures 3.13 and 3.14, the factors in the JDOS integrand, $N_{\mathrm{V}}(E)$ and $N_{\mathrm{C}}(E+\hbar\omega)$, are plotted as functions of energy, E, for two different selections of $\hbar\omega$, 1.7 and 2.3 eV, Figure 3.13 corresponding to the case of $\hbar\omega$ being set to 1.7 eV, i.e., $\hbar\omega < E_{\mathrm{C}\mu} - E_{\mathrm{V}\mu}$, and Figure 3.14 corresponding to the case of $\hbar\omega$ being set to 2.3 eV, i.e., $\hbar\omega \geq E_{\mathrm{C}\mu} - E_{\mathrm{V}\mu}$. For both Figures 3.13 and 3.14, the DOS modeling parameters are set to their nominal values, i.e., the values set in Table 3.1, with $E_{\mathrm{V}\mu}$ set to E_{vt} and $E_{\mathrm{C}\mu}$ set to E_{ct}.

The spectral dependence of JDOS integrand, $N_{\mathrm{V}}(E)N_{\mathrm{C}}(E+\hbar\omega)$, for the cases of $\hbar\omega$ set to 1.7 and 2.3 eV, are shown in Figures 3.15 and 3.16, respectively. As with Figures 3.13 and 3.14, the DOS modeling parameters are set to their nominal values, i.e., the values set in Table 3.1, for both Figures 3.15 and 3.16, with $E_{\mathrm{V}\mu}$ set to E_{vt} and $E_{\mathrm{C}\mu}$ set to E_{ct} for all cases. For the case of $\hbar\omega$ set to 1.7 eV (Figures 3.13 and 3.15), i.e., $\hbar\omega < E_{\mathrm{C}\mu} - E_{\mathrm{V}\mu}$, $E_{\mathrm{V}\mu}$ occurs at a lower energy than $E_{\mathrm{C}\mu} - \hbar\omega$. As a result, between energies $E_{\mathrm{V}\mu}$ and $E_{\mathrm{C}\mu} - \hbar\omega$, the distribution of VBL electronic states (associated with the $N_{\mathrm{V}}(E)$ factor in the JDOS integrand) coexists with the distribution of CBL electronic states (associated with the $N_{\mathrm{C}}(E+\hbar\omega)$ factor in the JDOS integrand). Given that the VBL electronic states are exponentially

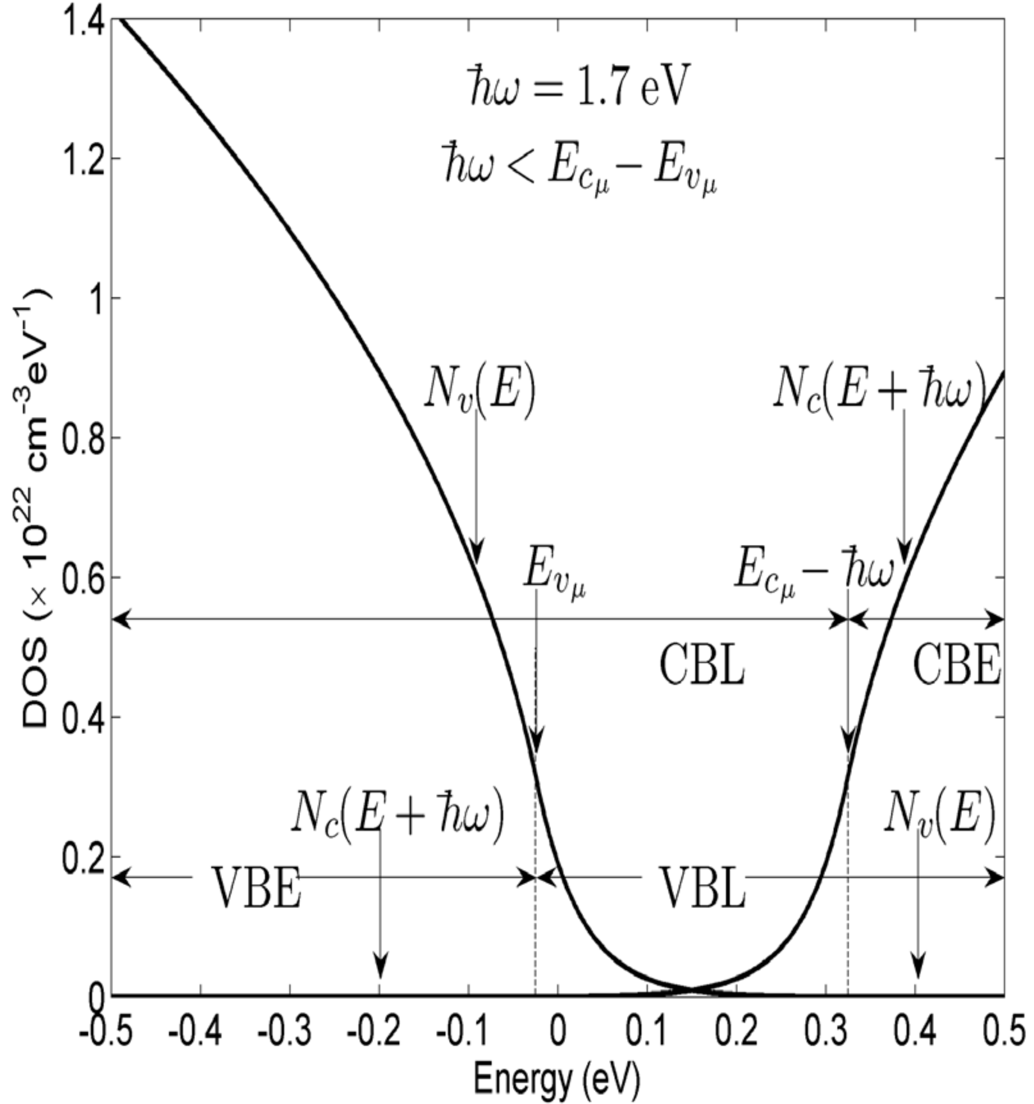

Figure 3.13: The factors in the JDOS integrand, $N_{\text{V}}(E)$ and $N_{\text{C}}(E + \hbar\omega)$, as functions of energy, E, for the photon energy, $\hbar\omega$, set to 1.7 eV, all DOS modeling parameter selections being set to their nominal values, i.e., the values set in Table 3.1, with $E_{\text{V}\mu}$ set to E_{vt} and $E_{\text{C}\mu}$ set to E_{ct}. It is noted that this case corresponds to the condition that $E_{\text{C}\mu} - \hbar\omega > E_{\text{V}\mu}$, i.e., $\hbar\omega < E_{\text{C}\mu} - E_{\text{V}\mu}$. The location of energies $E_{\text{C}\mu} - \hbar\omega$ and $E_{\text{V}\mu}$ are indicated with the light dotted lines and the arrows. The location of the VBE, VBL, CBE, and CBL electronic states are indicated.

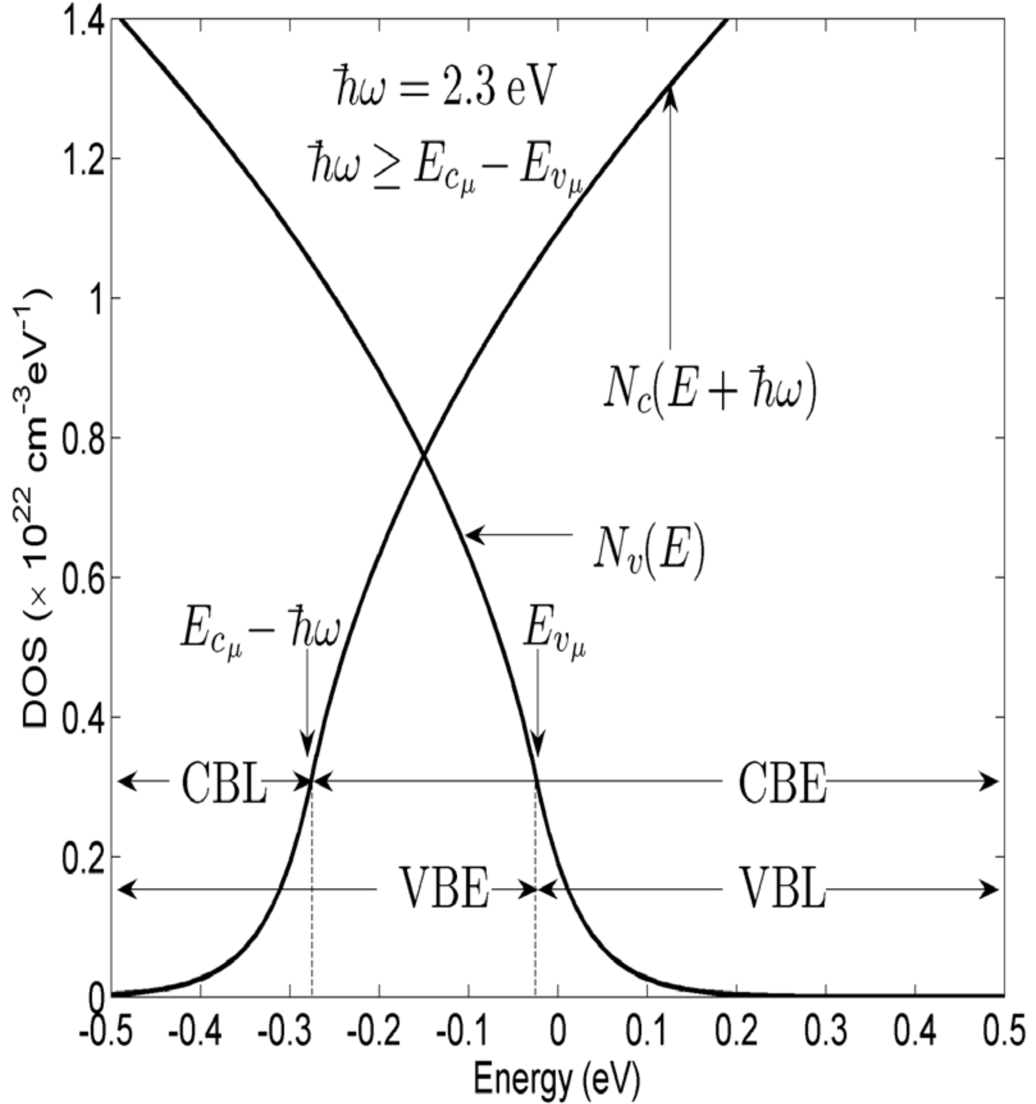

Figure 3.14: The factors in the JDOS integrand, $N_{\mathrm{V}}(E)$ and $N_{\mathrm{C}}(E + \hbar\omega)$, as functions of energy, E, for the photon energy, $\hbar\omega$, set to 2.3 eV, all DOS modeling parameter selections being set to their nominal values, i.e., the values set in Table 3.1, with $E_{\mathrm{V}\mu}$ set to E_{vt} and $E_{\mathrm{C}\mu}$ set to E_{ct}. It is noted that this case corresponds to the condition that $E_{\mathrm{C}\mu} - \hbar\omega \leq E_{\mathrm{V}\mu}$, i.e., $\hbar\omega \geq E_{\mathrm{C}\mu} - E_{\mathrm{V}\mu}$. The location of energies $E_{\mathrm{C}\mu} - \hbar\omega$ and $E_{\mathrm{V}\mu}$ are indicated with the light dotted lines and the arrows. The location of the VBE, VBL, CBE, and CBL electronic states are indicated.

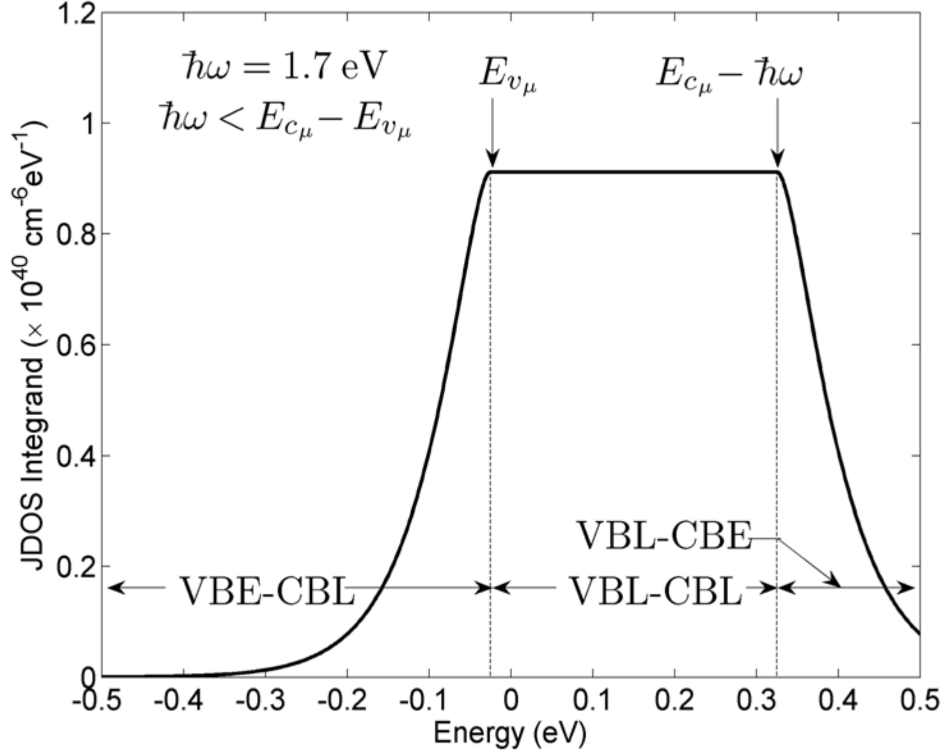

Figure 3.15: The JDOS integrand, $N_{\rm V}(E)N_{\rm C}(E+\hbar\omega)$, as a function of energy, E, for the photon energy, $\hbar\omega$, set to 1.7 eV, all DOS modeling parameter selections being set to their nominal values, i.e., the values set in Table 3.1, with $E_{{\rm V}\mu}$ set to $E_{\rm vt}$ and $E_{{\rm C}\mu}$ set to $E_{\rm ct}$. It is noted that this case corresponds to the condition that $E_{{\rm C}\mu} - \hbar\omega > E_{{\rm V}\mu}$, i.e., $\hbar\omega < E_{{\rm C}\mu} - E_{{\rm V}\mu}$. The location of energies $E_{{\rm V}\mu}$ and $E_{{\rm C}\mu} - \hbar\omega$ are indicated with the light dotted lines and the arrows. The region of the JDOS integrand corresponding to the overlap of the VBE electronic states and the CBL electronic states, this region corresponding to the contribution to the JDOS function corresponding to the VBE-CBL optical transitions, is indicated. The region of the JDOS integrand corresponding to the overlap of the VBL electronic states and the CBL electronic states, this region corresponding to the contribution to the JDOS function corresponding to the VBL-CBL optical transitions, is indicated. The region of the JDOS integrand corresponding to the overlap of the VBL electronic states and the CBE electronic states, this region corresponding to the contribution to the JDOS function corresponding to the VBL-CBE optical transitions, is indicated. For this particular selection of $\hbar\omega$, i.e., $\hbar\omega < E_{{\rm C}\mu} - E_{{\rm V}\mu}$, there is no overlap in the JDOS integrand between the VBE electronic states and the CBE electronic states, i.e., the contribution to the JDOS function corresponding to VBE-CBE optical transitions, is nil.

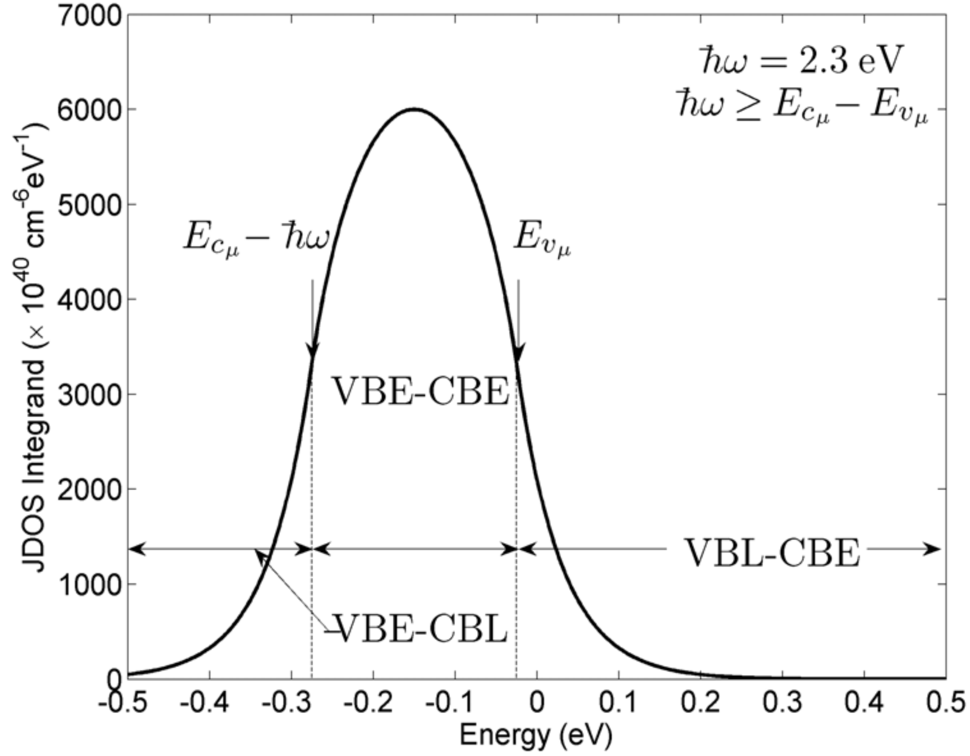

Figure 3.16: The JDOS integrand, $N_{\mathrm{V}}(E)N_{\mathrm{C}}(E+\hbar\omega)$, as a function of energy, E, for the photon energy, $\hbar\omega$, set to 2.3 eV, all DOS modeling parameter selections being set to their nominal values, i.e., the values set in Table 3.1, with $E_{\mathrm{V}\mu}$ set to E_{vt} and $E_{\mathrm{C}\mu}$ set to E_{ct}. It is noted that this case corresponds to the condition that $E_{\mathrm{C}\mu} - \hbar\omega \leq E_{\mathrm{V}\mu}$, i.e., $\hbar\omega \geq E_{\mathrm{C}\mu} - E_{\mathrm{V}\mu}$. The location of energies $E_{\mathrm{V}\mu}$ and $E_{\mathrm{C}\mu} - \hbar\omega$ are indicated with the light dotted lines and the arrows. The region of the JDOS integrand corresponding to the overlap of the VBE electronic states and the CBE electronic states, this region corresponding to the contribution to the JDOS function corresponding to the VBE-CBE optical transitions, is indicated. The region of the JDOS integrand corresponding to the overlap of the VBE electronic states and the CBL electronic states, this region corresponding to the contribution to the JDOS function corresponding to the VBE-CBL optical transitions, is indicated. The region of the JDOS integrand corresponding to the overlap of the VBL electronic states and the CBE electronic states, this region corresponding to the contribution to the JDOS function corresponding to the VBL-CBE optical transitions, is indicated. For this particular selection of $\hbar\omega$, i.e., $\hbar\omega \geq E_{\mathrm{C}\mu} - E_{\mathrm{V}\mu}$, there is no overlap in the JDOS integrand between the VBL electronic states and the CBL electronic states, i.e., the contribution to the JDOS function corresponding to VBL-CBL optical transitions, is nil.

decreasing in response to increasing energy, i.e., recall Eq. (3.1), and given that the CBL electronic states are exponentially increasing in response to increasing energy, i.e., recall Eq. (3.2), the tail breadth associated with the VBL electronic states being exactly the same as that associated with CBL electronic states, the JDOS integrand, seen in Figure 3.15, is constant between energies $E_{V\mu}$ and $E_{C\mu} - \hbar\omega$; recall that $E_{V\mu}$ is set to E_{vt} and that $E_{C\mu}$ is set to E_{ct} for this analysis. For the case of $\hbar\omega$ set to 2.3 eV (Figures 3.14 and 3.16), i.e., $\hbar\omega \geq E_{C\mu} - E_{V\mu}$, $E_{C\mu} - \hbar\omega$ occurs at a lower energy than $E_{V\mu}$. As a result, the distribution of VBL electronic states (associated with the $N_V(E)$ factor in the JDOS integrand) never overlaps with the distribution of CBL electronic states (associated with the $N_C(E + \hbar\omega)$ factor in the JDOS integrand). The resultant JDOS integrand is depicted in Figure 3.16. It is also noted that the JDOS integrand, $N_V(E)N_C(E+\hbar\omega)$, is considerably smaller for the case of $\hbar\omega$ set to 1.7 eV (Figure 3.15) as opposed to the case of $\hbar\omega$ set to 2.3 eV (Figure 3.16).

The overall JDOS function, $J(\hbar\omega)$, corresponds to the integration of the JDOS integrand, $N_V(E)N_C(E + \hbar\omega)$, over the entire energy range, i.e., from $-\infty$ to ∞; recall Eq. (3.12). For the case of $\hbar\omega$ set to 1.7 eV, i.e., $\hbar\omega < E_{C\mu} - E_{V\mu}$, from Figures 3.13 and 3.15, it is clear that the contributions to the JDOS function attributable to the VBE-CBL, VBL-CBE, and VBL-CBL optical transitions, corresponding to the regions of overlap in the JDOS integrand between the VBE and CBL electronic states, the VBL and CBE electronic states, and the VBL and CBL electronic states, respectively, denoted $J_{\text{VBE-CBL}}(\hbar\omega)$, $J_{\text{VBL-CBE}}(\hbar\omega)$, and $J_{\text{VBL-CBL}}(\hbar\omega)$, corresponds to the integration of the JDOS integrand, $N_V(E)N_C(E+\hbar\omega)$, between energies $-\infty$ and $E_{V\mu}$, $E_{C\mu} - \hbar\omega$ and ∞, and $E_{V\mu}$ and $E_{C\mu} - \hbar\omega$;

as VBE-CBE optical transitions do not occur for the case of $\hbar\omega < E_{C\mu} - E_{V\mu}$, $J_{\text{VBE-CBE}}(\hbar\omega) = 0$ for this case. For the case of $\hbar\omega$ set to 2.3 eV, i.e., $\hbar\omega \geq E_{C\mu} - E_{V\mu}$, from Figures 3.14 and 3.16, it is clear that the contributions to the JDOS function attributable to the VBE-CBE, VBE-CBL, and VBL-CBE optical transitions, corresponding to the regions of overlap in the JDOS integrand between the VBE and CBE electronic states, the VBE and CBL electronic states, and the VBL and CBE electronic states, denoted $J_{\text{VBE-CBE}}(\hbar\omega)$, $J_{\text{VBE-CBL}}(\hbar\omega)$, and $J_{\text{VBL-CBE}}(\hbar\omega)$, respectively, corresponds to the integration of the JDOS integrand, $N_V(E)N_C(E + \hbar\omega)$, between energies $E_{C\mu} - \hbar\omega$ and $E_{V\mu}$, $-\infty$ and $E_{C\mu} - \hbar\omega$, and $E_{V\mu}$ and ∞; as VBL-CBL optical transitions do not occur for the case of $\hbar\omega \geq E_{C\mu} - E_{V\mu}$, the contribution to the JDOS function attributable solely to VBL-CBL optical transitions, $J_{\text{VBL-CBL}}(\hbar\omega)$, is nil for this case.

Summarizing these results, it is seen that

$$J_{\text{VBE-CBE}}(\hbar\omega) = \begin{cases} \displaystyle\int_{E_{C\mu-\hbar\omega}}^{E_{V\mu}} N_V(E)N_C(E+\hbar\omega)dE, & \hbar\omega \geq E_{C\mu} - E_{V\mu} \\ 0, & \hbar\omega < E_{C\mu} - E_{V\mu} \end{cases} \tag{3.17}$$

$$J_{\text{VBE-CBL}}(\hbar\omega) = \begin{cases} \displaystyle\int_{-\infty}^{E_{C\mu-\hbar\omega}} N_V(E)N_C(E+\hbar\omega)dE, & \hbar\omega \geq E_{C\mu} - E_{V\mu} \\ \displaystyle\int_{-\infty}^{E_{V\mu}} N_V(E)N_C(E+\hbar\omega)dE, & \hbar\omega < E_{C\mu} - E_{V\mu} \end{cases} \tag{3.18}$$

$$J_{\text{VBL-CBE}}(\hbar\omega) = \begin{cases} \displaystyle\int_{E_{V\mu}}^{\infty} N_V(E)N_C(E+\hbar\omega)dE, & \hbar\omega \geq E_{C\mu} - E_{V\mu} \\ \displaystyle\int_{E_{C\mu-\hbar\omega}}^{\infty} N_V(E)N_C(E+\hbar\omega)dE, & \hbar\omega < E_{C\mu} - E_{V\mu} \end{cases} \tag{3.19}$$

and

$$J_{\text{VBL-CBL}}(\hbar\omega) = \begin{cases} 0, & \hbar\omega \geq E_{\text{C}\mu} - E_{\text{V}\mu} \\ \displaystyle\int_{E_{\text{V}\mu}}^{E_{\text{C}\mu}-\hbar\omega} N_{\text{V}}(E) N_{\text{C}}(E+\hbar\omega) dE, & \hbar\omega < E_{\text{C}\mu} - E_{\text{V}\mu} \end{cases} \tag{3.20}$$

Conservation, and Eqs. (3.12), (3.17), (3.18), (3.19), and (3.20), mandate that

$$J(\hbar\omega) = J_{\text{VBE-CBE}}(\hbar\omega) + J_{\text{VBE-CBL}}(\hbar\omega) + J_{\text{VBL-CBE}}(\hbar\omega) + J_{\text{VBL-CBL}}(\hbar\omega). \tag{3.21}$$

Note that the mobility gap, $E_{\text{C}\mu} - E_{\text{V}\mu}$, i.e., the energy difference between the valence band and the conduction band mobility edges, serves as a key parameter in this JDOS formalism. As will be seen shortly, many of the abrupt changes that occur in these JDOS functions occur in the vicinity of $\hbar\omega = E_{\text{C}\mu} - E_{\text{V}\mu}$, i.e., in the neighborhood of the mobility gap.

3.6 Numerical JDOS results

A selection of JDOS results, corresponding to the JDOS formalism that has been developed thus far, is now presented. In particular, the spectral dependencies of $J(\hbar\omega)$, $J_{\text{VBE-CBE}}(\hbar\omega)$, $J_{\text{VBE-CBL}}(\hbar\omega)$, $J_{\text{VBL-CBE}}(\hbar\omega)$, and $J_{\text{VBL-CBL}}(\hbar\omega)$, for a number of DOS modeling parameter selections, are presented. These results are obtained through numerical integrations of the JDOS integrand, i.e., $N_{\text{V}}(E)N_{\text{C}}(E+\hbar\omega)$, over the prescribed energy ranges set in Eqs. (3.12), (3.17), (3.18), (3.19), and (3.20), respectively. The spectral dependencies of the fractional JDOS contributions, $\frac{J_{\text{VBE-CBE}}(\hbar\omega)}{J(\hbar\omega)}$, $\frac{J_{\text{VBE-CBL}}(\hbar\omega)}{J(\hbar\omega)}$, $\frac{J_{\text{VBL-CBE}}(\hbar\omega)}{J(\hbar\omega)}$, and $\frac{J_{\text{VBL-CBL}}(\hbar\omega)}{J(\hbar\omega)}$, will also be examined, these fractional JDOS contributions providing a means of assessing the relative significance of the various types of optical transitions that occur.

The approach will be to first present baseline reference results, obtained by setting the DOS modeling parameters to their nominal values, i.e., the values set in Table 3.1, with $E_{\mathrm{V}\mu}$ set to E_{vt} and $E_{\mathrm{C}\mu}$ set to E_{ct}. The JDOS functions, J, $J_{\text{VBE-CBE}}$, $J_{\text{VBE-CBL}}$, $J_{\text{VBL-CBE}}$, and $J_{\text{VBL-CBL}}$, are plotted as functions of $\hbar\omega$ in Figure 3.17. It is noted that $J_{\text{VBE-CBE}} = 0$ for $\hbar\omega < E_{\mathrm{C}\mu} - E_{\mathrm{V}\mu}$ and that $J_{\text{VBL-CBL}} = 0$ for $\hbar\omega \geq E_{\mathrm{C}\mu} - E_{\mathrm{V}\mu}$, respectively. Owing to the symmetry in the DOS modeling parameter selections for this particular set of parameters, i.e., Table 3.1, $J_{\text{VBE-CBL}}(\hbar\omega)$ is found to be identical to $J_{\text{VBL-CBE}}(\hbar\omega)$ over the entire spectrum. This may be demonstrated to be the case by noting, for this particular selection of DOS modeling parameters, that the JDOS integrand, $N_{\mathrm{V}}(E)N_{\mathrm{C}}(E + \hbar\omega)$, is symmetrically distributed, both above $E_{\mathrm{C}\mu} - \hbar\omega$ and below $E_{\mathrm{V}\mu}$ for the case of $\hbar\omega < E_{\mathrm{C}\mu} - E_{\mathrm{V}\mu}$ (recall Figure 3.15), and above $E_{\mathrm{V}\mu}$ and below $E_{\mathrm{C}\mu} - \hbar\omega$ for the case of $\hbar\omega \geq E_{\mathrm{C}\mu} - E_{\mathrm{V}\mu}$ (recall Figure 3.16); with this symmetry in the JDOS integrand, $N_{\mathrm{V}}(E)N_{\mathrm{C}}(E+\hbar\omega)$, Eqs. (3.18) and (3.19) may be used in order to show that $J_{\text{VBE-CBL}}$ and $J_{\text{VBL-CBE}}$ are coincident over the entire spectrum.

From Figure 3.17, it is noted that $J(\hbar\omega)$ and $J_{\text{VBE-CBE}}(\hbar\omega)$, and that the coincident JDOS functions, $J_{\text{VBE-CBL}}$ and $J_{\text{VBL-CBE}}$, all monotonically increase in response to increases in $\hbar\omega$. The overall JDOS function, $J(\hbar\omega)$, increases monotonically with $\hbar\omega$ as the JDOS integrand, $N_{\mathrm{V}}(E)N_{\mathrm{C}}(E + \hbar\omega)$, increases as $\hbar\omega$ increases; recall Figures 3.15 and 3.16. The monotonic increase in $J_{\text{VBE-CBE}}(\hbar\omega)$, from zero at the mobility gap, i.e., when $\hbar\omega = E_{\mathrm{C}\mu} - E_{\mathrm{V}\mu}$, arises as a consequence of the increases in the magnitude of the JDOS integrand, $N_{\mathrm{V}}(E)N_{\mathrm{C}}(E + \hbar\omega)$, as $\hbar\omega$ increases, in conjunction with the increase in the energy range over which the JDOS integrand is integrated, i.e., between $E_{\mathrm{C}\mu} - \hbar\omega$ and $E_{\mathrm{V}\mu}$; recall Eq. (3.17)

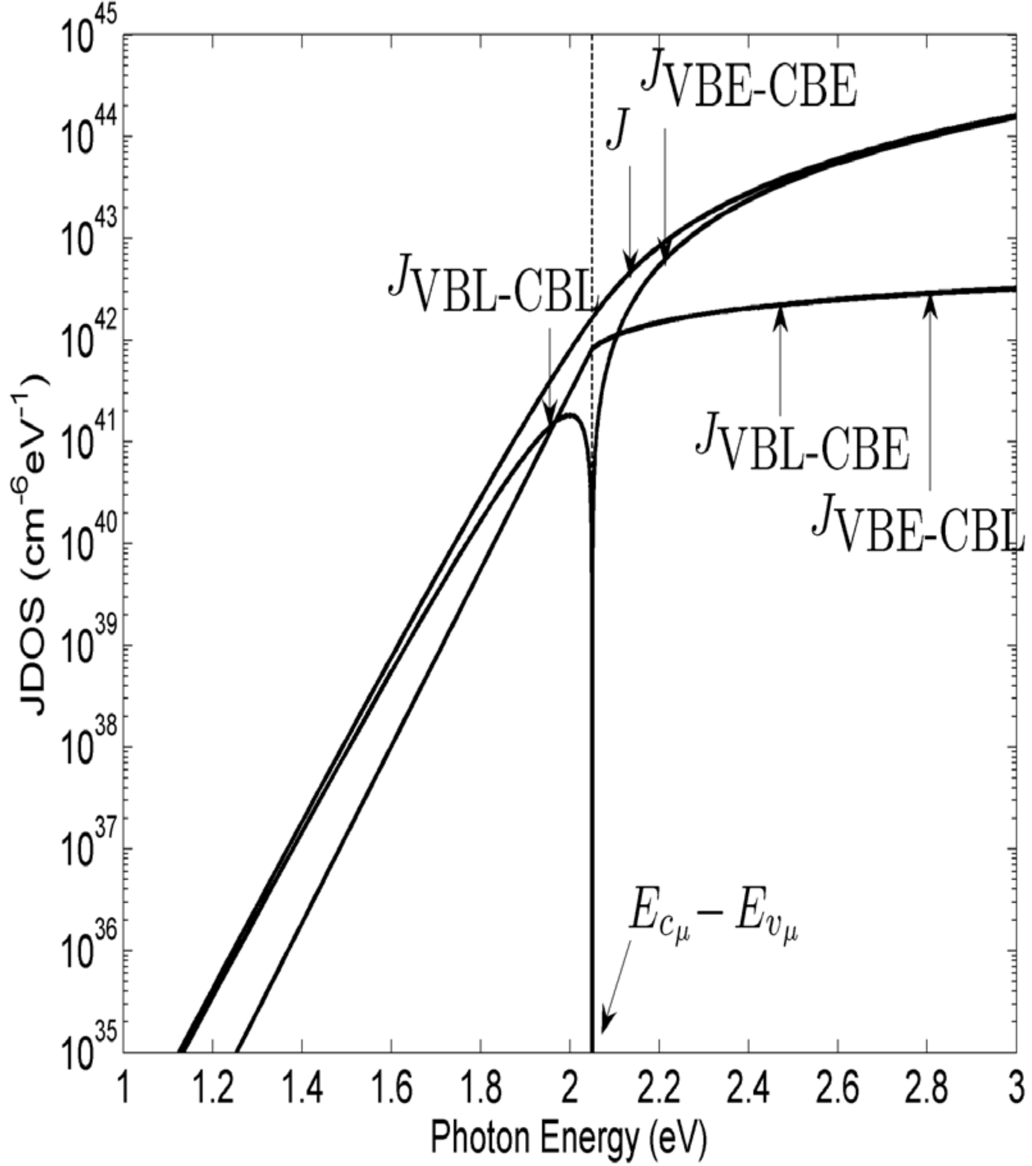

Figure 3.17: The contributions to the JDOS function corresponding to the VBE-CBE, VBE-CBL, VBL-CBE, and VBL-CBL optical transitions, i.e., J, $J_{\text{VBE-CBE}}$, $J_{\text{VBE-CBL}}$, $J_{\text{VBL-CBE}}$, and $J_{\text{VBL-CBL}}$, as functions of the photon energy, $\hbar\omega$, all DOS modeling parameter selections being set to their nominal values, i.e., the values set in Table 3.1, with $E_{\text{v}\mu}$ set to E_{vt} and $E_{\text{c}\mu}$ set to E_{ct}. The overall JDOS function, J, is also plotted as a function of the photon energy, $\hbar\omega$.

for $\hbar\omega \geq E_{C\mu} - E_{V\mu}$ and Figure 3.16, noting that at the mobility gap itself, i.e., when $\hbar\omega = E_{C\mu} - E_{V\mu}$, $E_{V\mu}$ and $E_{C\mu} - \hbar\omega$ are coincident and the energy range of the integration is reduced to zero, i.e., $J_{\text{VBE-CBE}}$ is reduced to zero. The monotonic increase in the coincident JDOS functions, $J_{\text{VBE-CBL}}$ and $J_{\text{VBL-CBE}}$, corresponding to increases in $\hbar\omega$, occurs as a result of the increases in the magnitude of the JDOS integrand, $N_V(E)N_C(E+\hbar\omega)$, as $\hbar\omega$ increases. $J_{\text{VBL-CBL}}$ exhibits a very different functional form from the other JDOS functions, initially increasing monotonically with increases in $\hbar\omega$, achieving a maximum at a certain value of $\hbar\omega$, and then diminishing to zero at the mobility gap, i.e., when $\hbar\omega = E_{C\mu} - E_{V\mu}$. There are two countervailing effects at play. There is the natural tendency for the magnitude of the JDOS integrand, $N_V(E)N_C(E+\hbar\omega)$, to increase in response to increases in $\hbar\omega$. This, however, is offset by the fact that the energy range over which the JDOS integrand is integrated, i.e. between $E_{V\mu}$ and $E_{C\mu} - \hbar\omega$, diminishes as $\hbar\omega$ increases; at the mobility gap itself, i.e., when $\hbar\omega = E_{C\mu} - E_{V\mu}$, $E_{V\mu}$ and $E_{C\mu} - \hbar\omega$ are coincident, and the energy range of the integration is reduced to zero, i.e., $J_{\text{VBL-CBL}}(\hbar\omega)$ is reduced to zero.

In order to obtain greater insight into the relative contribution of the various types of optical transitions that occur to the overall JDOS function, the fractional JDOS contributions, $\frac{J_{\text{VBE-CBE}}(\hbar\omega)}{J(\hbar\omega)}$, $\frac{J_{\text{VBE-CBL}}(\hbar\omega)}{J(\hbar\omega)}$, $\frac{J_{\text{VBL-CBE}}(\hbar\omega)}{J(\hbar\omega)}$, and $\frac{J_{\text{VBL-CBL}}(\hbar\omega)}{J(\hbar\omega)}$, are plotted as functions of $\hbar\omega$ in Figure 3.18, noting, from Eq. (3.21), that the sum of these fractional JDOS functions is unity. While $\frac{J_{\text{VBE-CBE}}(\hbar\omega)}{J(\hbar\omega)}$ monotonically increases from 0 as $\hbar\omega$ increases from the mobility gap, i.e., $E_{C\mu} - E_{V\mu}$, and $\frac{J_{\text{VBL-CBL}}(\hbar\omega)}{J(\hbar\omega)}$ monotonically increases from 0 as $\hbar\omega$ decreases from the mobility gap, i.e., $E_{C\mu} - E_{V\mu}$, the coincident fractional JDOS functions, $\frac{J_{\text{VBE-CBL}}(\hbar\omega)}{J(\hbar\omega)}$

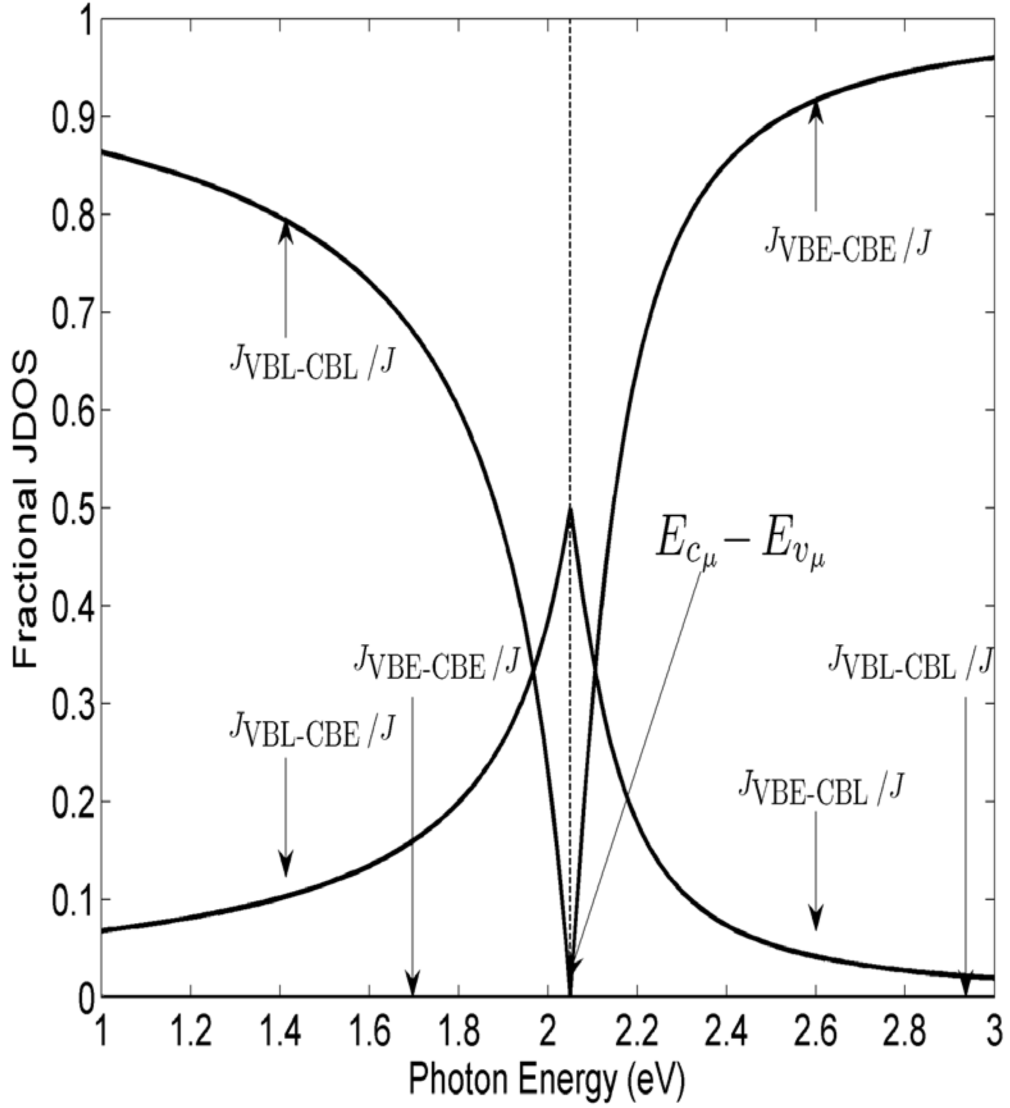

Figure 3.18: The fractional contributions to the JDOS function corresponding to the VBE-CBE, VBE-CBL, VBL-CBE, and VBL-CBL optical transitions, i.e., $\frac{J_{\text{VBE-CBE}}}{J}$, $\frac{J_{\text{VBE-CBL}}}{J}$, $\frac{J_{\text{VBL-CBE}}}{J}$, and $\frac{J_{\text{VBL-CBL}}}{J}$, as functions of the photon energy, $\hbar\omega$, all DOS modeling parameter selections being set to their nominal values, i.e., the values set in Table 3.1, with $E_{\text{v}\mu}$ set to E_{vt} and $E_{\text{c}\mu}$ set to E_{ct}.

and $\frac{J_{\text{VBL-CBE}}(\hbar\omega)}{J(\hbar\omega)}$, achieve their maxima exactly at the mobility gap, i.e., when $\hbar\omega = E_{\text{c}\mu} - E_{\text{v}\mu}$, i.e., these JDOS functions are continuous, the coincident fractional JDOS functions, $\frac{J_{\text{VBE-CBL}}(\hbar\omega)}{J(\hbar\omega)}$ and $\frac{J_{\text{VBL-CBE}}(\hbar\omega)}{J(\hbar\omega)}$, assuming values of $\frac{1}{2}$ when $\hbar\omega = E_{\text{c}\mu} - E_{\text{v}\mu}$. It is also noted that VBE-CBE optical transitions make an increasingly important contribution to the overall JDOS function as $\hbar\omega$ is increased beyond the mobility gap, i.e., $E_{\text{c}\mu} - E_{\text{v}\mu}$; this fractional contribution asymptotically approaches unity. Similarly, it is noted that VBL-CBL optical transitions make an increasingly important contribution to the overall JDOS function as $\hbar\omega$ is decreased below the mobility gap, i.e., $E_{\text{c}\mu} - E_{\text{v}\mu}$; this fractional contribution asymptotically approaches unity.

We now examine how these JDOS results change in response to variations in a number of key DOS modeling parameter selections. The JDOS results presented in Figures 3.17 and 3.18, corresponding to the nominal DOS modeling parameter selections, i.e., the values set in Table 3.1, with $E_{\text{v}\mu}$ set to E_{vt} and $E_{\text{c}\mu}$ set to E_{ct}, serve as a base line reference for this sensitivity analysis. In order to narrow the scope of this analysis, the impact that variations in the breadths of the valence band and conduction band tails, γ_{v} and γ_{c}, respectively, and the impact that variations in the locations of the mobility edges, $E_{\text{v}\mu}$ and $E_{\text{c}\mu}$, have upon the results are examined. The impact of variations in the other DOS modeling parameters, i.e., N_{vo}, N_{co}, E_{v}, E_{c}, E_{vt}, and E_{ct}, are deemed to be secondary importance, many such variations leading to a simple scaling or shifting of the results. For each of the cases that are examined, both the absolute and the fractional JDOS results are presented.

In Figure 3.19, the spectral dependence of the coincident JDOS functions, $J_{\text{VBE-CBL}}(\hbar\omega)$ and $J_{\text{VBL-CBE}}(\hbar\omega)$, for a number of selections of γ_{V} and γ_{C}, are plotted, i.e., for the cases of $\gamma_{\text{V}} = \gamma_{\text{C}} = 25$ meV, $\gamma_{\text{V}} = \gamma_{\text{C}} = 50$ meV, $\gamma_{\text{V}} = \gamma_{\text{C}} = 100$ meV, and $\gamma_{\text{V}} = \gamma_{\text{C}} = 200$ meV. The other DOS modeling parameters are set to their nominal values, i.e., the values set in Table 3.1, with $E_{\text{V}\mu}$ set to E_{vt} and $E_{\text{C}\mu}$ set to E_{ct}. It is noted that as γ_{V} and γ_{C} are increased, the coincident JDOS functions, $J_{\text{VBE-CBL}}(\hbar\omega)$ and $J_{\text{VBL-CBE}}(\hbar\omega)$, further encroach into the gap region. A detailed analysis indicates that the encroaching tails associated with the coincident JDOS functions, $J_{\text{VBE-CBL}}(\hbar\omega)$ and $J_{\text{VBL-CBE}}(\hbar\omega)$, are exponential in character, and that the corresponding exponential tail breadths are determined by γ_{V} and γ_{C}; recall that $\gamma_{\text{V}} = \gamma_{\text{C}}$ for the nominal DOS modeling parameter selections, i.e., Table 3.1. The location of the mobility gap, occurring at $\hbar\omega = E_{\text{C}\mu} - E_{\text{V}\mu}$, is seen to increase as γ_{V} and γ_{C} are increased; given that $E_{\text{V}t} = E_{\text{V}} - \frac{1}{2}\gamma_{\text{V}}$ and that $E_{\text{ct}} = E_{\text{C}} + \frac{1}{2}\gamma_{\text{C}}$, i.e., recall Table 3.1, considering that $E_{\text{V}\mu}$ is set to E_{vt} and $E_{\text{C}\mu}$ is set to E_{ct}, it may be shown that $E_{\text{C}\mu} - E_{\text{V}\mu} = E_{\text{C}} - E_{\text{V}} + \frac{1}{2}\gamma_{\text{C}} + \frac{1}{2}\gamma_{\text{V}}$. Finally, it is noted that for any fixed value of $\hbar\omega$, the value of the coincident JDOS functions, $J_{\text{VBE-CBL}}(\hbar\omega)$ and $J_{\text{VBL-CBE}}(\hbar\omega)$, increases with γ_{V} and γ_{C}.

In Figure 3.20, the spectral dependence of the coincident fractional JDOS functions, $\frac{J_{\text{VBE-CBL}}(\hbar\omega)}{J(\hbar\omega)}$ and $\frac{J_{\text{VBL-CBE}}(\hbar\omega)}{J(\hbar\omega)}$, for the same selections of γ_{V} and γ_{C} employed in Figure 3.19, are plotted, the other DOS modeling parameters being set to their nominal values, i.e., the values set in Table 3.1, with $E_{\text{V}\mu}$ set to E_{vt} and $E_{\text{C}\mu}$ set to E_{ct}. As with Figure 3.18, it is noted that the coincident fractional JDOS functions, $\frac{J_{\text{VBE-CBL}}(\hbar\omega)}{\text{J}(\hbar\omega)}$ and $\frac{J_{\text{VBL-CBE}}(\hbar\omega)}{\text{J}(\hbar\omega)}$, achieve their maxima of $\frac{1}{2}$ exactly at the mobility gap, $\hbar\omega = E_{\text{C}\mu} - E_{\text{V}\mu}$. In addition, it is found that the coincident fractional

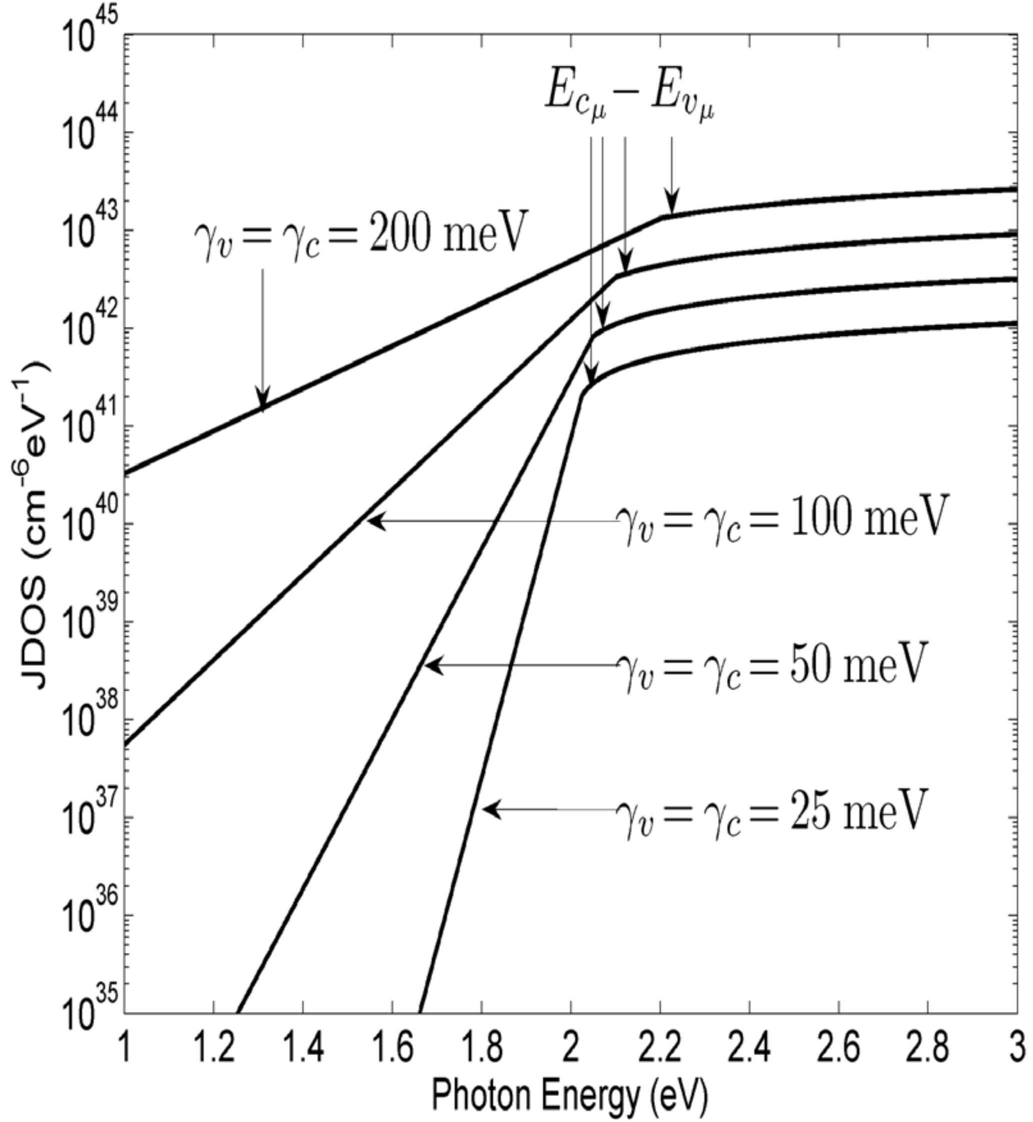

Figure 3.19: The contribution to the JDOS function corresponding to the VBE-CBL and VBL-CBE optical transitions, i.e., $J_{\text{VBL-CBE}}$ and $\text{J}_{\text{VBE-CBL}}$, as functions of the photon energy, $\hbar\omega$, with $\gamma_{\text{V}} = \gamma_{\text{C}} = 25$ meV, $\gamma_{\text{V}} = \gamma_{\text{C}} = 50$ meV, $\gamma_{\text{V}} = \gamma_{\text{C}} = 100$ meV, and $\gamma_{\text{V}} = \gamma_{\text{C}} = 200$ meV, all other DOS modeling parameters being set to their nominal values, i.e., the values set in Table 3.1, with $E_{\text{V}\mu}$ set to E_{vt} and $E_{\text{C}\mu}$ set to E_{ct}. Note that $J_{\text{VBE-CBL}}$ and $J_{\text{VBL-CBE}}$ are completely coincident over the entire spectrum for all cases. The mobility gap, $E_{\text{C}\mu} - E_{\text{V}\mu}$, marked with the arrows for the different cases, varies from case to case, $E_{\text{C}\mu} - E_{\text{V}\mu}$ being equal to $E_{\text{C}} - E_{\text{V}} + \frac{\gamma_{\text{V}}}{2} + \frac{\gamma_{\text{C}}}{2}$, for the case of $E_{\text{V}\mu}$ set to E_{vt} and $E_{\text{C}\mu}$ set to E_{ct}.

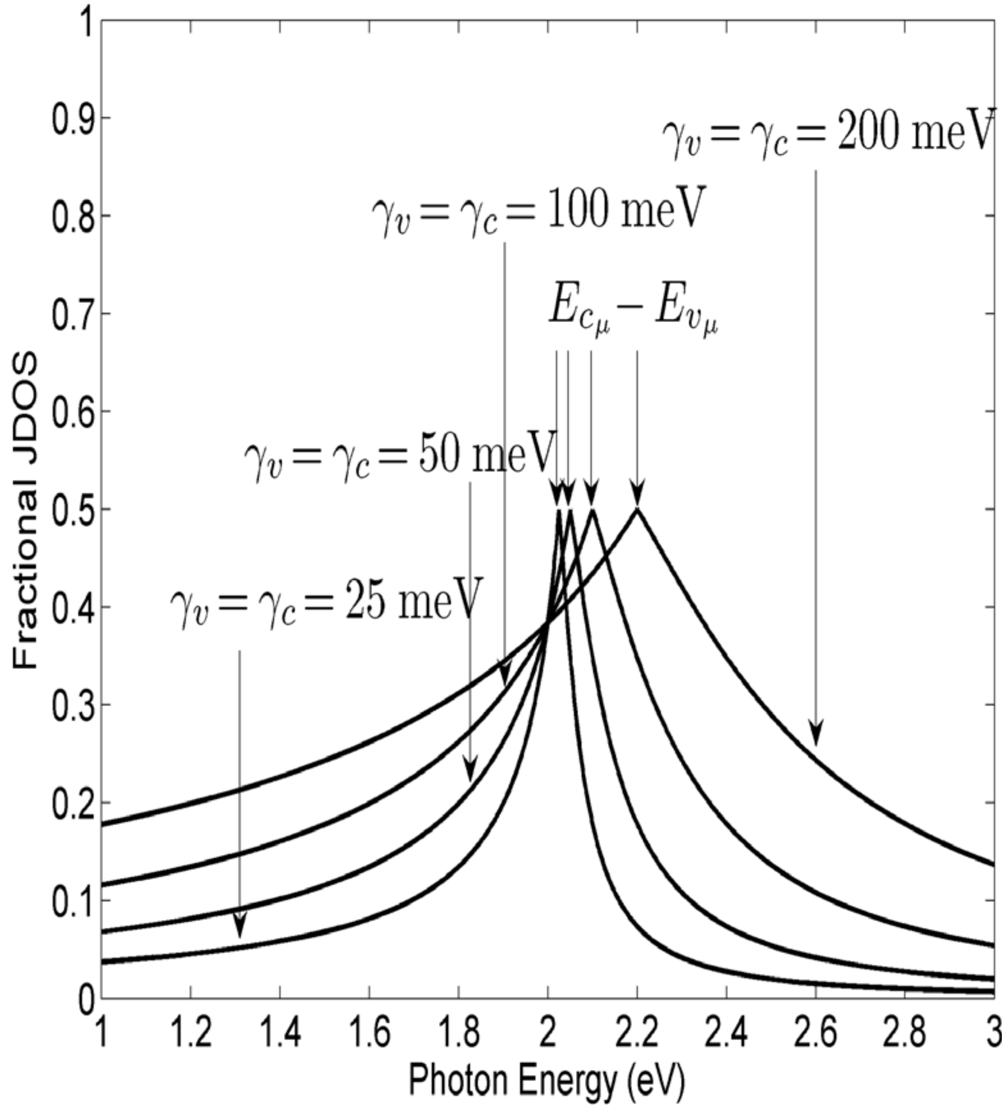

Figure 3.20: The fractional contributions to the JDOS function corresponding to the VBE-CBL and VBL-CBE optical transitions, i.e., $\frac{J_{\text{VBE-CBL}}}{J}$ and $\frac{J_{\text{VBL-CBE}}}{\text{J}}$, as functions of the photon energy, $\hbar\omega$, with $\gamma_{\text{V}} = \gamma_{\text{C}} = 25$ meV, $\gamma_{\text{V}} = \gamma_{\text{C}} = 50$ meV, $\gamma_{\text{V}} = \gamma_{\text{C}} = 100$ meV, and $\gamma_{\text{V}} = \gamma_{\text{C}} = 200$ meV, all other DOS modeling parameter selections being set to their nominal values, i.e., the values set in Table 3.1, with $E_{\text{V}\mu}$ set to E_{vt} and $E_{\text{C}\mu}$ set to E_{ct}. Note that $J_{\text{VBE-CBL}}$ and $J_{\text{VBL-CBE}}$ are completely coincident over the entire spectrum. The mobility gap, $E_{\text{C}\mu} - E_{\text{V}\mu}$, marked with the arrows for the different cases, varies from case to case, $E_{\text{C}\mu} - E_{\text{V}\mu}$ being equal to $E_{\text{C}} - E_{\text{V}} + \frac{\gamma_{\text{V}}}{2} + \frac{\gamma_{\text{C}}}{2}$ for the particular case of $E_{\text{V}\mu}$ set to E_{vt} and $E_{\text{C}\mu}$ set to E_{ct}.

JDOS functions, $\frac{J_{\text{VBE-CBL}}(\hbar\omega)}{J(\hbar\omega)}$ and $\frac{J_{\text{VBL-CBE}}(\hbar\omega)}{J(\hbar\omega)}$, asymptotically diminish to zero as $\hbar\omega$ is increased above the mobility gap and as $\hbar\omega$ is decreased below the mobility gap. The rate with which these attenuations occur is seen to be a strong function of the valence band and conduction band tail breadths, γ_{V} and γ_{C}, respectively.

In Figure 3.21, the spectral dependence of the coincident JDOS functions, $J_{\text{VBE-CBL}}(\hbar\omega)$ and $J_{\text{VBL-CBE}}(\hbar\omega)$, are plotted for a number of selections of $E_{\text{V}\mu}$ and $E_{\text{C}\mu}$, i.e., for the cases of $E_{\text{V}\mu} = E_{\text{vt}} - 200$ meV and $E_{\text{C}\mu} = E_{\text{ct}} + 200$ meV, $E_{\text{V}\mu} = E_{\text{vt}} - 100$ meV and $E_{\text{C}\mu} = E_{\text{ct}} + 100$ meV, $E_{\text{V}\mu} = E_{\text{vt}}$ and $E_{\text{C}\mu} = E\text{ct}$, $E_{\text{V}\mu} = E_{\text{vt}} + 100$ meV and $E_{\text{C}\mu} = E_{\text{ct}} - 100$ meV, and $E_{\text{V}\mu} = E_{\text{vt}} + 200$ meV and $E_{\text{C}\mu} = E_{\text{ct}} - 200$ meV, respectively, the other DOS modeling parameter selections being set to their nominal values, i.e., the values set in Table 3.1. With this particular selection of parameters, the impact of narrowing the mobility gap by simultaneously increasing $E_{\text{V}\mu}$ and decreasing $E_{\text{C}\mu}$ is examined, the case of $E_{\text{V}\mu} = E_{\text{vt}} - 200$ meV and $E_{\text{C}\mu} = E_{\text{ct}} + 200$ meV corresponding to a wide mobility gap, i.e., $E_{\text{C}\mu} - E_{\text{V}\mu} = E_{\text{ct}} - E_{\text{vt}} + 400$ meV, while the case of $E_{\text{V}\mu} = E_{\text{vt}} + 200$ meV and $E_{\text{C}\mu} = E_{\text{ct}} - 200$ meV corresponding to a narrower mobility gap, i.e., $E_{\text{C}\mu} - E_{\text{V}\mu} = E_{\text{ct}} - E_{\text{vt}} - 400$ meV.

It is seen that as the mobility gap, $E_{\text{C}\mu} - E_{\text{V}\mu}$, is narrowed, the contributions to the JDOS function attributable to the VBE-CBL and VBL-CBE optical transitions, i.e., $J_{\text{VBE-CBL}}$ and $J_{\text{VBL-CBE}}$, are diminished for high $\hbar\omega$. In particular, for high $\hbar\omega$, it is seen that the magnitude of the coincident JDOS functions, $J_{\text{VBE-CBL}}$ and $J_{\text{VBL-CBE}}$, decreases as $E_{\text{V}\mu}$ increases and $E_{\text{C}\mu}$ decreases. This occurs as the total density of VBL electronic states decreases as $E_{\text{V}\mu}$ increases (recall Figure 2.17), while the total density of CBL electronic states decreases as $E_{\text{C}\mu}$

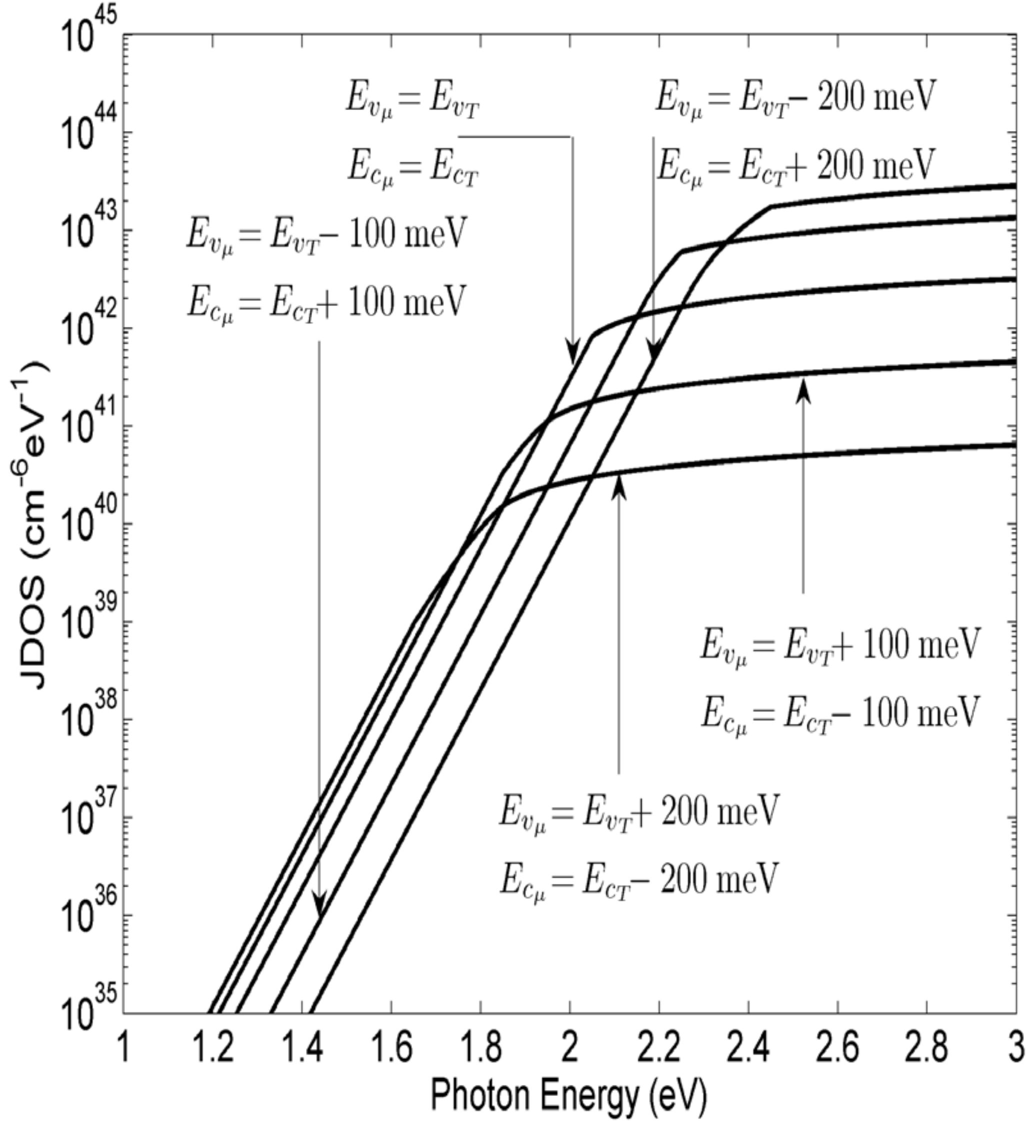

Figure 3.21: The contributions to the JDOS function corresponding to the VBE-CBL and VBL-CBE optical transitions, i.e., $J_{\text{VBE-CBL}}$ and $J_{\text{VBL-CBE}}$, as functions of the photon energy, $\hbar\omega$, with $E_{\text{v}\mu} = E_{\text{vt}} - 200$ meV and $E_{\text{c}\mu} = E_{\text{ct}} + 200$ meV, $E_{\text{v}\mu} = E_{\text{vt}} - 100$ meV and $E_{\text{c}\mu} = E_{\text{ct}} + 100$ meV, $E_{\text{v}\mu} = E_{\text{vt}}$ and $E_{\text{c}\mu} = E_{\text{ct}}$, $E_{\text{v}\mu} = E_{\text{vt}} + 100$ meV and $E_{\text{c}\mu} = E_{\text{ct}} - 100$ meV, and $E_{\text{v}\mu} = E_{\text{vt}} + 200$ meV and $E_{\text{c}\mu} = E_{\text{ct}} - 200$ meV, all other DOS modeling parameter selections being set to their nominal values, i.e., the values set in Table 3.1. Note that $J_{\text{VBE-CBL}}$ and $J_{\text{VBL-CBE}}$ are completely coincident over the entire spectrum. The mobility gap, $E_{\text{c}\mu} - E_{\text{v}\mu}$, varies from case to case.

decreases (recall Figure 2.18), thereby diminishing $J_{\text{VBE-CBL}}$ and $J_{\text{VBL-CBE}}$ for high $\hbar\omega$. The encroaching tail associated with the coincident JDOS functions, $J_{\text{VBE-CBL}}$ and $J_{\text{VBL-CBE}}$, are found to be exponential in character, and the corresponding exponential tail breadths are determined by γ_{V} and γ_{C}; recall that $\gamma_{\text{V}} = \gamma_{\text{C}}$ for the nominal DOS modeling parameter selections, i.e., Table 3.1. Finally, it is seen that the narrower mobility gap encroaches further into the gap region, as there is natural tendency for the coincident JDOS functions, $J_{\text{VBE-CBL}}$ and $J_{\text{VBL-CBE}}$, to position themselves with respect to the mobility gap location, $E_{\text{C}\mu} - E_{\text{V}\mu}$.

In Figure 3.22, the spectral dependence of the coincident fractional JDOS functions, $\frac{J_{\text{VBE-CBL}}(\hbar\omega)}{J(\hbar\omega)}$ and $\frac{J_{\text{VBL-CBE}}(\hbar\omega)}{J(\hbar\omega)}$, for the same selections of $E_{\text{V}\mu}$ and $E_{\text{C}\mu}$ employed in Figure 3.21, is plotted. As with Figures 3.18 and 3.20, it is noted that the coincident fractional JDOS functions, $\frac{J_{\text{VBE-CBL}}(\hbar\omega)}{J(\hbar\omega)}$ and $\frac{J_{\text{VBL-CBE}}(\hbar\omega)}{J(\hbar\omega)}$, achieve their maxima of $\frac{1}{2}$ exactly at the mobility gap, $\hbar\omega = E_{\text{C}\mu} - E_{\text{V}\mu}$. In addition, it is found that the coincident fractional JDOS functions, $\frac{J_{\text{VBE-CBL}}(\hbar\omega)}{J(\hbar\omega)}$ and $\frac{J_{\text{VBL-CBE}}(\hbar\omega)}{J(\hbar\omega)}$, asymptotically diminish to zero as $\hbar\omega$ is increased above the mobility gap and as $\hbar\omega$ is decreased below the mobility gap. The location of the mobility gap, $E_{\text{C}\mu} - E_{\text{V}\mu}$, is seen to be a strong function of the $E_{\text{V}\mu}$ and $E_{\text{C}\mu}$ selection.

3.7 Spectral dependence of the optical transition matrix element

The spectral dependence of the normalized dipole matrix element, $\Re^2(\hbar\omega)$, is now evaluated. The random phase analysis of Hindley [51] suggests that the matrix elements associated with optical transitions involving at most one localized electronic state are all of the same order of magnitude. The matrix elements associated with optical transitions between localized electronic states are found to

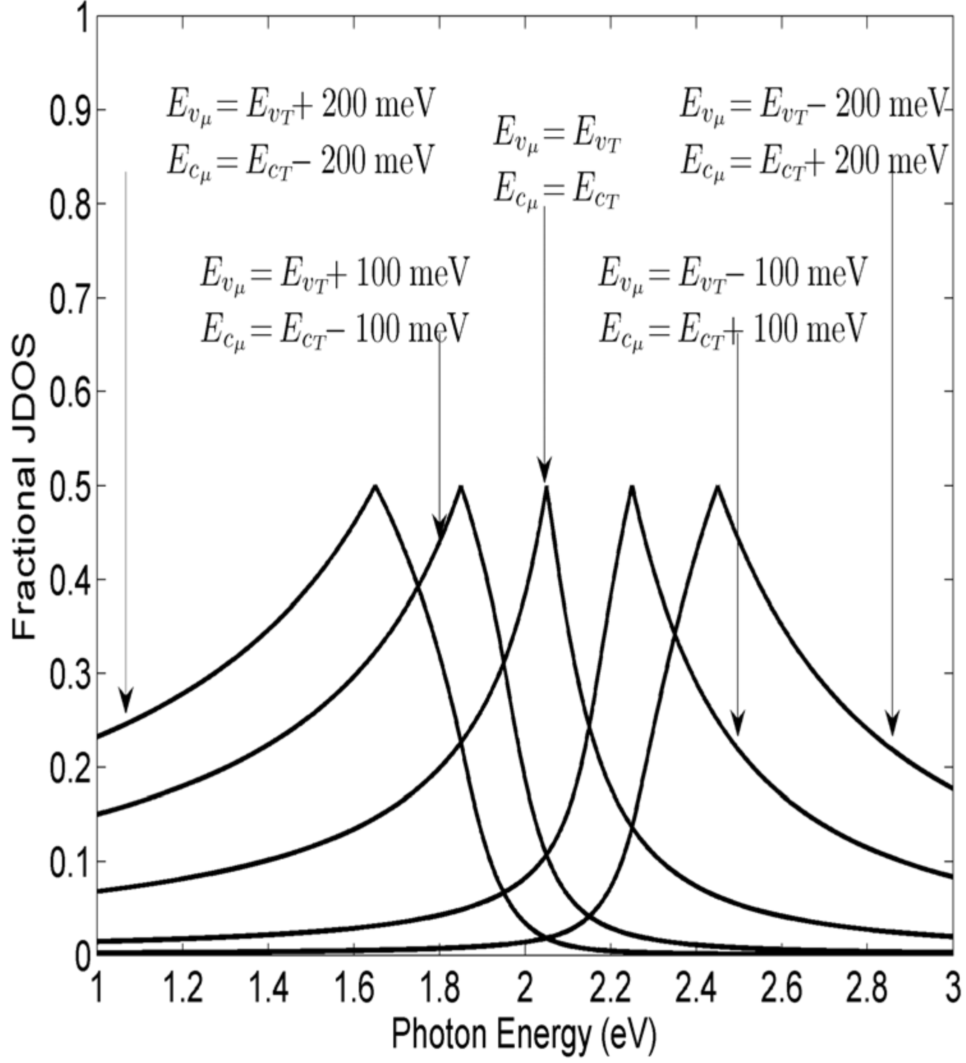

Figure 3.22: The fractional contributions to the JDOS function corresponding to the VBE-CBL and VBL-CBE optical transitions, i.e., $\frac{J_{\text{VBE-CBL}}}{J}$ and $\frac{J_{\text{VBL-CBE}}}{J}$, as functions of the photon energy, $\hbar\omega$, with $E_{\mathrm{v}\mu} = E_{\mathrm{vt}} - 200$ meV and $E_{\mathrm{c}\mu} = E_{\mathrm{ct}} + 200$ meV, $E_{\mathrm{v}\mu} = E_{\mathrm{vt}} - 100$ meV and $E_{\mathrm{c}\mu} = E_{\mathrm{ct}} + 100$ meV, $E_{\mathrm{v}\mu} = E_{\mathrm{vt}}$ and $E_{\mathrm{c}\mu} = E_{\mathrm{ct}}, E_{\mathrm{v}\mu} = E_{\mathrm{vt}} + 100$ meV and $E_{\mathrm{c}\mu} = E_{\mathrm{ct}} - 100$ meV, and $E_{\mathrm{v}\mu} = E_{\mathrm{vt}} + 200$ meV and $E_{\mathrm{c}\mu} = E_{\mathrm{ct}} - 200$ meV, all other DOS modeling parameter selections being set to their nominal values, i.e., the values set in Table 3.1. Note that $\frac{J_{\text{VBE-CBL}}}{J}$ and $\frac{J_{\text{VBL-CBE}}}{J}$ are completely coincident over the entire spectrum. The mobility gap, $E_{\mathrm{c}\mu} - E_{\mathrm{v}\mu}$, varies from case to case, this gap occurring when $\frac{J_{\text{VBE-CBL}}}{J}$ and $\frac{J_{\text{VBL-CBE}}}{J}$ achieve their maxima, i.e., $\frac{1}{2}$.

be negligible by comparison. If one let R_o^2 denote the matrix element associated with the VBE-CBE, VBE-CBL, and VBL-CBE optical transitions, and set the matrix element associated with the VBL-CBL optical transitions to nil, then it may be shown that

$$\Re^2(\hbar\omega) = R_o^2 \; J_{\text{frac}}(\hbar\omega), \tag{3.22}$$

where $J_{\text{frac}}(\hbar\omega)$ denotes the fraction of the overall JDOS function attributable to VBE-CBE, VBE-CBL, and VBL-CBE optical transitions. A detailed analysis shows that this fractional JDOS contribution function

$$J_{\text{frac}}(\hbar\omega) = \frac{J_{\text{VBE-CBE}}(\hbar\omega) + J_{\text{VBE-CBL}}(\hbar\omega) + J_{\text{VBL-CBE}}(\hbar\omega)}{J(\hbar\omega)}. \tag{3.23}$$

As may be seen from Eq. (3.22), the spectral dependence of this fractional JDOS contribution function, $J_{\text{frac}}(\hbar\omega)$, provides a means of determining the spectral dependence of $\Re^2(\hbar\omega)$.

In Figure 3.23, the fractional JDOS contribution, $J_{\text{frac}}(\hbar\omega)$, is plotted as a function of the photon energy, $\hbar\omega$, for the nominal DOS modeling parameters tabulated in Table 3.1. It is seen that for photon energies in excess of the mobility gap, i.e., $\hbar\omega \geq E_{\text{C}} - E_{\text{V}} + \frac{\gamma_{\text{V}}}{2} + \frac{\gamma_{\text{C}}}{2}$, that the fractional JDOS is unity. Below the mobility gap, however, an abrupt decrease in $J_{\text{frac}}(\hbar\omega)$ is observed. This decrease is related to the increasingly important role that VBL-CBL optical transitions play in determining the JDOS function, $J(\hbar\omega)$, VBL-CBL contributions taking away from the magnitude of $J_{\text{frac}}(\hbar\omega)$.

In Figure 3.24, the spectral dependence of the fractional JDOS contribution, $J_{\text{frac}}(\hbar\omega)$, is plotted as a function of the photon energy, $\hbar\omega$, for a number of selections of γ_{V} and γ_{C}, i.e., for the cases of $\gamma_{\text{V}} = \gamma_{\text{C}} = 25$ meV, $\gamma_{\text{V}} = \gamma_{\text{C}} = 50$ meV,

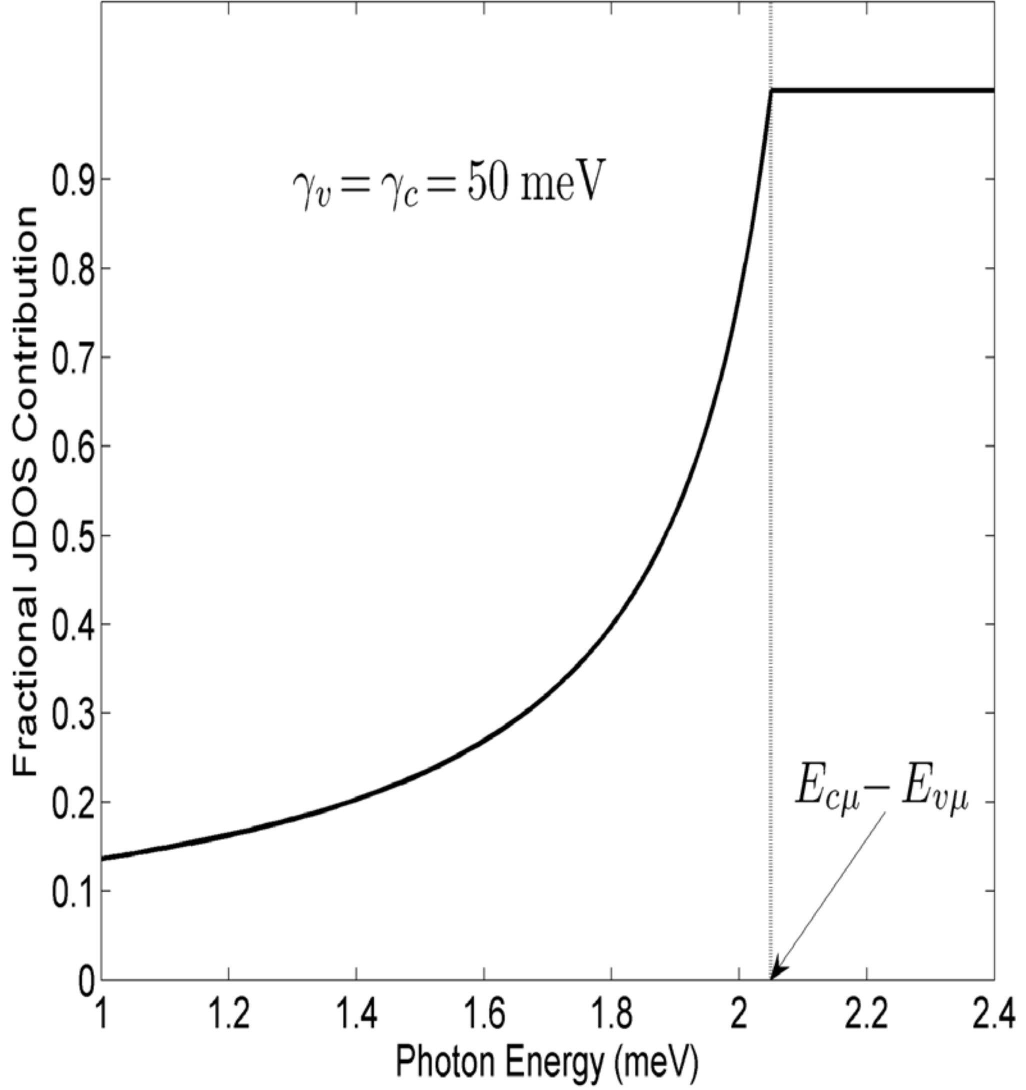

Figure 3.23: The fractional contribution to the JDOS function, J_{frac}, as defined in Eq. (3.23), as a function of the photon energy, $\hbar\omega$. All DOS modeling parameters are set to their nominal values, i.e., the values set in Table 3.1, with $E_{\text{v}\mu}$ set to E_{vt} and $E_{\text{c}\mu}$ set to E_{ct}.

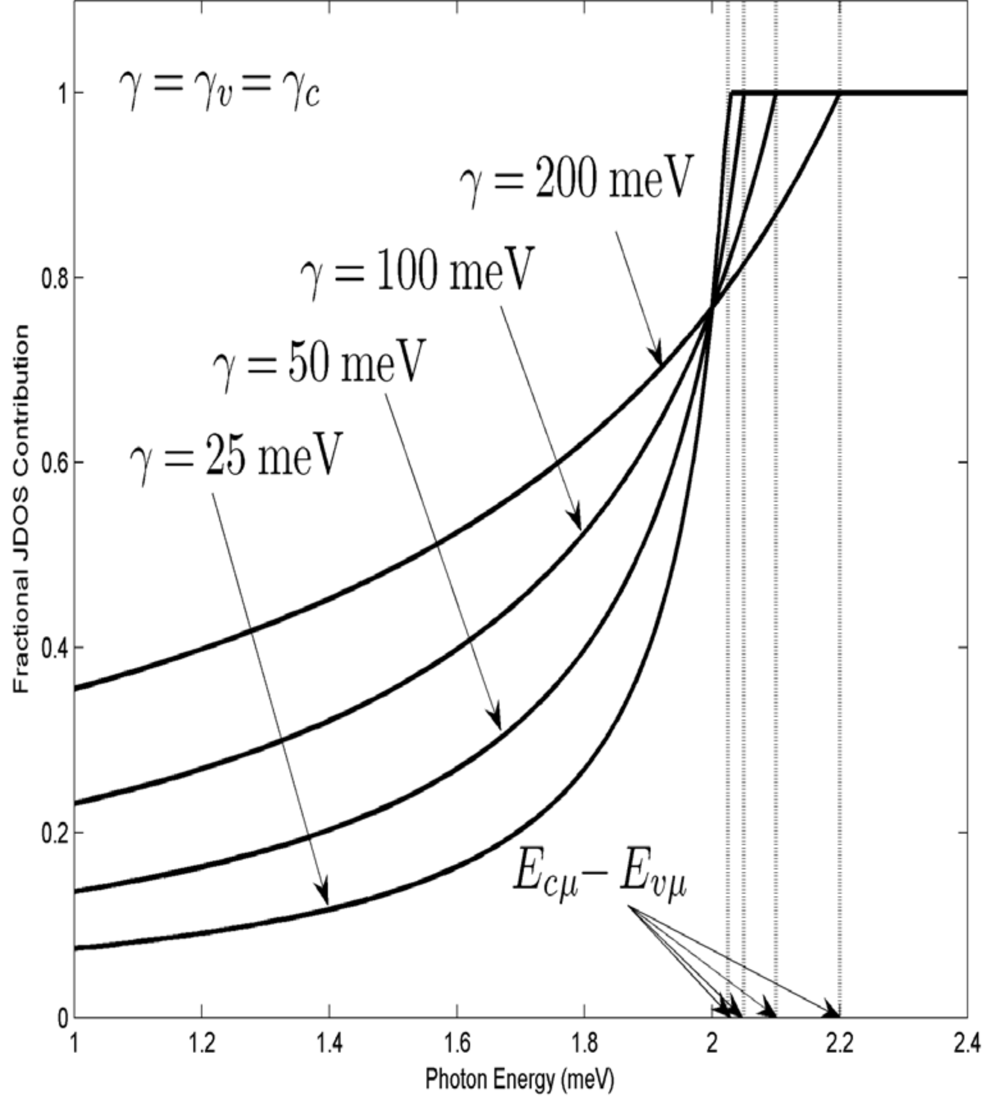

Figure 3.24: The fractional contributions to the JDOS function, J_{frac}, as defined in Eq. (3.23), as a function of the photon energy, $\hbar\omega$, for a number of selections of γ_{V} and γ_{C}, i.e., for the cases of $\gamma_{\mathrm{V}} = \gamma_{\mathrm{C}} = 25$ meV, $\gamma_{\mathrm{V}} = \gamma_{\mathrm{C}} = 50$ meV, $\gamma_{\mathrm{V}} = \gamma_{\mathrm{C}} = 100$ meV, and $\gamma_{\mathrm{V}} = \gamma_{\mathrm{C}} = 200$ meV. All DOS modeling parameters are set to their nominal values, i.e., the value set in Table 3.1, with $E_{\mathrm{V}\mu}$ set to E_{vt} and $E_{\mathrm{C}\mu}$ set to E_{ct}.

$\gamma_{\mathrm{V}} = \gamma_{\mathrm{C}} = 100$ meV, and $\gamma_{\mathrm{V}} = \gamma_{\mathrm{C}} = 200$ meV. The other DOS modeling parameters are set to their nominal values, i.e., the values set in Table 3.1, with $E_{\mathrm{V}\mu}$ set to E_{vt} and $E_{\mathrm{C}\mu}$ set to E_{ct}. It is noted that as γ_{V} and γ_{C} are increased, the location of the mobility gap, $E_{\mathrm{C}\mu} - E_{\mathrm{V}\mu} = E_{\mathrm{C}} - E_{\mathrm{V}} + \frac{\gamma_{\mathrm{V}}}{2} + \frac{\gamma_{\mathrm{C}}}{2}$, increases, as in seen in Figure 3.24. Below the mobility gap, the rate of decrease in the fractional JDOS contribution corresponding to decreased values of $\hbar\omega$ is found to be a strong function of γ_{V} and γ_{C}. It is also observed that when the photon energy, $\hbar\omega$, is set exactly to the energy gap, $E_{\mathrm{C}} - E_{\mathrm{V}}$, all the plots coincide. The reasons for this remain unknown at the present time.

In Figure 3.25, the spectral dependence of the fractional JDOS contribution, $J_{\mathrm{frac}}(\hbar\omega)$, is plotted as a function of the photon energy, $\hbar\omega$, for a number of selections of $E_{\mathrm{V}\mu}$ and $E_{\mathrm{C}\mu}$, i.e., for the cases of $E_{\mathrm{V}\mu} = E_{\mathrm{vt}} - 200$ meV and $E_{\mathrm{C}\mu} = E_{\mathrm{ct}} + 200$ meV, $E_{\mathrm{V}\mu} = E_{\mathrm{vt}} - 100$ meV, and $E_{\mathrm{C}\mu} = E_{\mathrm{ct}} + 100$ meV, $E_{\mathrm{V}\mu} = E_{\mathrm{vt}}$ and $E_{\mathrm{C}\mu} = E_{\mathrm{ct}}$, $E_{\mathrm{V}\mu} = E_{\mathrm{vt}} + 100$ meV and $E_{\mathrm{C}\mu} = E_{\mathrm{ct}} - 100$ meV, and $E_{\mathrm{V}\mu} = E_{\mathrm{vt}} + 200$ meV and $E_{\mathrm{C}\mu} = E_{\mathrm{ct}} - 200$ meV, respectively, the other DOS modeling parameter selections being set to their nominal values, i.e., the values set in Table 3.1. With this particular selection of parameters, the impact of narrowing the mobility gap by simultaneously increasing $E_{\mathrm{V}\mu}$ and decreasing $E_{\mathrm{C}\mu}$ is examined, the case of $E_{\mathrm{V}\mu} = E_{\mathrm{vt}} - 200$ meV and $E_{\mathrm{C}\mu} = E_{\mathrm{ct}} + 200$ meV corresponding to a wide mobility gap, i.e., $E_{\mathrm{C}\mu} - E_{\mathrm{V}\mu} = E_{\mathrm{ct}} - E_{\mathrm{vt}} + 400$ meV, while the case of $E_{\mathrm{V}\mu} = E_{\mathrm{vt}} + 200$ meV and $E_{\mathrm{C}\mu} = E_{\mathrm{ct}} - 200$ meV corresponding to a narrower mobility gap, i.e., $E_{\mathrm{C}\mu} - E_{\mathrm{V}\mu} = E_{\mathrm{ct}} - E_{\mathrm{vt}} - 400$ meV. It is noted that in all cases the fractional JDOS function, $J_{\mathrm{frac}}(\hbar\omega)$, is unity for photon energies greater than or equal to the mobility gap, $E_{\mathrm{C}\mu} - E_{\mathrm{V}\mu}$. The rate of decrease, seen below the

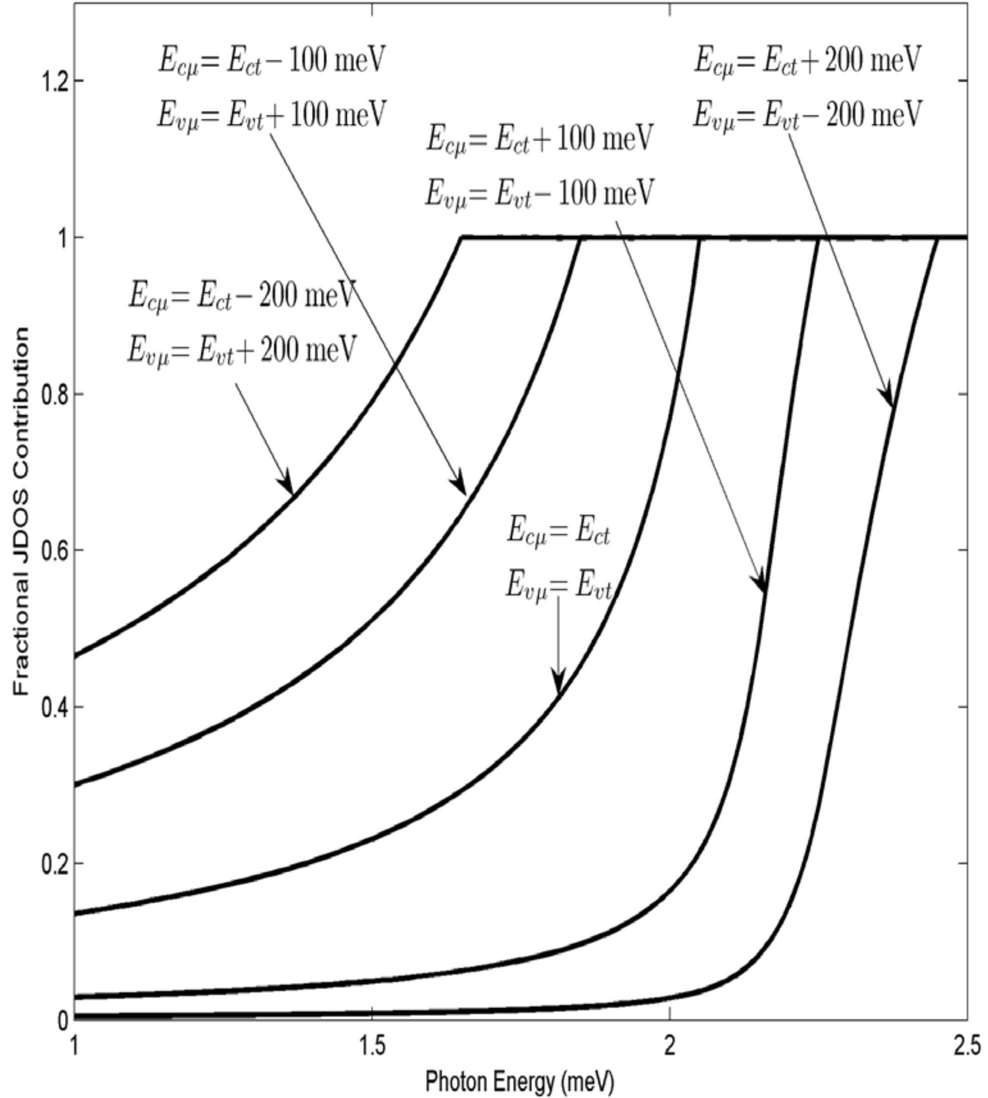

Figure 3.25: The fractional contributions to the JDOS function, J_{frac}, as defined in Eq. (3.23), as a function of the photon energy, $\hbar\omega$, for a number of selection of $E_{\text{v}\mu}$ and $E_{\text{c}\mu}$, i.e., for the cases of $E_{\text{v}\mu} = E_{\text{vt}} - 200$ meV and $E_{\text{c}\mu} = E_{\text{ct}} + 200$ meV, $E_{\text{v}\mu} = E_{\text{vt}} - 100$ meV, and $E_{\text{c}\mu} = E_{\text{ct}} + 100$ meV, $E_{\text{v}\mu} = E_{\text{vt}}$ and $E_{\text{c}\mu} = E\text{ct}$, $E_{\text{v}\mu} = E_{\text{vt}} + 100$ meV and $E_{\text{c}\mu} = E_{\text{ct}} - 100$ meV, and $E_{\text{v}\mu} = E_{\text{vt}} + 200$ meV and $E_{\text{c}\mu} = E_{\text{ct}} - 200$ meV, respectively. The other DOS modeling parameter selections are set to their nominal values, i.e., the values set in Table 3.1.

mobility gap, corresponding to decreases in the photon energy, $\hbar\omega$, is seen to be similar in all cases.

The spectral dependence of $\Re^2(\hbar\omega)$ is now plotted as a function of the photon energy, $\hbar\omega$. The experimental results of Jackson *et al.* [49], performed on PECVD a-Si:H, suggest that $R_o^2 \simeq 10$ Å^2; it should be noted, however, that there is some uncertainty associated with this value, as there is with any experimentally determined value. For the nominal DOS modeling parameters tabulated in Table 3.1, for $E_{\mathrm{v}\mu}$ set to E_{vt} and $E_{\mathrm{c}\mu}$ set to E_{ct}, with R_o^2 set to 10 Å^2, the resultant spectral dependence of the normalized optical transition matrix element squared average, $\Re^2(\hbar\omega)$, is depicted in Figure 3.26. It is seen that $\Re^2(\hbar\omega)$ is directly proportional to $J_{\mathrm{frac}}(\hbar\omega)$.

Finally, using Eq. (3.9), the spectral dependence of the imaginary part of the dielectric function, $\epsilon_2(\hbar\omega)$, is evaluated. For the spectral dependence of $\Re^2(\hbar\omega)$ as shown in Figure 3.26, the resultant spectral dependence of $\epsilon_2(\hbar\omega)$ is shown in Figure 3.27. The DOS modeling parameters are set to their nominal values, i.e., as specified in Table 3.1. It is seen that the spectral dependence of $\epsilon_2(\hbar\omega)$ is similar to that observed experimentally. The fitting of the results of this model with that of experiment will be pursued in Chapter 4.

3.8 The spectral dependence of the optical absorption coefficient

Thus far, means of evaluating the spectral dependence of the imaginary part of the dielectric function, $\epsilon_2(\hbar\omega)$, have been provided. While $\epsilon_2(\hbar\omega)$ is an important optical function in the characterization of materials, the spectral dependence of the optical absorption coefficient, $\alpha(\hbar\omega)$, is a more common measure of the op-

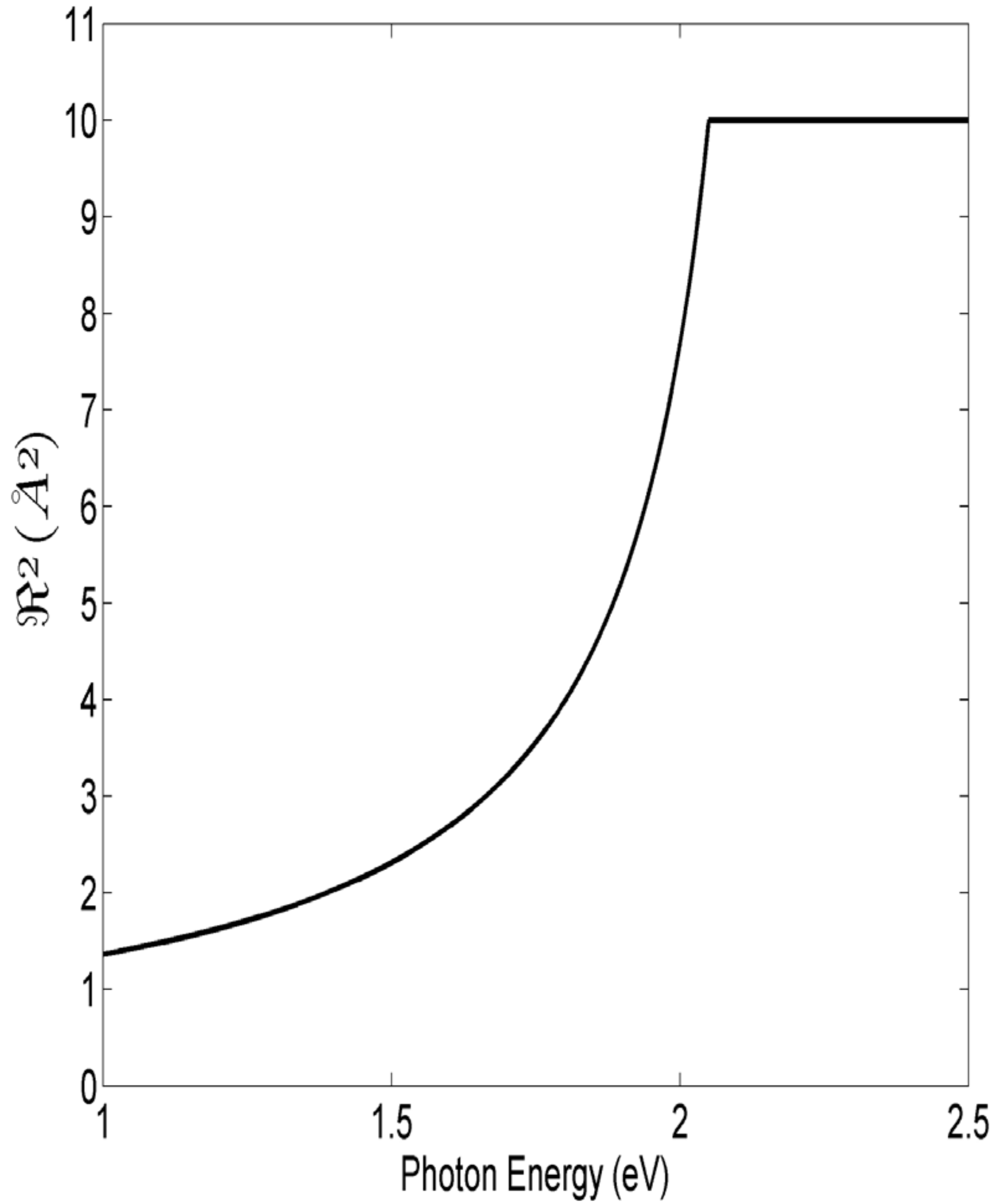

Figure 3.26: The spectral dependence of the normalized optical transition matrix element squared average, $\Re^2(\hbar\omega)$. The other DOS modeling parameter selections are set to their nominal values, i.e., the values set in Table 3.1.

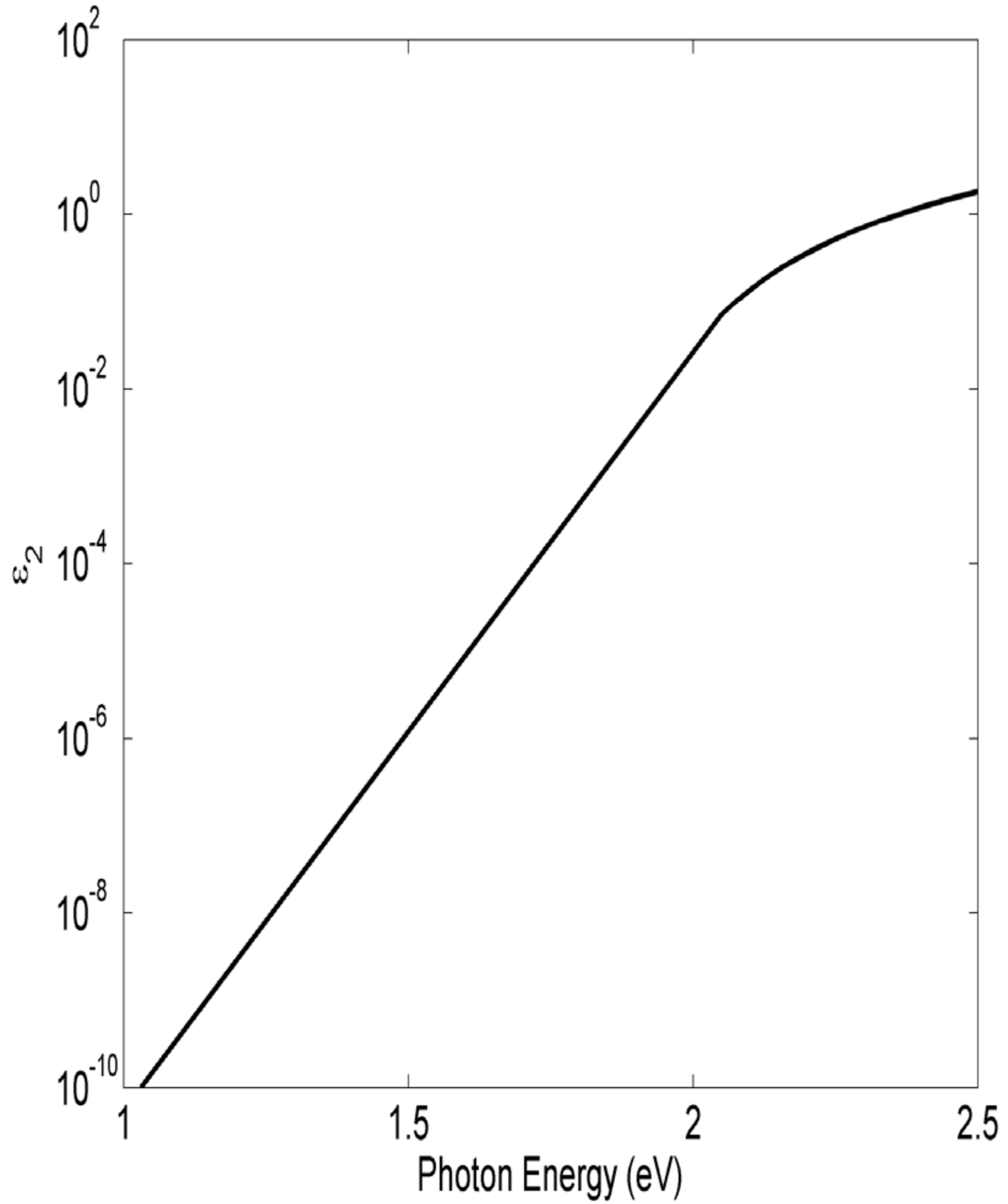

Figure 3.27: The spectral dependence of the imaginary part of the dielectric function, $\epsilon_2(\hbar\omega)$. Eq. (3.9) is used for the purposes of this analysis. $\Re^2(\hbar\omega)$ is as specified in Figure 3.26. The other DOS modeling parameter selections are set to their nominal values, i.e., the values set in Table 3.1.

tical response of materials. These functions are in fact related to each other. In particular, it may be shown that

$$\alpha(\hbar\omega) = \frac{\omega}{n(\hbar\omega)\ c}\epsilon_2(\hbar\omega), \tag{3.24}$$

where $n(\hbar\omega)$ denotes the spectral dependence of the refractive index, c represents the speed of light in vacuum, and ω is the angular frequency corresponding to photons of energy $\hbar\omega$. A representative optical absorption spectrum is depicted in Figure 3.28, for the nominal DOS modeling parameters tabulated in Table 3.1. For the purposes of this analysis, $n(\hbar\omega)$ is set to $\sqrt{11.7}$, this being the low-frequency refractive index associated with c-Si. Eq. (3.24) will be used when this JDOS formalism is applied to the specific case of PECVD a-Si:H. This will be seen in Chapter 4.

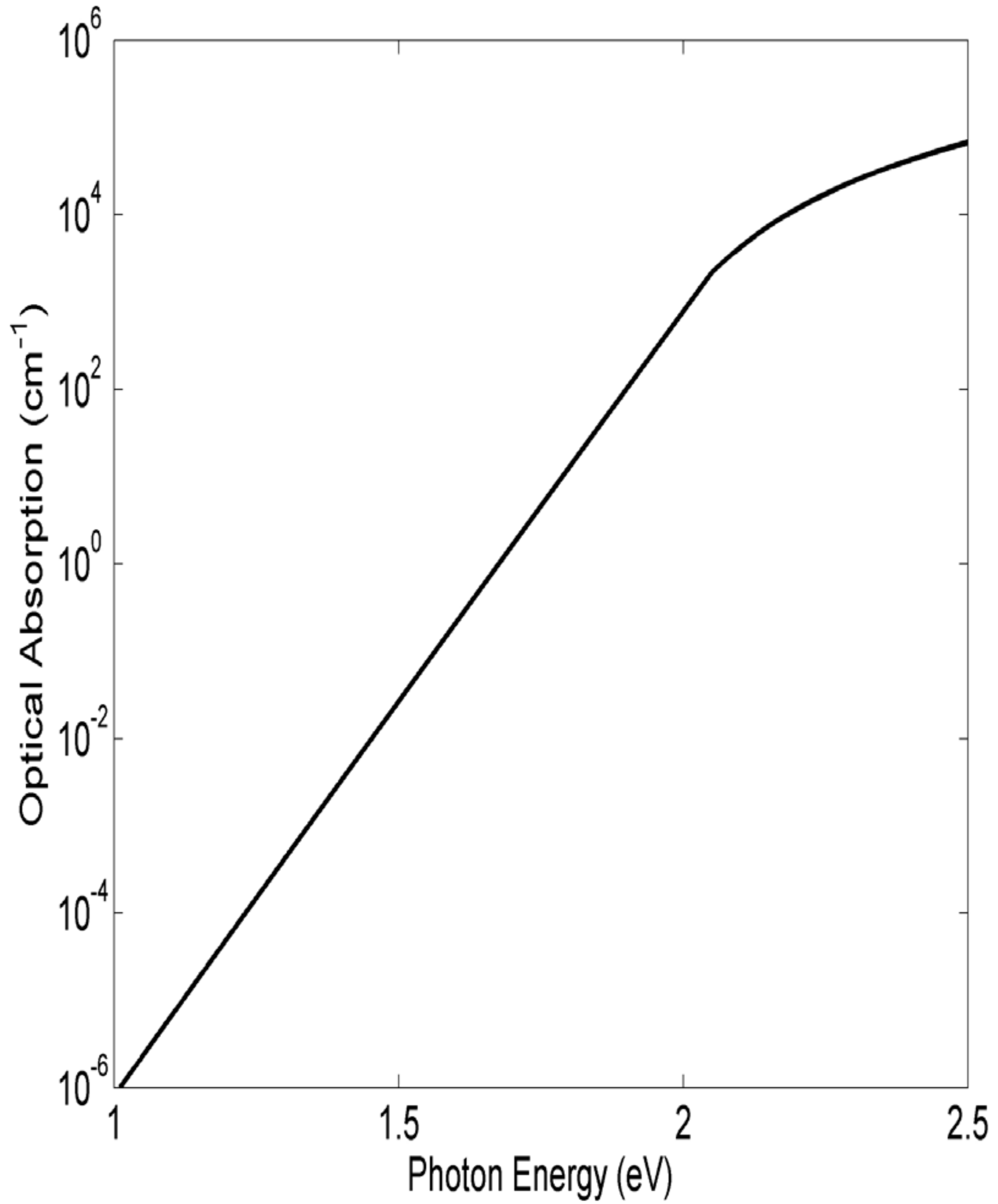

Figure 3.28: The spectral dependence of the optical absorption coefficient, $\alpha(\hbar\omega)$. Eq. (3.24) is employed for the purposes of this determination. This spectrum is determined assuming the nominal DOS modeling parameters selections specified in Table 3.1. For the purposes of this analysis, $n(\hbar\omega)$ is set to $\sqrt{11.7}$.

4. APPLICATION OF THE DOS AND JDOS FORMALISM TO THE SPECIFIC CASE OF PECVD A-SI:H

4.1 Introduction

Amorphous silicon has been prepared in a variety of different forms over the years. At present, PECVD a-Si:H is the most commonly found form of this material. It is the form of amorphous silicon that is found in contemporary electron device applications. One of the most attractive features of PECVD a-Si:H is the fact that it can be deposited uniformly and inexpensively over large areas. Crystalline silicon, by way of contrast, is very expensive to fabricate and can not be deposited uniformly over large areas. Additional qualities of PECVD a-Si:H, that further contribute to its allure, include the fact that it can be easily doped, junctions may be readily formed with it, and the same deposition process used to deposit the material itself may also be used to fabricate the dielectric and passivation layers needed for the realization of actual devices. The fact that the same silicon processing technologies, developed over a half century of work in conventional electronics, can also be applied to this material, further underscores the practicality of this material.

In this chapter, the DOS and JDOS formalism that has been developed in the two previous chapters is applied to the specific case of PECVD a-Si:H. Initially, a detailed analysis of the DOS functions associated with this material is presented. The aim of this analysis is the determination of the DOS modeling parameters corresponding to the specific case of PECVD a-Si:H, these parameters being used in the subsequent analysis. With these DOS modeling parameters determined, the

JDOS function, corresponding to PECVD a-Si:H, is then evaluated. With a nominal selection of PECVD a-Si:H DOS modeling parameter selections established, the dependence of the density of localized valence band electronic states and conduction band localized electronic states on the location of the valence band and conduction band mobility edges, $E_{V\mu}$ and $E_{C\mu}$, respectively, is then probed. The spectral dependence of the PECVD a-Si:H JDOS contributions are then evaluated. The spectral dependence of the normalized dipole matrix element squared average, $\Re^2(\hbar\omega)$, associated with PECVD a-Si:H, is then examined. The impact that these spectral variations have on the optical properties associated with PECVD a-Si:H is then considered. The spectral dependence of the optical absorption coefficient, $\alpha(\hbar\omega)$, is then evaluated. A means of quantitatively characterizing the optical absorption spectrum associated with PECVD a-Si:H is then developed. Finally, the effective mass of the electron and holes associated with PECVD a-Si:H are determined.

This chapter is organized in the following manner. In Section 4.2, DOS modeling parameters, corresponding to PECVD a-Si:H, are obtained through the fit of an empirical model for the DOS functions to the experimental PECVD a-Si:H DOS data of Jackson *et al.* [49]. The DOS modeling parameter selections, employed for the purposes of the subsequent analysis, are then laid out in Section 4.3. The spectral dependence of the JDOS function is then determined in Section 4.4, the resultant JDOS function being compared with the PECVD a-Si:H JDOS result of Jackson *et al.* [49]. The density of localized valence band electronic states and localized conduction band electronic states, corresponding to PECVD a-Si:H, are then determined in Section 4.5. The JDOS contributions, corresponding to PECVD

a-Si:H, are then evaluated in Section 4.6. In Section 4.7, the spectral dependence of the normalized dipole matrix element squared average associated with PECVD a-Si:H is determined. The impact that spectral variations in this matrix element have on the optical properties associated with PECVD a-Si:H are then explored in Section 4.8. In Section 4.9, the spectral dependence of the optical absorption coefficient associated with PECVD a-Si:H is evaluated. A means of characterizing the optical absorption spectrum associated with PECVD a-Si:H is then developed in Section 4.10. Finally, the effective masses associated with PECVD a-Si:H are evaluated in Section 4.11.

4.2 The DOS functions associated with PECVD a-Si:H

Experimental DOS data from Jackson *et al.* [49], obtained through measurements on PECVD a-Si:H, will be used in order to determine the DOS modeling parameters corresponding to this material. For the purposes of this analysis, the same empirical model for the DOS functions, used in the previous chapters, will be used here. That is, square-root functional dependencies in the band regions and exponential functional dependencies in the tail regions are assumed. Following the analysis presented in Chapters 2 and 3, the valence band DOS function

$$N_{\mathrm{v}}(E) = \begin{cases} N_{\mathrm{vo}}\sqrt{E_{\mathrm{v}} - E_{\mathrm{vt}}}\exp\left(\frac{E_{\mathrm{vt}}-E_{\mathrm{v}}}{\gamma_{\mathrm{v}}}\right)\exp\left(\frac{E_{\mathrm{v}}-E}{\gamma_{\mathrm{v}}}\right), & E > E_{\mathrm{vt}} \\ N_{\mathrm{vo}}\sqrt{E_{\mathrm{v}} - E} & E \leq E_{\mathrm{vt}} \end{cases}, \quad (4.1)$$

while the conduction band DOS function

$$N_{\mathrm{c}}(E) = \begin{cases} N_{\mathrm{co}}\sqrt{E - E_{\mathrm{c}}}, & E \geq E_{\mathrm{ct}} \\ N_{\mathrm{co}}\sqrt{E_{\mathrm{ct}} - E_{\mathrm{c}}}\exp\left(\frac{E_{\mathrm{c}}-E_{\mathrm{ct}}}{\gamma_{\mathrm{c}}}\right)\exp\left(\frac{E-E_{\mathrm{c}}}{\gamma_{\mathrm{c}}}\right), & E < E_{\mathrm{ct}} \end{cases}, \quad (4.2)$$

where N_{vo} and N_{co} denote the valence band and conduction band DOS prefactors, respectively, E_{v} and E_{c} correspond to the valence band and conduction band band edges, γ_{v} and γ_{c} are the valence band and conduction band tail breadths, and E_{vt} and E_{ct} represent the critical energies at which the square-root and exponential distributions interface; as before, $N_{\text{v}}(E)\triangle E$ and $N_{\text{c}}(E)\triangle E$ represent the number of one-electron valence band and one-electron conduction band states, between energies $[E, E+\triangle E]$, per unit volume, respectively. For Eqs. (4.1) and (4.2), it is assumed that $E_{\text{vt}} \leq E_{\text{v}}$ and that $E_{\text{ct}} \geq E_{\text{c}}$. The goal of the analysis here is to select the eight DOS modeling parameters, i.e., N_{vo}, N_{co}, E_{v}, E_{c}, γ_{v}, γ_{c}, E_{vt}, and E_{ct}, so that these empirical DOS functions, i.e., Eqs. (4.1) and (4.2), fit the experimental PECVD a-Si:H DOS results of Jackson *et al.* [49]. The error associated with each DOS modeling parameter is evaluated through the course of this analysis.

In order to narrow the scope of the parameter space, it will be assumed that the DOS functions, $N_{\text{v}}(E)$ and $N_{\text{c}}(E)$, and their derivatives, are continuous at the critical energies, E_{vt} and E_{ct}, at which points the square-root and exponential distributions interface, E_{vt} being set to $E_{\text{v}} - \frac{1}{2}\gamma_{\text{v}}$ and E_{ct} being set to $E_{\text{c}} + \frac{1}{2}\gamma_{\text{c}}$. As a result, Eqs. (4.1) and (4.2) reduce to

$$N_{\text{v}}(E) = \begin{cases} N_{\text{vo}}\sqrt{\frac{1}{2}\gamma_{\text{v}}}\exp\left(-\frac{1}{2}\right)\exp\left(\frac{E_{\text{v}}-E}{\gamma_{\text{v}}}\right), & E > E_{\text{v}} - \frac{1}{2}\gamma_{\text{v}} \\ N_{\text{vo}}\sqrt{E_{\text{v}} - E}, & E \leq E_{\text{v}} - \frac{1}{2}\gamma_{\text{v}} \end{cases}, \tag{4.3}$$

and

$$N_{\text{c}}(E) = \begin{cases} N_{\text{co}}\sqrt{E - E_{\text{c}}}, & E \geq E_{\text{c}} + \frac{1}{2}\gamma_{\text{c}} \\ N_{\text{co}}\sqrt{\frac{1}{2}\gamma_{\text{c}}}\exp\left(-\frac{1}{2}\right)\exp\left(\frac{E-E_{\text{c}}}{\gamma_{\text{c}}}\right), & E < E_{\text{c}} + \frac{1}{2}\gamma_{\text{c}} \end{cases}, \tag{4.4}$$

respectively, where the number of DOS modeling parameters has now been reduced by two, i.e., there are now six DOS modeling parameters, $N_{\mathrm{VO}}, N_{\mathrm{CO}}, E_{\mathrm{V}}, E_{\mathrm{C}}, \gamma_{\mathrm{V}}$, and γ_{C}. Eqs. (4.3) and (4.4) lie at the heart of this analysis.

The experimental PECVD a-Si:H DOS data of Jackson *et al.* [49] is depicted in Figures 4.1 and 4.2, Figure 4.1 being cast on a linear scale and Figure 4.2 being cast on a logarithmic scale. While the square-root and exponential regions are clearly in evidence, substantial deviations, that lie beyond the framework of the empirical DOS model used in this analysis, i.e., Eqs. (4.3) and (4.4), are also apparent. It is seen that the intrinsic disorder that is present, i.e., the variations in the bond lengths and bond angles, leads to the presence of exponential tails of electronic states that encroach into the otherwise empty gap region. States that reside deeper within the gap, related to the extrinsic disorder that is present, i.e., defects and dangling bonds, are also seen, especially in Figure 4.2. The model that is used for the DOS functions for the purposes of this analysis, i.e., Eqs. (4.3) and (4.4), does not consider defect states. Deviations from the square-root distributions are also observed, in both the valence band and conduction band DOS functions; they are particularly noticeable in Figure 4.1. These probably arise as a consequence of the finiteness of the bands.

Before fitting Eqs. (4.3) and (4.4) to the PECVD a-Si:H DOS results of Jackson *et al.* [49], a note of caution should be introduced. The experimental data that is presented in Figures 4.1 and 4.2 was obtained through a reading off of the experimental data presented in the figures of Jackson *et al.* [49]; access to the primary data was not possible. Inevitably, distortions will occur in such a process, and as a result, the two data sets will not exactly coincide. Another, perhaps even greater

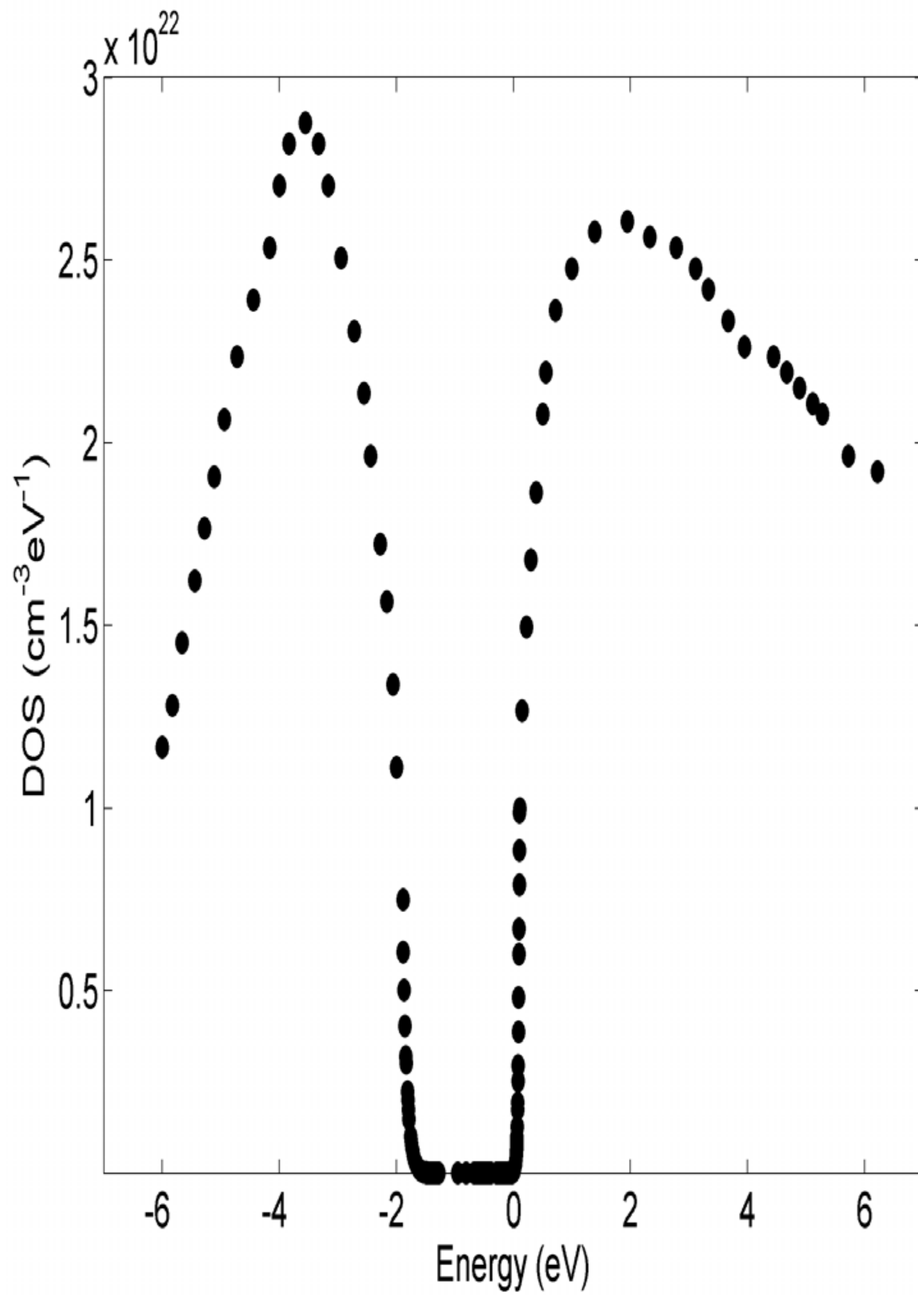

Figure 4.1: The experimental PECVD a-Si:H DOS data of Jackson *et al.* [49]. A linear scale is employed.

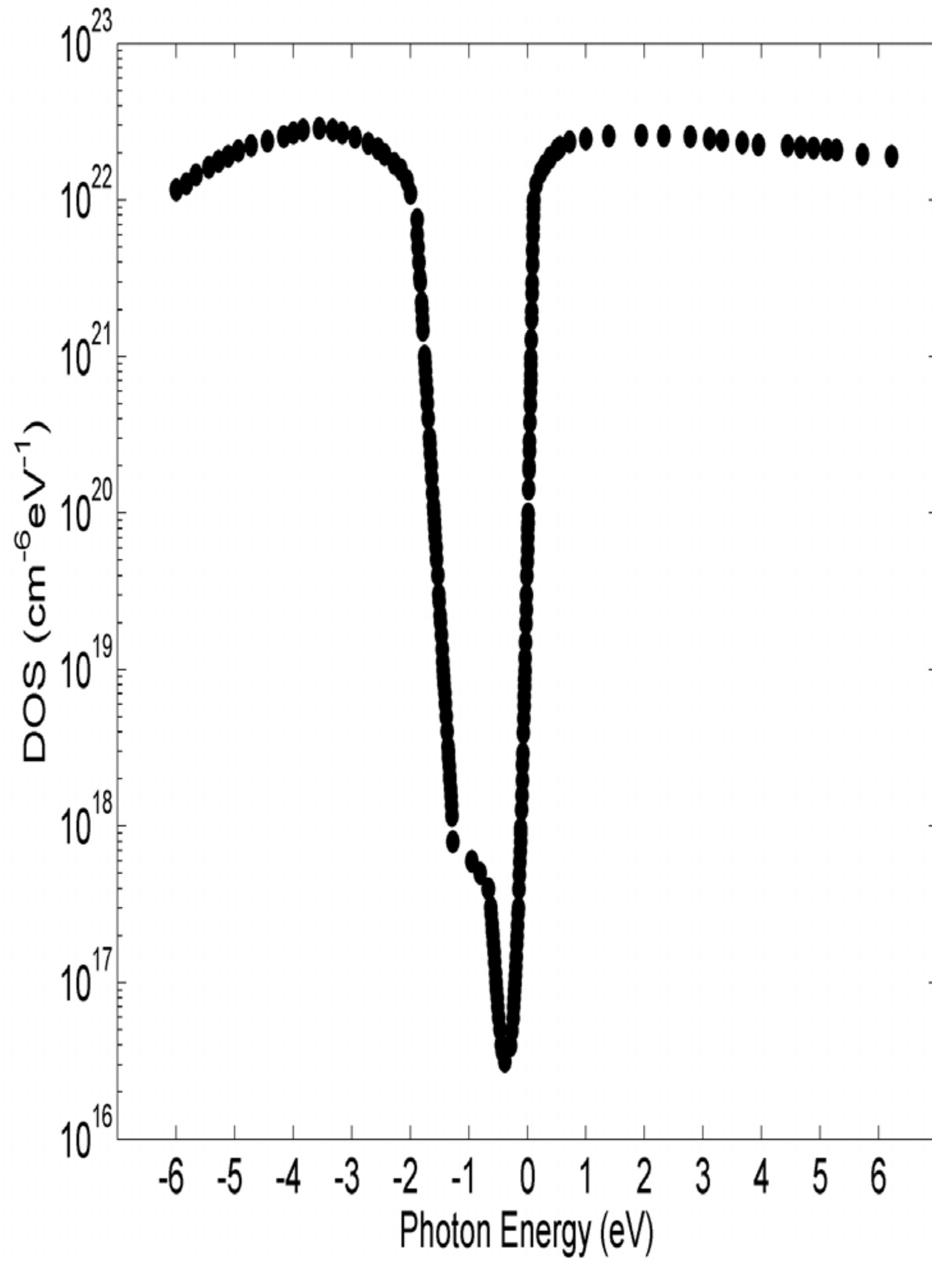

Figure 4.2: The experimental PECVD a-Si:H DOS data of Jackson *et al.* [49]. A logarithmic scale is employed.

challenge, is the fact that these two data sets focus on complementary regions of the DOS functions. The linear scale result, i.e., Figure 4.1, focuses on the bands, the exponential tail being virtually indistinguishable. In contrast, the logarithmic scale result, i.e., Figure 4.2, focuses on the tails, the exact structure of the bands being difficult to ascertain. As a consequence, some disjointness is expected in the DOS modeling parameter selections.

For the initial phase of this DOS analysis, the focus is on determining the DOS modeling parameters corresponding to the bands, i.e., N_{VO}, N_{CO}, E_{V}, and E_{C}. Rather than determining these DOS modeling parameters by directly fitting Eqs. (4.3) and (4.4) to the experimental PECVD a-Si:H DOS data of Jackson *et al.* [49], the tradition in this field is followed and instead linear fits are employed. That is, the determination of the band related DOS modeling parameters, N_{VO}, N_{CO}, E_{V}, and E_{C}, will be performed through a linear least-squares fit of the square of the valence band and conduction band DOS functions to the square of the experimental PECVD a-Si:H DOS data of Jackson *et al.* [49]. Focusing only on the bands, i.e., neglecting the tails, the empirical model for the DOS functions may instead be expressed as

$$N_{\mathrm{V}}(E) = \begin{cases} 0, & E > E_{\mathrm{V}} \\ N_{\mathrm{VO}}\sqrt{E_{\mathrm{V}} - E}, & E \leq E_{\mathrm{V}} \end{cases}, \tag{4.5}$$

and

$$N_{\mathrm{C}}(E) = \begin{cases} N_{\mathrm{CO}}\sqrt{E - E_{\mathrm{C}}}, & E \geq E_{\mathrm{C}} \\ 0, & E < E_{\mathrm{C}} \end{cases}, \tag{4.6}$$

where N_{VO}, N_{CO}, E_{V}, and E_{C} are as previously defined; this simplified model for the DOS functions is introduced for the purposes of enhanced clarity. Noting, from

Eqs. (4.5) and (4.6), that

$$N_{\mathrm{V}}^2(E) = \begin{cases} 0, & E > E_{\mathrm{V}} \\ \\ N_{\mathrm{VO}}^2(E_{\mathrm{V}} - E), & E \leq E_{\mathrm{V}} \end{cases}, \tag{4.7}$$

and that

$$N_{\mathrm{C}}^2(E) = \begin{cases} N_{\mathrm{CO}}^2(E - E_{\mathrm{C}}), & E \geq E_{\mathrm{C}} \\ \\ 0, & E < E_{\mathrm{C}} \end{cases}, \tag{4.8}$$

it is seen that the square-root regions should exhibit a linear dependence on energy when the DOS functions are squared. Thus, a linear least-squares fit of Eqs. (4.7) and (4.8) to the square of the experimental PECVD a-Si:H DOS data of Jackson *et al.* [49], should allow for the determination of the band related DOS modeling parameters, i.e., $N_{\mathrm{VO}}, N_{\mathrm{CO}}, E_{\mathrm{V}}$, and E_{C}, from the results of experiment.

In Figure 4.3, the square of the experimental PECVD a-Si:H DOS data of Jackson *et al.* [49] is plotted as a function of energy; the experimental data depicted in this figure is obtained through squaring the experimental data depicted in Figure 4.1. Linear regions of functional dependence are observed, both in the valence band and in the conduction band. In particular, for the valence band, a linear dependence on energy is observed between -3.0 and -1.75 eV, while for the conduction band, a linear dependence on energy is observed between 0.0 and 0.75 eV. These linear regions are the regions over which Eqs. (4.7) and (4.8) are fit to the square of the experimental data of Jackson *et al.* [49]. Linear least-squares fits over these regions yield $N_{\mathrm{VO}} = (2.39 \pm 0.35) \times 10^{22}$ cm^{-3}eV$^{-3/2}$, $N_{\mathrm{CO}} = (3.03 \pm 0.60) \times 10^{22}$ cm^{-3}eV$^{-3/2}$, $E_{\mathrm{V}} = -1.79 \pm 0.03$ eV, and $E_{\mathrm{C}} = 0.04 \pm 0.04$ eV. These DOS modeling parameter determinations are tabulated in Table 4.1. The fits obtained, using the mean values of these parameter selections, i.e., $N_{\mathrm{VO}} = 2.39 \times 10^{22}$

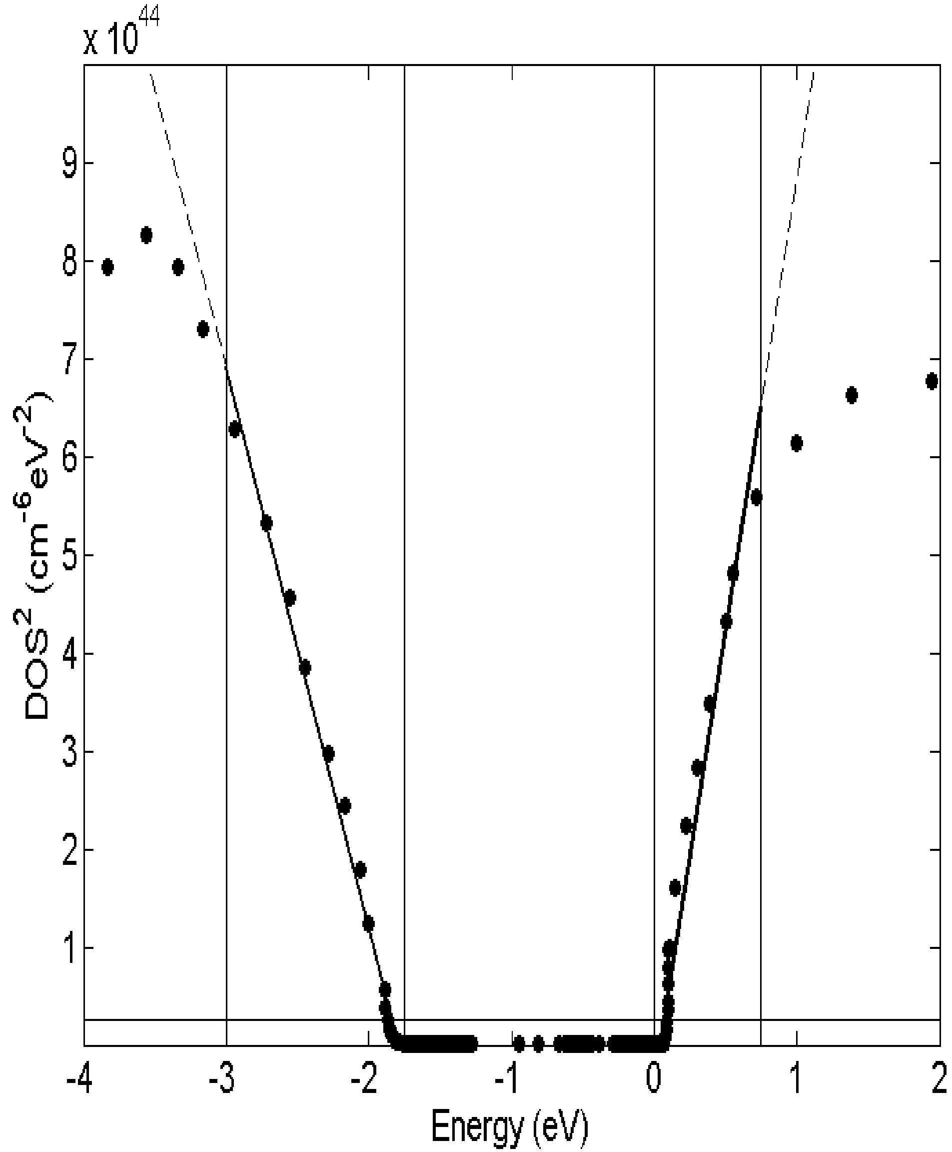

Figure 4.3: The square of the DOS functions corresponding to PECVD a-Si:H. The square of the experimental PECVD a-Si:H DOS data of Jackson *et al.* [49] is depicted with the solid points. The resultant fits, i.e., Eqs. (4.7) and (4.8), for the DOS modeling parameter selections $N_{\mathrm{VO}} = 2.39 \times 10^{22}$ cm^{-3}eV$^{-3/2}$, $N_{\mathrm{CO}} = 3.03 \times 10^{22}$ cm^{-3}eV$^{-3/2}$, $E_{\mathrm{V}} = -1.79$ eV, and $E_{\mathrm{C}} = 0.04$ eV, are clearly shown with the bold solid lines, between energies -3.0 and -1.75 eV for the valence band and between energies 0.0 and 0.75 eV for the conduction band. Extrapolations of these fits are depicted with the dashed lines. These fits were obtained in linear least-squares manners.

Table 4.1: The DOS modeling parameter determinations corresponding to PECVD a-Si:H. These parameters were determined through fits of Eqs. (4.7) and (4.8) to the square of the experimental PECVD a-Si:H DOS data of Jackson *et al* [49]. The values corresponding to γ_{V} and γ_{C} could not be determined.

Parameter (unit)	**Experimental determination**	**Mean value**
N_{VO} (cm^{-3}eV$^{-3/2}$)	$(2.39 \pm 0.35) \times 10^{22}$	2.39×10^{22}
N_{CO} (cm^{-3}eV$^{-3/2}$)	$(3.03 \pm 0.60) \times 10^{22}$	3.03×10^{22}
E_{V} (eV)	-1.79 ± 0.03	-1.79
E_{C} (eV)	0.04 ± 0.04	0.04
γ_{V} (meV)	–	–
γ_{C} (meV)	–	–

cm^{-3}eV$^{-3/2}$, $N_{\mathrm{CO}} = 3.03 \times 10^{22}$ cm^{-3}eV$^{-3/2}$, $E_{\mathrm{V}} = -1.79$ eV, and $E_{\mathrm{C}} = 0.04$ eV, are shown in Figure 4.3.

In Figure 4.4, the experimental PECVD a-Si:H DOS data of Jackson *et al.* [49] is plotted alongside the simplified DOS functions, i.e., Eqs. (4.5) and (4.6), for the specific case of the DOS modeling parameters tabulated in Table 4.1, these being determined from the aforementioned linear least-squares analysis. It is noted that there are substantial deviations from the square-root dependencies beyond these narrow square-root regions. The deviations, which occur below -3.0 eV and above -1.75 eV for the case of the valence band and below 0.0 eV and above 0.75 eV for the case of the conduction band, probably arise as a consequence of the finiteness of the bands, i.e., the electrons within these bands are not truly free [53].

To complete the selection of DOS modeling parameters, the two remaining DOS modeling parameter selections, i.e., the valence band and conduction band tail breadths, γ_{V} and γ_{C}, must be determined. This is done through a fit of the empirical expressions for the valence band and conduction band DOS functions,

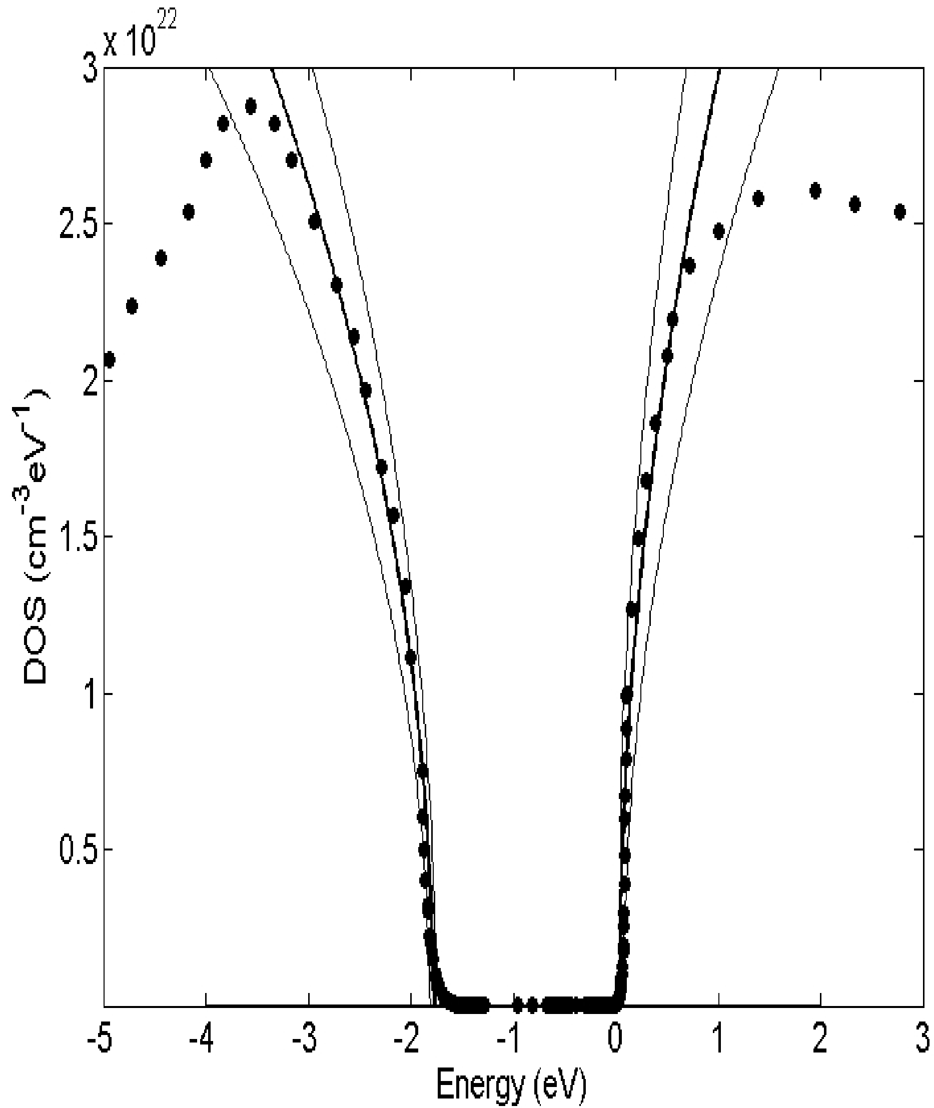

Figure 4.4: The experimental PECVD a-Si:H DOS data of Jackson *et al.* [49] and the fits of this data to Eqs. (4.5) and (4.6) for the DOS modeling parameter selections tabulated in Table 4.1. The experimental data points are depicted with the solid points. The fits are depicted with the bold solid lines. The light solid lines correspond to the upper and lower DOS prefactor selections specified in Table 4.1. This plot is cast on a linear scale.

i.e., Eqs. (4.3) and (4.4), to the experimental PECVD a-Si:H DOS data of Jackson *et al.* [49] over the exponential regions. As was mentioned earlier, these regions are barely observable using the linear scale, and thus, the logarithmic scale experimental data must be employed instead. Rather than focusing on the band regions, these fittings focus on the exponential tail regions associated with Eqs. (4.3) and (4.4). These fits, once again, are performed in a linear least-squares sense, and are shown in Figure 4.5. From this analysis, the breadth of the valence band tail and the breadth of the conduction band tail, γ_{V} and γ_{C}, respectively, are found to be $\gamma_{\mathrm{V}} = 68.7 \pm 1.00$ meV and $\gamma_{\mathrm{C}} = 19.8 \pm 0.30$ meV. These tail breadths are determined from the slopes of the fitting lines depicted in Figure 4.5.

A line is defined by its slope and its intercept. The fitting lines depicted in Figure 4.5 correspond to Eqs. (4.3) and (4.4) in their exponential tail regions, i.e.,

$$\ln\left(N_{\mathrm{V}}(E)\right) = \ln\left(N_{\mathrm{VO}}\sqrt{\frac{1}{2}\gamma_{\mathrm{V}}}\right) - \frac{1}{2} + \frac{E_{\mathrm{V}}}{\gamma_{\mathrm{V}}} - \frac{E}{\gamma_{\mathrm{V}}}, \tag{4.9}$$

and

$$\ln\left(N_{\mathrm{C}}(E)\right) = \ln\left(N_{\mathrm{CO}}\sqrt{\frac{1}{2}\gamma_{\mathrm{C}}}\right) - \frac{1}{2} - \frac{E_{\mathrm{C}}}{\gamma_{\mathrm{C}}} + \frac{E}{\gamma_{\mathrm{C}}}. \tag{4.10}$$

The line intercepts are determined by the DOS prefactors, the band edge parameters, and the tail breadth parameters. If one chooses to use the previously determined DOS modeling parameters, i.e., those tabulated in Table 4.1, as seed values, then there are two possible sets of parameter selections. Assuming that N_{VO} and N_{CO} are as prescribed in Table 4.1, the fits depicted in Figure 4.5 correspond to $E_{\mathrm{V}} = -1.83$ eV and $E_{\mathrm{C}} = 0.07$ eV. The corresponding complete set of DOS modeling parameters is depicted in Table 4.2. Alternatively, if E_{V} and E_{C} are as prescribed in Table 4.1, the fits depicted in Figure 4.5 correspond to

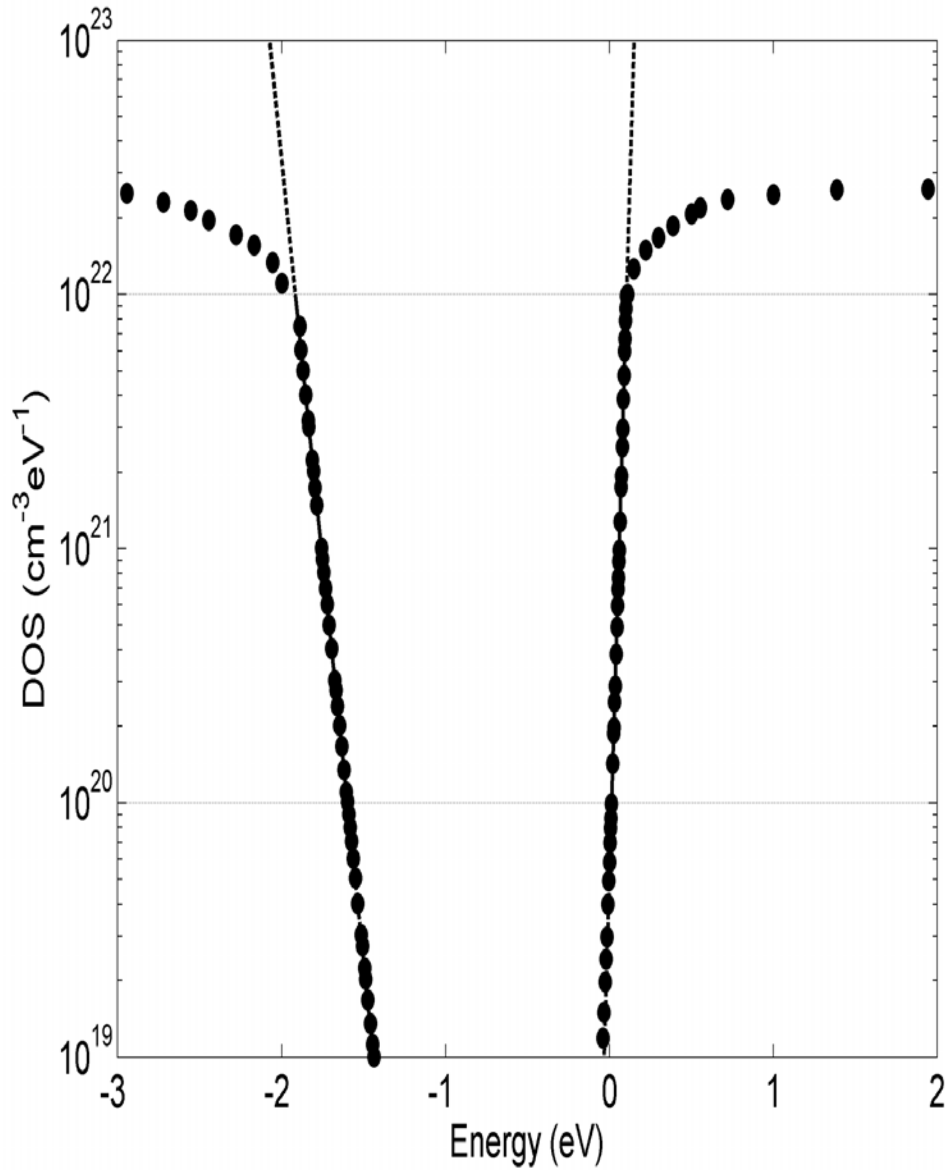

Figure 4.5: The DOS functions corresponding to PECVD a-Si:H. The experimental PECVD a-Si:H DOS data of Jackson *et al.* [49] is depicted with the solid points. The resultant exponential fits are shown with the solid lines over the regions over which these fits were determined. Extrapolations of these fits are depicted with the dashed lines. These fits were obtained in linear least-squares manners.

Table 4.2: The DOS modeling parameter determinations corresponding to PECVD a-Si:H. These parameters were determined through fits of Eqs. (4.3) and (4.4) to the PECVD a-Si:H DOS data of Jackson *et al.* [49] over the exponential regions. The first set of DOS modeling parameter selections is determined by setting N_{VO} and N_{CO} to the values set in Table 4.1. The second set of DOS modeling parameter selections is determined by setting E_{V} and E_{C} to the values set in Table 4.1

.

Parameter (unit)	**Experimental determination**	**Parameter selection 1**	**Parameter selection 2**
N_{VO} (cm^{-3}eV$^{-3/2}$)	–	2.39×10^{22}	1.39×10^{22}
N_{CO} (cm^{-3}eV$^{-3/2}$)	–	3.03×10^{22}	6.58×10^{21}
E_{V} (eV)	–	-1.83	-1.79
E_{C} (eV)	–	0.07	0.04
γ_{V} (meV)	68.7 ± 1.00	68.7	68.7
γ_{C} (meV)	19.8 ± 0.30	19.8	19.8

$N_{\mathrm{VO}} = 1.39 \times 10^{22}$ cm^{-3}eV$^{-3/2}$ and $N_{\mathrm{CO}} = 6.58 \times 10^{21}$ cm^{-3}eV$^{-3/2}$. The corresponding complete set of DOS modeling parameters is also depicted in Table 4.2. It is found that former DOS modeling parameter selections lead to a more satisfactory overall fit, as may be seen in Figure 4.6.

It is noted that the determination of the DOS prefactors, N_{VO} and N_{CO}, from selections of the band edges, E_{V} and E_{C}, is extremely sensitive to variations in E_{V} and E_{C}, as was seen in Figure 4.6. This sensitivity arises as it is not possible to determine the onset of the transition to the square-root bands only from knowledge of the exponential regions; recall that the fits shown in Figure 4.5 correspond only to the exponential regions. While the DOS modeling parameter selections introduced here have used the results obtained from the linear fits as seed values for the purposes of these logarithmic fits, other DOS modeling parameter selections could also be used for the logarithmic fits. This is because the intercepts corresponding

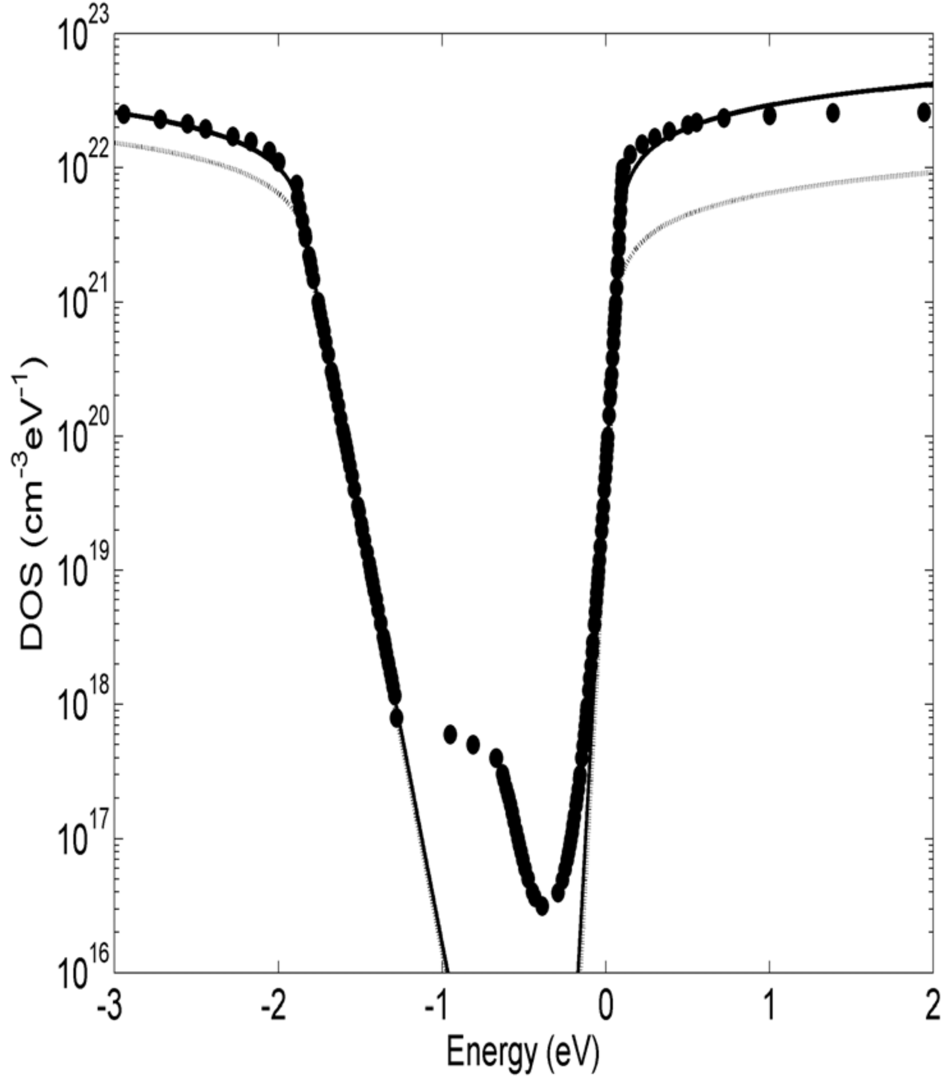

Figure 4.6: The DOS functions associated with PECVD a-Si:H. The experimental PECVD a-Si:H DOS results of Jackson *et al.* [49] are depicted with the solid points. The fits of Eqs. (4.3) and (4.4) to this experimental data are shown with the lines. For the first set of DOS modeling parameter selections provided in Table 4.2, the corresponding fits are shown with the heavy solid lines. For the second set of DOS modeling parameter selections provided in Table 4.2, the corresponding fits are shown with dotted lines. This plot is cast on a logarithmic scale.

to Eqs. (4.9) and (4.10) are determined by $N_{\mathrm{VO}}, E_{\mathrm{V}}$, and γ_{V}, and $N_{\mathrm{CO}}, E_{\mathrm{C}}$, and γ_{C}, respectively.

A reconciliation of these disjoint DOS modeling parameter selections may be possible if a more sophisticated model for these DOS functions is employed. Eqs. (4.3) and (4.4) may be oversimplified, and perhaps do not exactly represent the distribution of electronic states associated with this complex material. Further study would be required in order to draw any more definitive conclusions, however.

4.3 DOS modeling parameter selections for subsequent analysis

It should be pointed out that the experimental PECVD a-Si:H DOS data of Jackson *et al.* [49] corresponds to a particular sample of this material. Amorphous semiconductors, such as PECVD a-Si:H, are expected to exhibit sample-to-sample variations. These variations are likely to influence the DOS modeling parameters. Unfortunately, as Jackson *et al.* [49] appear to be the only researchers that have experimentally determined the valence band and conduction band DOS functions associated with PECVD a-Si:H, there is no way to directly assess the magnitude of the sample-to-sample variations in the DOS modeling parameters corresponding to this material. Tables 4.1 and 4.2 should thus be viewed as providing DOS modeling parameters that are representative of PECVD a-Si:H, rather to tabulating a unique set of values corresponding to all forms of this material.

A variety of indirect determinations of these DOS modeling parameters have been performed. Jiao *et al.* [44], for example, in the course of performing an analysis on the spectral dependence of the imaginary part of the dielectric function, $\epsilon_2(\hbar\omega)$, suggest that the square-root PECVD a-Si:H DOS bands are symmetric.

As a result, they find that the DOS prefactors, N_{VO} and N_{CO}, are equal. As a result of their analysis, Jiao *et al.* [44] conclude that $N_{\mathrm{VO}} = N_{\mathrm{CO}} = 2.2 \times 10^{22}$ cm^{-3}eV$^{-3/2}$. Later, O'Leary [46], in fitting an analytical expression for the JDOS function to experimental PECVD a-Si:H JDOS results corresponding to Jackson *et al.* [49], instead conclude that $N_{\mathrm{VO}} = N_{\mathrm{CO}} = 2.38 \times 10^{22}$ cm^{-3}eV$^{-3/2}$. It is noted that these results are of the same order of magnitude as the values found in Tables 4.1 and 4.2.

For a sample of device quality PECVD a-Si:H, Tiedje *et al.* [41] found that $\gamma_{\mathrm{V}} = 43$ meV and $\gamma_{\mathrm{C}} = 27$ meV. The tail breadth parameters corresponding to PECVD a-Si:H are known to vary, however, these variations corresponding to changes in the amount of disorder that is present. Experimentalists have reported variations in γ_{V}, between 43 and 103 meV, and variations in γ_{C}, between 20 and 43 meV [22]. In fact, Sherman *et al.* [22] provided experimental evidence for the existence of a correlation between the valence band tail and conduction band tail breadths, γ_{V} and γ_{C}, respectively, for the case of PECVD a-Si:H. In Figure 4.7, the experimental data of Sherman *et al.* [22] is depicted, along with the corresponding error bars. A linear least-squares fit to this experimental data, which is determined to be

$$\gamma_{\mathrm{v}}\ (\mathrm{meV}) = 0.765\gamma_{\mathrm{c}}\ (\mathrm{meV}) + 31.3, \tag{4.11}$$

is also indicated in Figure 4.7. The values determined by Tiedje *et al.* [41] are also depicted on this figure, although these values are not included in the determination of Eq. (4.11) owing to differences in the manner by which these experimental determinations were obtained; the error associated with the experimental data point of Tiedje *et al.* [41] is unknown, as the errors were not reported by Tiedje *et*

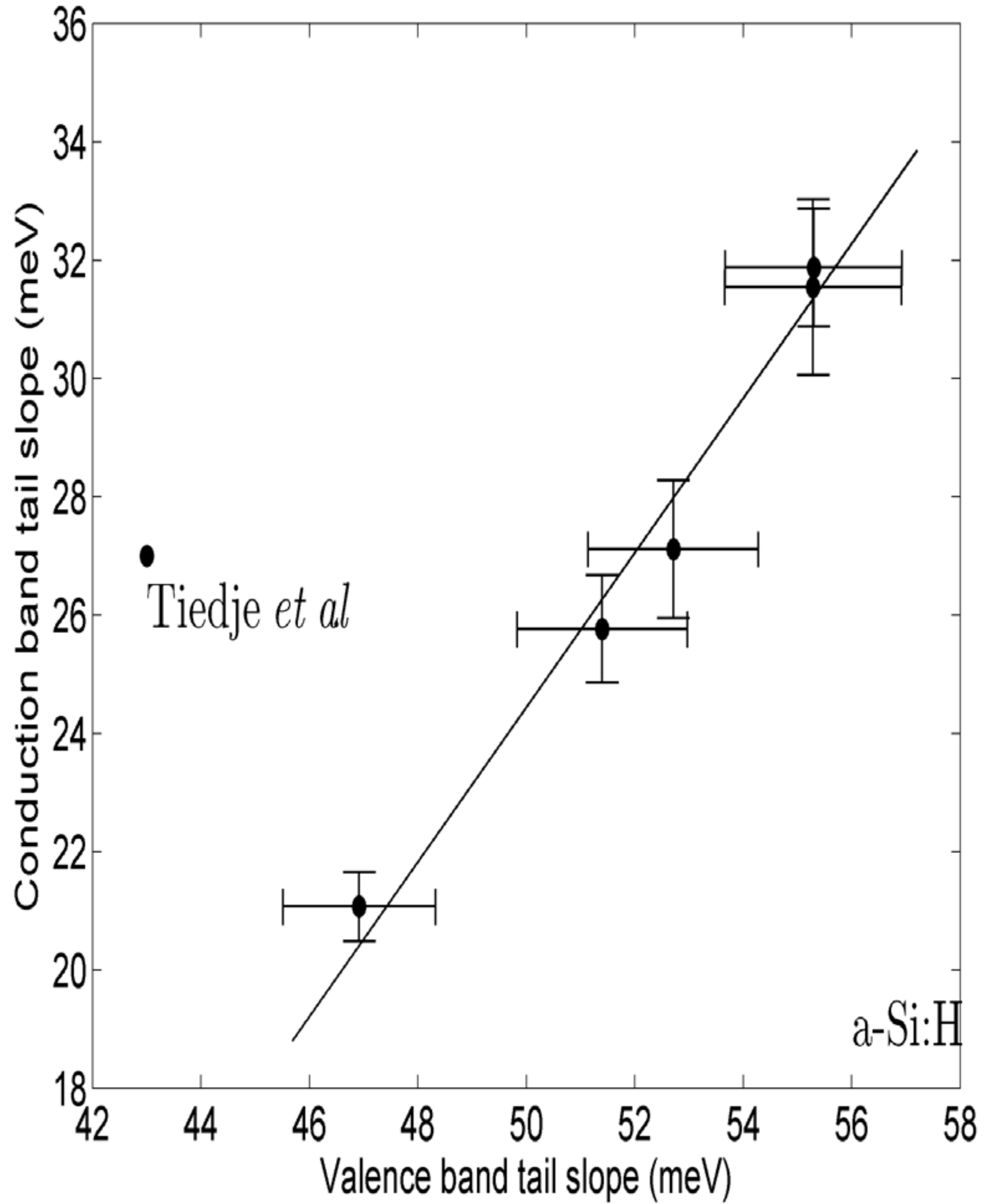

Figure 4.7: The correlation between the conduction band tail breadth and the valence band tail breadth. The line shows the resultant linear least-squares fit. The experimental data associated with the line is from Sherman *et al.* [22]. The other experimental data point is from Tiedje *et al.* [41]. This figure is after Sherman *et al.* [22].

al. [41]. The variations associated with γ_V that were found by Sherman *et al.* [22] are of the order of 3 meV while those associated with γ_C are of the order of 4 meV.

In order to simplify matters, symmetric square-root DOS functions will be used for the subsequent analysis for all cases. As the focus of this analysis is on the evaluation of the JDOS function, the symmetric DOS prefactor selections of O'Leary [46] are adopted; as was mentioned earlier, these DOS prefactor selections of O'Leary [46], $N_{VO} = N_{CO} = 2.38 \times 10^{22}$ cm^{-3}eV$^{-3/2}$, were determined so that the resultant JDOS function reproduces the experimental PECVD a-Si:H JDOS of Jackson *et al.* [49]. The energy gap value that is selected, i.e., the difference in energy between the valence band and conduction band band edges, E_V and E_C, respectively, is set to the value obtained by O'Leary [46] for all cases, 1.68 eV; once again, this value was determined through a fit with the PECVD a-Si:H JDOS result of Jackson *et al.* [49]. In terms of the valence band and conduction band tail breadths, two possible selections are made. For set tail breadth parameters, the values of Tiedje *et al.* [41] are adopted, i.e., $\gamma_V = 43$ meV and $\gamma_C = 27$ meV. When the impact of disorder is considered, however, i.e., how the evaluations change as the disorder is varied, the linear relationship of Sherman *et al.* [22], i.e., Eq. (4.11), is employed. These two sets of DOS modeling parameters are tabulated in Tables 4.3 and 4.4.

4.4 JDOS evaluation for PECVD a-Si:H

With a set of DOS modeling parameters for PECVD a-Si:H now established, i.e., Table 4.3, the JDOS function may now be evaluated. The JDOS function provides a measure of the number of possible optical transitions that can occur

Table 4.3: The DOS modeling parameters for fixed band tail breadths. All of the DOS modeling parameters are from O'Leary [46].

Parameter (unit)	**Value**
N_{VO} ($\mathrm{cm}^{-3}\mathrm{eV}^{-3/2}$)	2.38×10^{22}
N_{CO} ($\mathrm{cm}^{-3}\mathrm{eV}^{-3/2}$)	2.38×10^{22}
E_{V} (eV)	0
E_{C} (eV)	1.68
γ_{V} (meV)	43
γ_{C} (meV)	27

at a given photon energy, and as such, is an important determinant of the optical properties; recall Eq. (3.12). In Figure 4.8, the JDOS function corresponding to PECVD a-Si:H is computed, the DOS modeling parameter selections tabulated in Table 4.3 being used for the purposes of this analysis. The PECVD a-Si:H JDOS results that were determined by Jackson *et al.* [49] are also depicted. It is seen that the form of this calculated JDOS function is very similar to that obtained by Jackson *et al.* [49]. In particular, it is seen that the obtained JDOS results are essentially coincident with that obtained by Jackson *et al.* [49], except for $\hbar\omega <$ 1.4 eV and $\hbar\omega >$ 5.0 eV. The deviations that are found for $\hbar\omega <$ 1.4 eV are believed to be attributable to the presence of defect states, these not being taken into account in the empirical DOS functions, i.e., Eqs. (4.3) and (4.4). The deviations that are found for $\hbar\omega >$ 5.0 eV are believed to be attributable to deviations from the square-root distributions in the DOS functions; these deviations were seen previously in Figure 4.4.

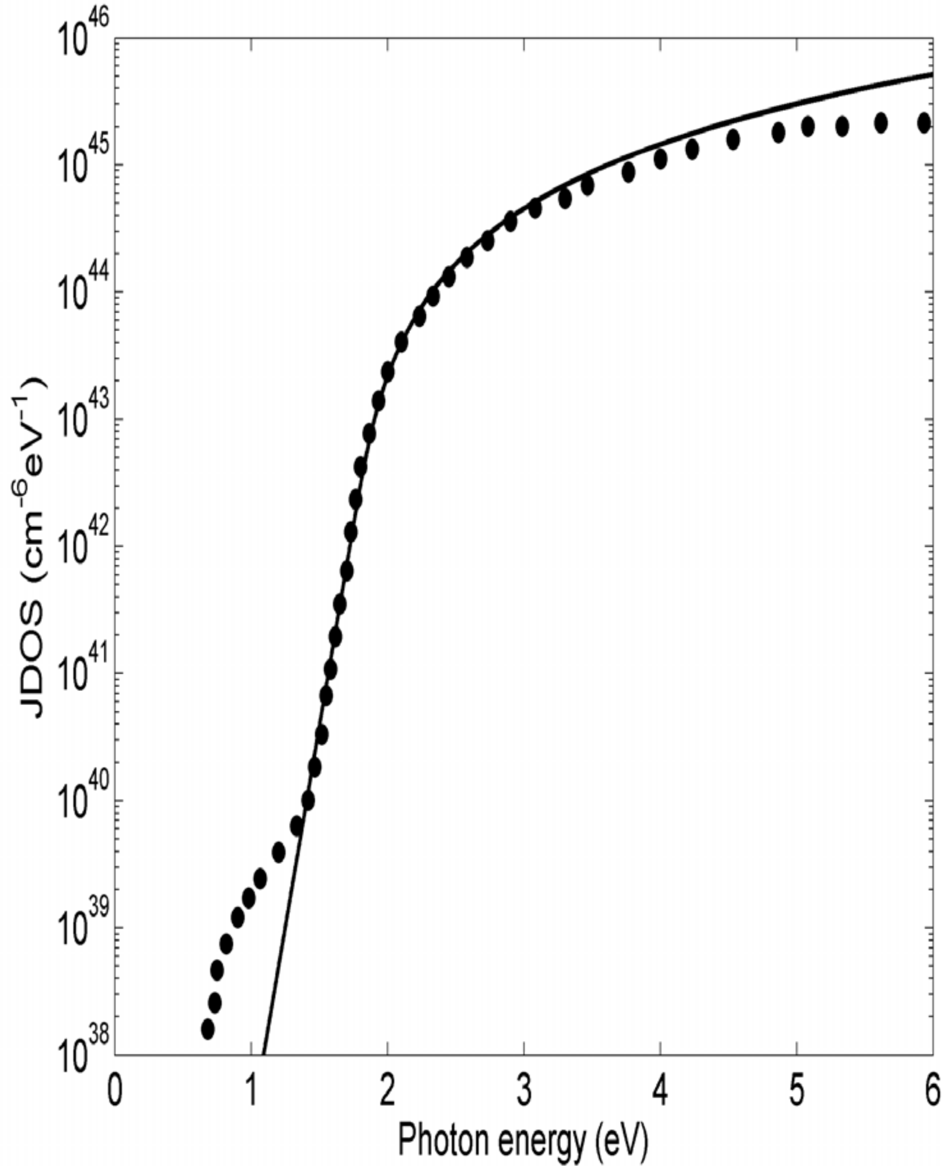

Figure 4.8: The JDOS function corresponding to a-Si:H. The experimental JDOS result of Jackson *et al.* [49] is depicted with solid points. The fit obtained is indicated with the solid line. It is seen that there is almost complete agreement, except for $\hbar\omega < 1.4$ eV, at which point defect absorption dramatically alters the character of the JDOS function, and for $\hbar\omega > 5$ eV, at which point the non-parabolically of the VBB and CBB distributions distorts the resultant JDOS function. Both of these effects are beyond the framework of the present analysis. The parameters used for this fitting are tabulated in Table 4.3.

Table 4.4: The DOS modeling parameters for varying tail breadths. All of the other DOS modeling parameters are from O'Leary [46].

Parameter (unit)	**Value**
N_{VO} (cm^{-3}eV$^{-3/2}$)	2.38×10^{22}
N_{CO} (cm^{-3}eV$^{-3/2}$)	2.38×10^{22}
E_{V} (eV)	0
E_{C} (eV)	1.68
γ_{V} (meV)	Eq. (4.11)
γ_{C} (meV)	Eq. (4.11)

4.5 Evaluation of n_{vloc} and n_{cloc} for PECVD a-Si:H

In order to relate the optical properties of PECVD a-Si:H with the density of localized valence band and conduction band electronic states, n_{vloc} and n_{cloc}, these densities must be evaluated. In this analysis, how these densities vary with the conduction band tail breadth, γ_{C}, will be determined, the tail breadth parameter providing a measure of the amount of disorder that is present; greater disorder corresponds to larger values of γ_{V} and γ_{C}. For the purposes of this PECVD a-Si:H analysis, the DOS modeling parameters are set to their nominal values assigned in Table 4.4. E_{vt} and E_{ct} are selected so that the DOS functions, and their derivatives, are continuous functions of energy, i.e., $E_{\mathrm{vt}} = E_{\mathrm{V}} - \frac{1}{2}\gamma_{\mathrm{V}}$ and $E_{\mathrm{ct}} = E_{\mathrm{C}} + \frac{1}{2}\gamma_{\mathrm{C}}$ [45]. The valence band and conduction band mobility edges, $E_{\mathrm{V}\mu}$ and $E_{\mathrm{C}\mu}$, are assumed to be coincident with E_{vt} and E_{ct}, respectively. Finally, γ_{V} and γ_{C} are assumed to be related in accordance with the linear least-squares relationship depicted in Figure 4.7, i.e., Eq. (4.11). The DOS modeling parameter selections, employed for the specific purposes of this PECVD a-Si:H analysis, are tabulated in Table 4.5, most of these parameters being from Table 4.4.

Table 4.5: The PECVD a-Si:H DOS modeling parameter selections used for the purposes of this analysis. The relationship between the valence band and conduction band tail breadths, γ_{V} and γ_{C}, is as described in Eq. (4.11). These modeling parameters were found through a fit with the PECVD a-Si:H JDOS experimental results of Jackson *et al.* [49]. Most of these DOS modeling parameter selections are from Table 4.4.

Conduction band		**Valence band**	
Parameter	**Value**	**Parameter**	**Value**
N_{CO}	2.38×10^{22} (cm^{-3}eV$^{-3/2}$)	N_{VO}	2.38×10^{22} (cm^{-3}eV$^{-3/2}$)
E_{C}	1.68 (eV)	E_{V}	0.0 (eV)
E_{ct}	$E_{\mathrm{C}} + \frac{1}{2}\gamma_{\mathrm{C}}$	E_{vt}	$E_{\mathrm{V}} - \frac{1}{2}\gamma_{\mathrm{V}}$
$E_{\mathrm{C}\mu}$	E_{ct}	$E_{\mathrm{V}\mu}$	E_{vt}

The total densities of VBL and CBL electronic states, n_{VBL} and n_{CBL}, respectively, are evaluated. In Figure 4.9, n_{VBL} and n_{CBL} are plotted as functions of the conduction band tail breadth, γ_{C}, the valence band tail breadth, γ_{V}, being determined from γ_{C}, i.e., through Eq. (4.11). It is seen that n_{VBL} exceeds n_{CBL}, by a considerable margin, for the range of γ_{C} considered. This is due to the fact that γ_{V} is greater than γ_{C} for the range of γ_{C} considered. Clearly, the greater the amount of disorder, i.e., the greater γ_{V} and γ_{C}, the larger the total densities of VBL and CBL electronic states. This is primarily due to the fact that the valence band mobility edge, $E_{\mathrm{V}\mu} = E_{\mathrm{V}} - \frac{1}{2}\gamma_{\mathrm{V}}$, decreases in response to increases in γ_{V}, thereby increasing the total density of VBL electronic states (recall Figure 2.17) and that the conduction band mobility edge, $E_{\mathrm{C}\mu} = E_{\mathrm{C}} + \frac{1}{2}\gamma_{\mathrm{C}}$, increases in response to increases in γ_{C}, thereby increasing the total density of CBL electronic states (recall Figure 2.18).

It should be noted that the range of γ_{C} considered in this analysis exceeds the range expected for PECVD a-Si:H; Sherman *et al.* [22] reported values of γ_{C}

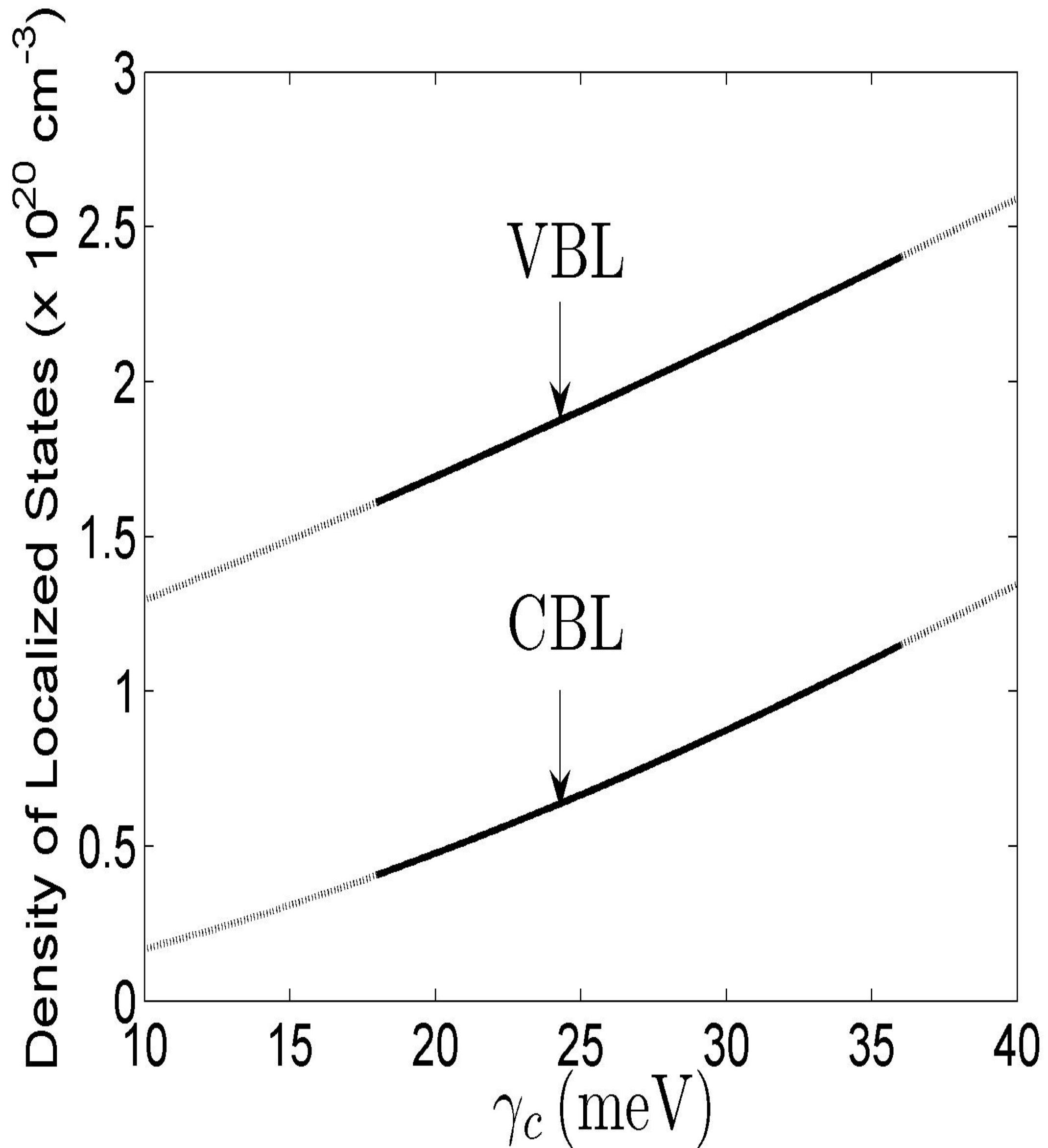

Figure 4.9: The dependence of the total densities of VBL and CBL electronic states, n_{VBL} and n_{CBL}, respectively, on the conduction band tail breadth, γ_{C}, for the case of PECVD a-Si:H. γ_{V} is determined assuming the validity of the linear least-squares fit relationship between γ_{V} and γ_{C}, i.e., Eq. (4.11). All DOS modeling parameters are set to their PECVD a-Si:H values, i.e., the values set in Table 4.5. Results corresponding to the range of γ_{C} specified in Figure 4.7 are indicated with the solid lines. Results beyond this range are indicated with dotted lines.

between 20 and 32 meV for the case of PECVD a-Si:H. This is done in order to amplify the differences between the low γ_{C} and high γ_{C} results. It should be pointed out that there are other types of disordered semiconductors, such as amorphous selenium, that are characterized with valence band and conduction band tail breadths that are narrower than that associated with PECVD a-Si:H [54], so the low γ_{C} results may be viewed as being representative of such cases; in selenium, tails as narrow as 10 meV have been reported.

4.6 Evaluation of the JDOS contributions corresponding to PECVD a-Si:H

With the PECVD a-Si:H DOS modeling parameters determined, the contributions to the JDOS function corresponding to the various types of optical transitions are determined. This analysis is performed for both narrow band tails and broad band tails, this covering the range of values expected for amorphous semiconductors. The DOS modeling parameter selections, specified in Table 4.5, are employed for the purposes of this analysis. In Figure 4.10, the PECVD a-Si:H JDOS functions, $J(\hbar\omega)$, $J_{\text{VBE-CBE}}(\hbar\omega)$, $J_{\text{VBE-CBL}}(\hbar\omega)$, $J_{\text{VBL-CBE}}(\hbar\omega)$, and $J_{\text{VBL-CBL}}(\hbar\omega)$, are plotted as functions of $\hbar\omega$ for the specific case of $\gamma_{\mathrm{C}} = 10$ meV, γ_{V} being determined from Eq. (4.11); all other DOS modeling parameters are set to their PECVD a-Si:H values, i.e., the values set in Table 4.5. As with Figure 3.17, it is noted that $J_{\text{VBE-CBE}}(\hbar\omega) = 0$ for $\hbar\omega < E_{\mathrm{C}\mu} - E_{\mathrm{V}\mu}$ and that $J_{\text{VBL-CBL}}(\hbar\omega) = 0$ for $\hbar\omega \geq E_{\mathrm{C}\mu} - E_{\mathrm{V}\mu}$. In addition, it is seen that $J(\hbar\omega)$, $J_{\text{VBE-CBE}}(\hbar\omega)$, $J_{\text{VBE-CBL}}(\hbar\omega)$, and $J_{\text{VBL-CBE}}(\hbar\omega)$, all monotonically increase in response to increases in $\hbar\omega$; $J_{\text{VBE-CBL}}(\hbar\omega)$ and $J_{\text{VBL-CBE}}(\hbar\omega)$ are no longer coinci-

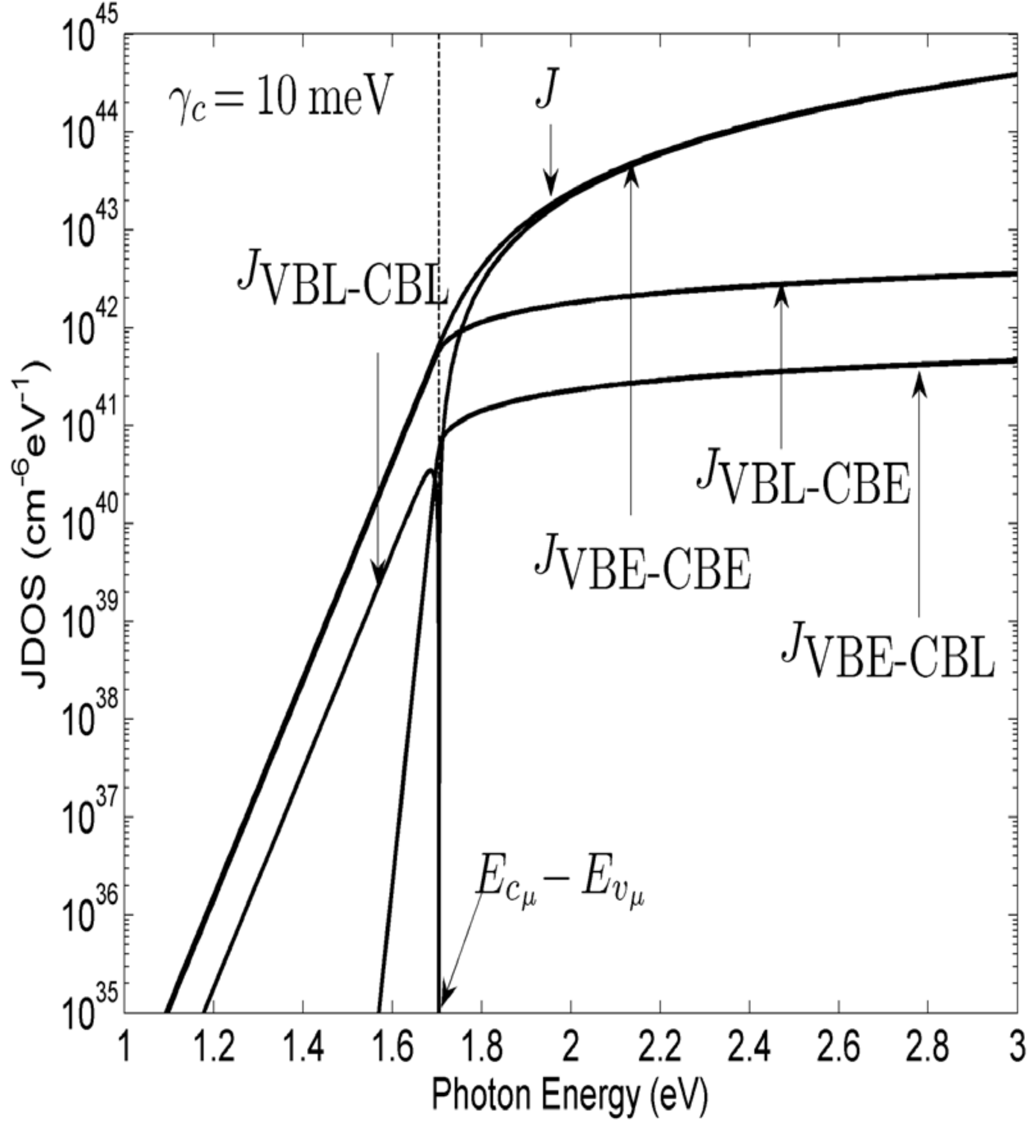

Figure 4.10: The contributions to the JDOS function corresponding to the VBE-CBE, VBE-CBL, VBL-CBE, and VBL-CBL optical transitions, i.e., $J_{\text{VBE-CBE}}$, $J_{\text{VBE-CBL}}$, $J_{\text{VBL-CBE}}$ and $J_{\text{VBL-CBL}}$, as functions of the photon energy, $\hbar\omega$, for PECVD a-Si:H. The overall JDOS function, J, is also plotted as a function of the photon energy, $\hbar\omega$. The PECVD a-Si:H DOS modeling parameter selections, used for the purposes of this analysis, are tabulated in Table 4.5.

dent, however, as there are now asymmetries in the PECVD a-Si:H DOS modeling parameter selections, i.e., recall Table 4.5. As with Figure 3.17, $J_{\text{VBL-CBL}}(\hbar\omega)$ initially increases monotonically in response to increases in $\hbar\omega$, achieving a maximum at a certain value of $\hbar\omega$, and then diminishing to zero at the mobility gap, i.e., when $\hbar\omega = E_{\text{C}\mu} - E_{\text{V}\mu}$. It is noted that the breadth of the tails in the JDOS functions, $J_{\text{VBL-CBE}}(\hbar\omega)$ and $J_{\text{VBL-CBL}}(\hbar\omega)$, are determined by the breadth of the valence band tail, γ_{V}, while that associated with $J_{\text{VBE-CBL}}(\hbar\omega)$ is determined by the breadth of the conduction band tail, γ_{C}; the overall JDOS function's tail breadth is determined by the largest of γ_{V} and γ_{C} [45], γ_{V} being the dominant tail breadth for the case of PECVD a-Si:H, the tail breadths associated with $J_{\text{VBE-CBL}}(\hbar\omega)$ and $J_{\text{VBL-CBE}}(\hbar\omega)$ being determined by which distribution of localized electronic states is involved, the tail breadth associated with $J_{\text{VBL-CBL}}(\hbar\omega)$ being determined by the largest of γ_{V} and γ_{C}, γ_{V} being the dominant tail breadth for the case of PECVD a-Si:H.

In Figure 4.11, the PECVD a-Si:H JDOS fractions, $\frac{J_{\text{VBE-CBE}}(\hbar\omega)}{J(\hbar\omega)}$, $\frac{J_{\text{VBE-CBL}}(\hbar\omega)}{J(\hbar\omega)}$, $\frac{J_{\text{VBL-CBE}}(\hbar\omega)}{J(\hbar\omega)}$, and $\frac{J_{\text{VBL-CBL}}(\hbar\omega)}{J(\hbar\omega)}$, are plotted as functions of $\hbar\omega$ for the case of $\gamma_{\text{C}} =$ 10 meV, γ_{V} being determined from Eq. (4.11); all other DOS modeling parameters are set to their PECVD a-Si:H values, i.e., the values set in Table 4.5. While $\frac{J_{\text{VBE-CBE}}(\hbar\omega)}{J(\hbar\omega)}$ monotonically increases from 0 as $\hbar\omega$ increases from the mobility gap, i.e., $E_{\text{C}\mu} - E_{\text{V}\mu}$, and $\frac{J_{\text{VBL-CBL}}(\hbar\omega)}{J(\hbar\omega)}$ monotonically increases from 0 as $\hbar\omega$ decreases from the mobility gap, i.e., $E_{\text{C}\mu} - E_{\text{V}\mu}$, the other fractional JDOS functions, $\frac{J_{\text{VBE-CBL}}(\hbar\omega)}{J(\hbar\omega)}$ and $\frac{J_{\text{VBL-CBE}}(\hbar\omega)}{J(\hbar\omega)}$, achieve their maxima exactly at the mobility gap, i.e., when $\hbar\omega = E_{\text{C}\mu} - E_{\text{V}\mu}$. It is noted that while $\frac{J_{\text{VBE-CBE}}(\hbar\omega)}{J(\hbar\omega)}$ asymptotically approaches unity as $\hbar\omega$ approaches high values of $\hbar\omega$, as was seen in Figure 3.18,

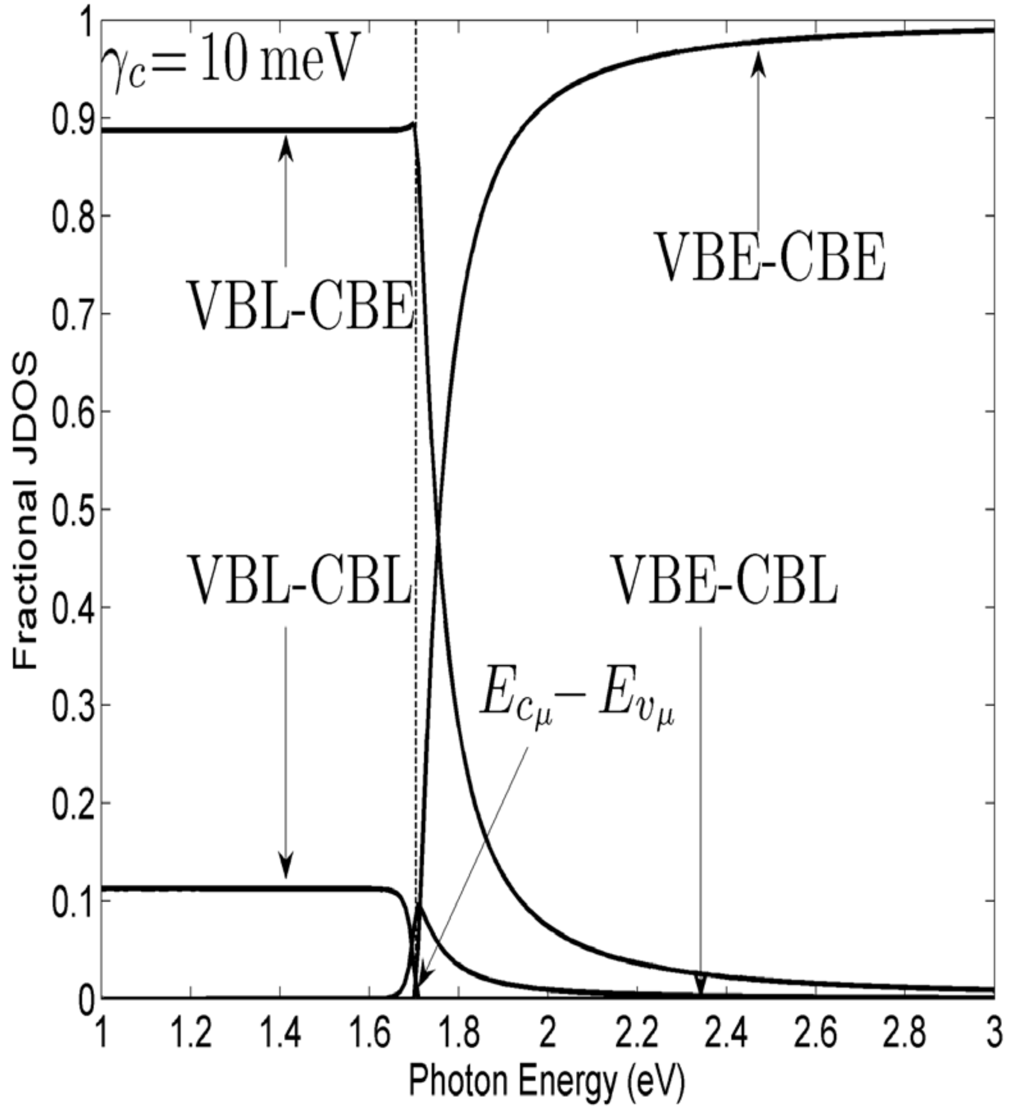

Figure 4.11: The fractional contributions to the JDOS function corresponding to the VBE-CBE, VBE-CBL, VBL-CBE, and VBL-CBL optical transitions, i.e., $\frac{J_{\text{VBE-CBE}}}{J}$, $\frac{J_{\text{VBE-CBL}}}{J}$, $\frac{J_{\text{VBL-CBE}}}{J}$ and $\frac{J_{\text{VBL-CBL}}}{J}$, as functions of the photon energy, $\hbar\omega$, for γ_{C} set to 10 meV. γ_{V} is determined using the linear least-squares fit relationship between γ_{V} and γ_{C}, i.e., Eq. (4.11). All DOS modeling parameters are set to their PECVD a-Si:H values, i.e., the values set in Table 4.5.

$\frac{J_{\text{VBL-CBL}}(\hbar\omega)}{J(\hbar\omega)}$ instead approaches 0.11 as $\hbar\omega$ approaches low values; in Figure 3.18 instead $\frac{J_{\text{VBL-CBL}}(\hbar\omega)}{J_(\hbar\omega)}$ approached unity. $\frac{J_{\text{VBL-CBE}}(\hbar\omega)}{J(\hbar\omega)}$, which asymptotically approached zero as $\hbar\omega$ approached low values for symmetric DOS modeling parameter selections, approaches the value of 0.89 for the case of $\gamma_{\text{C}} = 10$ meV. $\frac{J_{\text{VBE-CBL}}(\hbar\omega)}{J(\hbar\omega)}$ on the other hand, exhibits a behavior similar to that found in Figure 3.18, i.e., it asymptotically approaches zero for both high values of $\hbar\omega$ and low values of $\hbar\omega$. A detailed analysis indicates that this effect is due to the fact that γ_{V} exceeds γ_{C}, leading to a greater total density of VBL electronic states than CBL electronic states.

In Figure 4.12, the PECVD a-Si:H JDOS functions, $J(\hbar\omega)$, $J_{\text{VBE-CBE}}(\hbar\omega)$, $J_{\text{VBE-CBL}}(\hbar\omega)$, $J_{\text{VBL-CBE}}(\hbar\omega)$, and $J_{\text{VBL-CBL}}(\hbar\omega)$, are plotted as functions of $\hbar\omega$ for the case of $\gamma_{\text{C}} = 40$ meV, γ_{V} being determined from Eq. (4.11); all other DOS modeling parameters are set to the PECVD a-Si:H values, i.e., the values set in Table 4.5. It is seen that the functional dependencies found in Figure 4.10 are also found for this case. The tail breadths associated with the tails in the JDOS functions, however, are found to be considerably broader, owing to the fact that γ_{V} and γ_{C} are larger for the case of $\gamma_{\text{C}} = 40$ meV. As with Figures 3.17 and 4.10, it is noted that $J_{\text{VBE-CBE}}(\hbar\omega) = 0$ for $\hbar\omega < E_{\text{C}\mu} - E_{\text{V}\mu}$ and that $J_{\text{VBL-CBL}}(\hbar\omega) = 0$ for $\hbar\omega \geq E_{\text{C}\mu} - E_{\text{V}\mu}$. In addition, it is seen that $J(\hbar\omega)$, $J_{\text{VBE-CBE}}(\hbar\omega)$, $J_{\text{VBE-CBL}}(\hbar\omega)$, and $J_{\text{VBL-CBE}}(\hbar\omega)$ all monotonically increase in response to increases in $\hbar\omega$. As with Figures 3.17 and 4.10, $J_{\text{VBL-CBL}}(\hbar\omega)$ initially increases monotonically in response to increases in $\hbar\omega$, achieving a maximum at a certain value of $\hbar\omega$, and then diminishing to zero at the mobility gap, i.e., when $\hbar\omega = E_{\text{C}\mu} - E_{\text{V}\mu}$.

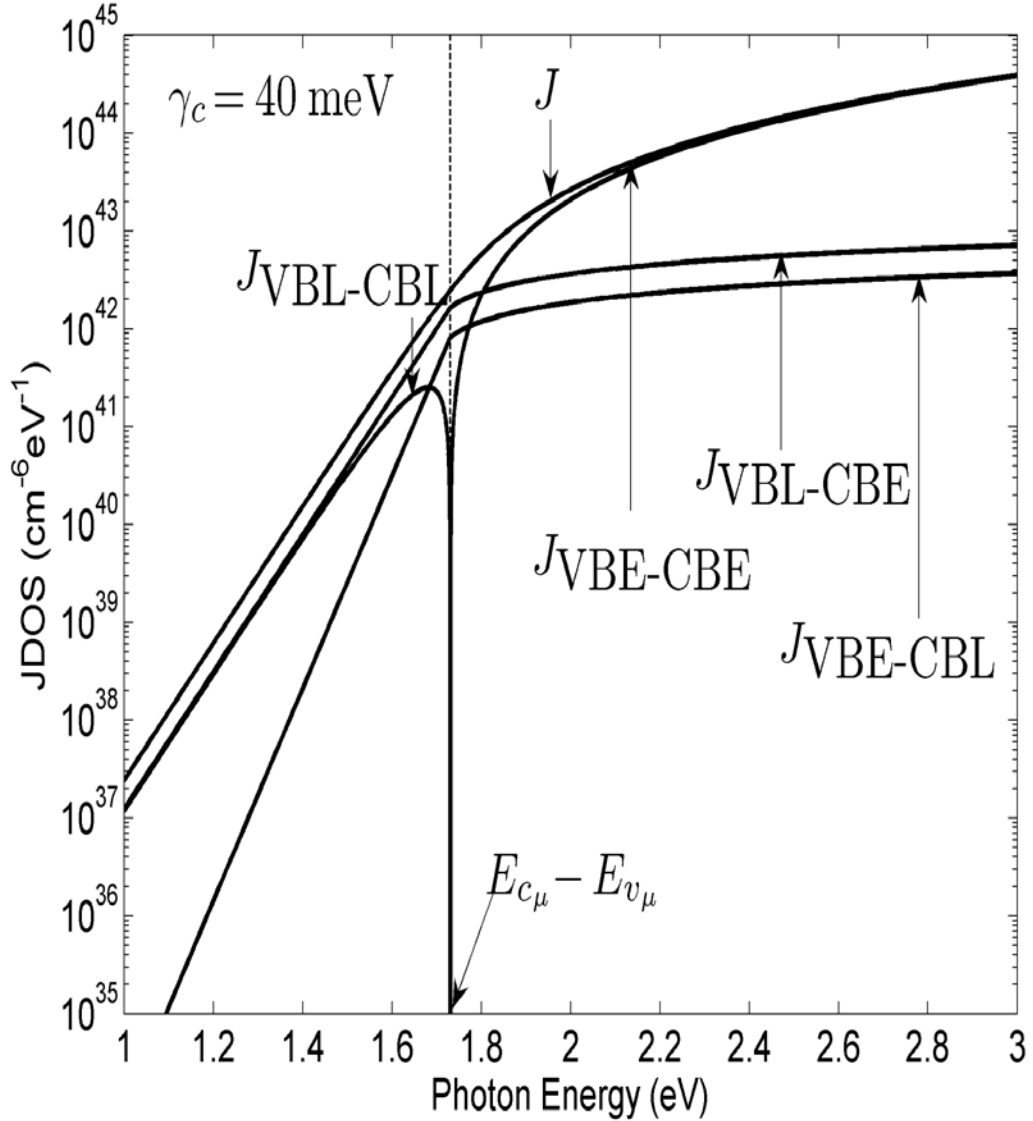

Figure 4.12: The contributions to the JDOS function corresponding to the VBE-CBE, VBE-CBL, VBL-CBE, and VBL-CBL optical transitions, i.e., $J_{\text{VBE-CBE}}$, $J_{\text{VBE-CBL}}$, $J_{\text{VBL-CBE}}$ and $J_{\text{VBL-CBL}}$, as functions of the photon energy, $\hbar\omega$, for $\gamma_{\text{C}} =$ 40 meV. γ_{V} is determined using the linear least-squares fit relationship between γ_{C} and γ_{V}, i.e., Eq. (4.11). All DOS modeling parameters are set to their PECVD a-Si:H values, i.e., the value set in Table 4.5. The overall JDOS function, J, is also plotted as a function of the photon energy, $\hbar\omega$.

In Figure 4.13, the fractional PECVD a-Si:H JDOS functions, $\frac{J_{\text{VBE-CBE}}(\hbar\omega)}{J(\hbar\omega)}$, $\frac{J_{\text{VBE-CBL}}(\hbar\omega)}{J(\hbar\omega)}$, $\frac{J_{\text{VBL-CBE}}(\hbar\omega)}{J(\hbar\omega)}$ and $\frac{J_{\text{VBL-CBL}}(\hbar\omega)}{J(\hbar\omega)}$, are plotted as functions of $\hbar\omega$ for the case of $\gamma_C = 40$ meV, γ_V being determined from Eq. (4.11); all other DOS modeling parameters are set to the PECVD a-Si:H values, i.e., the values set in Table 4.5. As with Figures 3.18 and 4.11, while $\frac{J_{\text{VBE-CBE}}(\hbar\omega)}{J(\hbar\omega)}$ monotonically increases from 0 as $\hbar\omega$ increases from the mobility gap, i.e., $E_{C\mu} - E_{V\mu}$, and $\frac{J_{\text{VBL-CBL}}(\hbar\omega)}{J(\hbar\omega)}$ monotonically increases from 0 as $\hbar\omega$ decreases from the mobility gap, i.e., $E_{C\mu} - E_{V\mu}$, the other fractional JDOS functions, $\frac{J_{\text{VBE-CBL}}(\hbar\omega)}{J(\hbar\omega)}$ and $\frac{J_{\text{VBL-CBE}}(\hbar\omega)}{J(\hbar\omega)}$, achieve their maxima exactly at the mobility gap, i.e., when $\hbar\omega = E_{C\mu} - E_{V\mu}$. As with Figure 4.11, while $\frac{J_{\text{VBE-CBE}}(\hbar\omega)}{J(\hbar\omega)}$ asymptotically approaches unity as $\hbar\omega$ approaches high values of $\hbar\omega$, $\frac{J_{\text{VBL-CBL}}(\hbar\omega)}{J(\hbar\omega)}$ instead approaches 0.49 as $\hbar\omega$ approaches low values; in Figure 3.18, instead $\frac{J_{\text{VBL-CBL}}(\hbar\omega)}{J(\hbar\omega)}$ approached unity as $\hbar\omega$ approaches low values. As with Figure 4.11, this occurs as there are a greater total density of VBL electronic states than CBL electronic states; recall Figure 4.9. $\frac{J_{\text{VBE-CBL}}(\hbar\omega)}{J(\hbar\omega)}$ on the other hand exhibits a behaviour similar to that found in Figures 3.18 and 4.11, i.e., it asymptotically approaches zero for both high values of $\hbar\omega$ and low values of $\hbar\omega$.

In Figure 4.14, the fractional PECVD a-Si:H JDOS functions, $\frac{J_{\text{VBL-CBE}}(\hbar\omega)}{J(\hbar\omega)}$ and $\frac{J_{\text{VBL-CBL}}(\hbar\omega)}{J(\hbar\omega)}$, are plotted as functions of γ_c for $\hbar\omega$ set to 1 eV, this serving as an approximation to the low $\hbar\omega$ asymptotic limit. As before, γ_V is determined from Eq. (4.11), all DOS modeling parameters being set to their PECVD a-Si:H values, i.e., the values set in Table 4.5. As γ_C is smaller than γ_V, $\frac{J_{\text{VBE-CBL}}(\hbar\omega)}{J(\hbar\omega)}$ asymptotically diminishes to zero in the low $\hbar\omega$ asymptotic limit, i.e., recall Figures 4.11 and 4.13, and thus, it is not plotted in this figure. It is seen that the VBL-CBL contribution

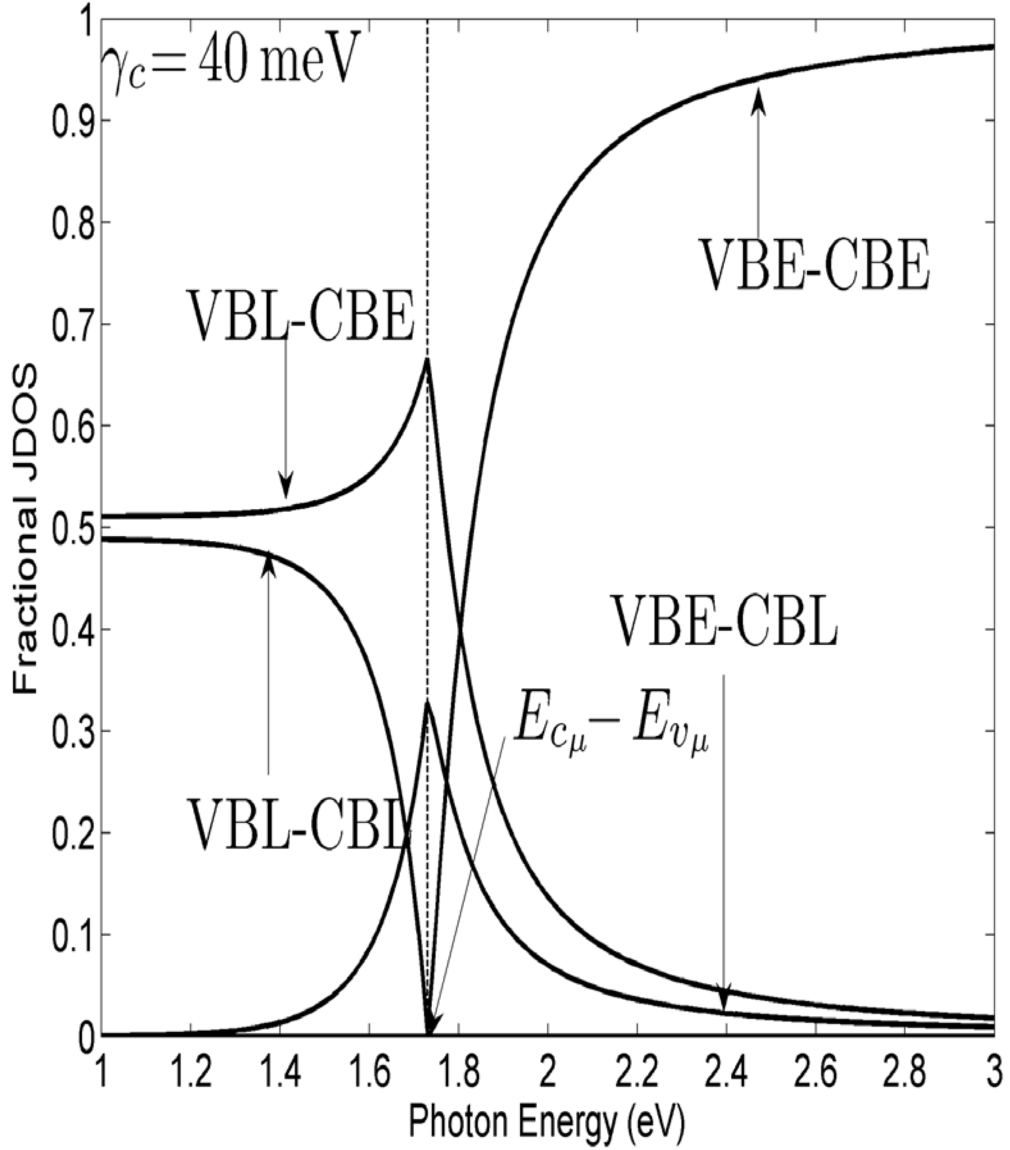

Figure 4.13: The fractional contributions to the JDOS function corresponding to the VBE-CBE, VBE-CBL, VBL-CBE, and VBL-CBL optical transitions, i.e., $\frac{J_{\text{VBE-CBE}}}{J}$, $\frac{J_{\text{VBE-CBL}}}{J}$, $\frac{J_{\text{VBL-CBE}}}{J}$ and $\frac{J_{\text{VBL-CBL}}}{J}$, as functions of the photon energy, $\hbar\omega$, for γ_{C} set to 40 meV. γ_{V} is determined using the linear least-squares fit relationship between γ_{V} and γ_{C}, i.e., Eq. (4.11). All DOS modeling parameters are set to their PECVD a-Si:H values, i.e., the values set in Table 4.5.

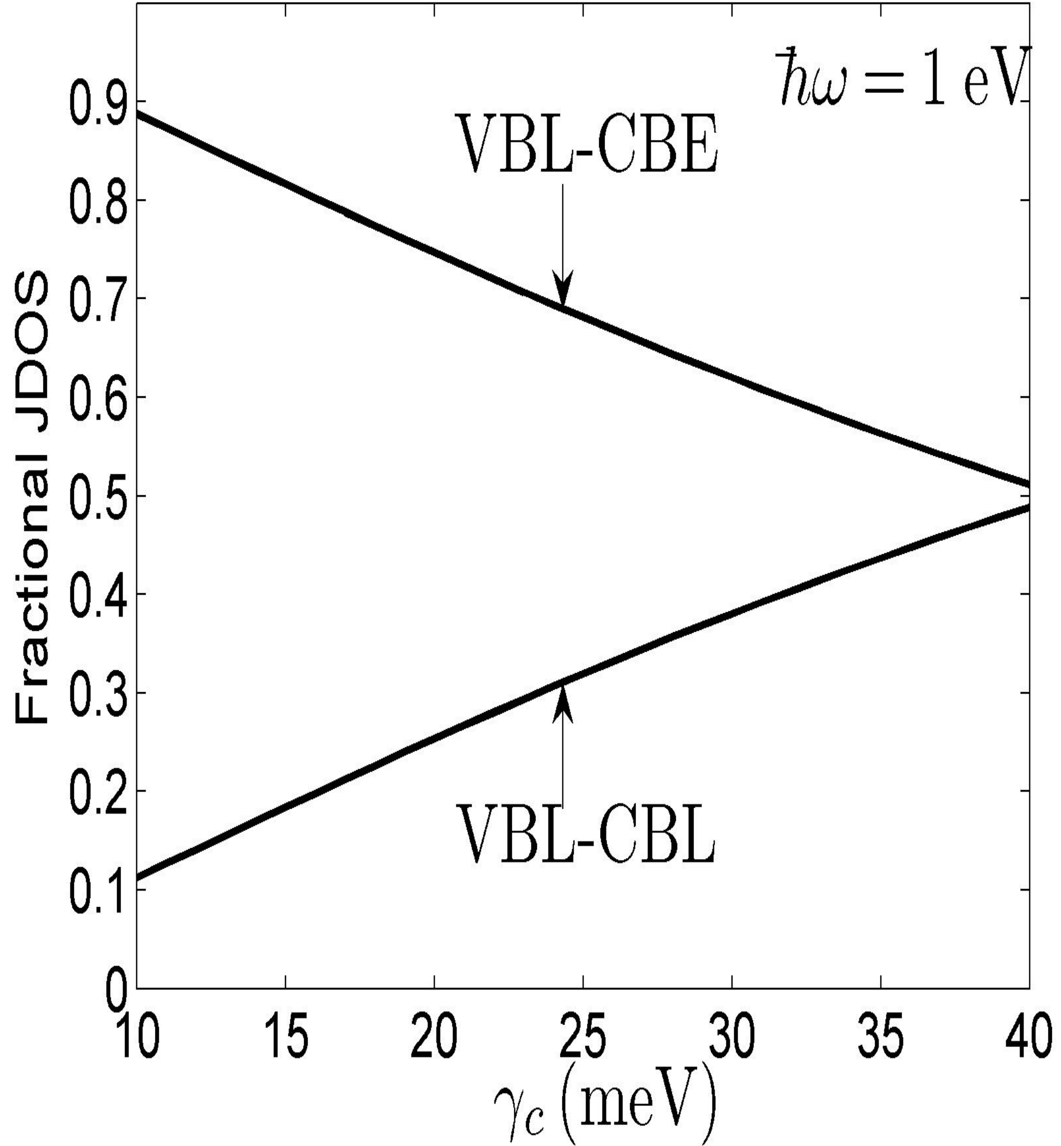

Figure 4.14: The fractional contributions to the JDOS function corresponding to the VBL-CBE and VBL-CBL optical transitions, i.e., $\frac{J_{\text{VBL-CBE}}}{J}$, and $\frac{J_{\text{VBL-CBL}}}{J}$, as functions of the conduction band tail breadth, γ_{C}, evaluated for $\hbar\omega$ set to 1 eV. γ_{V} is determined using the linear least-squares fit relationship between γ_{V} and γ_{C}, i.e., Eq. (4.11). All DOS modeling parameters are set to their PECVD a-Si:H values, i.e., the values set in Table 4.5.

to the JDOS function increases as γ_C is increased. This occurs as the total densities of VBL and CBL electronic states increase as γ_C is increased, i.e., recall Figure 4.9.

In Figure 4.15, the fractional PECVD a-Si:H JDOS functions, $\frac{J_\text{VBE-CBL}(\hbar\omega)}{J(\hbar\omega)}$ and $\frac{J_\text{VBL-CBE}(\hbar\omega)}{J(\hbar\omega)}$, are plotted as functions of γ_C for $\hbar\omega$ set to $E_{\text{C}\mu} - E_{\text{V}\mu}$, i.e., the mobility gap. As before, γ_V is determined from Eq. (4.11), all DOS modeling parameters being set to their PECVD a-Si:H values, i.e., the values set in Table 4.5. As $J_\text{VBE-CBE}(\hbar\omega)$ and $J_\text{VBL-CBL}(\hbar\omega)$ are exactly equal to zero when $\hbar\omega = E_{\text{C}\mu} - E_{\text{V}\mu}$, $J_\text{VBE-CBE}(\hbar\omega)$ and $J_\text{VBL-CBL}(\hbar\omega)$ are not plotted in this figure. It is seen that the contribution of the VBL-CBE optical transitions decreases as γ_C is increased. This is due to the fact that the ratio between γ_C and γ_V increases as γ_C increases; recall Eq. (4.11).

4.7 Evaluation of the spectral dependence of the matrix element associated with PECVD a-Si:H

The spectral dependence of the squared average optical transition matrix element associated with PECVD a-Si:H is now determined, the imaginary part of the dielectric function being proportional to the product of this matrix element and the overall JDOS function, $J(\hbar\omega)$ [50]. Within the framework of the developed JDOS formalism of Chapter 3, it was shown that this matrix element is proportional to the fraction of the overall JDOS function attributable to the VBE-CBE, VBE-CBL, and VBL-CBE optical transitions. That is, the fractional JDOS contribution function

$$J_\text{frac}(\hbar\omega) = \frac{J_\text{VBE-CBE}(\hbar\omega) + J_\text{VBE-CBL}(\hbar\omega) + J_\text{VBL-CBE}(\hbar\omega)}{J(\hbar\omega)}, \tag{4.12}$$

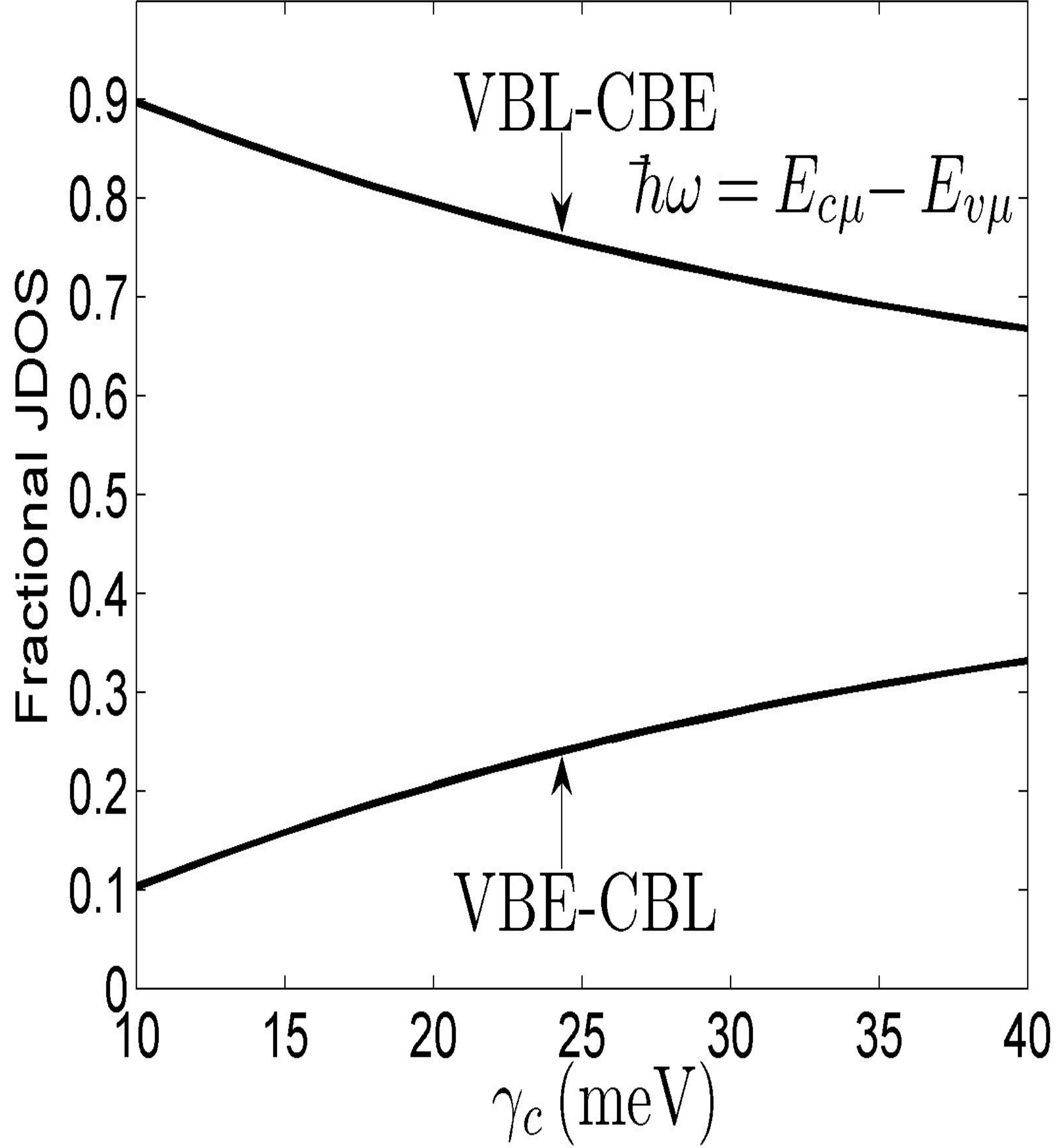

Figure 4.15: The fractional contributions to the JDOS function corresponding to the VBE-CBL and VBL-CBE optical transitions, i.e., $\frac{J_{\text{VBE-CBL}}}{J}$, and $\frac{J_{\text{VBL-CBE}}}{J}$, as functions of the conduction band tail breadth, γ_{C}, evaluated for $\hbar\omega$ set to $E_{\text{C}\mu} - E_{\text{V}\mu}$. γ_{V} is determined using the linear least-squares fit relationship between γ_{V} and γ_{C}, i.e., Eq. (4.11). All DOS modeling parameters are set to their PECVD a-Si:H values, i.e., the values of the set in Table 4.5.

is proportional to the squared average optical transition matrix element.

In Figures 4.16 and 4.17, the fractional JDOS contribution function, $J_{\text{frac}}(\hbar\omega)$, as defined in Eq. (4.12), is plotted as a function of the photon energy, $\hbar\omega$, for γ_{C} set to 10 and 40 meV, respectively; as before, the corresponding values of γ_{V} are determined using Eq. (4.11), all other DOS modeling parameters being set to their PECVD a-Si:H values, i.e., the values set in Table 4.5. It is noted that the location of the mobility gap, $\hbar\omega = E_{\text{C}\mu} - E_{\text{V}\mu}$, is clearly evident from the spectral dependence of $J_{\text{frac}}(\hbar\omega)$, values of $J_{\text{frac}}(\hbar\omega)$ for $\hbar\omega \geq E_{\text{C}\mu} - E_{\text{V}\mu}$ being unity, and values of $J_{\text{frac}}(\hbar\omega)$ for $\hbar\omega < E_{\text{C}\mu} - E_{\text{V}\mu}$ being less than unity. Analysis indicates that $J_{\text{frac}}(\hbar\omega)$ monotonically decreases from unity as $\hbar\omega$ is decreased below the mobility gap. This behaviour is due to the fact that $J_{\text{VBL-CBL}}(\hbar\omega)$ is zero for $\hbar\omega \geq E_{\text{C}\mu} - E_{\text{V}\mu}$ and that $J_{\text{VBL-CBL}}(\hbar\omega)$ monotonically increases as $\hbar\omega$ decreases below the mobility gap; as VBL-CBL optical transitions contribute to the overall JDOS function, $J(\hbar\omega)$, the fractional JDOS contribution, $J_{\text{frac}}(\hbar\omega)$, diminishes in response to increases in $J_{\text{VBL-CBL}}(\hbar\omega)$. It is also noted that the amount by which the fractional JDOS contribution is diminished is a strong function of the valence band and conduction band tail breadths, γ_{V} and γ_{C}, respectively, the low $\hbar\omega$ asymptotic value of $J_{\text{frac}}(\hbar\omega)$ decreasing from 0.89 for the $\gamma_{\text{C}} = 10$ meV case (Figure 4.16) to 0.51 for the $\gamma_{\text{C}} = 40$ meV case (Figure 4.17). Clearly, considerable insights into the location of the mobility gap and the nature of the electronic states may be gleaned through an analysis of the spectral dependence of $J_{\text{frac}}(\hbar\omega)$, which is directly proportional to the experimentally determinable squared average optical transition matrix element [49].

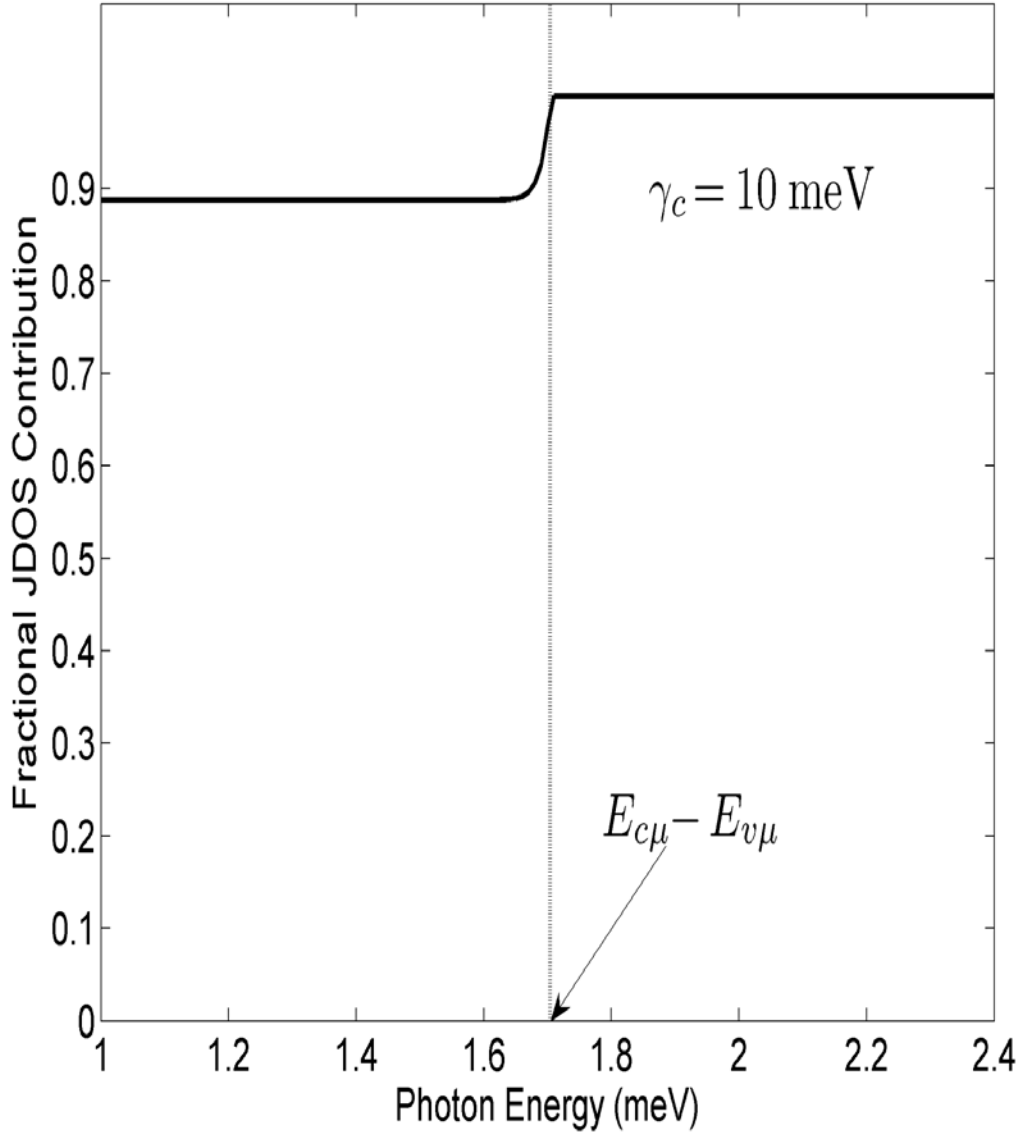

Figure 4.16: The fractional contributions to the JDOS function, J_{frac}, as defined in Eq. (4.12), as a function of the photon energy, $\hbar\omega$, for γ_{C} set to 10 meV, γ_{V} being determined using the linear least-squares fit relationship between γ_{V} and γ_{C}, i.e., Eq. (4.11). All DOS modeling parameters are set to their PECVD a-Si:H values, i.e., the values set in Table 4.5.

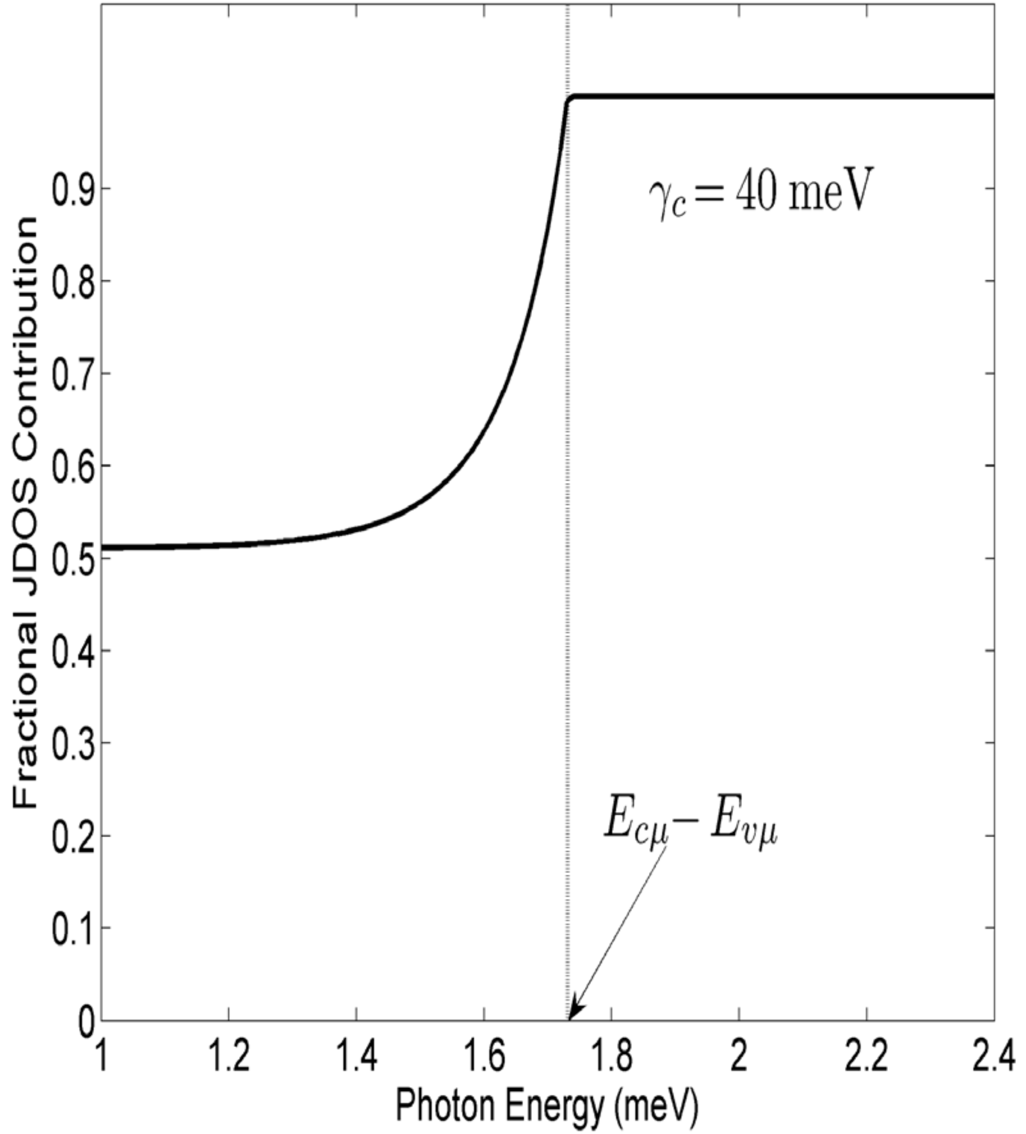

Figure 4.17: The fractional contributions to the JDOS function, J_{frac}, as defined in Eq. (4.12), as a function of the photon energy, $\hbar\omega$, for γ_{C} set to 40 meV, γ_{V} being determined using the linear least-squares fit relationship between γ_{V} and γ_{C}, i.e., Eq. (4.11). All DOS modeling parameters are set to their PECVD a-Si:H values, i.e., the values set in Table 4.5.

4.8 Spectral variations in the optical transition matrix element and their impact on the optical properties associated with PECVD a-Si:H

Using an empirical model for the DOS functions, in conjunction with an elementary model for the optical transition matrix elements, the spectral dependence of $\Re^2(\hbar\omega)$ was determined for the case of PECVD a-Si:H. It was found that $\Re^2(\hbar\omega)$ saturates at and beyond the mobility gap, decreases sharply just below the mobility gap as the photon energy is diminished, and then saturates again at sufficiently low photon energies. The saturated value of $\Re^2(\hbar\omega)$ at low photon energies was found to depend critically on the density of localized states. These results suggest that a careful examination of the spectral dependence of $\Re^2(\hbar\omega)$ will allow for a determination of the mobility gap associated with PECVD a-Si:H. In this section, the aim is to explore how such variations in the spectral dependence of $\Re^2(\hbar\omega)$ impact upon the spectral dependence of the optical properties associated with PECVD a-Si:H. It will also be ascertained as to whether or not the PECVD a-Si:H mobility gap result suggested by Jackson *et al.* [49] is consistent with the results of experiment. This analysis is performed within the framework of the JDOS formalism. For the purposes of this analysis, the DOS modeling parameters are set to the values set in Table 4.6.

In Figures 4.18, 4.19, and 4.20, the fractional JDOS contribution, $J_{\text{frac}}(\hbar\omega)$, is plotted as a function of $\hbar\omega$, for various mobility edge selections, Figure 4.18 corresponding to $E_{\text{c}\mu} - E_{\text{v}\mu}$ set to $E_{\text{ct}} - E_{\text{vt}} + 0.2$ eV, Figure 4.19 corresponding to $E_{\text{c}\mu} - E_{\text{v}\mu}$ set to $E_{\text{ct}} - E_{\text{vt}}$, and Figure 4.20 corresponding to $E_{\text{c}\mu} - E_{\text{v}\mu}$ set to $E_{\text{ct}} - E_{\text{vt}} - 0.2$ eV; a variety of selections of $E_{\text{v}\mu}$ and $E_{\text{c}\mu}$ are considered for each

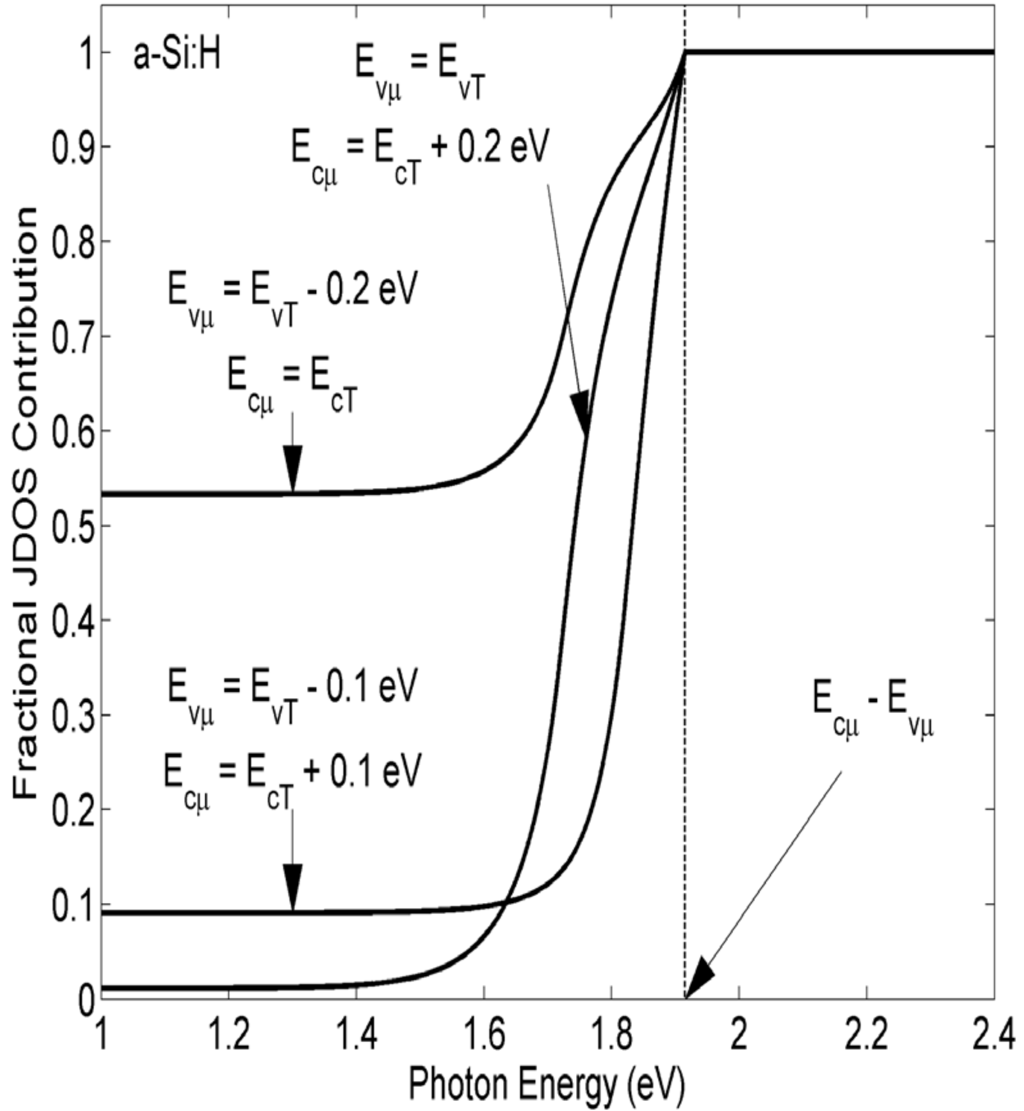

Figure 4.18: The fraction of the JDOS function that is attributable solely to the VBE-CBE, VBE-CBL, and VBL-CBE optical transitions, $J_{\text{frac}}(\hbar\omega)$, for the case of PECVD a-Si:H when the mobility gap, $E_{\text{c}\mu} - E_{\text{v}\mu}$, is set to $E_{\text{ct}} - E_{\text{vt}} + 0.2$ eV. Three cases are considered; (1) $E_{\text{v}\mu} = E_{\text{vt}}$ and $E_{\text{c}\mu} = E_{\text{ct}} + 0.2$ eV, (2) $E_{\text{v}\mu} = E_{\text{vt}} - 0.1$ eV and $E_{\text{c}\mu} = E_{\text{ct}} + 0.1$ eV, and (3) $E_{\text{v}\mu} = E_{\text{vt}} - 0.2$ eV and $E_{\text{c}\mu} = E_{\text{ct}}$. For all cases, the DOS modeling parameters are set to the PECVD a-Si:H values assigned in Table 4.6.

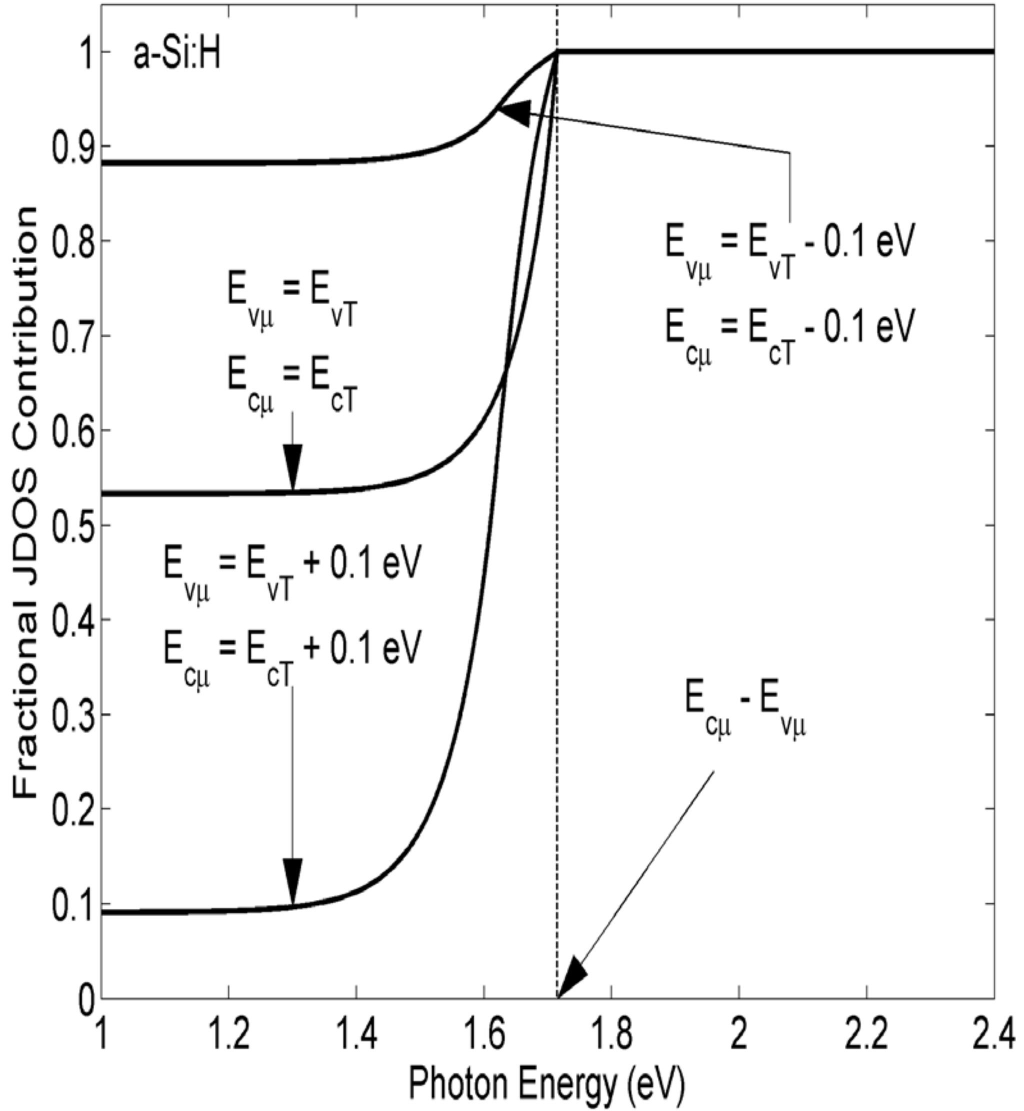

Figure 4.19: The fraction of the JDOS function that is attributable solely to the VBE-CBE, VBE-CBL, and VBL-CBE optical transitions, $J_{\mathrm{frac}}(\hbar\omega)$, for the case of PECVD a-Si:H when the mobility gap, $E_{\mathrm{c}\mu} - E_{\mathrm{v}\mu}$, is set to $E_{\mathrm{ct}} - E_{\mathrm{vt}}$. Three cases are considered; (1) $E_{\mathrm{v}\mu} = E_{\mathrm{vt}} + 0.1$ eV and $E_{\mathrm{c}\mu} = E_{\mathrm{ct}} + 0.1$ eV, (2) $E_{\mathrm{v}\mu} = E_{\mathrm{vt}}$ and $E_{\mathrm{c}\mu} = E_{\mathrm{ct}}$, and (3) $E_{\mathrm{v}\mu} = E_{\mathrm{vt}} - 0.1$ eV and $E_{\mathrm{c}\mu} = E_{\mathrm{ct}} - 0.1$ eV. For all cases, the DOS modeling parameters are set to the PECVD a-Si:H values assigned in Table 4.6.

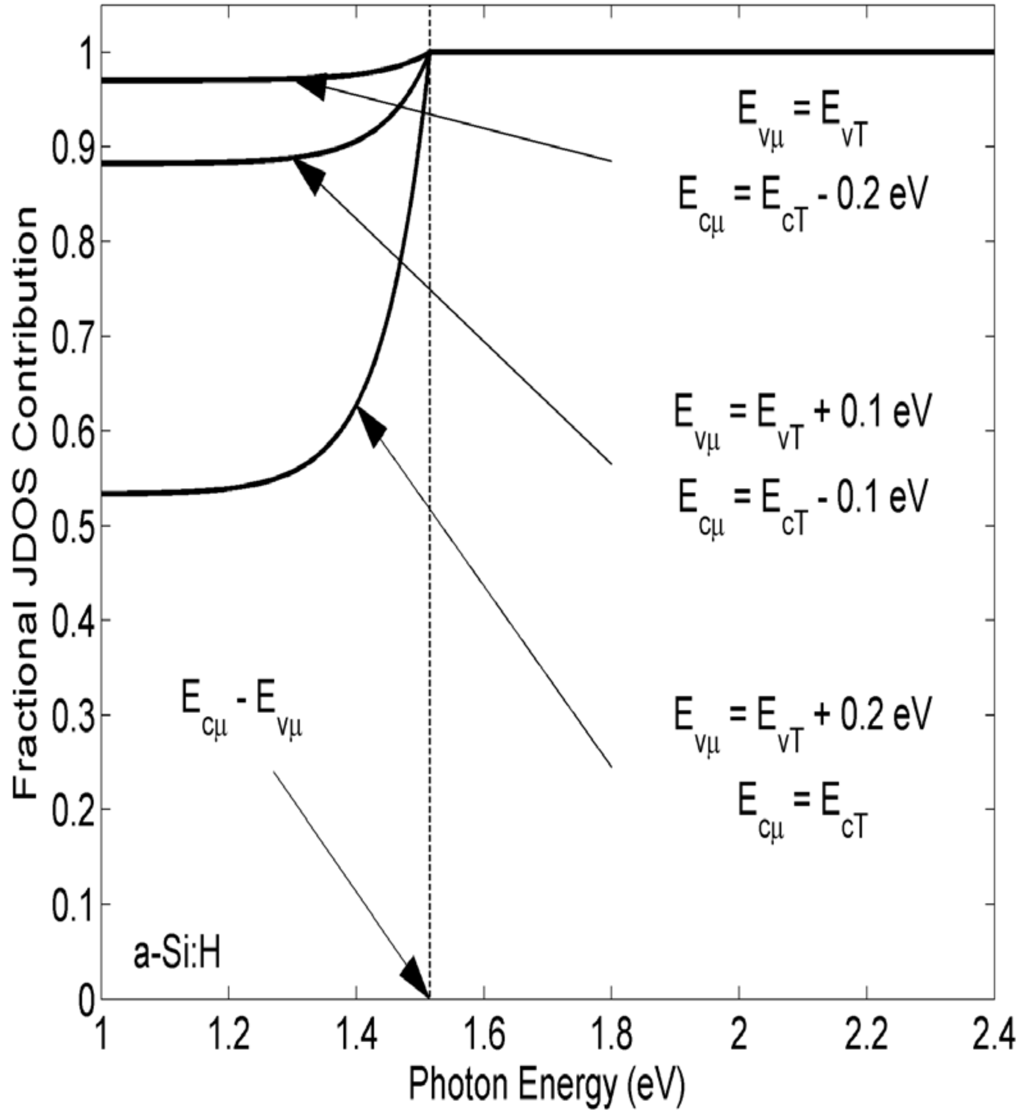

Figure 4.20: The fraction of the JDOS function that is attributable solely to the VBE-CBE, VBE-CBL, and VBL-CBE optical transitions, $J_{\text{frac}}(\hbar\omega)$, for the case of PECVD a-Si:H when the mobility gap, $E_{c\mu} - E_{v\mu}$, is set to $E_{ct} - E_{vt} - 0.2$ eV. Three cases are considered; (1) $E_{v\mu} = E_{vt} + 0.2$ eV and $E_{c\mu} = E_{ct}$, (2) $E_{v\mu} = E_{vt} + 0.1$ eV and $E_{c\mu} = E_{ct} - 0.1$ eV, and (3) $E_{v\mu} = E_{vt}$ and $E_{c\mu} = E_{ct} - 0.2$ eV. For all cases, the DOS modeling parameters are set to the PECVD a-Si:H values assigned in Table 4.6.

Table 4.6: The PECVD a-Si:H DOS modeling parameter selections used for the purposes of this analysis.

Conduction band		**Valence band**	
Parameter	**Value**	**Parameter**	**Value**
N_{co}	2.38×10^{22} (cm^{-3}eV$^{-3/2}$)	N_{vo}	2.38×10^{22} (cm^{-3}eV$^{-3/2}$)
E_{c}	1.68 (eV)	E_{v}	0.0 (eV)
γ_{c}	43 (meV)	γ_{v}	27 (meV)
E_{ct}	$E_{\mathrm{c}} + \frac{1}{2}\gamma_{\mathrm{c}}$	E_{vt}	$E_{\mathrm{v}} - \frac{1}{2}\gamma_{\mathrm{v}}$

case, however, the PECVD a-Si:H DOS modeling parameters specified in Table 4.6 being used for all cases. As was observed by O'Leary [50], it is seen that in all cases, $J_{\mathrm{frac}}(\hbar\omega)$ increases monotonically with $\hbar\omega$, abruptly saturating at a value of unity for $\hbar\omega \geq E_{\mathrm{C}\mu} - E_{\mathrm{V}\mu}$. For $\hbar\omega < E_{\mathrm{C}\mu} - E_{\mathrm{V}\mu}$, however, as the photon energy decreases from $E_{\mathrm{C}\mu} - E_{\mathrm{V}\mu}$, initially a sharp decline in $J_{\mathrm{frac}}(\hbar\omega)$ is observed, this decrease being attributed to the onset of a significant VBL-CBL contribution to the JDOS. Eventually, however, for sufficiently low $\hbar\omega$, a saturation in $J_{\mathrm{frac}}(\hbar\omega)$ is observed. The magnitude of $J_{\mathrm{frac}}(\hbar\omega)$ at low values of $\hbar\omega$ depends upon the density of localized states. It is noted that smaller mobility gaps favor $J_{\mathrm{frac}}(\hbar\omega)$ values that are closer to unity. This is a reflection of the fact that there tends to be smaller densities of localized electronic states corresponding to smaller mobility gaps, i.e., fewer VBL and CBL electronic states.

The impact that spectral variations in $J_{\mathrm{frac}}(\hbar\omega)$ play in shaping the optical properties of a-Si:H is now evaluated. Following the lead of Jackson *et al.* [49] and Thevaril and O'Leary [55], it will be assumed that

$$\mathcal{R}^2(\hbar\omega) = R_o^2 J_{\mathrm{frac}}(\hbar\omega) \begin{cases} \left(\dfrac{E_{\mathrm{d}}}{\hbar\omega}\right)^5, & \hbar\omega \geq E_{\mathrm{d}} \\ 1, & \hbar\omega < E_{\mathrm{d}} \end{cases}, \tag{4.13}$$

where the characteristic energy, $E_{\rm d} = 3.4$ eV, and the prefactor, $R_o^2 = 10$ Å^2. Using Eqs. (3.9) and (4.13), for the PECVD a-Si:H DOS modeling parameter selections specified in Table 4.6, the resultant spectral dependence of the imaginary part of the dielectric function, $\epsilon_2(\hbar\omega)$, is plotted in Figure 4.21. The corresponding experimental data of Jackson *et al.* [49] is also depicted.

In order to get a sense as to how $J_{\rm frac}(\hbar\omega)$ influences the results, upper bound results corresponding to $J_{\rm frac}(\hbar\omega)$ set to unity, i.e., a smaller mobility gap, and lower bound results corresponding to the case of $E_{{\rm v}\mu}$ set to $E_{\rm vt} - 0.1$ eV and $E_{{\rm c}\mu}$ set to $E_{\rm ct} + 0.1$ eV, i.e., the mobility gap, $E_{{\rm c}\mu} - E_{{\rm v}\mu} = E_{\rm ct} - E_{\rm vt} + 0.2$ eV, are depicted, this providing a reasonable representation of the span of results considered in Figures 4.18, 4.19, and 4.20. Jackson *et al.* [49] assume that the onset of the exponential tails occurs $\sim$ 0.1 eV beyond the mobility gap between $E_{{\rm v}\mu}$ and $E_{{\rm c}\mu}$. Casting this assumption into the framework of the empirical model for the DOS functions, i.e., Eqs. (4.3) and (4.4), the assumption of Jackson *et al.* [49] means that $E_{{\rm v}\mu}$ is set to $E_{\rm vt} - 0.1$ eV and that $E_{{\rm c}\mu}$ set to $E_{\rm ct} + 0.1$ eV, in exact accord with the lower bound result. It is noted that when the mobility gap, $E_{{\rm c}\mu}$ - $E_{{\rm v}\mu}$, is set to $E_{\rm ct} - E_{\rm vt} + 0.2$ eV, i.e., 1.915 eV[1], that the obtained spectral dependence of the imaginary part of the dielectric function, $\epsilon_2(\hbar\omega)$, seems to prematurely terminate when contrasted with the results of experiment. The fractional JDOS function, $J_{\rm frac}(\hbar\omega)$, is the factor responsible for this premature termination of $\epsilon_2(\hbar\omega)$. The spectral dependence of $\epsilon_2(\hbar\omega)$ determined with $J_{\rm frac}(\hbar\omega)$ set to unity, i.e., corresponding to a lower mobility gap, seems more in keeping with that of experiment. These experimental results suggest that the mobility gap associ-

[1]Jackson *et al.* [49] did not use this empirical model for DOS functions, and thus, slight numerical differences occur.

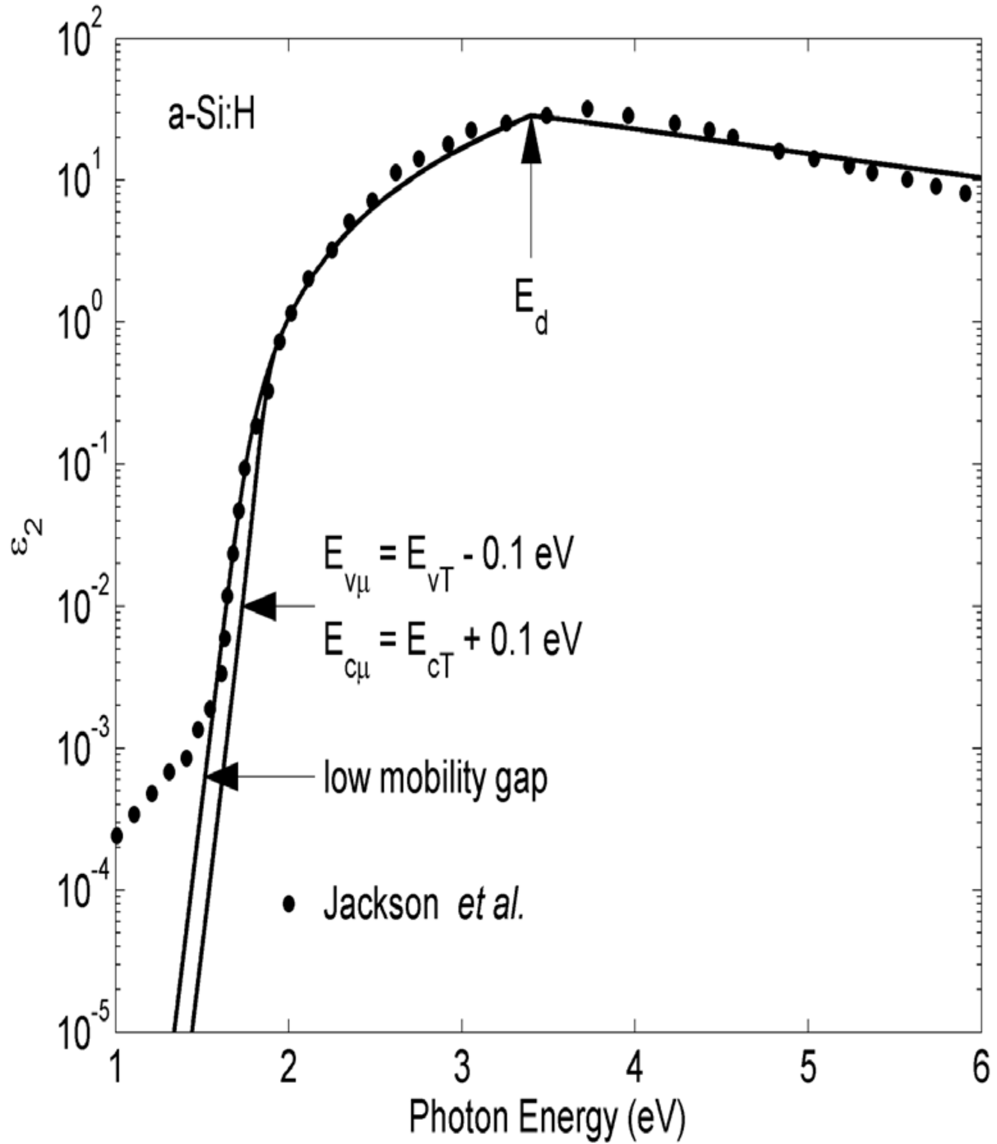

Figure 4.21: The imaginary part of the dielectric function corresponding to PECVD a-Si:H. The experimental data of Jackson *et al.* [49] is depicted with the solid points. The calculated result with $J_{\mathrm{frac}}(\hbar\omega)$ taken into account, for the specific case of $E_{\mathrm{v}\mu} = E_{\mathrm{vt}} - 0.1$ eV and $E_{\mathrm{c}\mu} = E_{\mathrm{ct}} + 0.1$ eV, is shown with the solid line and indicated with an arrow. The calculated result corresponding to the case of $J_{\mathrm{frac}}(\hbar\omega)$ set to unity, i.e., a low mobility gap, is also depicted with the solid line and the arrow. The PECVD a-Si:H DOS modeling parameters are set to the values assigned in Table 4.6.

ated with PECVD a-Si:H determined by Jackson *et al.* [49] is too large. While one can not uniquely determine the exact value of the mobility gap associated with this material, the termination of $\epsilon_2(\hbar\omega)$ being determined both by that associated with $J_{\text{frac}}(\hbar\omega)$ and $J(\hbar\omega)$, these experimental results suggest that the mobility gap associated with PECVD a-Si:H is upper bounded by the energy difference between E_{V} and E_{C}, i.e., 1.68 eV; for sufficient $J_{\text{frac}}(\hbar\omega)$ attenuation, the termination of $\epsilon_2(\hbar\omega)$ is determined by the larger of the mobility gap, $E_{\text{C}\mu} - E_{\text{V}\mu}$, or the energy gap, $E_{\text{C}} - E_{\text{V}}$. Further analysis would be required in order to make a more precise determination.

It is interesting to note that the analysis presented in this section has used experimental data of Jackson *et al.* [49] to refute a claim of Jackson *et al.* [49]. Prior to the development of a formalism for the spectral dependence of the normalized dipole matrix element, there would be no means whereby one could glean the mobility gap associated with PECVD a-Si:H from optical data. As a consequence, incongruities, between the spectral dependence of the optical functions and the postulated mobility gap values, such as those put forth by Jackson *et al.* [49], could occur without notice. The formalism that was developed herein provides researchers with a useful tool that will prevent this from occurring in the future. This represents an important development in the analysis of PECVD a-Si:H, and other amorphous semiconductors of interest.

While the analysis of Jackson *et al.* [49] focuses exclusively on the optical response of PECVD a-Si:H, insights into the mobility gap associated with this material may also be gleaned from electrical measurements. Street [8] provides evidence that suggests that the dark conductivity activation energy associated with undoped

a-Si:H is around 0.85 eV. If it is simplistically interpreted that this activation energy corresponds to half the mobility gap, it is concluded that the mobility gap associated with PECVD a-Si:H is 1.7 eV; there are some issues regarding the nature of the mobility edges associated with the valence and conduction bands that cast doubt on the exactitude of this interpretation, but certainly, if one does not excessively rely on the precise value obtained, it may be employed as a rough measure for the mobility gap. It is seen that this value for the mobility gap associated with PECVD a-Si:H is consistent with the bound that was set for the mobility gap. Clearly, future work would be required in order to draw any stronger conclusion.

4.9 Evaluation of the optical absorption coefficient associated with PECVD a-Si:H

The optical response of a-Si:H determines the performance of many of the important PECVD a-Si:H based electron devices that are commonly used. Accordingly, the evaluation of the spectral dependence of the optical absorption coefficient associated with this material, $\alpha(\hbar\omega)$, is an important application for this JDOS formalism. The results of such an analysis may be employed for two important purposes: (1) materials characterization, and (2) simulating the performance of PECVD a-Si:H based electron devices. A useful model for the optical absorption spectrum can not only be used in order to predict the performance of a particular PECVD a-Si:H based electron device, it provides a framework within which such a device design may be optimized. The modeling of the spectral dependence of the optical absorption coefficient, $\alpha(\hbar\omega)$, will be the focus of the analysis presented here, an application of this evaluation being presented in the subsequent section.

In Section 4.8, the JDOS formalism that was developed previously was applied in order to evaluate the spectral dependence of the dielectric function, $\epsilon_2(\hbar\omega)$. In this section, the spectral dependence of the optical absorption coefficient, $\alpha(\hbar\omega)$, based on the $\epsilon_2(\hbar\omega)$ evaluation, is determined. It is noted that the optical absorption coefficient

$$\alpha(\hbar\omega) = \frac{\omega}{n(\hbar\omega)c}\,\epsilon_2(\hbar\omega), \tag{4.14}$$

where $n(\hbar\omega)$ represents the spectral dependence of the refractive index as a function of the photon energy, $\hbar\omega$, ω is the corresponding angular frequency, and c is the speed of light in a vacuum. Thus, with a model of the spectral dependence of the refractive index, $n(\hbar\omega)$, the spectral dependence of $\alpha(\hbar\omega)$ may be determined.

In 1982, Klazes *et al.* [56] experimentally evaluated the spectral dependence of the refractive index for a sample of PECVD a-Si:H. The assumption will be made that the spectral dependence of $n(\hbar\omega)$ corresponding to other samples of PECVD a-Si:H does not deviate much from that of Klazes *et al.* [56]. For the purpose of this analysis, a polynomial fit to the experimental data of Klazes *et al.* [56] will be used to model the spectral dependence of the refractive index, $n(\hbar\omega)$. This polynomial fit should be valid over the range of photon energies over which the experimental data extends. In Figures 4.22, 4.23, and 4.24, first-order, third-order, and tenth-order polynomial fits to the experimental data of Klazes *et al.* [56] are depicted; the experimental data of Klazes *et al.* [56] is also depicted in these figures. It is noted that as the order of the polynomial fit is increased, the closeness between the fit and the experimental data of Klazes *et al.* [56] increases. For the purposes of the subsequent analysis, the tenth-order polynomial fit to the experimental data of Klazes *et al.* [56] will be used, i.e., Figure 4.24 [57]. The DOS prefactors are

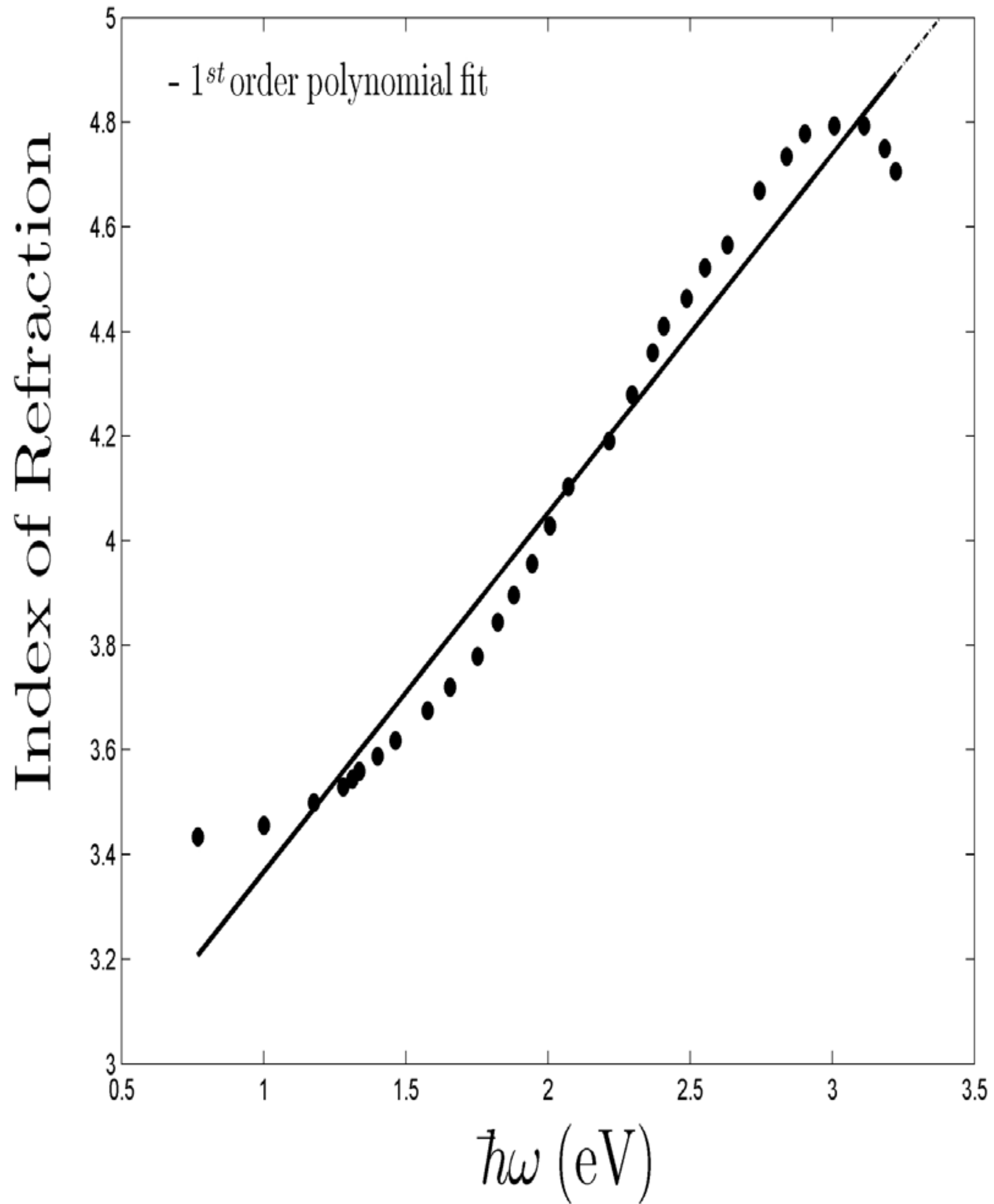

Figure 4.22: The index of refraction, n, of a PECVD a-Si:H sample. The experimental data, depicted with the solid points, is from Klazes *et al.* [56]. A first-order polynomial fit to this experimental data is depicted with the solid line.

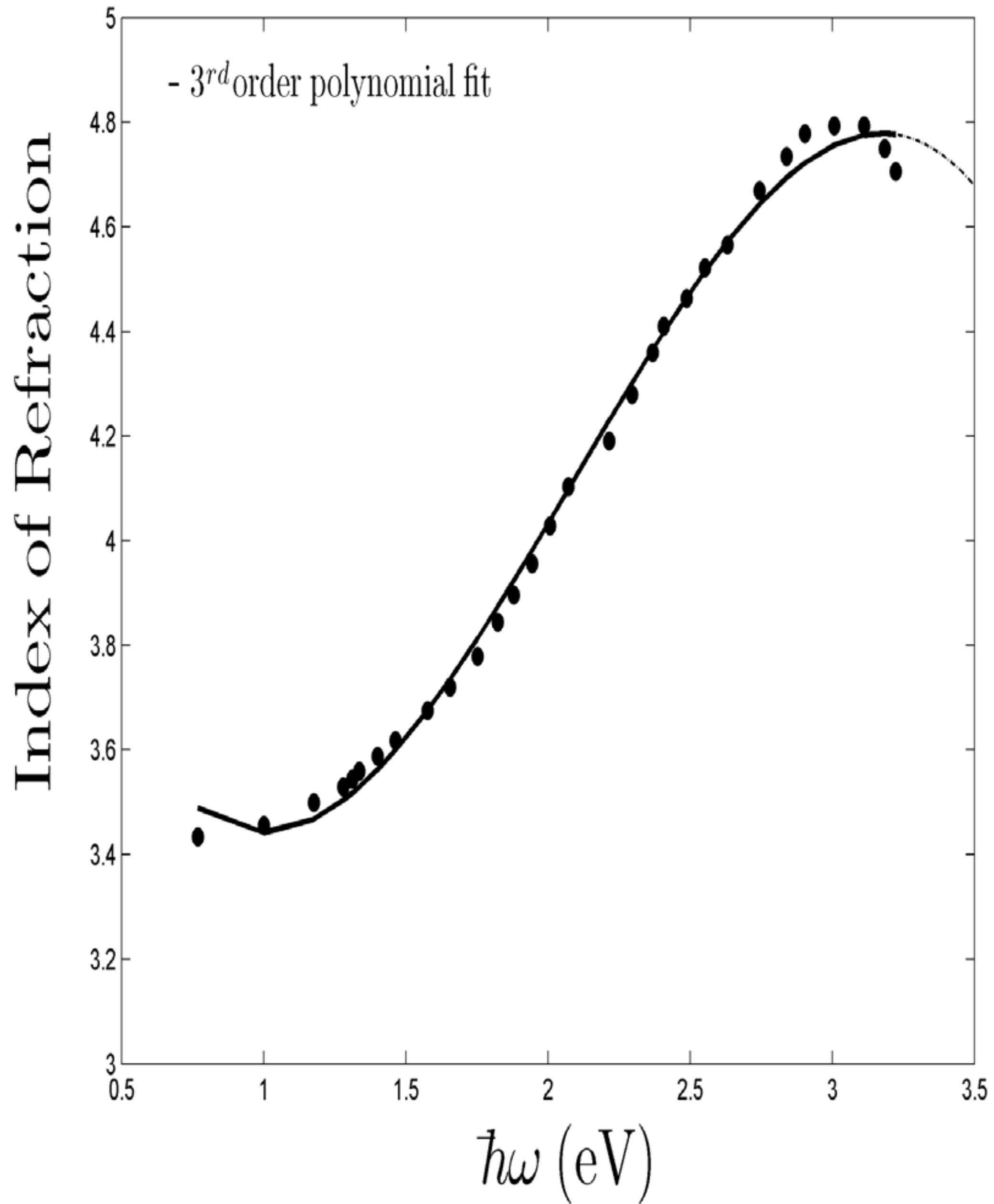

Figure 4.23: The index of refraction, n, of a PECVD a-Si:H sample. The experimental data, depicted with the solid points, is from Klazes *et al.* [56]. A third-order polynomial fit to this experimental data is depicted with the solid line.

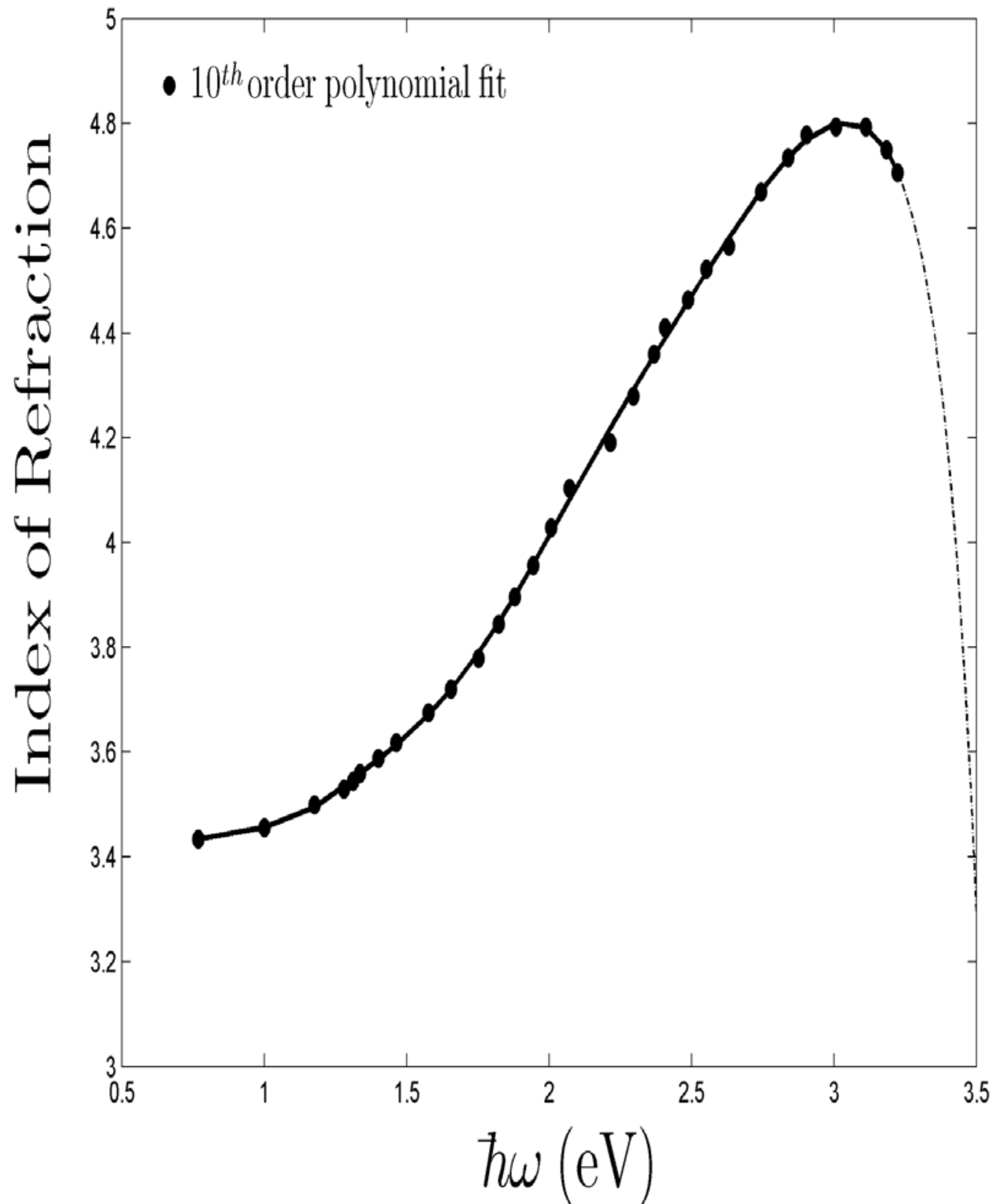

Figure 4.24: The index of refraction, n, of a PECVD a-Si:H sample. The experimental data, depicted with the solid points, is from Klazes *et al.* [56]. A tenth-order polynomial fit to this experimental data is depicted with the solid line. A similar fit is shown by Mok and O'Leary [57].

set to the values of O'Leary [46] for all cases, i.e., $N_{\mathrm{VO}} = N_{\mathrm{CO}} = 2.38 \times 10^{22}$ cm^{-3}eV$^{-3/2}$, the assumption being made that these parameters remain constant for all the samples of PECVD a-Si:H considered; while disorder will influence the tails, the band related DOS modeling parameters, N_{VO} and N_{CO}, will remain fixed.

Three experimental PECVD a-Si:H optical absorption data sets, from Cody *et al.* [12], Remeš [58], and Viturro and Weiser [59], are depicted in Figure 4.25, these data sets spanning over the range of spectral dependencies that are typically found for this material. Theoretical fits, corresponding to the JDOS formalism, are also shown on each figure, the modeling parameters corresponding to each data set being as tabulated in Table 4.7. For all cases, the tenth-order polynomial fit for $n(\hbar\omega)$, shown in Figure 4.24, is used. The fittings provided have been determined through variations in γ_{V} and E_g until the theoretical result agrees with that of experiment. γ_{C} was simply set to the value suggested by Tiedje *et al.* [41], i.e., γ_{C} is set to 27 meV for all cases; as γ_{C} is less than γ_{V}, its value is difficult to uniquely experimentally ascertain, the form of the optical absorption spectrum associated with PECVD a-Si:H being dominated by the value of γ_{V}. It is clear that the JDOS formalism that has been developed is able to capture most features of these optical absorption spectra. Some deviations are observed, however, particularly when the optical absorption coefficient exhibits a broad tail that encroaches into the otherwise empty gap region. Optical transitions involving defect states are most likely responsible for this spectral dependence. Further discussion on this point is provided by Thevaril and O'Leary [55].

For the fits depicted in Figure 4.25, it is seen that the energy gap, E_g, diminishes with increased γ_{V}. This dependence that is observed is depicted in Figure 4.26.

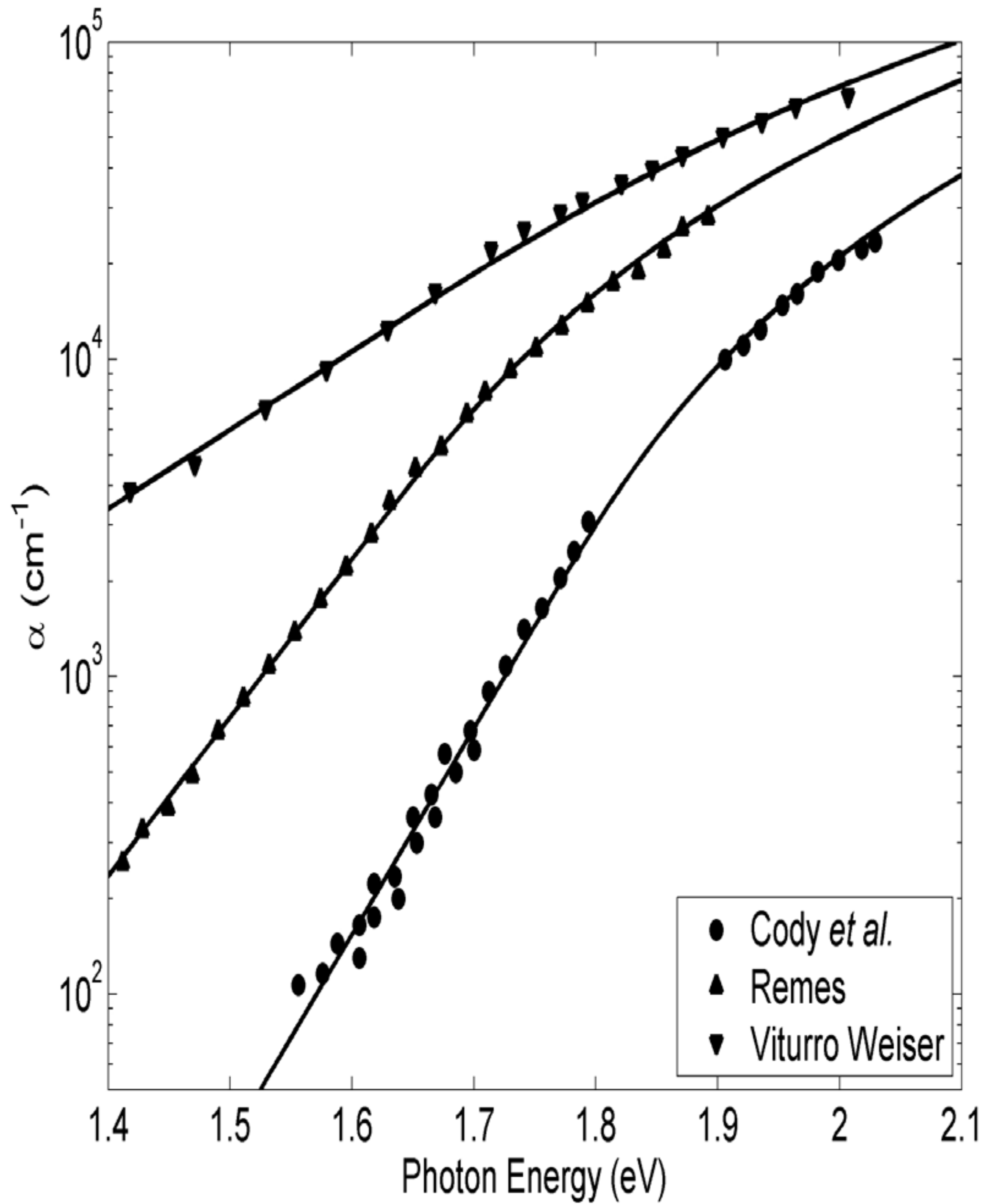

Figure 4.25: Three experimental PECVD a-Si:H optical absorption data sets, from Cody *et al.* [12], Remeš [58], and Viturro and Weiser [59], are depicted with the solid points, the upward triangles, and the downward triangles, respectively. The fit to these data sets are depicted with the corresponding solid lines.

Table 4.7: The DOS modeling parameters corresponding to each data set. Data sets from Cody *et al.* [12], Remeš [58], and Viturro and Weiser [59] are considered.

Parameter	**Cody *et al.* [12]**	**Remeš [58]**	**Viturro and Weiser [59]**
N_{VO} ($\text{cm}^{-3}\text{eV}^{-3/2}$)	2.38×10^{22}	2.38×10^{22}	2.38×10^{22}
N_{CO} ($\text{cm}^{-3}\text{eV}^{-3/2}$)	2.38×10^{22}	2.38×10^{22}	2.38×10^{22}
E_g (eV)	1.7268	1.5707	1.5251
R_o^2 (Å)	10	10	10
γ_{V} (meV)	68.9	91.2	187.5
γ_{C} (meV)	27.0	27.0	27.0

It should be noted that a similar observation was found by Cody *et al.* [12] for the case of PECVD a-Si:H, the energy gap decreasing with increases in the optical absorption tail breadth; the absorption tail breadth is essentially the breadth of the valence band tail for the case of PECVD a-Si:H, as γ_{V} is much larger than γ_{C} for this material. The results of Cody *et al.* [12] are also depicted in Figure 4.26. The trends observed appear to be consistent, with the exception of the fit corresponding to Viturro and Weiser [59].

In order to assess as to whether the data point corresponding to the experimental data of Viturro and Weiser [59] is simply an abberation, other optical absorption experimental data sets, corresponding to Viturro and Weiser [59], are also considered. The fits to this other experimental data are depicted in Figure 4.27, the corresponding DOS modeling fit parameters being specified in Table 4.8. Plotting this additional experimental data on Figure 4.26, it is seen that the trends corresponding to the experimental data of Viturro and Weiser [59] are consistent. However, it is seen that the results of Cody *et al.* [12] are only consistent with those of Viturro and Weiser [59] for the case of low γ_{V}, i.e., for low levels of disorder.

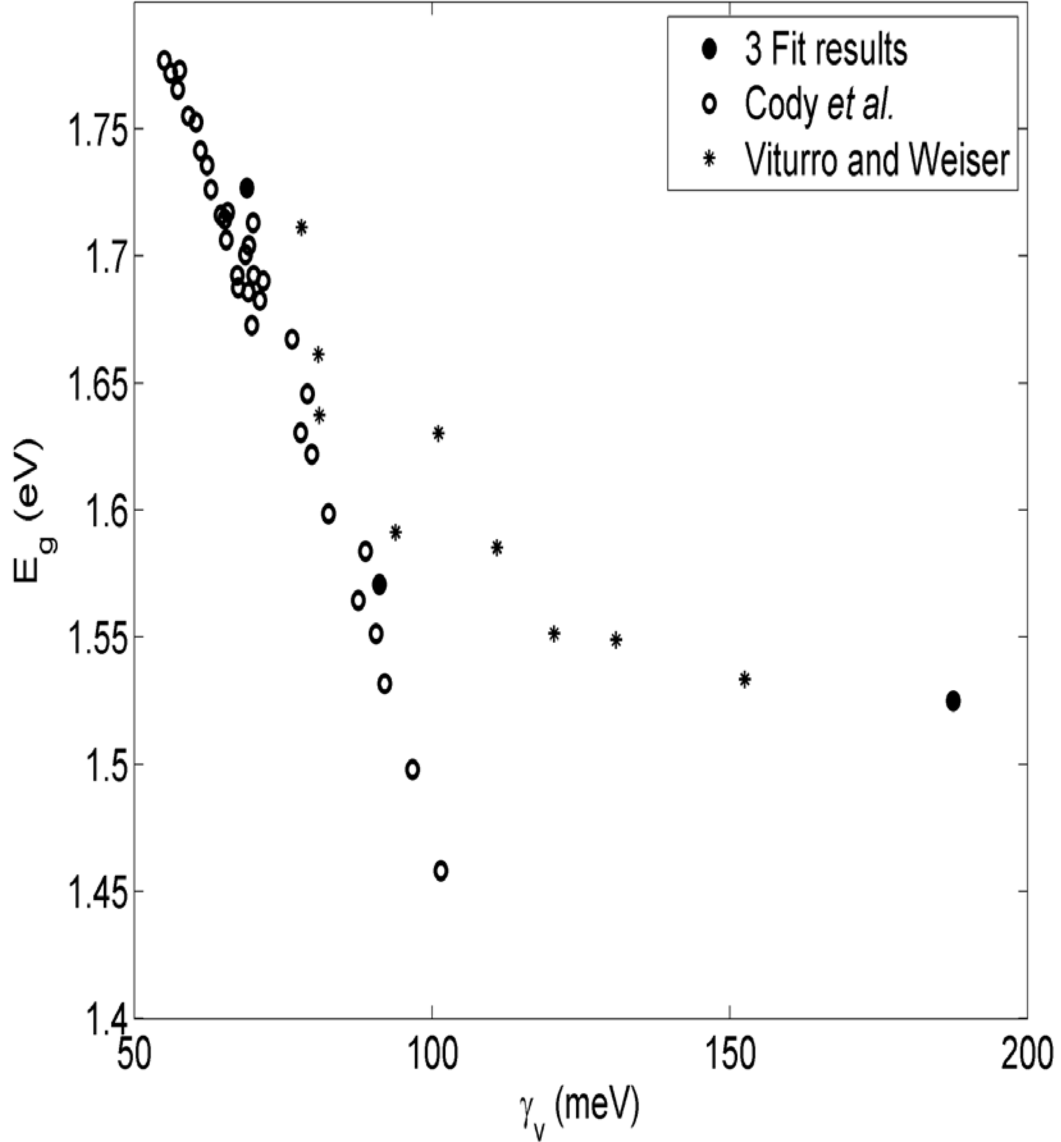

Figure 4.26: The energy gap as a function of the valence band tail breadth. The fit values, corresponding to the fits depicted in Figure 4.25, and tabulated in Table 4.7, are indicated with the solid points. Results corresponding to Cody *et al.* [12] are shown with the open points. The fit values, corresponding to the other experimental data from Viturro and Weiser [59], depicted in Figure 4.27, and tabulated in Table 4.8, are indicated with the asterisks.

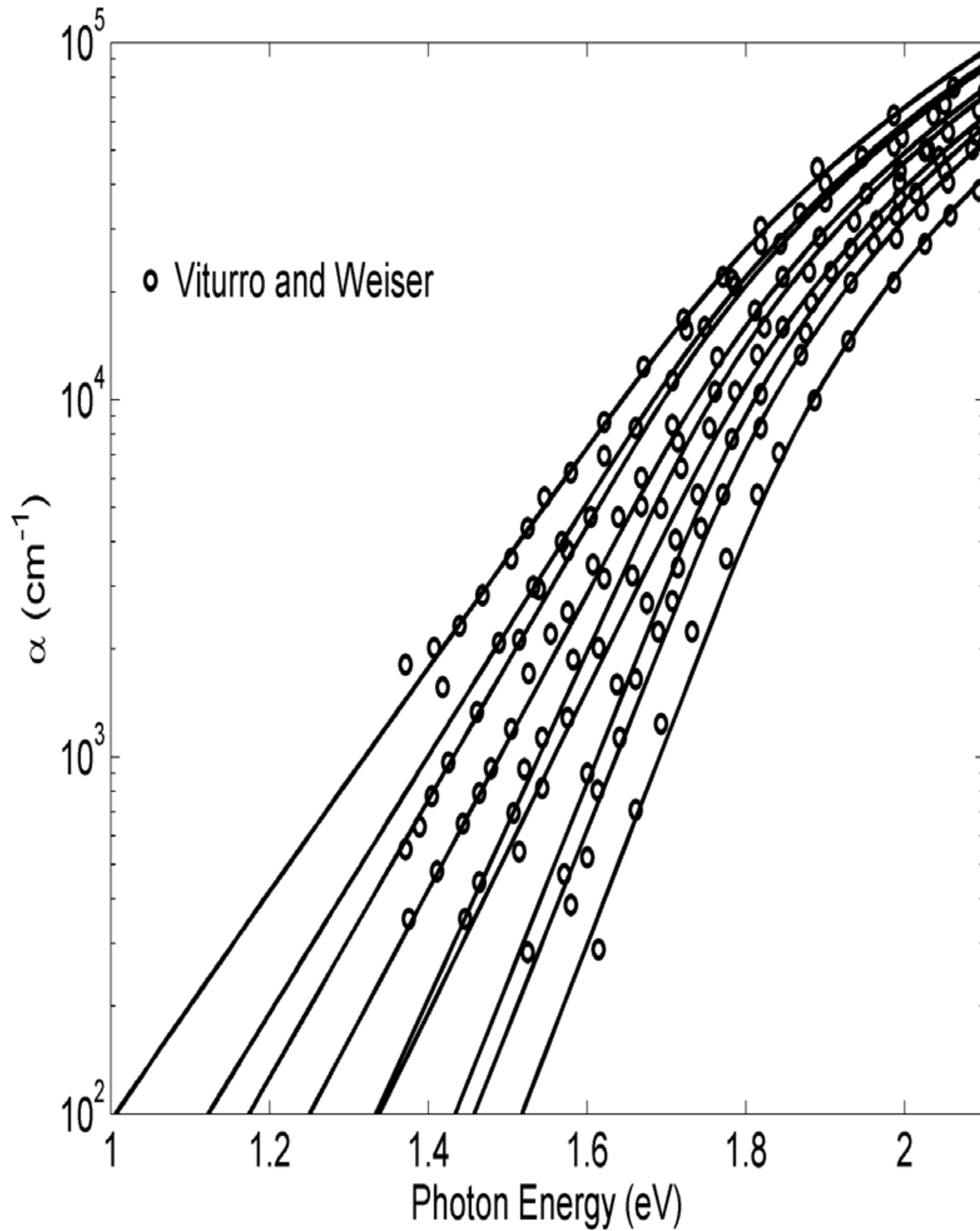

Figure 4.27: The 9 other experimental PECVD a-Si:H optical absorption data sets from Viturro and Weiser [59] are depicted with the open points. The fits to these data sets are depicted with the corresponding solid lines.

Table 4.8: The DOS modeling parameters corresponding to the other data sets from Viturro and Weiser [59] are tabulated.

Data Set	E_g (eV)	γ_{V} (meV)
1	1.5335	152.5
2	1.5514	120.5
3	1.5490	130.9
4	1.5853	110.9
5	1.5913	93.9
6	1.6613	80.9
7	1.7113	78.1
8	1.6303	101.1
9	1.6373	81.1

For sufficiently large levels of disorder, i.e., for γ_{V} in excess of 100 meV, the energy gap values of Viturro and Weiser [59] place an upper bound on those determined by Cody *et al.* [12]. Moreover, a saturation in the energy gap dependence on γ_{V} is observed. No saturation is observed for the case of Cody *et al.* [12].

There are a number of reasons why such a deviation may occur. First, it is noted that the samples of Viturro and Weiser [59], from whence these optical absorption spectra were determined, are not PECVD a-Si:H. While the samples were definitely a form of a-Si:H, they were deposited using a direct synthesis reaction between silicon and hydrogen in a high vacuum. Conventional PECVD a-Si:H, however, is fabricated using a plasma in which silane atoms are decomposed. This difference in the nature of the preparation of the samples could play a role in influencing the resultant optical properties. As a result, the relationship between the energy gap, E_g, and the breadth of the valence band tail, γ_{V}, determined using the experimental optical absorption spectra of Cody *et al.* [12], may be considerably different from

that determined using the experimental optical absorption spectra of Viturro and Weiser [59].

Another possible factor, contributing to differences between the trend observed by Cody *et al.* [12] and that corresponding to the experimental optical absorption spectra of Viturro and Weiser [59], is the fact that the samples of Viturro and Weiser [59] may have been influenced by distributions of defect states. An examination of the two leftmost experimental data sets of Viturro and Weiser [59] depicted in Figure 4.27, shows that there is some deviation between the experimental data and the theoretical fits observed at the lowest values of the optical absorption coefficient. These deviations hint at the presence of distributions of defect states. The apparent breadth of the optical absorption tail is strongly influenced by the presence of defect states, i.e., the breadth of the optical absorption tail increases with broader distributions of defect states, and thus, some of the larger values of γ_{V}, observed in Figure 4.26, may be due to the presence of defect absorption. Note that the large values of γ_{V} is where the energy gap saturation, observed in Figure 4.26, occurs.

There is another aspect of the analysis of Cody *et al.* [12] that could also contribute to this difference. The optical absorption spectra of Cody *et al.* [12] presented experimental optical absorption values between 10^2 and 2×10^4 cm^{-1}; recall Figure 4.25. The optical absorption spectra corresponding to Viturro and Weiser [59], for the large values of γ_{V} determined, correspond to optical absorption values between 10^3 and 3×10^4 cm^{-1}. The range of the data employed plays an important role in determining the DOS modeling parameters. This is particularly

true if there is a curvature in the optical absorption experimental data that lies beyond the framework of the present analysis.

Finally, it should be pointed out that the exact means whereby Cody *et al.* [12] determined their energy gap and tail breadth differs from that employed here. The energy gap determined by Cody *et al.* [12] was the Tauc gap [40]. The optical absorption tail breadth determined by Cody *et al.* [12] was the Urbach tail breadth. While this energy gap and tail breadth are similar to those determined here, there are differences, and these differences could contribute to the differences in the trends observed here and that observed by Cody [12]. Further analysis on this point would be necessary in order to identify how these differences in the definitions contribute to the observed trends, however.

The energy gap associated with PECVD a-Si:H plays an important role in determining the efficiency of a solar cell. Photons with energies lower than the energy gap will not be absorbed by the material, and thus, will simply pass through; for the case of a disordered semiconductor, such as PECVD a-Si:H, this is not quite the case, as the tails in the optical absorption spectrum will lead to some sub-gap optical absorption. Thus, the result depicted in Figure 4.26 provides some insight into the trade-off between amount of disorder that is present and the corresponding solar cell efficiency.

4.10 A quantitative characterization of the optical absorption spectrum associated with PECVD a-Si:H

In the course of a comparative study on the optical absorption spectra corresponding to three different bulk chalcogenide amorphous semiconductors, Wood

and Tauc [60] found that each of the spectra considered exhibits three distinct regions of behavior. The low optical absorption region (region I), where $\alpha(\hbar\omega) < 1$ cm^{-1}, is related to the defects and impurities which characterize these materials. It exhibits a spectral dependence that varies critically with the deposition conditions. For the mid optical absorption region (region II), however, where 1 cm$^{-1} \leq \alpha(\hbar\omega) \leq 10^4$ cm^{-1}, there is a dramatic exponential increase in the optical absorption spectrum corresponding to increases in $\hbar\omega$, this being due to the optical transitions involving the electronic states encroaching into the gap region [16, 17, 44, 45, 46, 61, 62, 63]. Finally, for the high optical absorption region (region III), where $\alpha(\hbar\omega) > 10^4$ cm^{-1}, the optical absorption spectrum continues to increase monotonically with the photon energy in an algebraic rather than an exponential manner. Optical transitions between the bands are responsible for this functional dependence [18]. A representative optical absorption spectrum, corresponding to PECVD a-Si:H, is depicted in Figure 4.28, the three regimes of behavior being clearly depicted [64].

This taxonomy of Wood and Tauc [60], which found its genesis in empirical observation, applies to a surprisingly broad range of amorphous semiconductors. In Figure 4.29, for example, the optical absorption spectrum associated with a sample of PECVD a-Si:H is depicted, the three regions suggested by Wood and Tauc [60] being clearly identified [58].[2] While this taxonomy has been used extensively by researchers in the field, the boundaries between these regions of behavior have yet to be satisfactorily characterized. This is unfortunate, as it is often necessary to

[2]The experimental data in Figure 4.29 corresponds to the standard glow discharge a-Si:H data set presented in Figure 5.2 of Remeš [58], i.e., it corresponds to PECVD a-Si:H. It should be noted that the exact ranges of $\alpha(\hbar\omega)$ corresponding to the three different regions of the optical absorption spectrum may differ from material to material and from sample to sample.

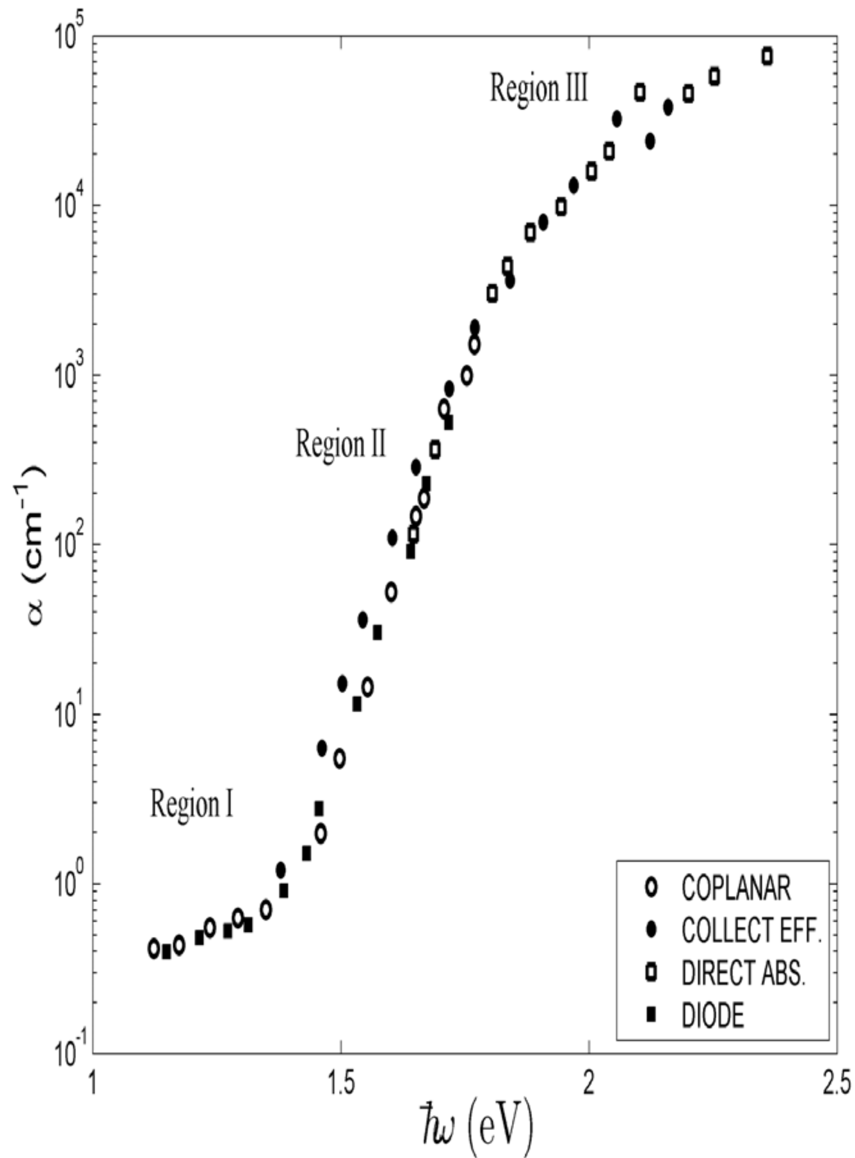

Figure 4.28: The optical absorption spectrum associated with PECVD a-Si:H. The three distinct regions of behavior, suggested by Wood and Tauc [60], are clearly indicated. The experimental data, determined from direct measurements of optical transmission, from the collection efficiency, and from the photoconductivity of the diode and coplanar structures, are from Abeles [64].

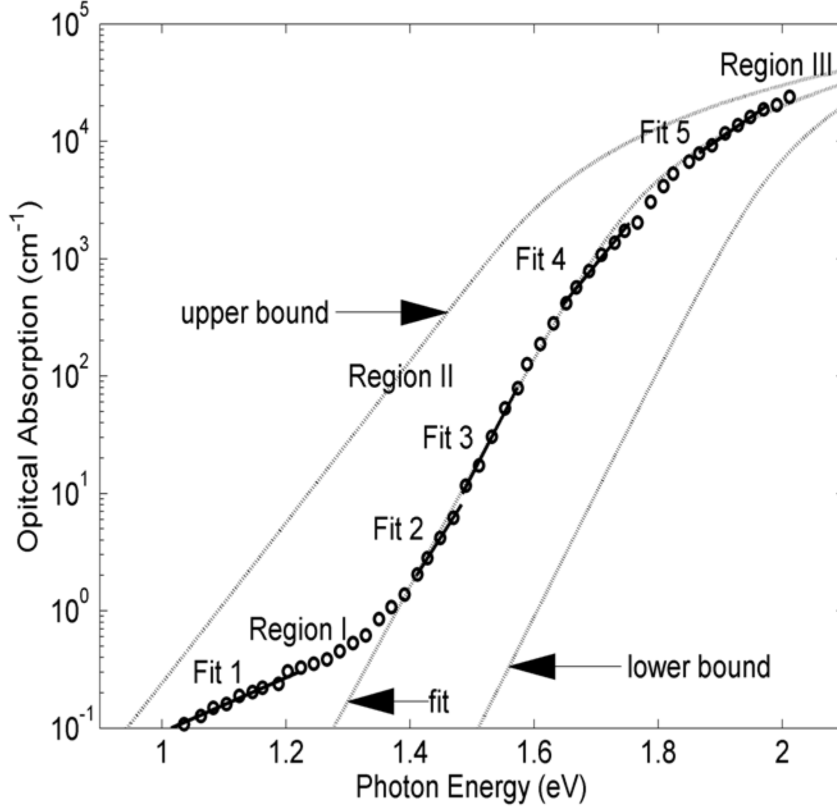

Figure 4.29: The determination of the breadth of the optical absorption tail for a number of different ranges of optical absorption. The PECVD a-Si:H experimental data, depicted with the open points, is from Remeš [58]. The linear least-squares fit of Eq. (4.15) to this experimental data are taken over the ranges 1×10^{-1} cm^{-1} $\leq \alpha(\hbar\omega) \leq 3 \times 10^{-1}$ cm^{-1}, 2×10^{0} cm^{-1} $\leq \alpha(\hbar\omega) \leq 8 \times 10^{0}$ cm^{-1}, 1×10^{1} cm^{-1} $\leq \alpha(\hbar\omega) \leq 8 \times 10^{1}$ cm^{-1}, 4×10^{2} cm^{-1} $\leq \alpha(\hbar\omega) \leq 2 \times 10^{3}$ cm^{-1}, and 8×10^{3} cm^{-1} $\leq \alpha(\hbar\omega) \leq 2 \times 10^{4}$ cm^{-1}, the resultant fits, labeled 1, 2, 3, 4, and 5, respectively, being depicted with the light solid lines. The E_o values found, for fits 1, 2, 3, 4, and 5, are 187 ± 9 meV, 52 ± 3 meV, 43 ± 2 meV, 67 ± 2 meV, and 119 ± 3 meV, respectively. The upper bound result, depicted with a light dotted line, corresponds to the DOS modeling parameter selections $N_{\mathrm{VO}} = N_{\mathrm{CO}} = 2.0 \times 10^{22}$ cm^{-3}eV$^{-3/2}$, $E_{\mathrm{V}} = 0.0$ eV, $E_{\mathrm{C}} = 1.5$ eV, $\gamma_{\mathrm{V}} = 60$ meV, and $\gamma_{\mathrm{C}} = 27$ meV. The lower bound result, also depicted with a light dotted line, corresponds to the DOS modeling parameter selections $N_{\mathrm{VO}} = N_{\mathrm{CO}} = 4.0 \times 10^{22}$ cm^{-3}eV$^{-3/2}$, $E_{\mathrm{V}} = 0.0$ eV, $E_{\mathrm{C}} = 1.9$ eV, $\gamma_{\mathrm{V}} = 40$ meV, and $\gamma_{\mathrm{C}} = 27$ meV. It is found that one is able to satisfactorily capture the experimental results of Remeš [58] with the DOS modeling parameter selections $N_{\mathrm{VO}} = 2.38 \times 10^{22}$ cm^{-3}eV$^{-3/2}$, $E_{\mathrm{V}} = 0.00$ eV, $E_{\mathrm{C}} = 1.66$ eV, $\gamma_{\mathrm{V}} = 43$ meV, and $\gamma_{\mathrm{C}} = 27$ meV. This fit is also depicted with a light dotted line.

distinguish between the various regions in the taxonomy of Wood and Tauc [60]. The distinction between region I and region II, for example, needs to be well defined if one wishes to discern between defect absorption and optical absorption related to the distributions of electronic states that encroach into the otherwise empty gap region of an amorphous semiconductor. The distinction between region II and region III also needs to be well defined if one wishes to delineate between optical absorption related to tail states and that related to band-to-band optical transitions [62].

In this section, a quantitative means of characterizing the classification scheme of Wood and Tauc [60] is proposed. In particular, following-up on an observation of Roxlo *et al.* [65], for a representative PECVD a-Si:H optical absorption experimental data set, through a series of linear least-squares fits of an exponential function to the optical absorption spectrum, taken over a number of optical absorption ranges, how the breadth of these exponential fits varies along the optical absorption spectrum of a-Si:H is determined; effectively, the reciprocal of the logarithmic derivative of the optical absorption spectrum is evaluated as a function of the optical absorption spectrum for the case of PECVD a-Si:H. It is found that the quantitative variations in the breadth of the exponential fits provides for a clear delineation between the different regions of the classification scheme of Wood and Tauc [60]. The analysis is completed by theoretically determining the form of the optical absorption spectrum using the JDOS functions corresponding to PECVD a-Si:H, this providing a theoretical basis for the interpretation of the results. This analysis builds upon the determination of the spectral dependence of the optical absorption coefficient that was presented in Section 4.9

In the interests of quantitatively characterizing region II, researchers have found it instructive to fit an exponential function to their experimental optical absorption data. That is, the function

$$\alpha(\hbar\omega) = \alpha_o \exp\left(\frac{\hbar\omega}{E_o}\right), \tag{4.15}$$

is fit to experimental optical absorption data, where α_o denotes a pre-exponential factor and E_o represents the breadth of the optical absorption tail. While extensive theoretical analyzes have suggested that region II is purely exponential in character [66, 67, 68], Roxlo *et al.* [65] noted, for the specific case of PECVD a-Si:H, that the optical absorption tail breadth, E_o, varies critically with the range of optical absorption values over which the fit of Eq. (4.15) to the experimental optical absorption data is taken. In particular, for their PECVD a-Si:H data set, Roxlo *et al.* [65] found that while fitting Eq. (4.15) to their experimental data, for 2×10^2 cm^{-1} $\leq \alpha(\hbar\omega) \leq 3\times10^3$ cm^{-1}, yielded E_o equal to 60 meV, fitting Eq. (4.15) to the same experimental data set, for 2×10^0 cm^{-1} $\leq \alpha(\hbar\omega) \leq 1 \times 10^3$ cm^{-1}, yielded E_o equal to 48 meV. This result hints at a logarithmic curvature in the PECVD a-Si:H optical absorption spectrum, $\alpha(\hbar\omega)$.

While a logarithmic curvature in the optical absorption spectrum of PECVD a-Si:H may very well account for the observation of Roxlo *et al.* [65], it is also possible that absorption corresponding to regions I and III is influencing the determination of E_o. The exact ranges of $\alpha(\hbar\omega)$ corresponding to the three different regions of the optical absorption spectrum depend critically on the material and the particular sample being considered. Thus, while Wood and Tauc [60] find, for their bulk chalcogenide amorphous semiconductor samples, that regions I, II, and III of the optical absorption spectrum correspond to $\alpha(\hbar\omega) < 1$ cm^{-1}, 1 cm^{-1} $\leq \alpha(\hbar\omega) \leq 10^4$

cm^{-1}, and $\alpha(\hbar\omega) > 10^4$ cm^{-1}, respectively, for other materials and samples, these ranges may differ. In addition, it should be noted that the boundaries between these regions may not be abrupt, regions I, II, and III possibly occurring over overlapping ranges of $\alpha(\hbar\omega)$; as the regions possibly overlap, "contamination" may occur, the obtained value of E_o corresponding to region II possibly being influenced by optical absorption corresponding to regions I and III. In order to develop some insight into this, a number of fits of Eq. (4.15) to a PECVD a-Si:H experimental data set will be performed over a variety of optical absorption ranges. From the variations in the optical absorption tail breadth, E_o, it is hoped to be able to observe boundaries in the optical absorption spectrum between regions I, II, and III.

For the purposes of this analysis, one representative PECVD a-Si:H data set, this experimental data set being from Remeš [58], is considered in this analysis. This PECVD a-Si:H experimental optical absorption data set is depicted in Figure 4.29. Representative linear least-squares fits of Eq. (4.15) to this experimental data set, taken over various ranges of the optical absorption spectrum, are depicted. Each such fit is performed for $\alpha_{\text{min}} \leq \alpha(\hbar\omega) \leq \alpha_{\text{max}}$, where α_{min} and α_{max} denote the lower and upper fit limits, respectively, these limits varying from fit to fit. It is clear that there are large variations in the obtained value of E_o, these reflecting the curvature in the optical absorption spectrum associated with PECVD a-Si:H. In Figure 4.30, the dependence of E_o on α is plotted, the representative fits depicted in Figure 4.29 being a subset of the total number of linear least-squares fits of Eq. (4.15) to the experimental data that was performed; the geometric mean

of $\alpha_{\min}$ and $\alpha_{\max}$, i.e., $\sqrt{\alpha_{\min}\alpha_{\max}}$, is taken as the representative optical absorption value corresponding to each fit.

As most theoretical analyzes suggest a purely exponential optical absorption tail over region II [66, 67, 68], the region of relatively constant E_o is interpreted as corresponding to "uncontaminated" region II, i.e., without any influence from regions I and III. In Figure 4.30, this region is seen to extend from 8 to 80 cm^{-1}, the corresponding characteristic value of E_o being 42 ± 2 meV. Concomitantly, the increases in E_o, corresponding to optical absorption values less than 8 cm^{-1} and greater than 80 cm^{-1}, are viewed as signaling that optical absorption corresponding to regions I and III, respectively, are making an impact. Similar results are found for other PECVD a-Si:H data sets, although the exact numerical values of E_o, and the range of optical absorption values over which "uncontaminated" region II extends, vary from sample-to-sample. Thus, the approach employed offers a means of delineating between regions I, II, and III.

In order to provide some theoretical structure for the interpretation of these experimental results, the optical absorption spectrum corresponding to PECVD a-Si:H is modeled. For the purposes of this analysis, the previously developed formalism for the JDOS function, $J(\hbar\omega)$, is used in order to determine the spectral dependence of the optical absorption coefficient, $\alpha(\hbar\omega)$. The corresponding optical absorption spectrum is then evaluated by noting that

$$\alpha(\hbar\omega) = D^2(\hbar\omega)J(\hbar\omega), \tag{4.16}$$

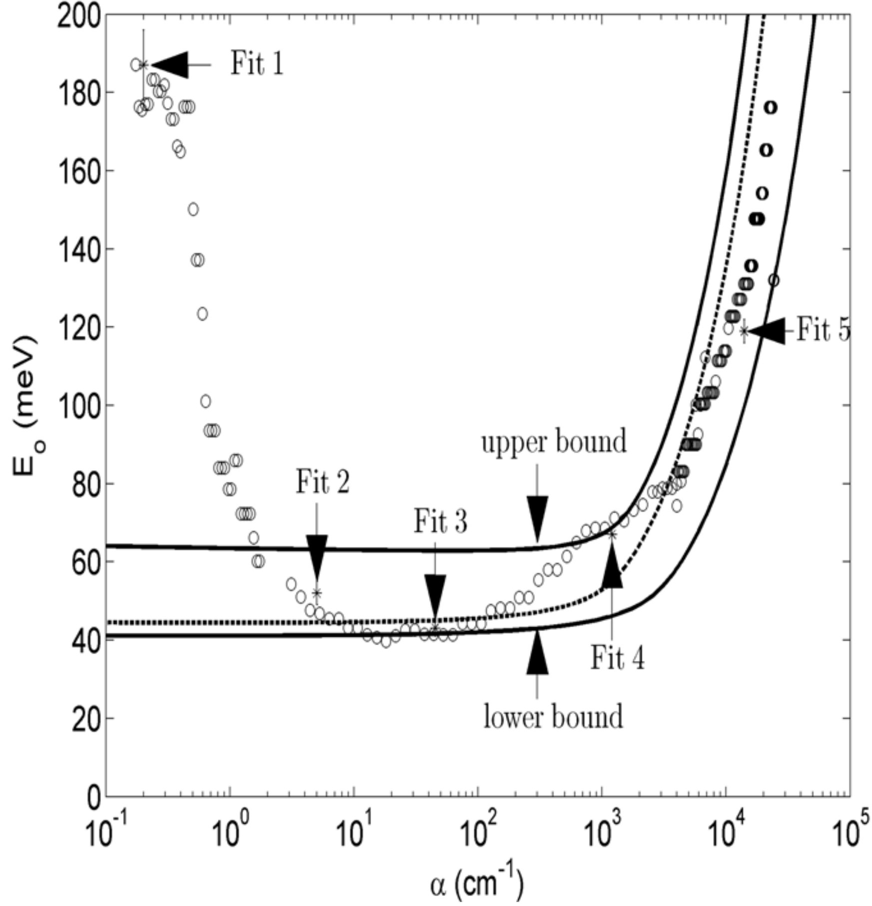

Figure 4.30: The dependence of E_o on α. The data points, depicted with the open points, correspond to the fit of Eq. (4.15) to the experimental data for various ranges of optical absorption. Results corresponding to the representative fits depicted in Figure 4.29 are shown with the asterisk points, the corresponding error bars being explicitly shown for these particular points. The evaluation of Eq. (4.18), for the case of the upper bound result, i.e., for the DOS modeling parameter selections $N_{\rm VO} = N_{\rm CO} = 2.0 \times 10^{22}$ cm^{-3}eV$^{-3/2}$, $E_{\rm V} = 0.0$ eV, $E_{\rm C} = 1.5$ eV, $\gamma_{\rm V} = 60$ meV, and $\gamma_{\rm C} = 27$ meV, is shown with a heavy solid line. The evaluation of Eq. (4.18), for the case of the lower bound result, i.e., for the DOS modeling parameter selections $N_{\rm VO} = N_{\rm CO} = 4.0 \times 10^{22}$ cm^{-3}eV$^{-3/2}$, $E_{\rm V} = 0.0$ eV, $E_{\rm C} = 1.9$ eV, $\gamma_{\rm V} = 40$ meV, and $\gamma_{\rm C} = 27$ meV, is also shown with a heavy solid line. The evaluation of Eq. (4.18), for the case of this fit with the experimental results of Remeš [58], i.e., for the DOS modeling parameter selections $N_{\rm VO} = N_{\rm CO} = 2.38 \times 10^{22}$ cm^{-3}eV$^{-3/2}$, $E_{\rm V} = 0.0$ eV, $E_{\rm C} = 1.66$ eV, $\gamma_{\rm V} = 43$ meV, and $\gamma_{\rm C} = 27$ meV, is shown with the dotted line.

where $D^2(\hbar\omega)$ may be related $n(\hbar\omega), c$, and ω, i.e., from Eqs. (3.9) and (4.14), it may be seen that

$$D^2(\hbar\omega) = 4.3 \times 10^{-45} \frac{\omega}{n(\hbar\omega)c} \Re^2(\hbar\omega). \tag{4.17}$$

With some reasonable assumptions made regarding the spectral dependence of $D^2(\hbar\omega)$ [45, 49, 50], the resultant optical absorption spectrum may be determined.

In Figure 4.29, this theoretical result is contrasted with the experimental results of Remeš [58]. Three different DOS modeling parameter selections are used for the purposes of this comparison, these DOS modeling parameter selections spanning over the range of values expected for the case of PECVD a-Si:H; (1) $N_{\mathrm{VO}} = N_{\mathrm{CO}} = 2.0 \times 10^{22}$ cm^{-3}eV$^{-3/2}$, $E_{\mathrm{V}} = 0.0$ eV, $E_{\mathrm{C}} = 1.5$ eV, $\gamma_{\mathrm{V}} = 60$ meV, and $\gamma_{\mathrm{C}} = 27$ meV, this forming a loose upper bound to the experimental results of Remeš [58], (2) $N_{\mathrm{VO}} = N_{\mathrm{CO}} = 4.0 \times 10^{22}$ cm^{-3}eV$^{-3/2}$, $E_{\mathrm{V}} = 0.0$ eV, $E_{\mathrm{C}} = 1.9$ eV, $\gamma_{\mathrm{V}} = 40$ meV, and $\gamma_{\mathrm{C}} = 27$ meV, this forming a loose lower bound to the experimental results of Remeš [58], and (3) $N_{\mathrm{VO}} = N_{\mathrm{CO}} = 2.38 \times 10^{22}$ cm^{-3}eV$^{-3/2}$, $E_{\mathrm{V}} = 0.0$ eV, $E_{\mathrm{C}} = 1.66$ eV, $\gamma_{\mathrm{V}} = 43$ meV, and $\gamma_{\mathrm{C}} = 27$ meV, this selection of DOS modeling parameters being made in order to fit the theoretical result with the experimental results of Remeš [57, 58]; this selection of DOS modeling parameters almost coincides with that set forth in Table 4.3, except the E_{C} value employed for this analysis is a little lower than that specified in Table 4.3. For the specific case of the fit, i.e., $N_{\mathrm{VO}} = N_{\mathrm{CO}} = 2.38 \times 10^{22}$ cm^{-3}eV$^{-3/2}$, $E_{\mathrm{V}} = 0.0$ eV, $E_{\mathrm{C}} = 1.66$ eV, $\gamma_{\mathrm{V}} = 43$ meV, and $\gamma_{\mathrm{C}} = 27$ meV, it is noted that while there are substantive differences observed for $\alpha(\hbar\omega) < 1$ cm^{-1}, i.e., region I, where defect absorption plays a critical role in influencing the form of the optical absorption spectrum, for most of regions II and III the agreement is reasonably satisfactory, the minor

discrepancies found probably being attributable to the overly simplistic selection of $D^2(\hbar\omega)$; recall that defect states are not accounted for in the empirical model for the DOS functions.

In order to further quantitatively contrast the results of the theoretical analysis with those of experiment, the breadth of the optical absorption spectrum is redefined as the inverse logarithmic derivative of $\alpha(\hbar\omega)$ at a particular value of α, i.e.,

$$E_o \equiv \left[\frac{d\ln[\alpha(\hbar\omega)]}{d(\hbar\omega)}\right]^{-1}_{\alpha(\hbar\omega)=\alpha}, \tag{4.18}$$

noting that this revised definition for E_o, while consistent with Eq. (4.15), provides for an analytical means whereby the evaluation of E_o, corresponding to the theoretical analysis, may be facilitated. Plotting E_o as a function of α in Figure 4.30, it is found that one is generally able to account for the increases in E_o as the optical absorption values move beyond "uncontaminated" region II, i.e., as optical absorption corresponding to region III starts to influence the results. It is noted, however, that discrepancies between the theoretical and experimental results are observed; the minor discrepancies between the theoretical optical absorption result and those of experiment account for these quantitative differences, the minor discrepancies observed in Figure 4.29 being amplified by the differential operator employed in Eq. (4.18). Nevertheless, it is found that the determined values of E_o are essentially sandwiched between the upper bound and lower bound results. As defect absorption is not included in the DOS model, no increases in E_o corresponding to optical absorption values below region II occur. However, it seems plausible that if the empirical DOS model was modified in order to include defect states

that such an increase in E_o would be noted as the influence of region I optical absorption becomes apparent.

Following-up on the observation of Roxlo *et al.* [65], it is found that through the fitting of Eq. (4.15) to an optical absorption PECVD a-Si:H experimental data set, over a number of ranges of the optical absorption spectrum, a means of delineating between regions I, II, and III of the optical absorption spectrum is obtained. In particular, it is found, for the PECVD a-Si:H experimental optical absorption data set that was considered, that the "uncontaminated" region II occurs between 8 to 80 cm^{-1}, the corresponding characteristic value of E_o being 42 ± 2 meV. This result suggests that the fit of Eq. (4.15) between $2 \times 10^2 \text{ cm}^{-1} \leq \alpha(\hbar\omega) \leq 3 \times 10^3 \text{ cm}^{-1}$ of Roxlo *et al.* [65], yielding an E_o equal to 60 meV, was "contaminated" with region III optical absorption. In addition, it suggests that the fit of Eq. (4.15) between $2 \text{ cm}^{-1} \leq \alpha(\hbar\omega) \leq 10^3 \text{ cm}^{-1}$ of Roxlo *et al.* [65], yielding an E_o equal to 48 meV, may have been "contaminated" both with region I and region III optical absorption. Given that this latter fit, i.e., $2 \text{ cm}^{-1} \leq \alpha(\hbar\omega) \leq 10^3 \text{ cm}^{-1}$, was more closely centered about the 8 to 80 cm^{-1} optical absorption range than the other fit, i.e., $2 \times 10^2 \text{ cm}^{-1} \leq \alpha(\hbar\omega) \leq 3 \times 10^3 \text{ cm}^{-1}$, it should come as no surprise that the E_o value determined from the latter fit of Roxlo *et al.* [65], i.e., 48 meV, is more similar to the 42 ± 2 meV determination than the other fit.

It should be pointed out that the analysis presented here could potentially help in improving the performance of amorphous semiconductor based electron devices. In particular, the "uncontaminated" value of E_o corresponding to region II plays a crucial role in determining the performance of solar cells. In large measure, the performance of a solar cell may be determined by: (1) the generation rate of

electron-hole pairs within the active electronic material, and (2) how readily these generated charge carriers may be extracted from this material. The larger that E_o is, the greater the absorption, and the greater the corresponding electron-hole pair generation rate. Unfortunately, greater E_o usually corresponds to greater amounts of disorder, and this detracts from the ability of the carriers to be extracted from the material, i.e., the transport becomes poorer. Clearly, there is a trade-off at play, as was alluded to earlier by Cody *et al.* [12]. The determination of an optimal value for E_o remains a subject of investigation. This quantitative characterization tool may help in this quest.

Finally, attention should be drawn to a limitation of this analysis. Since the pioneering work of Tauc *et al.* [40], square-root distributions of band states have been assumed in many amorphous semiconductor analyses. There is reason to believe that in many amorphous semiconductors that there may be deviations from this assumption. Singh [69], for example, points out that the exact form of the DOS functions depends critically on the material system. The empirical DOS model that is employed here for the purposes of this analysis, i.e., Eqs. (4.3) and (4.4), assume square-root distributions of band states. Perhaps this limitation in the analysis may account for some of the differences that are observed between the theoretical results and that of experiment. This will have to be investigated further in the future.

4.11 Effective mass determinations

In the study of crystalline semiconductors, the effective mass of the electrons and holes plays an important role in determining the properties of these materials.

In a crystalline semiconductor, the effective masses associated with the holes and electrons provides a measure of the sharpness of the parabolic form of the band maximum associated with the valence band and the band minimum associated with the conduction band, respectively, the sharper these parabola, the lower the effective masses. For the case of a-Si:H, $\vec{k}$ is a poor quantum number, and, as a consequence, bands, in the crystalline sense of the word, do not exist. Nevertheless, using the DOS prefactor selections, they can be defined for the case of PECVD a-Si:H, as was previously suggested by Malik and O'Leary [48].

Following the analysis of Malik and O'Leary [48], the hole and electron DOS effective masses may be readily ascertained from the valence band and conduction band DOS functions, $N_{\mathrm{V}}(E)$ and $N_{\mathrm{C}}(E)$, respectively. Assuming parabolic bands, as in the case of a crystalline semiconductor, it can be shown that the valence band DOS prefactor,

$$N_{\mathrm{VO}} = \sqrt{2}\frac{m_{\mathrm{V}}^{*3/2}}{\pi^2 \hbar^3}, \tag{4.19}$$

and that the conduction band DOS prefactor

$$N_{\mathrm{CO}} = \sqrt{2}\frac{m_{\mathrm{C}}^{*3/2}}{\pi^2 \hbar^3}, \tag{4.20}$$

where m_{V}^* and m_{C}^* represent the valence band and conduction band DOS effective masses, respectively; recall Eq. (2.15), the free-electron DOS model. The fits depicted in Figures 4.3 and 4.4, by fitting Eqs. (4.7) and (4.8) to the square of the experimental PECVD a-Si:H DOS results of Jackson *et al.* [49], correspond to DOS effective mass selections $m_{\mathrm{V}}^* = 2.59\ m_e$ and $m_{\mathrm{C}}^* = 3.02\ m_e$, where m_e denotes the free electron mass; the errors in these determinations are 0.25 m_e and 0.40 m_e, respectively; the symmetric DOS parameter selections of O'Leary [46],

i.e., $N_{\mathrm{VO}} = N_{\mathrm{CO}} = 2.38 \times 10^{22}$ cm^{-3}eV$^{-3/2}$, are not employed as the asymmetries which occur play an important role in determining the corresponding effective masses, but play no role in influencing the form of the JDOS function. These results contrast rather dramatically with the case of c-Si, for which $m_{\mathrm{V}}^{*} = 0.56\ m_e$ and $m_{\mathrm{C}}^{*} = 1.08\ m_e$ [70]. A comparison of these DOS effective masses, for the cases of PECVD a-Si:H and c-Si, is depicted in Figure 4.31. Similar results were obtained by Malik and O'Leary [48].

The exact reasons for the differences in the effective masses are at present unknown. Noting that the effective mass of carriers deeper into the bands is greater than those near the band edges, one could speculate that the fact that the greater energy gap associated with PECVD a-Si:H rather than c-Si is leading to a sampling of the 'pseudo' band structure associated with a-Si:H into regions with much heavier effective masses. A detailed theoretical analysis of this issue, which is beyond the scope of this thesis, would be interesting.

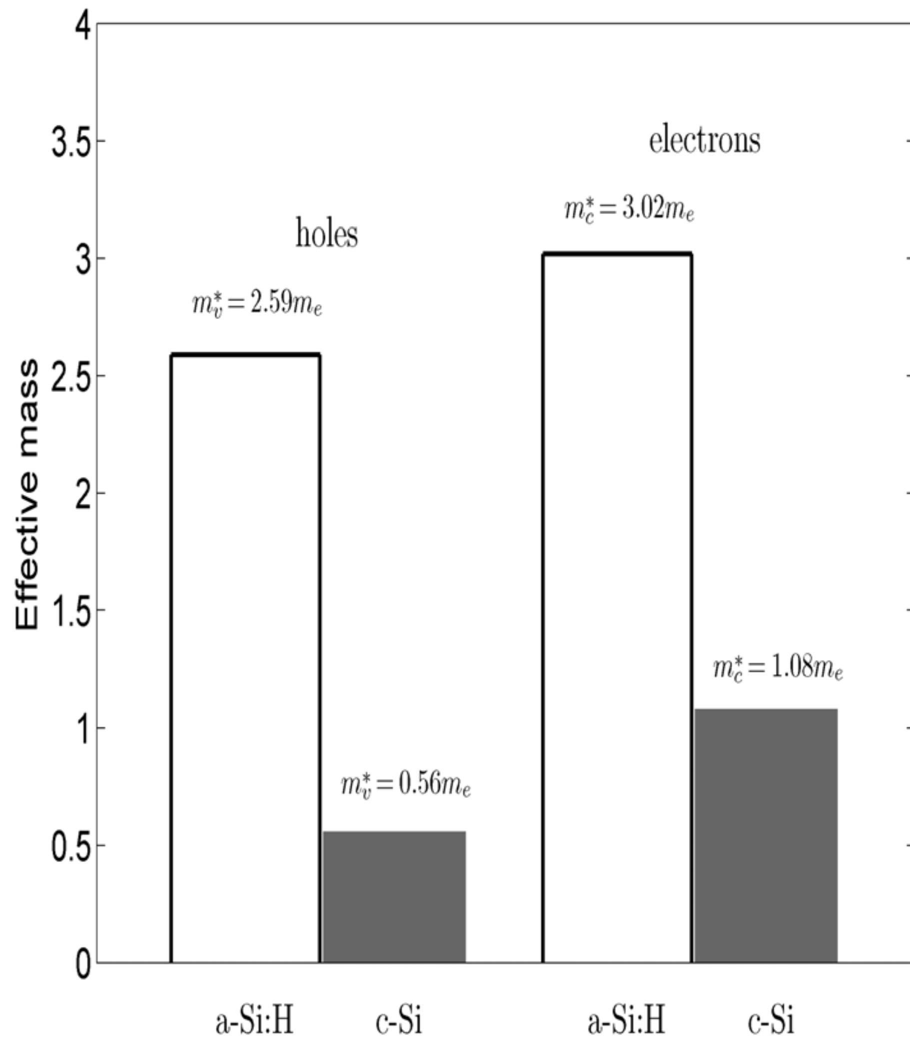

Figure 4.31: A comparison of the DOS effective masses associated with PECVD a-Si:H and c-Si.

5. CONCLUSIONS

In this thesis, a quantitative analysis of the optical response of amorphous semiconductors was presented. The entire analysis was cast within the framework of an empirical model for the valence band and conduction band DOS functions, $N_{\mathrm{V}}(E)$ and $N_{\mathrm{C}}(E)$, respectively, that captures the basic features expected of these functions. A novel aspect of this analysis was the introduction of the density of localized valence band electronic states, n_{VBL}, and the density of localized conduction band electronic states, n_{CBL}, and the establishment of a means of evaluating these densities from knowledge of the DOS functions coupled with the locations of the valence band and conduction band mobility edges, $E_{\mathrm{V}\mu}$ and $E_{\mathrm{C}\mu}$, respectively. The determination of the contributions to the JDOS function attributable to the VBE-CBE, VBE-CBL, VBL-CBE, and VBL-CBL optical transitions, as a function of the location of these mobility edges, was another novel feature of this analysis. This formalism was then applied in order to determine the spectral dependence of the normalized dipole matrix element squared average, $\Re^2(\hbar\omega)$. A means of determining the spectral dependence of the optical absorption coefficient, $\alpha(\hbar\omega)$, was also provided. Finally, the DOS and JDOS formalisms that were developed were applied to the specific case of PECVD a-Si:H, this being the most widely used amorphous semiconductor at present, and conclusions were drawn concerning the nature of this particular material.

In Chapter 2, the empirical model for the valence band and conduction band DOS functions, $N_{\mathrm{V}}(E)$ and $N_{\mathrm{C}}(E)$, respectively, was introduced. This empirical model for these DOS functions, which is used throughout the entire thesis,

captures the basic features expected of these functions. In particular, it exhibits a square-root functional dependence in the band states and an exponential functional dependence in the tail states, the breadths of these tails reflecting the amount of disorder that is present. In the valence band, two types of states occur, VBE and VBL, these states being separated by the valence band mobility edge, $E_{\mathrm{V}\mu}$. Similarly, in the conduction band, two types of states occur, CBE and CBL, these states being separated by the conduction band mobility edge, $E_{\mathrm{C}\mu}$. From knowledge of the location of the mobility edge associated with the valence band, $E_{\mathrm{V}\mu}$, the empirical model for the valence band DOS function was employed in order to evaluate the density of localized valence band electronic states, n_{VBL}. Similarly, from knowledge of the location of the mobility edge associated with the conduction band, $E_{\mathrm{C}\mu}$, the empirical model for the conduction band DOS function was employed in order to evaluate the density of localized conduction band electronic states, n_{CBL}. The sensitivity of n_{VBL} to the location of the valence band mobility edge, $E_{\mathrm{V}\mu}$, and the sensitivity of n_{CBL} to the location of the conduction band mobility edge, $E_{\mathrm{C}\mu}$, was then explored.

Then, in Chapter 3, the valence band and conduction band DOS functions, $N_{\mathrm{V}}(E)$ and $N_{\mathrm{C}}(E)$, respectively, were related to the spectral dependence of the imaginary part of the dielectric function, $\epsilon_2(\hbar\omega)$, this being a key function in the characterization of the optical response of an amorphous semiconductor. The JDOS function, $J(\hbar\omega)$, was introduced as a corollary. Then, within the framework of the empirical model for the DOS functions, the spectral dependence of the JDOS integrand, $N_{\mathrm{V}}(E)N_{\mathrm{C}}(E+\hbar\omega)$, and the JDOS itself, $J(\hbar\omega)$, was examined. Noting that four types of optical transitions are possible within the framework

of the empirical model for the DOS functions, i.e., VBE-CBE optical transitions, VBE-CBL optical transitions, VBL-CBE optical transitions, and VBL-CBL optical transitions, a means of determining the contributions to the JDOS function corresponding to these four different types of optical transitions was developed, the dependence of these contributions on the valence band and conduction band mobility edges, $E_{\mathrm{V}\mu}$ and $E_{\mathrm{C}\mu}$, respectively, being probed. Using this formalism, in conjunction with an elementary model for the optical transition matrix elements, the spectral dependence of the normalized dipole matrix element squared average, $\Re^2(\hbar\omega)$, was then demonstrated. Finally, a means of evaluating the spectral dependence of the optical absorption coefficient, $\alpha(\hbar\omega)$, this being another important function in the characterization of the optical response of an amorphous semiconductor, was provided.

In Chapter 4, the DOS and JDOS formalisms, developed in the previous chapters, were applied to the specific case of PECVD a-Si:H, this being the most widely used amorphous semiconductor at present. The analysis started with a determination of the underlying DOS modeling parameters from the experimental PECVD a-Si:H DOS results of Jackson *et al.* [49]. Then, the JDOS corresponding to PECVD a-Si:H was computed and compared with that determined by Jackson *et al.* [49]. The JDOS function contributions, corresponding to the VBE-CBE, VBE-CBL, VBL-CBE, and VBL-CBL optical transitions, were then evaluated for the specific case of PECVD a-Si:H. The spectral dependence of the normalized dipole matrix element squared average, $\Re^2(\hbar\omega)$, was also examined for the specific case of this material, the sensitivity of this spectral dependence to the location of

the valence band and conduction band mobility edges, $E_{\mathrm{V}\mu}$ and $E_{\mathrm{C}\mu}$, respectively being examined.

Then, three interesting applications of this formalism were presented. For the first application, we examined how variations in the spectral dependence of the normalized dipole matrix element squared average, $\Re^2(\hbar\omega)$, impact upon the spectral dependence of the optical properties associated with PECVD a-Si:H. It was also ascertained as to whether or not the PECVD a-Si:H mobility gap result suggested by Jackson *et al.* [49] is consistent with the results of experiment. We found that the mobility gap value suggested by Jackson *et al.* [49] is too large. An upper bound on the mobility gap associated with PECVD a-Si:H of 1.68 eV was suggested instead. Electrical measurements, performed by others on undoped PECVD a-Si:H, were shown to yield mobility gap values that are consistent with this bound. For the second application, a quantitative means of characterizing the optical absorption spectrum associated with an amorphous semiconductor was proposed. In particular, for a representative PECVD a-Si:H optical absorption experimental data set, through a series of linear least-squares fits of an exponential function to this experimental data set, taken over a number of optical absorption ranges, how the breadth of the optical absorption tail varies along the optical absorption spectrum of PECVD a-Si:H was examined. It was found that the quantitative variations in the breadth of the optical absorption tail that are found provide for a clear delineation between the different regions of the optical absorption spectrum of PECVD a-Si:H. This analysis was completed by theoretically determining the form of the optical absorption spectrum using the DOS and JDOS formalism for the specific

case of PECVD a-Si:H, this analysis providing a theoretical basis for the interpretation of the results.

A third and final application of the results determined in this thesis focused on the determination of the effective masses associated with the electrons and holes within PECVED a-Si:H. Employing the DOS prefactor values that the fits with the experimental PECVD a-Si:H DOS results of Jackson *et al.* [49] produced, these effective masses were found to be $(3.02 \pm 0.40)m_e$ and $(2.59 \pm 0.25)m_e$, for the electrons and holes, respectively. These values were noted to be much greater than those associated with c-Si suggesting something fundamental to the character of PEVD a-Si:H that plays a role in this. A speculation as to the source of this observation was provided.

Within the framework of the DOS and JDOS formalism that has been developed within the body of this thesis, there are a variety of issues that could be further examined. In general, these issues include further developments to the empirical DOS model itself, further analysis using the already developed DOS and JDOS formalism, and an examination of the device implications of this formalism. Clearly, there a wide array of topics of interest that could be considered within the framework of these overarching research themes. Three issues that are particularly prescient at the present moment have been identified. These issues are: (1) the implementation of further refinements to this formalism, these refinements addressing some of its shortcomings, (2) the application of this formalism to a broader range of amorphous semiconductors, and (3) the device implications of this formalism. Each of these topics is further discussed below.

Further refinements to the empirical model for the DOS functions, that address its shortcomings, would be useful. As was seen in Chapter 4, the assumption of square-root band DOS functions for PECVD a-Si:H was shown to be only valid in the immediate range of the valence band and conduction band band edges, $E_{\rm V}$ and $E_{\rm C}$, respectively. Beyond these narrow square-root regions, however, dramatic departures from the square-root functional form were observed. These differences likely arise as a consequence of the finiteness of the bands. Developing an empirical model for the valence band and conduction band DOS functions, $N_{\rm V}(E)$ and $N_{\rm C}(E)$, respectively, that takes into account the finiteness of the bands, would allow for the development of an empirical model for these DOS functions that more adequately captures the results of experiment. The inclusion of defect states would also be a useful addition to the empirical model for the DOS functions. With these refinements, the resultant JDOS function, $J(\hbar\omega)$, would be in greater accord with that of experiment.

The applicability of this formalism to other amorphous semiconductors of interest would certainly be a topic worthy of further investigation. Unfortunately, at the present moment, the DOS functions associated with other amorphous semiconductors have yet to be determined with the degree of thoroughness with which PECVD a-Si:H was investigated. Experimental determinations of these DOS functions would allow for the determination of the DOS modeling parameters corresponding to other amorphous semiconductors of interest. The resultant JDOS function, $J(\hbar\omega)$, would then be evaluated, and, from such an analysis, the spectral dependence of $\Re^2(\hbar\omega)$ could be ascertained. From such an analysis, it is hoped to determine whether of not Eq. (3.9) applies to a broad range of materials

Finally, how the presence of localized electronic states within an amorphous semiconductor detracts from the performance of an amorphous semiconductor based electron device could be examined. As the charge carriers, be they electrons or holes, that reside within localized electronic states are not able to participate in the usual charge transport processes, i.e, they remain localized, the performance of an electron device will be degraded through the introduction of these types of electronic states. This degradation occurs as a natural consequence of the disorder that is present within these materials, i.e., their atomic distributions are disordered, and, as a consequence, localized electronic states are present. The JDOS formalism that has been developed within this thesis will allow for the quantitative evaluation of how these localized electronic states detract from the corresponding device performance. A comparison with the results of experiment may be used in order to validate this analysis.

REFERENCES

[1] "Displays as key driver for large area electronics in intelligent environments: A vision for Europe 2007+," in *A proposal for the advancement of the IST thematic priority.* Information Society Technologies, May 2005.

[2] M. G. Clark, "Current status and future prospects of poly-Si devices," *IEE Proceedings-Circuits, Devices and Systems*, vol. 141, pp. 3–8, 1994.

[3] D. E. Carlson and C. R. Wronski, "Amorphous silicon solar cell," *Applied Physics Letters*, vol. 28, pp. 671–673, 1976.

[4] M. Zeman, J. A. Willemen, L. L. A. Vosteen, G. Tao, and J. W. Metselaar, "Computer modeling of current matching in a-Si:H/a-Si:H tandem solar cells on textured TCO substrates," *Solar Energy Materials and Solar Cells*, vol. 46, pp. 81–99, 1997.

[5] J. H. Daniel, B. Krusor, R. B. Apte, M. Mulato, K. Van Schuylenbergh, R. Lau, T. Do, R. A. Street, A. Goredema, D. C. Boils-Boissier, and P. M. Kazmaier, "Micro-electro-mechanical system fabrication technology applied to large area x-ray image sensor arrays," *Journal of Vacuum Science and Technology A*, vol. 19, pp. 1219–1223, 2001.

[6] S. O. Kasap and J. A. Rowlands, "X-ray photoconductors and stabilized a-Se for direct conversion digital flat-panel X-ray image-detectors," *Journal of Materials Science: Materials in Electronics*, vol. 11, pp. 179–198, 2000.

[7] J. I. Pankove, *Optical Processes in Semiconductors.* Englewood Cliffs, NJ: Prentice-Hall, 1971.

[8] R. A. Steet, *Hydrogenated Amorphous Silicon.* New York, NY: Cambridge University Press, 1991.

[9] D. W. Greve, *Field Effect Devices and Applications.* Upper Saddle River, NJ: Prentice-Hall, 1998.

[10] M. H. Cohen, H. Fritzsche, and S. R. Ovshinsky, "Simple band model for amorphous semiconducting alloys," *Physical Review Letters*, vol. 22, pp. 1065–1068, 1969.

[11] M. Shur, *Introduction to Electronic Devices.* New York: John Wiley and Sons Inc., 1996.

[12] G. D. Cody, T. Tiedje, B. Abeles, B. Brooks, and Y. Goldstein, "Disorder and the optical-absorption edge of hydrogenated amorphous silicon," *Physical Review Letters*, vol. 47, pp. 1480–1483, 1981.

[13] J. Tauc, *The Optical Properties of Solids*, F. Abeles, Ed., North Holland, Amsterdam, 1972.

[14] M. H. Brodsky, R. S. Title, K. Weiser, and G. D. Pettit, "Structural, optical, and electrical properties of amorphous silicon films," *Physical Review B*, vol. 1, pp. 2632–2641, 1970.

[15] W. B. Jackson, "The correlation energy of the dangling silicon bond in a-Si:H," *Solid State Communicatons*, vol. 44, pp. 477–480, 1982.

[16] S. K. O'Leary, S. Zukotynski, and J. M. Perz, "Semiclassical density-of-states and optical-absorption analysis of amorphous semiconductors," *Physical Review B*, vol. 51, pp. 4143–4149, 1995.

[17] S. K. O'Leary, S. Zukotynski, and J. M. Perz, "Optical absorption in amorphous semiconductors," *Physical Review B*, vol. 52, pp. 7795–7797, 1995.

[18] S. M. Malik and S. K. O'Leary, "Optical transitions in hydrogenated amorphous silicon," *Applied Physics Letters*, vol. 80, pp. 790–792, 2002.

[19] R. S. Crandall, "Band-tail absorption in hydrogenated amorphous silicon," *Physical Review Letters*, vol. 44, pp. 749–752, 1980.

[20] D. Dasgupta, F. Demichelis, C. F. Pirri, and A. Tagliaferro, "π bands and gap states from optical absorption and electron-spin-resonance studies on amorphous carbon and amorphous hydrogenated carbon films," *Physical Review B*, vol. 43, pp. 2131–2135, 1991.

[21] S. O. Kasap, *Priniciples of Electrical Engineering Materials and Devices*. Boston: Irwin McGraw-Hill, 1997.

[22] S. Sherman, S. Wagner, and R. A. Gottscho, "Correlation between the valence- and conduction-band-tail energies in hydrogenated amorphous silicon," *Applied Physics Letters*, vol. 69, pp. 3242–3244, 1996.

[23] F. Orapunt and S. K. O'Leary, "The Urbach focus and hydrogenated amorphous silicon," *Applied Physics Letters*, vol. 84, pp. 523–525, 2004.

[24] K. Weiser and M. H. Brodsky, "dc conductivity, optical absorption, and photoconductivity of amorphous arsenic telluride films," *Physical Review B*, vol. 1, pp. 791–799, 1970.

[25] T. Datta and J. A. Woollam, "Generalized model for the optical absorption edge in a-Si:H," *Physical Review B*, vol. 39, pp. 1953–1954, 1989.

[26] S. K. O'Leary, B. J. Fogal, D. J. Lockwood, J.-M. Baribeau, M. Noël, and J. C. Zwinkels, "Optical dispersion relationships in amorphous silicon grown by molecular beam epitaxy," *Jounal of Non-Crystalline Solids*, vol. 290, pp. 57–63, 2001.

[27] B. J. Fogal, S. K. O'Leary, D. J. Lockwood, J.-M. Baribeau, M. Noël, and J. C. Zwinkels, "Disorder and the optical properties of amorphous silicon grwon by melocular beam epitaxy," *Solid State Communications*, vol. 120, pp. 429–434, 2001.

[28] G. D. Cody, in *Semiconductors and Semimetals*, J. I. Pankove, Ed., vol. 21B. New York: Academic Press, 1984, p. 11.

[29] "Science in the making," E. A. Davis, Ed., vol. 4: 1950-Present. London: Taylor and Francis, 1999.

[30] T. H. Nguyen, "A theory of occupation statistics for disordered semiconductors with applications," Master's thesis, University of Regina, Regina, Saskatchewan, 2000.

[31] B. G. Streetman, *Solid State Electronic Devices*, 3rd ed. Englewood Cliffs, New Jersey: Prentice-Hall, 1990.

[32] S. M. Malik, "A density of states and joint density of states analysis of hydrogenated amorphous silicon," Master's thesis, University of Regina, Regina, Saskatchewan, 2002.

[33] S. C. Moss and J. F. Craczyk, "Evidence of voids within the As-deposited structure of glass silicon," *Physical Review Letters*, vol. 20, pp. 1167–1171, 1969.

[34] A. Barna, P. B. Barna, G. Rodnoczi, L. Toth, and P. Thomas, "Comparative study of the structure of evaporate and glow discharge silicon," *Physica Status Solidi A*, vol. 41, pp. 81–84, 1977.

[35] P. W. Anderson, "Absence of diffusion in certain random lattices," *Physical Review*, vol. 109, pp. 1492–1505, 1958.

[36] N. F. Mott and E. A. Davis, *Electronic Processes in Non-Crystalline Materials*, 2nd ed. Oxford: Clarendon Press, 1979.

[37] F. Seitz, *The Modern Theory of Solids.* New York: McGraw-Hill, 1940.

[38] J. J. Thevaril, "The optical response of hydrogenated amorphous silicon," Ph. D. Thesis, University of Windsor, Windsor, Ontario, Canada, 2011.

[39] T. H. Nguyen and S. K. O'Leary, "The dependence of the Fermi level on temperature, doping concentration, and disorder in disordered semiconductors," *Journal of Applied Physics*, vol. 88, pp. 3479–3483, 2000.

[40] J. Tauc, R. Grigorovici, and A. Vancu, "Optical properties and electronic structure of amorphous germanium," *Physica Status Solidi B*, vol. 15, pp. 627–637, 1966.

[41] T. Tiedje, J. M. Cebuka, D. L. Morel, and B. Abeles, "Evidence of exponential band tails in amorphous silicon hydride," *Physical Review Letters*, vol. 46, pp. 1425–1428, 1981.

[42] W.-C. Chen, B. J. Feldman, J. Bajaj, F.-M. Tong, and G. K. Wong, "Thermalization gap excitation photoluminescence and optical absorption in amorphous silicon-hydrogen alloys," *Solid State Communications*, vol. 38, pp. 357–363, 1981.

[43] D. Redfield, "Energy-band tails and the optical absorption edge; the case of a-Si:H," *Solid State Communications*, vol. 44, pp. 1347–1349, 1982.

[44] L. Jiao, I. Chen, R. W. Collins, C. R. Wronski, and N. Hata, "An improved analysis for band edge optical absorption spectra in hydrogenated amorphous silicon from optical and photoconductivity measurements," *Applied Physics Letters*, vol. 72, pp. 1057–1059, 1998.

[45] S. K. O'Leary, S. R. Johnson, and P. K. Lim, "The relationship between the distribution of electronic states and the optical absorption spectrum of and amorphous semiconductor: An empirical analysis," *Journal of Applied Physics*, vol. 82, pp. 3334–3340, 1997.

[46] S. K. O'Leary, "An empirical density of states and joint density of states analysis of hydrogenated amorphous silicon: a review," *Journal of Materials Science: Materials in Electronics*, vol. 15, pp. 401–410, 2004.

[47] S. K. O'Leary, "An analytical density of states and joint density of states analysis of amorphous semiconductors," *Journal of Applied Physics*, vol. 96, pp. 3680–3686, 2004.

[48] S. M. Malik and S. K. O'Leary, "An analysis of the distributions of electronic states associated with hydrogenated amorphous silicon," *Journal of Materials Science: Materials in Electronics*, vol. 16, pp. 177–181, 2005.

[49] W. B. Jackson, S. M. Kelso, C. C. Tsai, J. W. Allen, and S.-J. Oh, "Energy dependence of the optical matrix element in hydrogenate amorphous and crystalline silicon," *Physical Review B*, vol. 31, pp. 5187–5198, 1985.

[50] S. K. O'Leary, "Spectral dependence of the squared average optical transition matrix element associated with hydrogenated amorphous silicon," *Applied Physics Letters*, vol. 82, pp. 2784–2786, 2003.

[51] N. K. Hindley, "Random phase model of amorphous semiconductors I. Transport and optical properties," *Jounal of Non-Crystalline Solids*, vol. 5, pp. 17–30, 1970.

[52] J. Tauc, *Amorphous and Liquid Semiconductors*, J. Tauc, Ed. New York: Plenum Press, 1984.

[53] J. Singh and K. Shimakawa, *Advances in Amorphous Semiconductors.* London: Taylor and Francis, 2003.

[54] M. Abkowitz, "Density of states in a-Se from combined analysis of xerographic potentials and transient transport data," *Philosophical Magazine Letters*, vol. 58, pp. 53–57, 1988.

[55] J. J. Thevaril and S. K. O'Leary, "A dimensionless joint density of states formalism for the quantitative charaterization of the optical response of hydrogenated amorphous silicon," *Journal of Applied Physics*, vol. 107, pp. 083 105–1–6, 2010.

[56] R. H. Klazes, M. H. L. M. van den Broek, J. Bezemer, and S. Radelaar, "Determination of the optical bandgap of amorphous silicon," *Philosophical Magazine B*, vol. 45, pp. 377–383, 1982.

[57] T. M. Mok and S. K. O'Leary, "The dependence of the Tauc and Cody optical gaps associated with hydrogenated amorphous silicon on the film thickness: αl experimental limitations and the impact of curvature in the Tauc and Cody plots," *Journal of Applied Physics*, vol. 102, pp. 113 525–1–9, 2007.

[58] Z. Remeš, "Study of defects and microstructure of amorphous and microcrystalline silicon thin films and polycrystalline diamond using optical methods," Ph. D. Thesis, Charles University, Prague, 1999.

[59] R. E. Viturro and K. Weiser, "Some properties of hydrogenated amorphous silicon produced by direct reaction of silicon and hydrogen atoms," *Philosophical Magazine B*, vol. 53, pp. 93–103, 1986.

[60] D. L. Wood and J. Tauc, "Weak absorptions tail in amorphous semiconductors," *Physical Review B*, vol. 5, pp. 3144–3151, 1972.

[61] S. K. O'Leary and S. M. Malik, "A simplified joint density of state analysis of hydrogenated amorphous silicon," *Journal of Applied Physics*, vol. 92, pp. 4276–4282, 2002.

[62] S. M. Malik and S. K. O'Leary, "Deviations from square-root distributions of electronic states in hydrogenated amorphous silicon and their impact upon the resultant optical properties," *Jounal of Non-Crystalline Solids*, vol. 336, pp. 64–70, 2004.

[63] S. K. O'Leary, L. S. Sidhu, S. Zukotynski, and J. M. Perz, "Optical absorption, disorder, and hydrogen in amorphous silicon," *Canadian Journal of Physics (Suppl.)*, vol. 74, pp. S256–S259, 1996.

[64] B. Abeles, C. R. Wronski, T. Tiedje, and G. D. Cody, "Exponential absorption edge in hydrogenated a-Si films," *Solid State Communications*, vol. 36, pp. 537–540, 1980.

[65] C. B. Roxlo, B. Abeles, C. R. Wronski, G. D. Cody, and T. Tiedje, "Comment on the optical absorption edge in a-Si:H," *Solid State Communications*, vol. 47, pp. 985–987, 1983.

[66] S. John, C. Soukoulis, M. H. Cohen, and E. N. Economou, "Theory of electron band tails and the Urbach optical-absorption edge," *Physics Review Letters*, vol. 57, pp. 1777–1780, 1986.

[67] G. D. Cody, "Urbach edge of crystalline and amorphous silicon: a personal review," *Jounal of Non-Crystalline Solids*, vol. 141, pp. 3–15, 1992.

[68] S. K. O'Leary and P. K. Lim, "Influence of the kinetic energy of localization on the distribution of electronic states in amorphous semiconductors," *Applied Physics A - Materials Science and Processing*, vol. 66, pp. 53–58, 1998.

[69] J. Singh, "Influence of disorder on the electronic structure of amorphous silicon," *Physical Review B*, vol. 23, pp. 4156–4168, 1981.

[70] D. A. Neamen, *Semiconductor Physics and Devices*. Boston: Irwin, 1992.